A Travelling Wave Zeeman Decelerator For Atoms and Molecules

LEWIS ALEXANDER MCARD

How to cite:

MCARD, LEWIS ALEXANDER (2018) A Travelling Wave Zeeman Decelerator For Atoms and Molecules. Doctoral thesis, Durham University.

A Travelling Wave Zeeman Decelerator For Atoms and Molecules

Lewis A. McArd

A Thesis presented for the degree of
Doctor of Philosophy

Department of Physics,

Durham University,

England.
September 2017

Abstract

The design of a modular moving trap Zeeman decelerator capable of decelerating gas pulses produced from a supersonic source is presented here. Unlike the conventional form of Zeeman decelerator, paramagnetic particles are confined in a 3D potential throughout the deceleration process. The decelerator field is produced by flattened helical coils and currents of up to 1000 A peak. As the coils are periodic in nature, each coil produces a number of deep, quadrupole traps along the molecular beam axis. The resultant periodic field is described as a travelling wave. The application of the appropriate time dependent current allows the traps to move through the four coil modules. In order to compensate for the weaker transverse confinement, a quadrupole guide, operating at 700 A DC, is required to prevent further losses during the deceleration process. The operation of the decelerator relies on the power electronics developed specifically for the quadrupole and the decelerator coils. Due to the electromagnetic interference generated through the switching of the large currents, much of the electronics used to control the power electronics had to be developed specifically. The quadrupole power electronics have been designed to produce fast switching edges. This is necessary to minimise the interaction of the particles within the fringe field regions while maximising the interaction time within the pure quadrupole field. Even at a modest voltage applied to the circuitry, the rise time in current to 700 A has been reduced by a half. The decelerator power electronics must be capable of producing an alternating waveform with an amplitude of at least 500 A for each of the coil phases. Furthermore, the frequency of the waveforms must be tunable within a range of 10 kHz to 0 Hz. Through a combination of pulse width modulation and knowledge of the electrical properties of the coil it is possible to synthesise an alternating current waveform from a 800 V DC supply using a suitable switching circuit.

Modelling the magnetic fields generated by the decelerator coils has been necessary in order to understand the phase space acceptance of the decelerator. The helical nature of the coils required the development of a specific algorithm in order to calculate the field generated by each wire element. The resultant potential can then be interpolated using a tricubic interpolator to extract the field gradients necessary for numerical simulations of the particle trajectories. Including the effects of the pulse width modulated on the trap facilitates the characterisation of the acceptance of the decelerator and the limitations of the current iteration of the design. The numerical simulations can also be compared to experimental results gathered for metastable argon. The 3D guiding, or velocity bunching, of the gas packet over a range of velocities has been demonstrated. The ability to 3D guide and decelerate were severely hampered by the failure of key electronic components, limiting three coils to 100 A peak, moreover, these traps were sub-optimally loaded. Deceleration from 350 to 347 $\mathrm{m\,s^{-1}}$ and 342 to 310 $\mathrm{m\,s^{-1}}$ has been observed. The design of a trap capable of simultaneously loading samples of decelerated CaH and Li while allowing the cooling of Li would potentially allow for the sympathetic cooling of a molecular species with an atomic refrigerant. This particular atom-molecule system would also facilitate the examination of controlled chemistry and collisions over a range of temperatures through state selection of the reactants. The loading of the trap has been optimised in 1D for CaH with a loading efficiency of 52.2 % while only 7.3 % of Li is loaded when each of the gas packets has a mean velocity of 11 $\mathrm{m\,s^{-1}}$. This implies that the source of the Li must be at least 130 times brighter than that of the CaH.

Declaration

The work in this thesis is based on research carried out at the Department of Physics, Durham, England. It is all my own work unless referenced to the contrary in the text. I confirm that no part of the material offered has previously been submitted by myself for a degree in this or any other University.

Lewis A. McArd
Durham, February 5, 2018

”In the face of overwhelming odds, I’m left with only one option:
I’m going to have to science the shit out of this.”
-Andy Weir, The Martian.

Acknowledgements

I would like to start by thanking my supervisor, David Carty, for his guidance, support and patience throughout my Masters and PhD. Over the course of those five years he has been nothing but a brilliant supervisor who has always been enthusiastic and has had a positive lookout despite the tribulations along the way. I am also grateful that he gave me an opportunity, to not only continue to learn, but also gave me the possibility to develop skills that I suspect otherwise I would never have had chance to. I would also like to acknowledge the UK Engineering and Physical Sciences Research Council and the MicroKelvin Molecules in a Quantum Array (MMQA) programme which funded this PhD.

Projects such as this one rely heavily on the expertise of the technicians of both the mechanical and electronics workshops. Although Paul White and Lee Mcalpine have both been assigned to work on this project, many member of the physics mechanical workshop have also spent time producing parts for the decelerator. Similarly, each of the technicians in the electronics workshop have also spent some fair time working on the project. I thank each and everyone of these technicians, without whom this would not have been possible. I am particularly indebted to John Scott, who I spent the majority of my first year working with developing the power electronics. Since then John has always made time to discuss problems with me and any possible improvements to anything electrical. On a similar note, I'd like to thank Barry Moss for his insight and guidance throughout the prototyping phase of the power electronics.

During my time working on the project I have worked closely with previous group members: Vijay Singh and Arin Mizouri. It has certainly been a blast (pun fully intended). Both took the time to help get me familiar with a project which, at least initially, seemed extremely daunting. I'm thankful for Arin in particular who besides keeping me on my toes in the lab also found time to read through parts of this thesis. Finally, I would like to thank Paul Walker who helped in the final few months I spent in the lab. I wish him all the best in the future while working on the decelerator.

I certainly would not be at this point without the support of family and friends. I am greatly appreciative of my friends both new and old. I've been lucky that I have met a fantastic bunch of people who have reminded me that there is far more to life than just the PhD. In short, you have kept me sane but without you I probably would have finished sooner. I'm particularly thankful to Chris, Jen, Joe, and Laurence. These fine people provided (or at least enabled) all the beer, cake, and literal gallons of tea that have apparently kept me going over the last four years. My family have been nothing but encouraging at each step of the way. My parents and sister in particular have been a relentless cheering section. I am grateful for the hours of proof reading that mum put in. I'm also thankful to those of you who flicked through to look at the pictures... Lydia.

I am also grateful to my godparents, Mary and Sean Lawson, both of whom greatly shaped my life and are deeply missed.

Contents

List of Figures

List of Tables

Chapter 1

Introduction and Background

Phenomena that are observed in atomic and molecular systems are often given the criteria of occurring in either the ‘cold’ or ‘ultracold’ regime. The cold regime follows from the thermodynamic definition which ultimately originates from the lower limit of the temperature achievable in the liquefaction of ^{3}He (about 2 mK) [5]. Since the development of laser cooling in the late 1970s [6] and further cooling techniques, such as evaporative cooling, even lower temperatures have been reached. For instance, a combination of cooling techniques has produced ensembles of atoms at temperatures below 500 pK [7]. The concept of ‘cold’, therefore, had to be adjusted. In the broadest sense the cold regime is valid for temperatures above 1 mK, while the ultracold regime is applicable for temperatures below 1 mK. Additionally, in atomic physics, a further characteristic of the ultracold regime is when s-wave scattering dominates the atomic collisions. The temperature so far discussed is associated with the spread of translational motion of a molecular or atomic gas packet. Unlike atoms, molecular samples have additional degrees of freedom arising from rotational and vibrational motion. The energy scales of the vibrational and rotational motion are 0.01 to 0.1 eV and 10^{-6} to 10^{-2} eV respectively [8]. In comparison the translational motion has energies on the order of several eV associated with it. Therefore, in order to observe phenomena that result from the vibrational or rotational structure with high resolution, the molecules must be cooled to a point where these energy scales are no longer dominated by the larger ones. Furthermore, as the de Broglie wavelength increases as the temperature of the molecules is decreased, the system behaves more as a quantum system. This paves the way towards the observation of a ground state molecular Bose Einstein condensate (BEC) for example.

Driven by the successes in atomic physics and a wide range of possible applications of cold and ultracold molecules, great efforts have been made to produce large ensembles of molecules at very low temperatures. This pursuit motivated the development of the travelling wave Zeeman decelerator discussed in this thesis. Section 1.1 begins with a brief overview of current techniques to produce cold and ultracold molecules. This is followed with a discussion of a selection of the applications of cold and ultracold molecules in section 1.2. The Zeeman effect in atoms and molecules is explained in section 1.3 while section 1.4 describes how the Zeeman effect is used in the conventional Zeeman decelerator. This section explains the limitations of this form of decelerator and why the development of moving trap decelerators (such as that presented here) was necessary.

1.1 Techniques to Produce Cold and Ultracold Molecules

Various methods have been developed to produce cold and ultracold molecules. A more complete overview of this topic can be found in references [5, 9, 10, 11, 12]. A universal method of producing ensembles of such molecules has not been developed. With the success of laser cooling atomic samples, it would be reasonable to assume that this too is a convenient method for producing ultracold molecules. Laser cooling requires closed or near-closed transitions for hundreds of thousands of cycles of photon absorption and spontaneous emission. The complex structure of molecules often makes laser cooling difficult due to the presence of additional decay channels that are not necessarily excited with the laser. This limits the number of photon interactions and the effectiveness of the cooling. Few molecules have an ideal energy structure for laser cooling, however, possible candidates have been proposed by Di Rosa [13] and Stuhl *et al.* [14]. These molecules tend to have decay channels of near unity from the excited state back to the ground state of the electronic and vibrational levels. To date, laser cooling has been achieved with SrF [15], CaF [16, 17] and YO [18]. CaF has also been shown to be laser cooled using Bichromatic laser cooling [19]. In order to expand the species that can be cooled other techniques have been developed. These are generally divided into direct and indirect methods of cooling. Direct methods of cooling are techniques designed to cool existing molecules or molecules that are sometimes referred to as chemist's molecules. These are molecules bound with energies of 0.01 to 10 eV. As such these include molecular ions, Rydberg states and radicals. Indirect methods, on the other hand, begin with one or more species of ultracold atomic samples, which are then bound through photo-association or magneto-association. The molecules produced are highly excited and weakly bound with binding energies that are typically within a range of a fraction to a couple of tens of cm^{-1} [5], so the molecules must be rapidly transferred to the ground state. As such, these molecules have been referred to by Jones *et al.* as physicist's molecules [20].

Figure 1.1 shows a selection of published densities and temperatures of the molecules produced using some of the techniques described below. The values included are not necessarily the limiting values for a particular method but indicate a typical phase space density that can be achieved to date. For instance, the buffer gas cooling technique employed by Singh *et al.* produces vastly different number densities of Li and CaH. This emphasises that the effectiveness of any method is somewhat species dependent. The figure shows the merits of molecules produced from ensembles of ultracold atoms which routinely produce low temperatures and high number densities. Direct cooling methods, until recently, have only been able to obtain samples of moderate number densities with temperatures in the range of a few tens to a few hundred milliKelvin. Secondary cooling schemes have been employed to achieve far lower temperatures than previously possible.

1.1.1 Synthesising Molecules from Ultracold Atoms

Ultracold samples of atoms have successfully been bound together using photo-association [34, 35, 36, 37, 38] and magneto-association [26, 39, 40, 41, 42, 43]. The former produces molecules by inducing a transition from the pair of atoms in the ground state to the excited electronic state of the dimer. This involves the collision between the ground state atoms. Provided a certain separation is reached, a photon on resonance with a transition between the unbound ground state pair of atoms to a highly excited molecular state is absorbed forming a molecular-dimer. Magneto-association is achieved using a Feshbach resonance. A Feshbach resonance occurs when the collision energy of the atomic pair is degenerate with an excited bound energy level of the molecule. At such a resonance the scattering length and, as a result, the scattering cross section can vary dramatically. The excited state of the molecule depends on the hyperfine state of the atoms. Therefore, the bound states can

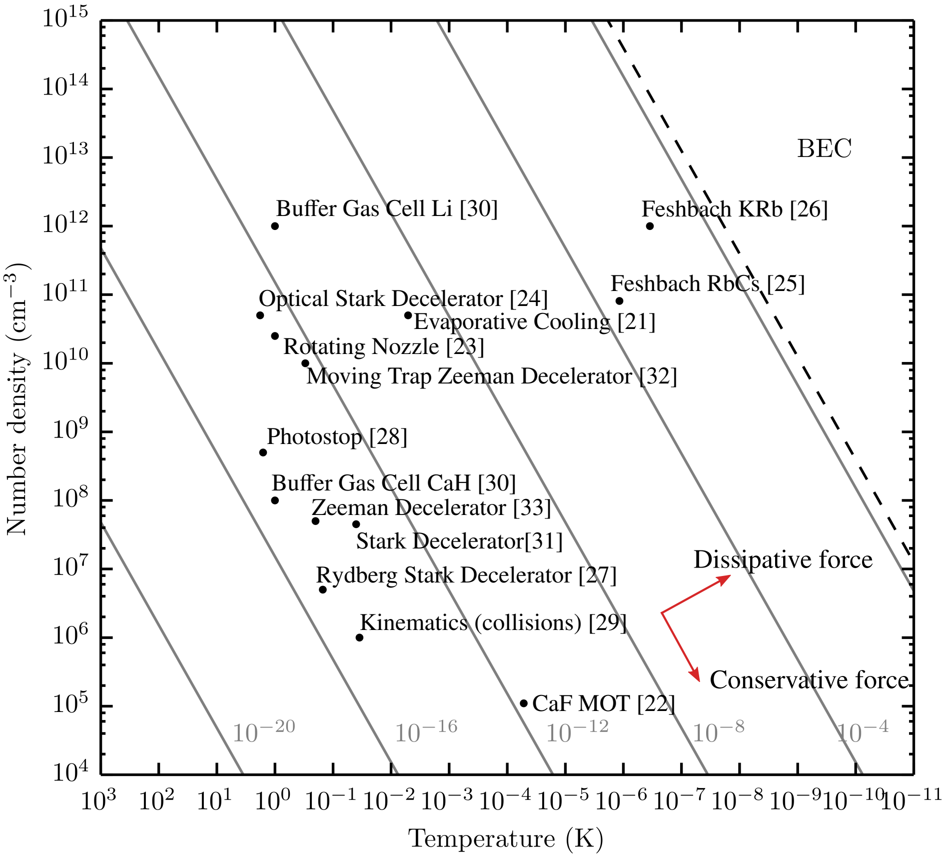

Figure 1.1: A sample of published densities and temperatures of the molecules produced using some of the techniques described in the main text. The values included are not necessarily the limiting values for a particular method but indicate a typical phase space density that can be achieved to date. The constant phase space density lines (grey) and BEC threshold (black dashed) are plotted for ^{87}Rb, which is routinely cooled to low temperatures.

be brought into resonance with the colliding atoms by varying the applied magnetic field. These techniques have led to the first observation of an excited state molecular BEC [44, 45, 46].

The techniques described above both create molecules which are weakly bound and highly vibrationally excited (i.e. vibrationally hot). Rather than relying on spontaneous emission to transfer the molecular population to the electronic and vibrational ground state, the molecules are transferred by stimulated Raman adiabatic passage (STIRAP). This allows a highly efficient transfer of the molecular population to the ground state. Spontaneous emission, on the other hand, generally results in the molecule dissociating. For instance, Molony *et al.* has shown that STIRAP can be used to transfer 88 % of the excited RbCs molecules from the $a^3\Sigma^+$ state to the $X^1\Sigma^+$ ground state [47]. The advantage of the production of molecules from ultracold atoms is that the sample is created in the ultracold regime and possesses large number densities. For example, the same group above has reported roughly 2000 molecules at a temperature of 1.17 μK with a peak number density of 8.1×10^{10} cm^{-3} [25]. Achieving both low temperatures while maintaining a high number density is still a goal for direct methods of cooling. The drawback, however, of synthesising molecules from ultracold atoms is that these techniques are fundamentally limited by the range of constituent atoms that can be laser cooled. In fact, many chemically important species (such as hydrides and oxides) can not currently be formed in this way. To date the range of molecules produced using these methods are limited to the alkali and alkaline earth metals.

1.1.2 Producing Cold and Ultracold Samples from Molecular Beams

The diversity of direct methods of producing cold and ultracold molecules is extensive and therefore only a brief review of the range of methods available shall be given here. The discussion will begin with the production of cold molecules from a molecular beam. These experiments often begin with molecules that are produced with supersonic expansion since the molecules are initially cold in each degree of freedom. Additionally, the sample is dense, however, the gas packet has high mean longitudinal velocities (for more details see chapter 2). This requires additional cooling techniques to be applied in order to further cool the sample.

External Field Decelerators

External inhomogeneous fields can be used to manipulate molecules. Forces can be applied to molecules by electric fields or magnetic fields provided the molecule has an electric or a magnetic dipole moment respectively. Stark decelerators use periodic switching of electric fields and the Stark effect to manipulate the longitudinal motion of the molecules. The first operation of such a device was reported in 1999 by Bethlem *et al.* with metastable CO [48]. Stark decelerators have since been employed by various groups to decelerate a wide range of molecules including ND_3 [49], NH_3 [50], OH [51], OD [52], NH ($^1a\Delta$) [53], formaldehyde (H_2CO) [54], SO_2 [55], NO [56] and SD [57]. The design of the Stark decelerator was later improved by Osterwalder *et al.* to enhance the efficiency of the decelerated gas packet [58]. This was achieved using a moving 3D trapping potential and has been used to decelerate LiH [59], CaF [60], YbF [61] and SrF [62]. A combination of the two types of decelerators has also been used to decelerate CH_3F [31]. Stark deceleration has been shown to work successfully with Rydberg states [63]. Rydberg states are highly excited electronic states of both atoms and molecules and possess large dipole moments which makes them ideal candidates for Stark deceleration. Additionally, this technique could prove to be fairly universal and could further diversify the range of molecules that can be decelerated. There are, however, difficulties associated with this technique. The interaction of the Rydberg state and the intense electric fields limits the lifetime of the highly excited state. Furthermore, molecules in Rydberg states are likely to undergo predissociation and the complex energy structure contains many crossings which further limits the lifetime of the prepared state. It should also be noted that the miniaturisation of the Stark decelerator to chip-based devices has also been successfully demonstrated with both metastable CO [64, 65] and H_2 in a range of Rydberg states[66]. Another notable form of Stark decelerator allows the deceleration of molecules in the absolute ground state. The alternating gradient Stark decelerator has been shown to decelerate molecules such as metastable CO [67, 68], YbF [69], benzonitrile (C_7H_5N) [70], and CaF [71]. The magnetic field analogue of the Stark decelerator can be used to manipulate the longitudinal motion of molecules by employing the Zeeman effect. This was demonstrated in 2007 by Vanhaecke *et al.* [72] and separately by Narevicius *et al.* [73]. As with the Stark decelerator, 3D trapping potentials have also been produced for Zeeman decelerators [74, 75]. A more complete discussion of Zeeman decelerators can be found in section 1.4.

A thermal gas packet with a velocity spread which follows a Maxwell-Boltzmann distribution contains a fraction of particles moving at low velocities. The extraction of the coldest fraction of the gas packet from a thermal source is possible through velocity selection. For instance, a bent electrostatic quadrupole guide can be used to select a range of velocities depending on the electric dipole moment of the gas, the electric field strength and the radius of the bend. The maximum velocity accepted by the guide can therefore be tuned allowing the variation of the temperature of the gas packet. Electrostatic guides have been demonstrated to selectively filter formaldehyde and ND_3 [76], H_2O, D_2O and HDO [77], and NH_3, CH_3I, C_6H_5CN, and C_6H_5Cl [78]. The magnetic analogue has also been successfully demonstrated with O_2 [79].

Deep optical potentials have been employed to decelerate NO and benzene. This approach relies on the second order Stark effect and this technique is generally referred to as optical-Stark deceleration [80]. The interference pattern created by two counter-propagating laser beams can be used to manipulate the longitudinal motion of polarisable molecules. A slight difference in frequencies allows the interference pattern to move at a constant velocity, however, it is the rotation of the molecules in phase space that results in the deceleration or acceleration of the particles [24]. In similar experiments, the motion of hydrogen molecules has also been manipulated using a stationary interference pattern [81], while microwave fields have been employed to decelerate ammonia [82]. Such methods are fairly general since the magnitude of the force scales with the polarisablity, however, factors such as the photodissociation limit of the molecule sets an upper bound on the maximum laser intensity that can be used.

Laser cooling of molecules has already been discussed, however, a novel approach, proposed by Fitch *et al.*, combines a periodic magnetic field with laser light to decelerate molecules in a device known as the Zeeman Sisyphus slower [83]. Like laser cooling, this technique not only decelerates the molecular packet but also compresses its longitudinal velocity spread, moreover, this approach promises to overcome the complexity of laser cooling experiments. Furthermore, the scheme promises to decelerate a higher fraction of the gas packet than other methods previously discussed, making this device ideal for a high flux effusive source. Further Sisyphus cooling schemes such as the opto-electrical method demonstrated by Zeppenfeld *et al.* for CH_3F [84] and Prehn *et al.* for formaldehyde [85] have also been reported.

Mechanical Techniques

Despite the advantages of a supersonic expansion, the obvious drawback of this approach is the high longitudinal velocity. Several groups have developed methods in order to mechanically remove the kinetic energy of the beam. The introduction of the rotating nozzle source is credited to Gupta *et al.* [86]. The high longitudinal velocity of a supersonic source can be largely cancelled by placing the nozzle on the arm of a high-speed rotor. The cancellation occurs in the laboratory frame if the arm rotates in the opposite direction to the beam direction. The resulting gas packet is significantly colder and often described as enhancing the supersonic expansion due to the centrifugal action. This method has been shown to work for O_2 and CH_3F seeded in Xe, and SF_6 [87]. For completeness other sources have been demonstrated such as allowing the supersonic beam to collide with a rotating paddle [88]. Narevicius *et al.* proposed that this particular method would be suitable for some light molecules such as H_2, D_2, and CH_4.

More recently, another form of mechanical decelerator has been introduced. Chervenkov *et al.* have been able to observe deceleration with a quadrupole mounted on a rotating disk [89]. Molecules enter a two stage electrostatic quadrupole guide, one of which is fixed while the inner part is allowed to rotate and is spiral shaped to account for the deceleration of the molecules. The initial angular speed of the guide sets which of the molecules are placed into the rotating frame. A typical trajectory of the particles is therefore spiral in shape as the two parts of the quadrupole decelerates the particles from the edge to the centre of the device. In the reference frame of the disk the quadrupole is used to guide the molecules; it is the centrifugal potential that decelerates the molecules. In the laboratory frame, however, the electric field of the quadrupole guide decelerates the molecules. This is because the electric field is no longer normal to the longitudinal motion. The group has demonstrated the deceleration of CH_3F, CF_3H, and CF_3CCH.

1.1.3 Cold Molecules from Collision Based Techniques

Molecules can also be cooled using collision based methods. Buffer gas cooling relies on the elastic collisions between a cold buffer gas (such as He at 4 K) to rethermalise a molecular sample. The first instance of buffer gas cooling was reported in the mid-1980s. Where the technique was originally developed to allow the investigation of the collisional broadening process between CO and He [90]. In the years following, the technique has been largely pioneered by Doyle and co-workers [91] and has been employed to cool a variety of molecules and atoms (see table 2 in [92]). A full theoretical study of buffer gas cooling is beyond the scope of this thesis but may be found in reference [92]. Buffer gas cooling relies on elastic collisions to dissipate the thermal energy of a particular species with a cold, inert gas. Therefore buffer gas sources tend to be based around Neon or, more commonly, Helium. Since Buffer gas cooling does not depend on the internal structure, the technique is therefore fairly generic to atoms [93], diatomic molecules [94, 95], and a selection of larger molecules [96, 97]. This approach is advantageous since all internal degrees of freedom of the molecule are cooled. With high buffer gas densities and cyropumping the final temperature of the molecules is typically on the order of a few hundred milliKelvin. Buffer gas cells have been employed in the trapping region of the experiment but can also be used as a source of cold molecules. This is possible if the molecules are allowed to effusively leave the cell through an aperture.

Other approaches based around the collision of particles have also been developed. Techniques based around kinematic cooling using either inelastic collisions [29] or reactive collisions [98] have been explored. The former has shown the production of cold NO through ‘billiard-ball’ like collisions with Ar atoms in a crossed beam experiment. The latter has used counter-propagating beams of HBr and K to produce KBr and H. This experiment relies on the careful selection of beam velocity and ratio of masses of H and KBr in order to limit the recoil velocity of the molecule. The photostop technique can also be used to produce stationary molecules [28]. This process relies on the photo-dissociation of a triatomic molecule and the conservation of momentum. The photo-dissociation produces a heavy diatomic molecule and a single atom. The atom, being less massive than the molecule, carries away most of the kinetic energy, leaving a slow moving sample of diatomic molecules. For example, Trottier *et al.* has shown the photostop method to work for NO_2 to produce NO while Eardley *et al.* has used the method to produce SH radicals from H_2S molecules [99] to load in a magnetic trap. The process, is not limited to producing slow molecules, it can also be used to produce slow packets of Br atoms [100].

1.1.4 Reaching the Ultracold Regime: Secondary Cooling Schemes

Most of the direct methods described above will bring the molecular temperature to the cold regime. Zeeman decelerators for instance will reach final temperatures of a few tens of milliKelvin. Secondary cooling schemes are therefore required to reach the ultracold regime. Again, due to the sheer scope of methods available only a few examples will be discussed. Once the cold packet of molecules has been created, the second stage of cooling may begin. The first step in this process generally involves loading the packet in to a trap. With the application of a set of lasers, applied in a suitable geometry, a 3D Magneto-Optical Trap (MOT) can be formed. Norrgard *et al.* have developed a rf MOT which has been observed to further cool 2000 SrF molecules to 400 μK with a number density of 6×10^4 cm^{-3} [101]. Truppe *et al.*, using a combination of a DC MOT and a blue detuned optical molasses, has been able to cool 1.8×10^4 CaF molecules to 52 μK with a number density of 1.1×10^5 cm^{-3} [22]. The limiting factor in these experiments has thus far been the low number of molecules generated in the initial deceleration process. Non-laser coolable molecules can be further cooled using sympathetic cooling and evaporative cooling. Sympathetic cooling of the cold sample of molecules occurs through collisions with a second ultracold sample. Ultracold atoms produced through laser cooling would be an ideal candidate for the coolant species. The elastic collisions between the two species rethermalises the molecules to the temperature of the atoms while inelastic collisions between the species result in heating of the sample and losses from the trap. A rule of thumb is that the rate of elastic collisions must be 100 times greater than that of the inelastic collisions. This field is ultimately in its infancy and the experimental and theoretical study of the collisions between molecules and atoms is still ongoing to find appropriate coolants for particular molecules (see chapter 6). Finally, evaporative cooling of molecules has been achieved with the hydroxyl radical [21]. Evaporative cooling of atoms or molecules works by removing the hottest particles from a gas packet which is in thermal equilibrium. This corresponds to the removal of a fraction of the high velocity tail of the Maxwell-Boltzmann distribution. Elastic collisions can then rethermalise the sample before the process is repeated. The peak number density of the final sample of the hydroxyl radical was greater than 5×10^{10} cm^{-3} while the temperature of the sample was reduced from 51 mK and cooled to a temperature of 5.1 mK. This technique has been particularly successful in atomic systems, such as in achieving the degeneracy of atomic gases. It is therefore conceivable that, with more efficient loading of molecules and lower initial temperatures, that this process will, in the future, be a valuable technique in molecular physics.

1.2 Applications of Cold and Ultracold Molecules

The range of applications for cold and ultracold molecules extend to many areas in both chemistry and physics. The motivation behind the development of the multitude of techniques to produce cold and ultracold molecules is that different approaches benefit different applications. Although a complete list of possible applications will not be given here (see review articles [9, 10, 102, 103]) a few examples, relevant to this thesis, will be given below.

1.2.1 Precision Spectroscopy

The limiting factor in spectroscopy experiments is the interaction time of the molecules with the measuring device. Although it is possible to trap a sample of gas to dramatically increase the interaction time, the concern is that the trapping potentials alter the measured transitions and make the spectral analysis more complex. Moreover, producing slow beams of molecules makes full use of the narrow-bandwidth of the current generation sources of radiation. One of the earliest applications of the Stark decelerator was to increase the resolution of spectroscopy with decelerated molecules. For example, after decelerating a beam of ND_3 from 280 $\mathrm{m\,s^{-1}}$ to 52 $\mathrm{m\,s^{-1}}$ it was possible to resolve the hyperfine structure of the inversion transition of the molecule [104].

Cold molecules have also been used in the search for the electric dipole moment of the electron (eEDM). The standard model predicts that the electron is slightly aspherical, which results in the electron possessing a non-zero electric dipole moment. The standard model is also known to be incomplete, with a series of possible extensions put forward to describe the missing physics. The value that the eEDM takes has bearing on aspects such as CP-symmetry breaking [105]. This is intimately connected to the ratio of matter and anti-matter in the universe. To date, experiments have not been able to measure a value of the eEDM which is not consistent with zero, however, they have been used to fix upper bounds on the value of the eEDM. This has aided in ruling out some extensions to the standard model. Polar molecules are particularly useful in the measurement of the eEDM. This is due to the local environment of the molecule enhancing the observable effects by several orders of magnitude. Metastable PbO, YbF, and ThO have already been employed in such measurements [106, 107, 108]. Higher accuracy can be achieved if the mean velocity of the molecular packet was further reduced. YbF, for instance, has already been Stark decelerated [69, 61] and the $X^2\Sigma^+$ ground state would allow for Zeeman deceleration. Similarly, molecules could be used to test the time variation of fundamental constants such as the electron-proton mass ratio. If this ratio were to change the vibrational and rotational energy levels will move relative to the electronic states. Moreover, the degree of which the states are effected depends on how deeply bound that particular state is. Therefore, precise measurement of the relative variation of these select energy levels can be used to infer any time dependence [109].

1.2.2 Quantum Simulation

The original goal of this project was to investigate different techniques as a possible first step towards a quantum simulator. In 1982, Richard Feynman argued that trying to recreate quantum phenomena using classical methods of computation has limited feasibility [110]. He suggested that quantum machines could be built to not only simulate quantum mechanical problems but also the physical world. The computer he envisioned would be created from elements which obey the laws of quantum mechanics. The formalism behind this claim was realised more than a decade later by Seth Lloyd [111, 112]. The motivation behind building quantum simulators is that the direct simulation of quantum systems on classical computers is limited by the sheer amount of memory required. The problem arises because of the exponential dependence required to describe a system of N particles with certain number of quantum states. Consider a system of N particles with 1/2 spin. It follows that 2^N must be stored in memory. In order to calculate the time evolution it is necessary to exponentiate a $2^N \times 2^N$ matrix. Even a system of 40 particles requires a ludicrous amount of memory. Feynman's proposal is appealing as it simultaneously solves the problems of the exponential explosion in storing the quantum state and simulating the evolution.

Rather than relying on the emulation of a Hamiltonian of a quantum system using classical means, a tunable quantum system could be used to recreate a similar Hamiltonian. This type of quantum computer is perhaps the first tier towards a universal quantum computer (a system that evolves through gate based operations) and quantum information processing. The form of quantum simulator discussed here is used to emulate an effective many-body model of the target system. Once the simulator has been initialised into a state observed in the target system, it is allowed to evolve. The final state of the simulation can then be directly compared to the target system in order to extract vital information about the target system. This allows the physical model used to describe the system to be further refined to better encapsulate the underlying physics. Further iterations allows greater refinement, eventually resulting in a more complete theory. Such a device would be useful in many condensed matter systems such as high temperature superconductivity [113], and spin models [114, 115] as well as other applications such as investigating Hawking radiation [116]. There are, however, difficulties with quantum simulators. The initialisation of the device into a state observed in the target system is likely to be problematic. It is thought that this can be circumnavigated if the simulator behaves sufficiently like the target system [117]. It should be stressed however, that state preparation techniques will probably still need to be developed. Error correction of analogue quantum computers is more difficult than the digital variant, however, uncertainties can be used to further infer information on the system such as the effects on impuries in condensed matter systems [118]. The characteristics of such a device makes this form of quantum computer an attractive first step towards quantum information processing.

Various architectures have been proposed for quantum simulators. The basis of which include atoms, superconducting circuits and quantum dots. A full review of such techniques can be found in references [119, 120, 117]. Each have merits and disadvantages. In broad terms, systems tend to be either highly scalable but each component is difficult to individually control and read out or vice-versa. Each architecture is suited more towards simulating a particular physical problem (see tables 2 and 3 in [117]). A quantum simulator built from molecules would require ultracold molecules (in the region of 1 μK) to be loaded into an optical lattice. An optical lattice is preferable to a magnetic field to ensure that the entirety of the molecular sample is trapped [121]. Moreover, if the molecules are anti-trapped then the ground and excited rotational states are trapped by an almost identical potential [122]. A 1D optical lattice is created by counter propagating laser beams. These produce a standing wave as a result of the interference between the beams. By introducing more beams, two- and three-dimensional trapping potentials can be created. The orientation of the beams defines the geometry of the trap. The electric dipole interactions of polar molecules trapped in the lattice form the basis of the computation. Electric fields can be employed to align the dipole moments induced in this interaction. Additionally, these interactions are long-ranged and are necessary if the separation between lattice sites is larger than ∼ μm. These dipole-dipole interactions scale as $r^{-}3$ and can be attractive or repulsive depending on the orientation of the molecular dipoles. Moreover, the spatial extent of these interactions can be easily tuned using either external DC or AC microwave fields. In summary, it is the combination of microwave excitations, dipole-dipole interactions, spin-spin and spin-rotation couplings which makes polar molecules an appealing candidate for quantum simulators. Finally, Carr *et al.* remarked that the range of physics that can be simulated with molecules is greater than that of ultracold atomic systems due to the uniqueness of the interactions between polar molecules [10]. Further details of the formalism behind quantum simulators can be found in references [123, 119].

A range of applications have already been put forwards for a quantum simulator based around molecules mainly focusing on quantum magnetism [124, 125] and quantum phase transitions [126, 127]. A system designed to investigate topological order will be discussed. First consider an array of trapped molecules as shown in figure 1.2. The quantum simulator shown is constructed from a square optical lattice created from counter-propagating laser beams with wavevector $\mathbf{K}_{\mathrm{L}}$. The DC electric field, $\mathbf{E}_{\mathrm{DC}}$, and AC electric field, $\mathbf{E}_{\mathrm{AC}}$, component of a microwave field is also shown. The former is used to polarise the rotational ground state of the molecules to induce the dipole-dipole interactions between the molecules. The electric field of the microwave field is used to drive transitions between the ground state to a excited rotational state. In the case where the molecules have no spin, the interactions between the molecules can be increased by inducing a larger dipole moment. In the weak interaction limit the structure is largely unorganised and behaves much as a superfluid. In the strong interaction limit the molecules become highly ordered and enters a crystalline phase. Büchler *et al.* have theoretically shown the behaviour in the intermediate range for up to 90 particles. Such an ensemble exhibits a first order phase transition between the two regimes [128]. The model can be further complicated when molecular spin is introduced. Now the long range dipole-dipole interactions can be further tuned by accounting for the spin-rotation splitting of the molecular rotational levels. As a result, these interactions can be made spin-dependent, providing a means to investigate lattice

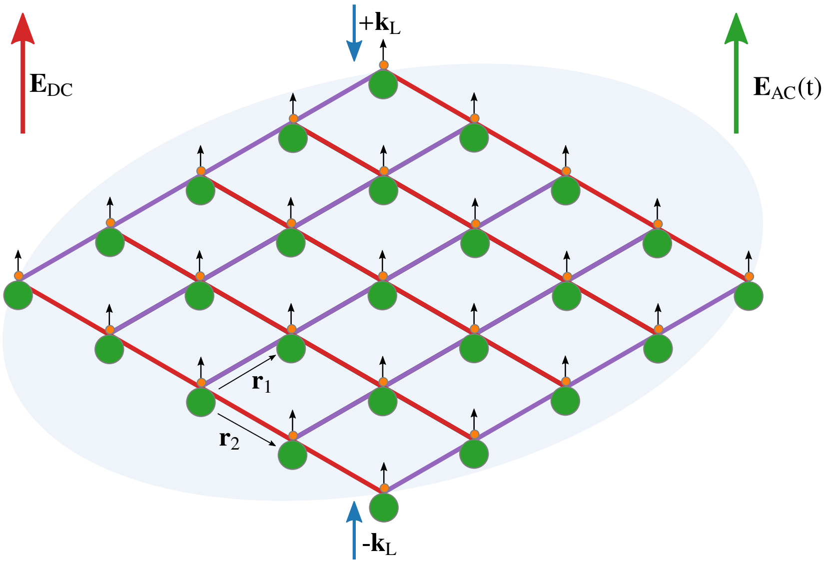

Figure 1.2: A simple quantum simulator architecture based around polar molecules. The molecules are trapped in a 2D plane by an optical lattice made from two anti-propagating laser beams with wavevectors $\pm\mathbf{K}_{\mathrm{L}}$. In this example a square lattice is given, $\mathbf{r}_1 = \mathbf{r}_2$. The dipoles of the molecules are aligned using the static electric field $\mathbf{E}_{\mathrm{DC}}$. The microwave field $\mathbf{E}_{\mathrm{AC}}$ induces the dipoledipole interactions between the adjacent molecules which provide the basis of the simulation.

spin models. Micheli *et al.* [129] began to theoretically study small systems of 1/2 spin molecules in the context of spin models. Later, the group generalised their models to allow for higher spin states which was possible through the inclusion of the hyperfine interaction [118]. Pupillo *et al.* has suggested that a molecule based quantum simulator would be ideal to further explore complex lattice geometries such as the bipartite lattice [119].

1.2.3 Collision Dynamics and Cold Chemistry

The study of collision dynamics is closely linked to reactions dynamics. The range of methods to manipulate the collisions and reactions through the choice of molecular state and orientation of the molecule, in the presence of an external field, provides a means to explore controllable molecular collisions and reactions at low temperatures. The latter is an interesting problem as a wide range of chemical reactions must be thermally activated in order for the reactants to overcome the activation barrier of a particular reaction pathway. The rate constant, $k(T)$, of many chemical reactions can be approximated by Arrhenius' equation,

$$k(T) = A\exp\left(\frac{-E_{\mathrm{a}}}{k_{\mathrm{B}}T}\right). \tag{1.1}$$

This predicts that the rate of such a reaction decreases as the temperature, T, decreases, provided the activation energy, E_{a}, is greater than zero. At very low temperatures, real systems diverge from this relationship as the system becomes increasingly more quantum in nature. Effects such as quantum tunnelling through the activation barrier become important factors. For instance, tunnelling can allow classically forbidden reactions to take place. A series of experiments have began to explore the reaction dynamics of cold molecules. For example, a crossed-beam experiment has observed and modelled the cross sections in the threshold region of a CO rotational transition during CO-

H_2 collisions [130]. The apparatus allowed the first sensitive study of the potential energy surfaces of collisions close to the cold regime defined previously. This experiment was the first to observe the partial wave resonances in the integral cross section during inelastic collisions. Merged- and crossed-beam experiments have been unable to reach very low collision energies because, even at small crossing angles, the mean velocities of the supersonic beams contribute to the collision energy. Furthermore, the finite temperature of the gas packet further limits the energy resolution. Henson *et al.*, however, have been able to employ the thermal expansion of a supersonic beam to spatially address a particular narrow range of velocities, much smaller than the thermal width of the packet [131]. This allowed the observation of non-classical effects in reactions such as vibrational resonances in He*-H_2 and He*-Ar Penning ionisation.

The development of molecular beam decelerators has allowed further investigation of the collisions in crossed molecular beams at lower collision energies. For instance, the inelastic cross sections of near threshold collisions has been explored over a range of collision energies. For example, Gilijamse *et al.* has performed such measurements between Stark decelerated OH and Xe [132]. The collision energies were in the range of 50 to 400 cm^{-1}. Van de Meerakker and collaborators have since begun to exploit the ability to tune the collision energy of Stark decelerated open-shell species of molecules with particular focus on OH and NO. The collisions of these species with a range of noble gases and with each other have been examined [133, 134, 135, 136]. More recently the group have presented the experimental details used to study the inelastic and reactive cross sections of NO [137, 138]. These systems are particularly interesting as multiple Born-Oppenheimer potential energy surfaces coupled with non-adiabatic transitions govern the dynamics of the collisions. The longitudinal velocity of the NO molecules is tuned using a Stark decelerator. This simultaneously state selected the final distribution such that 99 % of the molecules occupied the $X^2\Pi_{1/2}$ vibronic ground state. The NO packet prepared by the Stark decelerator was then allowed to collide with beams of pure He, Ne or Ar. Previous experiments have been limited by the initial velocity spread of the reagents, however, the Stark decelerator produced the NO packet with a sufficiently narrow spread of velocities resulting in high resolution of the detection scheme. The combination of the velocity map imaging [139] with other target specific detection schemes allows images of the recoiling molecules to be generated which reflect the differential cross sections involved in the collisions. Consequently, quantum diffraction oscillations (and as a result oscillations in the differential cross sections) could be resolved in the inelastic scattering images produced. Further refinement of experiments such as these has allowed the imaging of other quantum effects such as quantum stereodynamics. This describes the dependence on the product states on the initial orientation of the molecule prior to the collision. Onvlee *et al.* have recently observed rich diffraction structure consisting of regular and irregular diffraction peaks [140]. The latter is predicted by the analytical Fraunhofer model [141, 142] and has lead to the discovery of a previously unseen Δm propensity rule. The presence of the irregular diffraction pattern has been shown to result from the orientation of the molecule during the collision as predicted by the Fraunhofer model. A simplified summary of this effect is given by Huygen's principle applied to molecular collisions. This states that maximum diffraction occurs when an atom collides with a molecule whose orientation is such that the anisotropy is maximised (i.e. scattering off a hard edged object). In this particular experiment this condition is fulfilled when the noble gas atom collides with the NO side on.

A similar set of experiments has been performed by Jun Ye and co-workers to explore the collision dynamics of atom-molecule and molecule-molecule systems. Initially, OH radicals are loaded into a permanent magnet trap from a Stark decelerator. He and D_2 beams are produced by a pulsed valve and guided towards the trapping volume [143]. By varying the collision energy of the He beam from 60 to 230 cm^{-1} and the D_2 from 145 to 510 cm^{-1} the collision cross sections can be determined. This variation in collision energy was achieved by varying the temperature of the valve and altering the expansion characteristics of the gas. This particular study has demonstrated quantum threshold scattering and resonant energy transfer between the colliding particles. The same group proposed using a similar trap configuration to study the H-abstraction channel in the reaction of formaldehyde and OH ($H_2CO + OH \rightarrow CHO + H_2O$) [54]. Evidence of the reaction would have to be inferred through monitoring the population of OH as the detection of the CHO product would be difficult given the low product densities per quantum state. This experiment was ultimately unfeasible due to the properties of the decelerated formaldehyde gas which had a temperature of 100 mK with a density on the order of 10^6 cm^{-3}. Given these properties the group predicted a production of a CHO molecule every 250 pulses which would be a 'heroic' endeavor to measure. The goal of this particular experiment was to directly measure the activation energy of the H-abstraction by the variation of collision energy tuned by the Stark decelerator rather than through kinematics techniques combined with the fitting of Arrhenius' equation. Additionally, emphasis was put on the theoretical observation of the dependence of this reaction on the orientation of the molecules in an external field.

Another approach to investigate reactions at low temperatures between multiple species of molecules is with the simultaneous expansion of reactants from a continuous flow CRESU (Cinétique de Réaction en Ecoulement Supersonique Uniforme, or Reaction Kinetics in Uniform Supersonic Flow) apparatus has allowed for the observation of reactions on the order of a few tens of Kelvin. In one experiment Carty *et al.* have been able to measure the rate coefficients of CN (cyanogen), and C_2H (ethynyl) radicals with $CH_2{=}C{=}CH_2$ (allene) and $CH_2C{\equiv}C$ (methyl-acetylene) [144]. Studies such as this one are intended to explore the reactions that occur in interstellar gas clouds where hydrocarbons are of particular interest. This particular experiment wished to examine the reaction rates of cyanopolynes which are generally found in interstellar environments.

1.3 The Zeeman Effect in Atoms and Molecules

The effect of a magnetic field on the energy levels of atoms was discovered in 1896 by Pieter Zeeman. He discovered the line spectra (in particular the D-line) produced from a sodium flame could be broadened in the presence of a magnetic field [145]. Similar results were noticed in Zinc spectral lines. This interaction was named the normal Zeeman effect. Other experiments showed further splitting of the line spectra into higher order multiplicities which could not be explained by classical physics. This became known as the anomalous Zeeman effect. The Zeeman effect describes the energy perturbation, V_Z, of an atom or molecule with a magnetic dipole moment, μ_Z, in the presence of a magnetic field $\mathbf{B}$,

$$V_Z = -\mu_Z \cdot \mathbf{B}. \tag{1.2}$$

In the presence of an inhomogeneous magnetic field the dipole experiences a force

$$F_Z = -\nabla V_Z = \nabla(\mu_Z \cdot \mathbf{B}). \tag{1.3}$$

In 1922, Otto Stern and Walther Gerlach exploited this force in an experiment involving a strong, inhomogeneous magnetic field in order to observe the deflection of a beam of silver atoms [146]. Rather than a classical result, the pair observed a doublet that demonstrated for the first time space quantisation. With this discovery, the normal and anomalous Zeeman effects could be reconciled. The normal Zeeman effect is the special case where there is no electron spin contribution to the dipole moment. Experiments such as the Stern-Gerlach experiment and the one presented in this thesis hinge on the Zeeman effect. This section will describe the Zeeman effect in atoms and molecules. The majority of this thesis will focus around metastable argon and therefore is a reasonable starting point. The Zeeman effect in Li will then be discussed for a more general example. Finally, the Zeeman interaction of calcium monohydride will be presented as an example of a molecule interacting with a magnetic fields.

1.3.1 The Zeeman Effect in Atoms

In atoms, the magnetic moment has contributions from the total electron spin $\hat{S}$, the total electron orbital angular momentum $\hat{L}$ and the total nuclear spin $\hat{I}$. The interaction of this dipole with an external magnetic field will be considered, for convenience it is assumed that the external field, **B**, is uniform and points along the z axis. This interaction can be expressed in terms of the Zeeman Hamiltonian operator

$$\hat{H}_\mathrm{Z} = B_\mathrm{z}\frac{\mu_\mathrm{B}}{\hbar}\left[g_\mathrm{L}\left(\hat{L}_\mathrm{z}\otimes\mathbb{I}_\mathrm{S}\otimes\mathbb{I}_\mathrm{I}\right) - g_\mathrm{e}\left(\mathbb{I}_\mathrm{L}\otimes\hat{S}_\mathrm{z}\otimes\mathbb{I}_\mathrm{I}\right)\right] - B_\mathrm{z}\frac{\mu_\mathrm{N}}{\hbar}g_\mathrm{N}\left(\mathbb{I}_\mathrm{L}\otimes\mathbb{I}_\mathrm{S}\otimes\hat{I}_\mathrm{z}\right). \tag{1.4}$$

Where $\mathbb{I}_\mathrm{S}$, $\mathbb{I}_\mathrm{S}$ and $\mathbb{I}_\mathrm{S}$ are the identity matrices for each of the contributors to the magnetic moment. The equation can be separated into the electronic and nuclear components of the Zeeman interaction. The former couples to the magnetic field with the Bohr magneton ($^{e\hbar}/_{2m_\mathrm{e}}$) and the appropriate g-factors. Where g_e = -2.0023 and g_L = 1. The latter half of the Zeeman Hamiltonian describes the coupling of the nuclear magneton ($^{e\hbar}/_{2m_\mathrm{p}}$) and nuclear g-factor, g_N, to the external field. Since $\left|g_\mathrm{N}\mu_\mathrm{N}\right| \ll \left|g_\mathrm{e}\mu_\mathrm{B}\right|$, the nuclear contribution to the Zeeman interaction will be negligible to that of the electron and thus will be ignored. Therefore The Zeeman Hamiltonian can be approximated as

$$\hat{H}_\mathrm{Z} \approx B_\mathrm{z}\frac{\mu_\mathrm{B}}{\hbar}\left[g_\mathrm{L}\left(\hat{L}_\mathrm{z}\otimes\mathbb{I}_\mathrm{S}\right) - g_\mathrm{e}\left(\mathbb{I}_\mathrm{L}\otimes\hat{S}_\mathrm{z}\right)\right]. \tag{1.5}$$

The following sections will describe the effect the Zeeman Hamiltonian in equation 1.5 has on the metastable $^3\mathrm{P}_2$ state of argon and on the $^2\mathrm{S}_{1/2}$ electronic ground state of Lithium-7.

Metastable Argon ($^3\mathrm{P}_2$)

In the ^{3}P state the total electron spin is $S = 1$ while the total orbital angular momentum L is 1. Argon has no nuclear spin ($I = 0$) and therefore the total electron angular momentum does not interact with the nucleus. States with both non-zero spin and orbital angular momentum undergo spin-orbit interactions. The ^{3}P state of argon is therefore affected due to these interactions. The state is split into three components consisting of $^3\mathrm{P}_0$, $^3\mathrm{P}_1$, and $^3\mathrm{P}_2$ with energies of 11.72, 11.62, and 11.54 eV respectively [147]. This notation introduces the total electron angular momentum quantum number, **J**, and is defined as **J** = **L** + **S**. The Hamiltonian for the spin-orbit interaction is

$$\hat{H}_\mathrm{SO} = \frac{A_\mathrm{SO}}{\hbar^2}\hat{L}\cdot\hat{S}. \tag{1.6}$$

Where A_SO is the coupling strength of the spin-orbit interaction. The matrix representation of equation 1.5 can be diagonalised when transformed into the uncoupled basis $|m_\mathrm{S}, m_\mathrm{L}\rangle = |S, m_\mathrm{S}\rangle \otimes |L, m_\mathrm{L}\rangle$. However, the spin-orbit interactions are not diagonal in this representation. Equation 1.6 can be further simplified by neglecting the $^3\mathrm{P}_1$ and $^3\mathrm{P}_0$ states. This is justifiable since the energy separation of the states is so large they will not become close enough to interact at field strengths of a couple of Tesla. Secondly, the $^3\mathrm{P}_1$ state is radiative and has a short lifetime while the $^3\mathrm{P}_0$ state has a negligible magnetic moment. Thus, the Hamiltonian reduces further to

$$\hat{H}_\mathrm{Z} = B_\mathrm{z}\frac{\mu_\mathrm{B}}{\hbar}\left[g_\mathrm{L}\left(\hat{L}_\mathrm{z}\otimes\mathbb{I}_\mathrm{S}\right) - g_\mathrm{e}\left(\mathbb{I}_\mathrm{L}\otimes\hat{S}_\mathrm{z}\right)\right] \tag{1.7}$$

The matrix representation of which can be diagonalised with the appropriate transformation matrix

$$T = \begin{pmatrix} 1 & 0 & 0 & 0 & 0 & 0 & 0 & 0 & 0 \\ 0 & 1/\sqrt{2} & 0 & 1/\sqrt{2} & 0 & 0 & 0 & 0 & 0 \\ 0 & 0 & 1/\sqrt{6} & 0 & \sqrt{2/3} & 0 & 1/\sqrt{6} & 0 & 0 \\ 0 & 0 & 0 & 0 & 0 & 1/\sqrt{2} & 0 & 1/\sqrt{2} & 0 \\ 0 & 0 & 0 & 0 & 0 & 0 & 0 & 0 & 1 \end{pmatrix}. \tag{1.8}$$

The transformation matrix can be populated by the decomposition of the $|J, m_\mathrm{J}\rangle$ states to $|m_\mathrm{S}, m_\mathrm{L}\rangle$ components by calculating the Clebsch-Gordan coefficients. Therefore, the Hamiltonian for the $^3\mathrm{P}_2$ state can be written as

$$\begin{aligned} \hat{H}_\mathrm{Z} &= B_\mathrm{z}\frac{\mu_\mathrm{B}}{\hbar} T \left[g_\mathrm{L} \left(\hat{L}_\mathrm{z} \otimes \mathbb{I}_\mathrm{S} \right) - g_\mathrm{e} \left(\mathbb{I}_\mathrm{L} \otimes \hat{S}_\mathrm{z} \right) \right] T^\mathrm{T} \\ &\approx B_\mathrm{z}\mu_\mathrm{B} \begin{pmatrix} 3 & 0 & 0 & 0 & 0 \\ 0 & 1.5 & 0 & 0 & 0 \\ 0 & 0 & 0 & 0 & 0 \\ 0 & 0 & 0 & -1.5 & 0 \\ 0 & 0 & 0 & 0 & -3 \end{pmatrix} \end{aligned}. \tag{1.9}$$

Figure 1.3 shows the Zeeman interaction of this state. The plot clearly demonstrates the five ($2J + 1$) sublevels which, without the external field, would otherwise be degenerate. These states are often labelled m_J which represents the projection of the total angular momentum onto the magnetic field axis (the z direction in this example). The $m_\mathrm{J} = 2$ state is highlighted as it will be discussed throughout this thesis. One can determine that this sublevel has an effective magnetic moment of approximately $3\mu_\mathrm{B}$. Figure 1.3 shows the linear nature of the Zeeman effect of the metastable $^3\mathrm{P}_2$ state in argon. Moreover, the figure also demonstrates the concept of high-field-seeking and low-field-seeking states. Low-field-seeking states (m_J = 1, 2) experiences lower energies in lower fields. Conversely, high-field-seeking states (m_J = -1, -2) experience lower energies in higher fields.

As an aside, Earnshaw's theorem states that it is not possible to trap charges, magnets and masses using solely static electric, magnetic, or gravitational forces. The force experienced by such a particle is proportional to the gradient of the field potential applied. As a result of Laplace's equation, the force is always located on an unstable saddle point where the divergence of the force is zero. Therefore, there are no local maxima or minima in the potential meaning trapping is not possible with static potentials. Unlike charges, magnets and masses, the force experienced by the magnetic dipoles of neutral atoms or molecules is dependent upon its quantum state. These states are either low-field-seeking or high-field-seeking depending on the resulting change in energy experienced by the atom or molecule. Additionally, the force due to the external field is linearly proportional to the gradient of the field strength of the external field potential which does contain local minima. Through similar calculations of the Laplace equation of the field magnitude, it can be shown that local maxima of the external field are forbidden. Therefore, only low-field-seeking states can be trapped using static potentials [148]. Thus, unless stated otherwise, only the low-field- seeking states shall be considered in the following chapters.

Ground state Lithium ($^2\mathrm{S}_{1/2}$)

The lithium-7 isotope has a $^2\mathrm{S}_{1/2}$ ground state which implies that the system has a total electron spin of 1/2 and total orbital angular momentum of zero. It also possesses a nuclear spin of $I = 3/2$. The non-zero nuclear spin results in the hyperfine interaction which describes the interaction of the total angular momentum of the electron, **J**, with the nuclear spin, **I**. The general form of the equation is given by

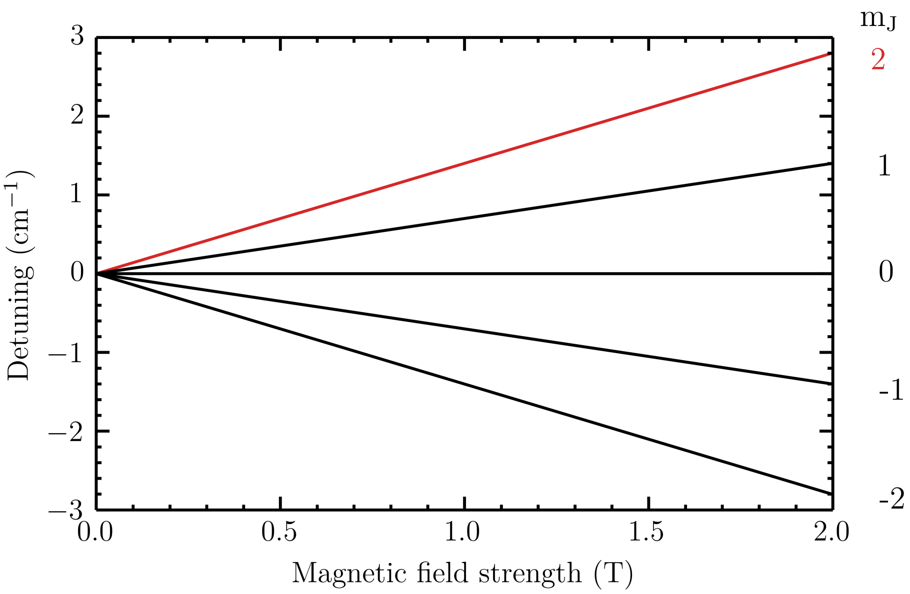

Figure 1.3: The ^{3}P$_2$ state of argon in the presence of an external magnetic field. The $m_\mathrm{J} = 2$ state, which will be discussed throughout the thesis, has been highlighted.

$$\hat{H}_\mathrm{HF} = \frac{A_\mathrm{HF}}{\hbar^2}\hat{I} \cdot \hat{S}. \tag{1.10}$$

The coupling constant is given by A_HF and for ground state Lithium has a value of 401.75 MHz [149]. The total angular momentum quantum number is therefore $\mathbf{F} = \mathbf{I} + \mathbf{J} = \mathbf{I} + \mathbf{L} + \mathbf{S}$ and has a projection on the z axis of m_F. In the coupled basis, $|F, m_\mathrm{F}\rangle = |F, m_\mathrm{F}, S, I\rangle$, the matrix representation of the Hamiltonian is diagonal. The Hamiltonian of the ground state of Lithium in an external magnetic field is

$$\hat{H} = \frac{A_\mathrm{HF}}{\hbar^2}\hat{I} \cdot \hat{S} - \frac{g_\mathrm{e}\mu_\mathrm{B}}{\hbar}B_\mathrm{z}\hat{S}_\mathrm{z}. \tag{1.11}$$

The hyperfine interaction has been simplified since $L = 0$. Once again, the Hamiltonian of the Zeeman interaction must be transformed from the uncoupled to the coupled basis. This is achieved with the appropriate transformation matrix

$$T = \begin{pmatrix} 0 & 0 & 0 & 1/2 & 0 & 0 & \sqrt{3}/2 & 0 \\ 0 & 0 & 0 & \sqrt{3}/2 & 0 & 0 & -1/2 & 0 \\ 0 & 0 & 1/\sqrt{2} & 0 & 0 & 1/\sqrt{2} & 0 & 0 \\ 0 & 0 & 1/\sqrt{2} & 0 & 0 & -1/\sqrt{2} & 0 & 0 \\ 0 & -1/2 & 0 & 0 & \sqrt{3}/2 & 0 & 0 & 0 \\ 0 & \sqrt{3}/2 & 0 & 0 & 1/2 & 0 & 0 & 0 \\ 1 & 0 & 0 & 0 & 0 & 0 & 0 & 0 \\ 0 & 0 & 0 & 0 & 0 & 0 & 0 & 1 \end{pmatrix} \tag{1.12}$$

The transformation matrix is populated using the Clebsch-Gorgan coefficients to decompose the $|F, m_\mathrm{F}\rangle$ into $|S, m_\mathrm{S}, I, m_\mathrm{I}\rangle$ states. Applying this transform results in the matrix representation of the

Zeeman interaction in the coupled basis given by

$$\begin{aligned}\hat{H} &= \frac{A_{\mathrm{HF}}}{\hbar^2}\hat{I}\cdot\hat{S} - \frac{g_{\mathrm{e}}\mu_{\mathrm{B}}}{\hbar}B_{\mathrm{z}}T\hat{S}_{\mathrm{z}}T^{\mathrm{T}} \\ &\approx \frac{A_{\mathrm{HF}}}{4}\begin{pmatrix} 3 & 0 & 0 & 0 & 0 & 0 & 0 & 0 \\ 0 & -5 & 0 & 0 & 0 & 0 & 0 & 0 \\ 0 & 0 & 3 & 0 & 0 & 0 & 0 & 0 \\ 0 & 0 & 0 & -5 & 0 & 0 & 0 & 0 \\ 0 & 0 & 0 & 0 & -5 & 0 & 0 & 0 \\ 0 & 0 & 0 & 0 & 0 & 3 & 0 & 0 \\ 0 & 0 & 0 & 0 & 0 & 0 & 3 & 0 \\ 0 & 0 & 0 & 0 & 0 & 0 & & 3 \end{pmatrix} \\ &\quad - \frac{g_{\mathrm{e}}\mu_{\mathrm{B}}B_{\mathrm{z}}}{2}\begin{pmatrix} -1/2 & \sqrt{3}/2 & 0 & 0 & 0 & 0 & 0 & 0 \\ \sqrt{3}/2 & 1/2 & 0 & 0 & 0 & 0 & 0 & 0 \\ 0 & 0 & 0 & 1 & 0 & 0 & 0 & 0 \\ 0 & 0 & 1 & 0 & 0 & 0 & 0 & 0 \\ 0 & 0 & 0 & 0 & -1/2 & -\sqrt{3}/2 & 0 & 0 \\ 0 & 0 & 0 & 0 & \sqrt{3}/2 & 1/2 & 0 & 0 \\ 0 & 0 & 0 & 0 & 0 & 0 & 1 & 0 \\ 0 & 0 & 0 & 0 & 0 & 0 & 0 & -1 \end{pmatrix}\end{aligned} \quad . \tag{1.13}$$

Finally, plotting the eigenvalues of this system as a function of magnetic field strength results in figure 1.4. Initially the ground state is split into the $F = 1$ and $F = 2$ states (resulting from $F = |I - J|$, $|I - J| + 1$, ... $(I + J)$). These states are further composed of $2F + 1$ sublevels which are degenerate at zero field. At low field, the m_{F} quantum number provides the best means to describe the states whereas at high fields the spin projection, m_{S} describes the states. Figure 1.4 also highlights the $|F = 2, m_{\mathrm{F}} = 2\rangle$ state. This particular sublevel, which is the spin stretched state, and has an effective magnetic moment of $1\mu_{\mathrm{B}}$. The relevance of this state shall be discussed in chapter 6.

1.3.2 The Zeeman Effect in Molecules

The effect of an external magnetic field on a molecule can also be calculated in a similar way. To achieve this, the effective Hamiltonian of the molecule must be formulated. This Hamiltonian encapsulates the major components of the actual molecular Hamiltonian limited to only the rotational, spin, and hyperfine energy levels of a certain vibrational state of a single electronic state. Although one can find the eigenvalues for a more complete molecular Hamiltonian, the effective Hamiltonian allows for faster calculation because of the reduced size. The level of accuracy can be improved by including additional terms and corrections.

In a particular vibrational state, within a certain electronic state, the effective Hamiltonian has only contributions from the rotational motion, electronic spin, and the nuclear spin. A rigorous derivation of the components of the effective Hamiltonian components can be found in [3]. It should be further noted that this study will focus on diatomic molecules. Polyatomic molecules tend to be asymmetric rotors and therefore require further consideration as each rotation axis has different properties. An example for constructing an effective Hamiltonian for a planar molecule can be found in reference [150].

Table 1.1 lists the commonly used components to construct an effective Hamiltonian. In most cases, the formulation of the Hamiltonian is given in terms of an angular momentum vector-operator. This is represented by a spherical tensor operator of rank k with Cartesian $p = 2k+1$ components. More

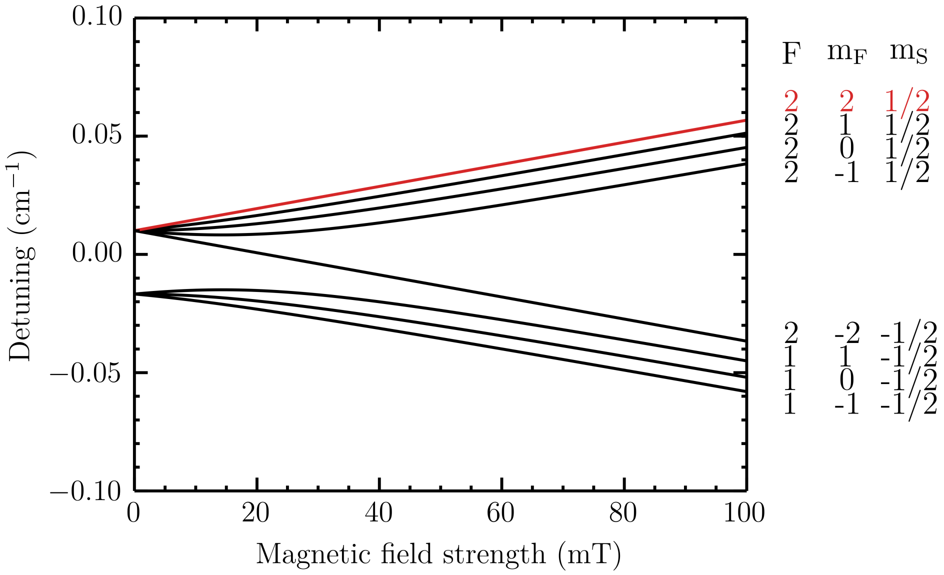

Figure 1.4: The Zeeman interaction of the ground state Lithium ($^2S_{1/2}$). The Hyperfine interaction splits the ground state into two states $|I - J| \ldots I + J$. In addition, this state is further split into $2F + 1$ sublevels which are degenerate at zero field. At low fields the interaction is described best by the m_F quantum number. At higher fields, however, the m_s quantum number is more appropriate. The spin stretched $|F = 2, m_F = 2\rangle$ state is highlighted in red. This is typically used for magnetic trapping of lithium-7.

details on spherical tensors can be found in appendix A. A brief description of the origin of each term is given along with the constants that term introduces.

To illustrate the calculation of the Zeeman interaction of a molecule using the effective Hamiltonian the following section will give an example. Calcium monohydride (CaH) in the electronic ground state ($X^2\Sigma^+$) will be investigated, limited to the lowest vibrational state ($v = 0$).

Effective Hamiltonian Component	**Symbol**	**Formulation**	**Description**
Rotational Kinetic Energy	H_{rot}	$B_v\hat{\mathbf{N}}^2$	The contribution of the rotational kinetic energy of the molecule. This forms a diagonal matrix in **N**. B_v is the rotational constant for the vibrational state v.
Centrifugal Distortion	H_{cd}	$-D_v(\hat{\mathbf{N}}^2)^2 + \left[H_v(\hat{\mathbf{N}}^2)^3 + ...\right]$	The higher order centrifugal distortion terms for the rotational kinetic energy. D_v and H_v are the first and second centrifugal distortion corrections for the vibrational state. The first order term is sufficient for most applications. These terms also forms a diagonal matrix in **N**.
Spin-Orbit Interaction	H_{so}	$\frac{1}{2}\left\{\left(A_v + A_{\text{D}v}\hat{\mathbf{N}}^2\right), \text{T}^{k=1}_{q=0}\left(\hat{\mathbf{L}}\right) \cdot \text{T}^{k=1}_{q=0}\left(\hat{\mathbf{S}}\right)\right\}$	The interaction between the electron spin and electron orbital angular momentum and has been included for completeness. The equation shows the first and second order terms with the coupling strengths of A_v and $A_{\text{D}v}$ respectively. These terms introduce off-diagonal elements in **N**.
Spin-Spin Interaction	H_{ss}	$\frac{\sqrt{6}}{3}\left\{\left(\lambda_v + \lambda_{\text{D}v}\hat{\mathbf{N}}^2\right), \text{T}^{k=2}_{q=0}\left(\hat{\mathbf{S}}, \hat{\mathbf{S}}\right)\right\}$	The interaction between two unpaired electron spins included for completeness. These terms require second order tensors to calculate the matrix elements which can be found in reference [3]. Once again, these terms introduce off-diagonal elements in **N**. The equation is shown to the second order and couples with strengths λ_v and $\lambda_{\text{D}v}$ respectively.
Spin-Rotation Interaction	H_{sr}	$\frac{1}{2}\left\{\left(\gamma_v + \gamma_{\text{D}v}\hat{\mathbf{N}}^2\right), \text{T}^{k=1}_{q=0}\left(\hat{\mathbf{N}}\right) \cdot \text{T}^{k=1}_{q=0}\left(\hat{\mathbf{S}}\right)\right\}$	The interaction between the electron spin and rotational motion of the molecule. Once again the equation shows the first and second order terms and the interaction couples with strengths γ_v and $\gamma_{\text{D}v}$ respectively. These terms introduce off-diagonal elements in **N**.

Continued on next page

Effective Hamiltonian Component	**Symbol**	**Formulation**	**Description**
Hyperfine Interaction	H_{hf}	$\sum_{\sigma}\left[b^{\sigma}_{\mathrm{F}\eta v}\mathrm{T}^{k=1}_{q=0}\left(\hat{\mathbf{I}}_{\sigma}\right)\cdot\mathrm{T}^{k=1}_{q=0}\left(\hat{\mathbf{S}}\right)\right.$ $\left.-\sqrt{10}g_{\mathrm{e}}g_{\mathrm{N}}\mu_{\mathrm{B}}\frac{\mu_{\mathrm{o}}}{4\pi}\mathrm{T}^{k=1}\left(\hat{\mathbf{I}}_{\sigma}\right)\cdot\mathrm{T}^{k=1}\left(\hat{\mathbf{S}},\hat{\mathbf{C}}^{2}\right)\right]$	The Hyperfine interaction describes the coupling of the nuclear spins of any of the constituent atoms with the electronic spin components of the molecule. The first sum has the index of σ which represents each nuclei of the molecule that possesses a non-zero nuclear spin. The second sum depends on the molecule-fixed axis and, in most cases, the $q = 0$ component is sufficient as this removes any coupling to other higher electronic states. The hyperfine splitting term consists of two separate Hamiltonians with their own coupling strengths. Firstly, the interaction of the electron spin and the total nuclear spin, this is known as the Fermi contact interaction. The second term is the classic magnetic dipole interaction. See appendix B for details on calculating the hyperfine structure for CaH.
Electric Quadrupole Interaction	H_{eq}	$-e\sum_{\sigma}\left[\mathrm{T}^{k=2}\left(\nabla\hat{\mathbf{E}}_{\sigma}\right)\cdot\mathrm{T}^{k=2}\left(\hat{\mathbf{Q}}_{\sigma}\right)\right]$	This interaction is included for completeness and results from the interaction of the electrostatic interaction between the nuclei of the molecule and the electrons. Again, the $q \neq 0$ terms are usually neglected since these terms tend to involve higher order electronic states. The magnitude of this interaction is dependent on the nuclear charges, $\hat{\mathbf{Q}}_{\sigma}$, of the atoms, where e is the charge of an electron. The interaction is also dependent on the gradient of the electric field that is produced $\nabla\hat{\mathbf{E}}_{\sigma}$.
Zeeman Interaction	H_{Z}	$-g_{\mathrm{e}}\mu_{\mathrm{B}}B_{\mathrm{z}}\mathrm{T}^{k=1}_{q=0}\left(\hat{\mathbf{S}}\right) + g_{\mathrm{l}}\mu_{\mathrm{B}}B_{\mathrm{z}}\mathrm{T}^{k=1}_{q=0}\left(\hat{\mathbf{L}}\right) -$ $g_{\mathrm{R}}\mu_{\mathrm{B}}B_{\mathrm{z}}\mathrm{T}^{k=1}_{q=0}\left(\hat{\mathbf{N}}\right) - g_{\mathbb{I}}\mu_{\mathrm{N}}B_{\mathrm{z}}\mathrm{T}^{k=1}_{q=0}\left(\hat{\mathbf{I}}\right)$	The interaction of each of the magnetic moments and the magnetic field. In order from left to right the interaction term consists of the electron spin, electron orbital angular momentum, the rotation of the molecule, and the nuclear spin. The coupling strength in each case is dictated by the g-factor.

Table 1.1: A brief summary of the common components that form the Effective Hamiltonian (adapted from [3]). The $\{A, B\}\,(= AB + BA)$ indicates an anticommutator to ensure that the operator is Hermitian.

Parameter	**Value (cm^{-1})**
$B_{v=0}$	4.2766
$D_{v=0}$	0.0001837
$\gamma_{v=0}$	0.0424

Table 1.2: A Summary of the parameters used in the calculation of the CaH energy levels. Values taken from [4].

Calcium Monohydride in the Electronic Ground state $\mathrm{X}^2\Sigma^+$

The ground state of CaH is a $\mathrm{X}^2\Sigma^+$ state. As such the total electron spin is $S = 1/2$ and the total electronic orbital angular momentum $L = 0$. There is therefore no spin-spin or spin-orbit interactions. As a result it conforms to Hund's case b) coupling. In the most general case of this regime, $\hat{\mathbf{L}}$ precesses around the molecular axis (chosen to be z in this example) rapidly. It couples with the rotational angular momentum of the nuclei, $\hat{\mathbf{R}}$, to form $\hat{\mathbf{N}}$. This is the total angular momentum of the system excluding the electron spin. Finally the total angular momentum of the system, $\hat{\mathbf{J}}$, is defined as $\hat{\mathbf{N}} + \hat{\mathbf{S}}$. Thus the good quantum numbers are Λ (the projection of $\hat{\mathbf{L}}$ onto the molecular axis), N, S and J. CaH has a nuclear spin of $I = 1/2$ due to the hydrogen atom. To include the hyperfine interaction, the new total angular momentum is $\hat{\mathbf{F}} = \hat{\mathbf{J}} + \hat{\mathbf{I}}$. The complete form of the Hund's case b) basis functions are therefore $|\eta, \Lambda, N, S, J, I, F, m_\mathrm{F}\rangle$ in the hyperfine-coupled basis. Where η encapsulates all other quantum numbers such as vibrational state and electronic state numbers.

The first order effective Hamiltonian for CaH $\mathrm{X}^2\Sigma^+$ in a magnetic field is

$$\begin{aligned} H_\mathrm{eff} &= H_\mathrm{rot} + H_\mathrm{cd} + H_\mathrm{sr} + H_\mathrm{Z} \\ &= \left(B_{v=0}\hat{\mathbf{N}}^2 - D_{v=0}\hat{\mathbf{N}}^4\right) + \gamma_{v=0}\mathrm{T}^1\left(\hat{\mathbf{N}}\right)\cdot\mathrm{T}^1\left(\hat{\mathbf{S}}\right) - g_\mathrm{e}\mu_\mathrm{B}B_z\mathrm{T}^1\left(\hat{\mathbf{S}}\right) - g_\mathrm{R}\mu_\mathrm{B}B_z\mathrm{T}^1\left(\hat{\mathbf{N}}\right). \end{aligned} \tag{1.14}$$

Where the relevant constants for CaH in both the electronic and vibrational ground state can be found in table 1.2.

In order to populate the matrix representation of the Hamiltonian the tensor relationships in appendix A can be used. The $p = 0$ component of the tensor is used since the quantisation axis is once again selected to be in the z direction. The general form of each matrix element will be calculated starting with the Hamiltonian associated with the rotational contribution

$$\begin{aligned} &\frac{1}{\hbar^4}\left\langle \eta, \Lambda, N, S, J, m_\mathrm{J} \middle| \hbar^2 B_{v=0}\hat{\mathbf{N}}^2 - D_{v=0}\hat{\mathbf{N}}^4 \middle| \eta, \Lambda, N, S, J, m_\mathrm{J}\right\rangle \\ &= \left(B_{v=0} - D_{v=0}N\left(N+1\right)\right)N\left(N+1\right). \end{aligned} \tag{1.15}$$

The contribution of these terms forms a diagonal matrix. This is also true of the spin-rotation interaction. Using the tensor relationships in appendix A, one can generate an equation for the element of the matrix representation of this Hamiltonian component,

$$
\begin{aligned}
&\frac{1}{\hbar^2}\left\langle \eta,\Lambda,N,S,J,m_{\mathrm{J}}\,\middle|\,\gamma_{v=0}\mathrm{T}^1\left(\hat{\mathbf{N}}\right)\cdot\mathrm{T}^1\left(\hat{\mathbf{S}}\right)\,\middle|\,\eta,\Lambda,N',S',J',m_{\mathrm{J}}'\right\rangle \\
&= \frac{\gamma_{v=0}}{\hbar^2}\delta_{JJ'}\delta_{m_{\mathrm{J}}m_{\mathrm{J}}'}\left(-1\right)^{N'+J+S}\begin{Bmatrix} S' & N' & J \\ N & S & 1 \end{Bmatrix}\left\langle \eta,\Lambda,N,J,m_{\mathrm{J}}\,\middle\|\hat{\mathbf{N}}\middle\|\,\eta,\Lambda,N,J,m_{\mathrm{J}}\right\rangle \\
&\qquad\times\left\langle \eta,\Lambda,S,J,m_{\mathrm{J}}\,\middle\|\hat{\mathbf{S}}\middle\|\,\eta,\Lambda,S,J,m_{\mathrm{J}}\right\rangle \\
&= \gamma_{v=0}\delta_{JJ'}\delta_{m_{\mathrm{J}}m_{\mathrm{J}}'}\delta_{SS'}\delta_{NN'}\left(-1\right)^{N+J+S}\begin{Bmatrix} S & N & J \\ N & S & 1 \end{Bmatrix}\sqrt{N\left(N+1\right)\left(2N+1\right)S\left(S+1\right)\left(2S+1\right)} \\
&= \gamma_{v=0}\left(-1\right)^{N+J+S}\begin{Bmatrix} S & N & J \\ N & S & 1 \end{Bmatrix}\sqrt{N\left(N+1\right)\left(2N+1\right)S\left(S+1\right)\left(2S+1\right)} \\
&= \begin{cases} \gamma_{v=0}N & ,\ J=N+1 \\ -\gamma_{v=0} & ,\ J=N \\ \gamma_{v=0}\left(N+1\right) & ,\ J=N-1 \end{cases}
\end{aligned}
\qquad . \qquad (1.16)
$$

The final term to evaluate is the Zeeman Hamiltonian in this instance the effects of the hyperfine structure will be neglected. This is simply because the solution can be expressed readily as an analytic function. Further details on the Zeeman effect and hyperfine structure of CaH can be found in appendix B. The two parts of the Zeeman interaction in CaH originate from the interaction of the field with the electronic spin and with the rotation of the molecule. The strength of the rotational coupling to the field is set with the g-factor, g_{R}. In this treatment it is assumed that for CaH the g_{e} is much larger than g_{R} and can be ignored, since high precision results are not required in this particular application. Choosing the magnetic field to point along the z axis, the matrix elements have the form

$$
\begin{aligned}
&-\frac{g_{\mathrm{e}}\mu_{\mathrm{B}}B_{\mathrm{z}}}{\hbar}\left\langle \eta,\Lambda,N,S,J,m_{\mathrm{J}}\,\middle|\,\hat{S_{\mathrm{z}}}\,\middle|\,\eta,\Lambda,N',S',J',m_{\mathrm{J}}'\right\rangle \\
&= -\frac{g_{\mathrm{e}}\mu_{\mathrm{B}}B_{\mathrm{z}}}{\hbar}\left(-1\right)^{J-m_{\mathrm{J}}}\begin{pmatrix} J & 1 & J' \\ -m_{\mathrm{J}} & 0 & m_{\mathrm{J}}' \end{pmatrix}\left\langle \eta,\Lambda,N,S,J,m_{\mathrm{J}}\,\middle\|\mathrm{T}^1\left(\hat{\mathbf{S}}\right)\middle\|\,\eta,\Lambda,N',S',J',m_{\mathrm{J}}'\right\rangle \\
&= -\frac{g_{\mathrm{e}}\mu_{\mathrm{B}}B_{\mathrm{z}}}{\hbar}\left(-1\right)^{J-m_{\mathrm{J}}+J'+N+S+1}\delta_{NN'}\begin{pmatrix} J & 1 & J' \\ -m_{\mathrm{J}} & 0 & m_{\mathrm{J}}' \end{pmatrix}\begin{Bmatrix} S' & J' & N \\ J & S & 1 \end{Bmatrix}\sqrt{\left(2J+1\right)\left(2J'+1\right)} \\
&\qquad\times\left\langle \eta,\Lambda,S,J,m_{\mathrm{J}}\,\middle\|\mathrm{T}^1\left(\hat{\mathbf{S}}\right)\middle\|\,\eta,\Lambda,S',J',m_{\mathrm{J}}'\right\rangle \\
&= -\frac{g_{\mathrm{e}}\mu_{\mathrm{B}}B_{\mathrm{z}}}{\hbar}\left(-1\right)^{J-m_{\mathrm{J}}+J'+N+S+1}\delta_{NN'}\delta_{SS'}\begin{pmatrix} J & 1 & J' \\ -m_{\mathrm{J}} & 0 & m_{\mathrm{J}}' \end{pmatrix}\begin{Bmatrix} S & J' & N \\ J & S & 1 \end{Bmatrix} \\
&\qquad\times\sqrt{\left(2J+1\right)\left(2J'+1\right)S\left(S+1\right)\left(2S+1\right)} \\
&= -\frac{g_{\mathrm{e}}\mu_{\mathrm{B}}B_{\mathrm{z}}}{\hbar}\left(-1\right)^{J-m_{\mathrm{J}}+J'+N+S+1}\begin{pmatrix} J & 1 & J' \\ -m_{\mathrm{J}} & 0 & m_{\mathrm{J}}' \end{pmatrix}\begin{Bmatrix} S & J' & N \\ J & S & 1 \end{Bmatrix} \\
&\qquad\times\sqrt{\left(2J+1\right)\left(2J'+1\right)S\left(S+1\right)\left(2S+1\right)}
\end{aligned}
\qquad . \qquad (1.17)
$$

The form of the Zeeman interaction produces off-diagonal terms since the triangular rules for the j symbols produce non-zero elements for $J' = J$ and $J' = J \pm 1$. This results in

$$
-\frac{g_{\mathrm{e}}\mu_{\mathrm{B}}B_{\mathrm{z}}}{\hbar}\left\langle \eta,\Lambda,N,S,J,m_{\mathrm{J}}\,\middle|\,\hat{S_{\mathrm{z}}}\,\middle|\,\eta,\Lambda,N,S,J,m_{\mathrm{J}}\right\rangle = \begin{cases} -\frac{g_{\mathrm{e}}\mu_{\mathrm{B}}B_{\mathrm{z}}}{N+1} & ,\ J=N+1 \\ -\frac{g_{\mathrm{e}}\mu_{\mathrm{B}}B_{\mathrm{z}}}{N(N+1)} & ,\ J=N \\ \frac{g_{\mathrm{e}}\mu_{\mathrm{B}}B_{\mathrm{z}}}{N} & ,\ J=N-1 \end{cases} \qquad (1.18)
$$

for $J' = J$,

$$-\frac{g_{\mathrm{e}}\mu_{\mathrm{B}}B_{\mathrm{z}}}{\hbar}\left\langle \eta,\Lambda,N,S,J,m_{\mathrm{J}}\middle|\hat{S_{\mathrm{z}}}\middle|\eta,\Lambda,N,S,J+1,m_{\mathrm{J}}\right\rangle = \begin{cases} -g_{\mathrm{e}}\mu_{\mathrm{B}}B_{\mathrm{z}}\sqrt{\frac{N\left((N+1)^2-m_{\mathrm{J}}\right)}{(N+1)^2(2N+1)}} & ,J=N+1 \\ -g_{\mathrm{e}}\mu_{\mathrm{B}}B_{\mathrm{z}}\sqrt{\frac{\left(N^2-m_{\mathrm{J}}^2\right)(N+1)}{N^2(2N+1)}} & ,J=N \\ 0 & ,J=N-1 \end{cases} \tag{1.19}$$

for $J' = J + 1$ and,

$$-\frac{g_{\mathrm{e}}\mu_{\mathrm{B}}B_{\mathrm{z}}}{\hbar}\left\langle \eta,\Lambda,N,S,J,m_{\mathrm{J}}\middle|\hat{S_{\mathrm{z}}}\middle|\eta,\Lambda,N,S,J-1,m_{\mathrm{J}}\right\rangle = \begin{cases} 0 & ,J=N+1 \\ -g_{\mathrm{e}}\mu_{\mathrm{B}}B_{\mathrm{z}}\sqrt{\frac{N\left((N+1)^2-m_{\mathrm{J}}\right)}{(N+1)^2(2N+1)}} & ,J=N \\ -g_{\mathrm{e}}\mu_{\mathrm{B}}B_{\mathrm{z}}\sqrt{\frac{\left(N^2-m_{\mathrm{J}}^2\right)(N+1)}{N^2(2N+1)}} & ,J=N-1 \end{cases} \tag{1.20}$$

for $J' = J + 1$. In order to calculate the eigenvalues of the matrix for a particular m_{J} state one must remove the J states which are less than m_{J}. This is a consequence of $J >= |m_{\mathrm{J}}|$. This is allowed as a result of different m_{J} sublevels not interacting.

Finally, one can plot the eigenvalues of the Hamiltonian as a function of field to study the Zeeman interaction in CaH. Figure 1.5 shows the Zeeman effect in the first two rotational states of CaH. Figure 1.5a) shows the relatively large splitting between the rotational states owing to the large rotational constant of CaH. CaH may prove to be a good candidate for future experiments since the first state crossing does not occur in the field strengths achievable with the decelerator. The inset of figure 1.5a) shows the hyperfine structure of the N = 0 state. The hyperfine structure occurs due to the 1/2 nuclear spin of the hydrogen atom. The model includes the Fermi contact interaction and dipolar interaction terms with coupling constants of 159.19 and 1.39 MHz respectively [151]. More details on the hyperfine levels of CaH can be found in appendix B. Figure 1.5b) shows the close-up of the rotational states. The $N = 1$ state is split into two J components each with $2J + 1$ sublevels. At low fields the m_{J} quantum number describes the states well, however, at larger fields m_{S} quantum number is more suitable. The $|N = 0, J = 1/2, m_{\mathrm{J}} = 1/2\rangle$ spin stretched state has been highlighted which has a effective magnetic moment of $1\mu_{\mathrm{B}}$. This state will be discussed more fully in chapter 6.

1.4 The Conventional Zeeman Decelerator

Zeeman decelerators make use of the force felt by a paramagnetic atom or molecule by a time-dependent magnetic field. The operation of a Zeeman decelerator (although referred to here as a conventional Zeeman decelerator to avoid ambiguity) was originally reported independently by Vanhaecke *et al.* and Narevicius *et al.* in 2007. It should be noted that, although the designs of elements are subtly different, the deceleration process in much the same. Such a device can be described as a quasi-moving potential generated by a series of solenoid coils. A conventional Zeeman decelerator functions by converting the kinetic energy of low-field-seeking particles with high longitudinal velocity into Zeeman potential energy. The magnetic field is generated by a current carrying solenoid, which creates a longitudinal field as shown in figure 1.6a). The presence of the field slows the particles as the kinetic energy is converted into potential energy, in much the same way a car coasting

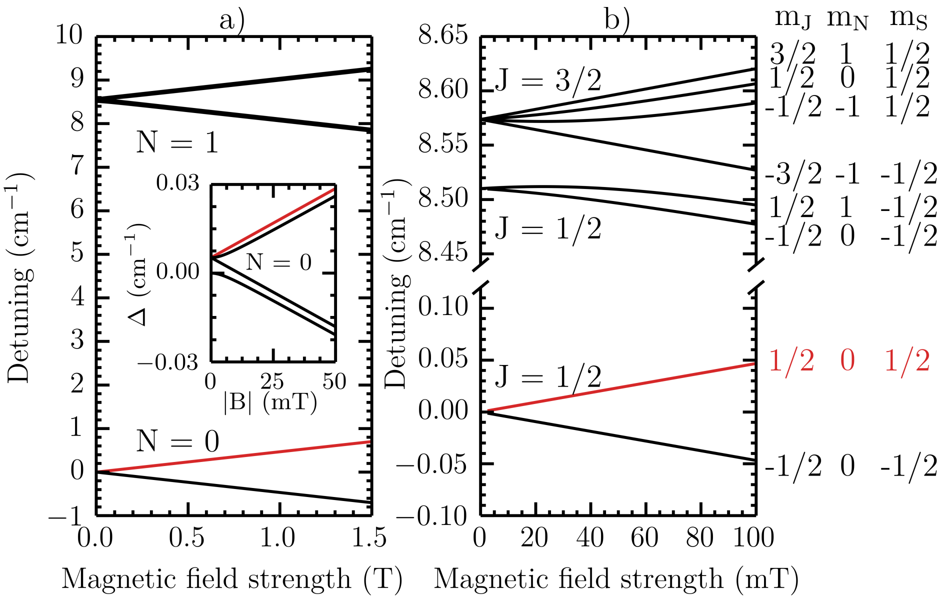

Figure 1.5: The Zeeman interaction of the $X^2\Sigma^+$ state of CaH in the vibrational ground state. Panel a) shows the first two rotational states. The energy levels do not cross in the region of magnetic field strength that the decelerator operates in. The inset shows the detuning, Δ, of the hyperfine structure of the N = 0 state, details can be found in appendix B. Panel b) shows the states at lower magnetic field strengths. Each rotational state is split into states corresponding to $|N - J|, ..., N + J$. Additionally these J states are composed of $2J + 1$ sublevels which are degenerate without the application of the external field. At low fields the m_J quantum number describes the states well, however, at larger fields m_S quantum number is more suitable. Finally, the spin stretched $|N = 0, J = 1/2, m_J = 1/2\rangle$ state is highlighted in red. This state has an effective magnetic moment of $1\mu_B$ and would make an ideal state to trap magnetically.

up a hill is decelerated. Before the particle reaches the maxima (and would begin to accelerate) the field is switched off thus permanently removing the kinetic energy. Multiple stages are used in order to further reduce the kinetic energy of the gas particle.

When describing this type of Zeeman decelerator, it is convenient to describe the longitudinal position of the particles in terms of a phase angle ϕ. This is because of the periodicity of the deceleration process. The definition of this phase angle is shown pictorially in figure 1.6a). A phase angle of 90° corresponds to the centre of the solenoid while a phase angle of 0° corresponds to the centre of the space between two adjacent solenoids. The amount of kinetic energy removed from a particle per coil is dependent on the particle's position along the beam axis at the point the magnetic field is switched off. Before trajectory optimisation was introduced, the deceleration pulse sequence was created by choosing an equilibrium phase angle, ϕ_o at which the coil would be switched off. This would occur when the synchronous particle, which is defined as a particle travelling along the beam axis with longitudinal velocity v_o, reaches that phase angle in a given coil. By definition, the synchronous particle will travel through one period (of length L) without oscillation and will thus have the same amount of kinetic energy removed per stage. An asynchronous particle will experience oscillations as it passes through the decelerator. For example a particle in the same spatial location as the synchronous particle but with a higher longitudinal velocity will travel further into the solenoid before the field is switched off. Over a series of deceleration stages, the asynchronous particle will gain in phase angle until it acquires a longitudinal velocity of v_o. At this point the relative phase angle between the asynchronous and synchronous particles begins to decrease along the longitudinal velocity. The asynchronous particle will return to the same equilibrium phase angle as the synchronous particle but this time with a lower longitudinal velocity. The opposite process then occurs to complete the oscillation.

Figure 1.7 (taken from [1]) has been included to highlight the phase space acceptance of deuterium atoms in a conventional Zeeman decelerator and a summarised version of the results is given here. In each case the separatrix has been included. This marks the boundary between stable and unstable trajectroies in phase space. A slightly more formal definition can be derived by finding the curve in phase space where total energy of a particle is zero (i.e. the sum of the kinetic and potential energies is zero). The trajectories of the particles within the separatrix are closed and therefore trapped whereas particles outside the separatrix cannot be considered trapped. The trajectory of the particles through the decelerator will be explained first in the 1D case. The phase space acceptance plots corresponding to the 1D decelerator are shown in the first column of figure 1.7. In this case, the accepted particles fill the phase space region up to the separatrix for each of the equilibrium phase angles tested. Additionally, a high velocity and high phase angle tail outside of the separatrix exists. Wiederkehr *et al.* suggests both the thickness and number of particles that form the tail is dependent on the length of the decelerator [1]. In general longer decelerators (or equivalently higher values of ϕ_o) results in a thinner, sparser tails. The transverse effects can also be included into the trajectory simulations to further investigate the phase stability in the conventional Zeeman decelerator. A 3D plot of the typical solenoid field is shown in the middle column of figure 1.6. The transverse field of the solenoid varies as a function of longitudinal position. Close to the centre of the solenoid the transverse field is concave, leading to the focusing of low-field seeking states back on axis. At large distances from the centre of the coil, however, the field is convex and this defocuses the low-field seeking states. This relationship between the longitudinal and transverse fields couples the longitudinal and transverse motion of the particles. The effect this has on the phase space acceptance can be seen in the middle column of figure 1.7. For low values of ϕ_o a halo of accepted particles form around the synchronous particle, closely conforming to the shape of the separatrix. The size of the particle distribution that is not accepted decreases as the value of ϕ_o increases. Wiederkehr *et al.* [1] have shown that the missing central region of the separatrix results from the convex nature of the transverse magnetic field away from the centre of the solenoid. The defocusing that a particle experiences can be corrected provided the longitudinal oscillation allows the particle to reach the focusing region of the field. It should be noted that the forces which cause focusing are typically

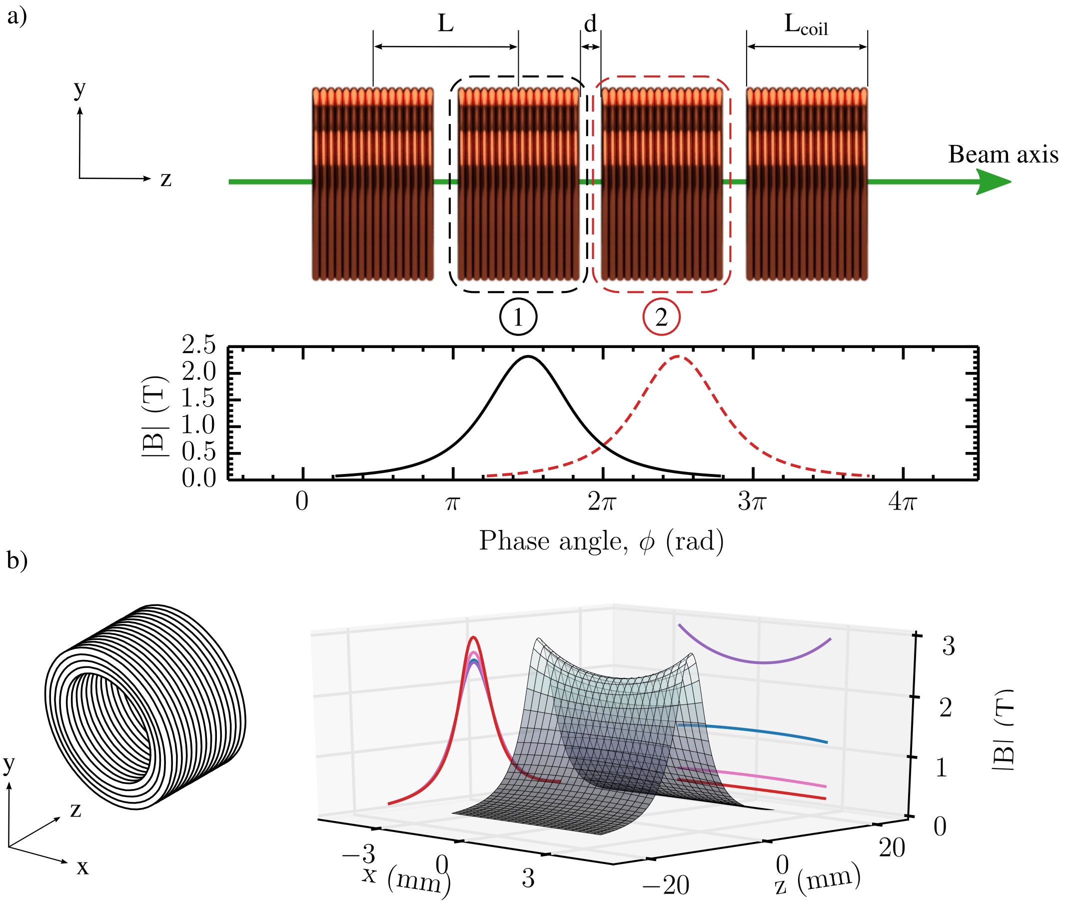

Figure 1.6: A simplified schematic of a conventional Zeeman decelerator. Panel a) shows the period layout of solenoids centred on the beam axis and the periodic fields produced by the solenoid. The diagram shows the field generated by solenoid 1 (black) and subsequently solenoid 2 (red). The positions of the coils are given in terms of the phase angle, ϕ. Panel b) shows a 3D plot of the central region of the solenoid displayed. A typical solenoid consists of regions of concave and convex transverse fields. These are defocusing at large distances from the centre and focusing near to the centre of the solenoid respectively. Contour projections of the field in the transverse and longitudinal directions have also been included.

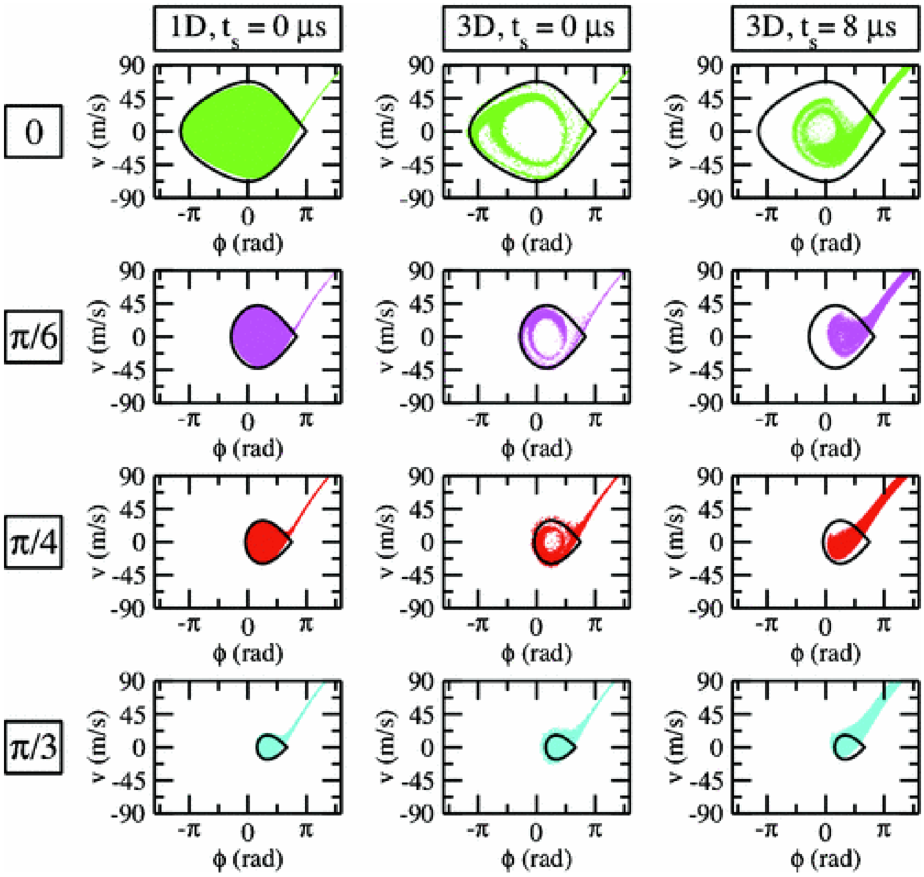

Figure 1.7: The phase space acceptance of deuterium atoms decelerated using a conventional Zeeman decelerator. The deceleration is shown for a series of equilibrium phase angles, ϕ_0. The first and second columns show the deceleration in 1D and 3D where the coils are switched instantaneously. The right most column shows the deceleration in 3D with a realistic rise and fall time in current, in this instance t_s = 8 μs. In each plot the 1D separatrix has been plotted (black). Taken from [1].

greater in magnitude than those that cause the defocusing. For low values of ϕ_0, the oscillations must be fairly large in order to reach the central regions of the coil. Thus, particles with a large relative phase angle with respect to the synchronous particle are accepted by the decelerator. Higher values of ϕ_0 result in the synchronous particle moving further into the coil before the field is removed. Therefore, particles with a smaller relative phase angle, with respect to the synchronous particle, can reach the focusing region. Furthermore, additional transverse losses occur if the particles spend too much time in the focusing region of the field. The net gain in transverse velocity though the many oscillations can eventually become so large the defocusing fields can not compensate any longer. This 'over-focusing' results in loss as a selection of slower moving particles will be driven into the walls of the experiment. Finally, real coils take a finite time for current to reach a certain value and then decay to zero. This also effects the acceptance of the decelerator. For the same switching sequence as above, the synchronous particle will now experience a higher equilibrium phase angle due to the lag in the rise in current. Therefore, more kinetic energy is lost per stage. The results of these simulations are shown in the right-most column of figure 1.7, where the coils have a rise and fall time in current of 8 μs. The high equilibrium phase angle explains the reduced size of the accepted particles with respect to the separatrix. The central area of the acceptance plots are now filled which is a result of the synchronous particle reaching further into the coil. The high-velocity, high phase angle tail is now thicker due to the reduced number of stages required to decelerate the packet.

To overcome the issue of coupling of longitudinal and transverse motion, improvements to the design and operation of the decelerator can be made. For example, higher order modes of operation can be used [1]. For instance, the third order mode can be achieved by increasing the spacing between decelerator stages. If coil N was used to decelerate (i.e. is switched off once the synchronous particle reaches the phase angle ϕ_o), coil N-1 is used to focus the beam. This is achieved by maintaining the field in the N-1 coil as the gas packet travels through the bore of the solenoid. The higher order modes of operation come at the expense of the length of the decelerator, for the third order mode of operation the decelerator length would have to be doubled. Another method demonstrated by Dulitz *et al.* periodically uses two of the solenoids to produce an anti-Helmholtz configuration. The transverse confinement is enhanced by the quadrupole field generated [152]. Similarly, Cremers *et al.* alternate the solenoids stages with permanent magnets in a hexapole configuration in order to achieve transverse confinement [153]. This form of dynamic confinement has demonstrated an overall increase in phase space stability. Another solution to this problem is to design a Zeeman decelerator which not only confines the particle longitudinally but also transversely. This requires the generation of 3D moving magnetic traps to confine the particles throughout the deceleration process. This technique is analogous to the moving trap Stark decelerators [59, 58, 60, 61, 31, 62]. To date, two designs of moving trap Zeeman decelerators have been reported. The decelerators differ in the coils used to generate the magnetic field. The first relies on a series of interwoven anti-helmholtz coils, proposed by Lavert-Ofir *et al.* [154]. The second, developed by Trimeche *et al.*, employs flattened helical coils and a quadrupole guide [75]. Additionally, moving trap decelerators can decelerate one or more isotopes and even multiple species simultaneously. This is not possible in conventional Zeeman decelerator because the difference in the masses and magnetic dipole moments of the species results in inefficient deceleration for all species apart from the one that the pulse sequence was optimised for. A summary of the accomplishments to date of both conventional and moving trap Zeeman decelerators can be found in table 1.3. Since the work of Vanhaecke *et al.* and Narevicius *et al.*, other groups have adopted the conventional Zeeman decelerator to slow both atoms and molecules. Table 1.3 describes the key results from the groups, the length of the decelerator, and the species that were decelerated. The table is further divided into groups working with conventional or moving trap Zeeman decelerators.

Group	Description	Reference
Merkt	**2007** - Deceleration of H, seeded in Xe, from 313 $\mathrm{m\,s^{-1}}$ to 225 $\mathrm{m\,s^{-1}}$ over 6 stages.	[72]
	2007 - Deceleration of H and D seeded in both Ar and Kr. The latter were decelerated from 422 $\mathrm{m\,s^{-1}}$ to 278 m/s and 367 m/s respectively, using 7 stages.	[155]
	2008 - H, seeded in Kr, decelerated from 435 $\mathrm{m\,s^{-1}}$ to 107 $\mathrm{m\,s^{-1}}$ by 12 stages.	[156]
	2008 - H, again seeded in Kr, was trapped after being decelerated from 520 $\mathrm{m\,s^{-1}}$ to 100 $\mathrm{m\,s^{-1}}$ using 12 stages.	[157]
	2010 - D, seeded in Kr, was trapped after being decelerated from 475 $\mathrm{m\,s^{-1}}$ to 80 $\mathrm{m\,s^{-1}}$ over 24 stages.	[158]
	2011 - Deceleration of metastable Ne from 580 $\mathrm{m\,s^{-1}}$ to 105 $\mathrm{m\,s^{-1}}$ using 91 stages. The effect of isotope separation between ^{20}Ne and ^{22}Ne was also studied.	[159]
	2012 - Deceleration of O_2 from both 450 and 390 $\mathrm{m\,s^{-1}}$ to final velocities from 280 to 150 $\mathrm{m\,s^{-1}}$ using 90 stages.	[160]
	2014 - He_2 was decelerated from 500 $\mathrm{m\,s^{-1}}$ to velocities as low as 100 $\mathrm{m\,s^{-1}}$ with 55 stages.	[161]
Raizen	**2007** - Deceleration of metastable Ne from 461 ± 7 $\mathrm{m\,s^{-1}}$ to 403 ± 16 $\mathrm{m\,s^{-1}}$ over 18 stages.	[73]
	2008 - O_2, seeded in Kr, was decelerated from 389 ± 5 $\mathrm{m\,s^{-1}}$ to 83 ± 3 $\mathrm{m\,s^{-1}}$ over 64 stages.	[162]
	2008 - Metastable Ne was decelerated from 446.5 ± 2.5 $\mathrm{m\,s^{-1}}$ to 55.8 ± 4.7 $\mathrm{m\,s^{-1}}$ using 64 stages.	[163]
Momose	**2013** - Methyl radicals, CH_3, decelerated from 510 $\mathrm{m\,s^{-1}}$ to 480 $\mathrm{m\,s^{-1}}$ over 14 working stages.	[164]
	2015 - O_2, seeded in Kr, was decelerated from 320 $\mathrm{m\,s^{-1}}$ to 42 $\mathrm{m\,s^{-1}}$ using 80 stages. The molecules were then trapped using anti-Helmholtz coils.	[165]
	2016 - CH_3, seeded in Kr, was decelerated from 340 $\mathrm{m\,s^{-1}}$ to 60 $\mathrm{m\,s^{-1}}$ using 85 stages. The molecules were then trapped using anti-Helmholtz coils.	[33]
Softley	**2014** - H, seeded in Kr, was decelerated from 500 $\mathrm{s^{-1}}$ to 240 $\mathrm{s^{-1}}$ over 12 stages.	[152]
	2015 - Metastable He, seeded in Ar, was decelerated from 490 $\mathrm{s^{-1}}$ to 370 $\mathrm{s^{-1}}$ over 12 stages.	[166]
	2016 - N, seeded in Ar, was decelerated from 460 $\mathrm{s^{-1}}$ to 410 $\mathrm{s^{-1}}$ over 12 stages.	[167]

Continued on next page

Group	Description	Reference
Van de Meer-akker	**2017** - Deceleration of metastable He from 520 $\mathrm{m\,s^{-1}}$ to 333 $\mathrm{m\,s^{-1}}$ over 24 solenoids stages interspersed with 25 hexapole stages.	[153]
Narevicius	**2011** - Deceleration of metastable Ne from 429.7 ± 6.0 $\mathrm{m\,s^{-1}}$ to 53.8 ± 1.1 $\mathrm{m\,s^{-1}}$ using a moving trap Zeeman decelerator consisting of 213 overlapping quadrupole traps extending over 114 cm.	[74]
	2015 - Simultaneous deceleration of O_2 and metastable Ar from 430 $\mathrm{m\,s^{-1}}$ to 100 $\mathrm{m\,s^{-1}}$ using 480 overlapping quadrupole traps.	[168]
	2016 - Deceleration of O_2 and Li, seeded in Kr, from 375 $\mathrm{m\,s^{-1}}$ to as low as 20 $\mathrm{m\,s^{-1}}$. Both species were then trapped using permanent magnets.	[32]
Vanhaecke	**2011** - Trapping of metastable Ar atoms at 463 $\mathrm{m\,s^{-1}}$ in a 3D travelling wave.	[75]
	2011 Thesis - Deceleration of metastable Ar from 392 $\mathrm{m\,s^{-1}}$ to 365 $\mathrm{m\,s^{-1}}$ over 2 coil stages (approximately 28 cm long).	[169]

Table 1.3: A summary of published work using conventional and moving trap Zeeman decelerators. The table is divided by groups and the relevant paper cited. The upper proportion of the table covers the conventional style of Zeeman decelerator while the lower section details the moving trap Zeeman decelerators.

1.5 Aims of the Project and This Thesis

The major goal of this project is to demonstrate the deceleration of paramagnetic molecules using the travelling wave Zeeman decelerator presented in this thesis. As described above, the motivation behind such a decelerator is to overcome the limitation of the conventional Zeeman decelerators. The ultimate goal of this project is to use the decelerator as a first stage to produce molecules over a range of temperatures as low as the ultracold regime. The intention is to control the inelastic and reactive collisions in atom-molecule systems to empirically study these systems. The motivation behind this pursuit is that the theoretical prediction of cross-section for collisions and reactions are typically computationally intensive. The calculations are further complicated with the introduction of external fields which have been shown to strongly effect the collision and reaction cross-sections [170, 171]. Fortunately, Zeeman decelerators provide a versatile tool for the deceleration of a wide range of atoms, molecules, and radicals. If the molecules can be cooled with ultracold atoms it would be possible to examine the dependence of reaction and collision cross-sections on the molecular orientation (in the presence of an external field) and quantum state of both the molecule and atomic species over a wide range of temperatures. Moreover, through state selection of atoms and molecules, the outcome of collisions can be controlled. This thesis, however, will focus on the former aim: the development of a travelling wave Zeeman decelerator.

This thesis is structured in the following way: The overview of the design and components that make up the 4 module long decelerator is presented in chapter 2. This provides a brief discussion of the background of supersonic expansion, the design and specification of the decelerator and quadrupole coils and a description of the detection scheme used. Chapter 3 goes on to explain the development of the power electronics required to generate the currents that ultimately produce the magnetic fields used in the decelerator. This chapter includes a brief description of the control electronics but mainly focuses on the specification, operation and the evaluation of the quadrupole and decelerator power electronics. Chapter 4 explains the method used to simulate the various aspects of the decelerator including the source and magnetic fields generated by the decelerator coils. The tricubic interpolator is also described here as well as the justifications for the method used to simulate the motion of the trap. Chapter 5 presents the experimental results of the decelerator with metastable argon. Comparison is made to the simulated data and the phase space acceptance of the decelerator is evaluated. Chapter 6 describes the outlook of the project. This chapter is broken down into the short term and long term goals of the project. The latter centres around the co-deceleration of Li and CaH into a magnetic trap. The atoms can then be cooled using conventional methods and sympathetic cooling would then facilitate the production of ultracold molecules. Finally, the contents of this thesis is summarised in chapter 7.

Chapter 2

An Overview of the Decelerator Project

This chapter will provide a general overview of the decelerator. As such, it is convenient to separate the discussion into the three major components of the device: the source, the decelerator stage and the detection scheme. The source and detector are located in separate chambers which are some 670 mm apart. They are linked together with a stainless steel tube, around which the decelerator modules are centred. For reference, figure 2.1 has been included to show the three parts of the decelerator. An important point to make is that the coil modules are located outside of vacuum. The figure shows how the three sections are joined together as well as the vacuum equipment and other measurement apparatus used in the project. Details on the vacuum system and other pieces of equipment can be found in reference [172]. This chapter will begin by discussing the source used to produce the gas samples in section 2.1. This includes a brief description of the process of supersonic expansion which forms the basis of the source of cold (~1 K) atoms and molecules. This section also includes a description of the excitation scheme employed. Next the deceleration stage will be presented in section 2.2. This section includes details of the design of the decelerator and quadrupole coils as well as an explanation of the operation principle of the decelerator. Details of the driving electronics of the decelerator can be found in chapter 3. A brief comparison of the travelling wave and the moving trap decelerator developed by Narevicius and co-workers will also be presented here. The detection scheme employed in the experiment is outlined in section 2.3. Finally, section 2.4 provides a summary of the individual elements described which combine to form the four module long decelerator.

2.1 The Source

For the last five decades, supersonic expansion has been used as a source of cold, dense, highly collimated gas packets [173]. Sources such as these have been used in experiments ranging from the study of collision dynamics of atom-molecule [174] and molecule-molecule systems [136] to precision spectroscopy of molecules [104]. This section will briefly describe the principles behind supersonic expansion, although a more complete description can be found in reference [172]. A brief description of the operation and properties of the pulsed valve currently employed will be given. Similarly, the excitation scheme used to produce the gas packets of metastable atoms or molecular radicals will also be presented. The design of the current iteration of the source and vacuum chamber will be elaborated upon in this section.

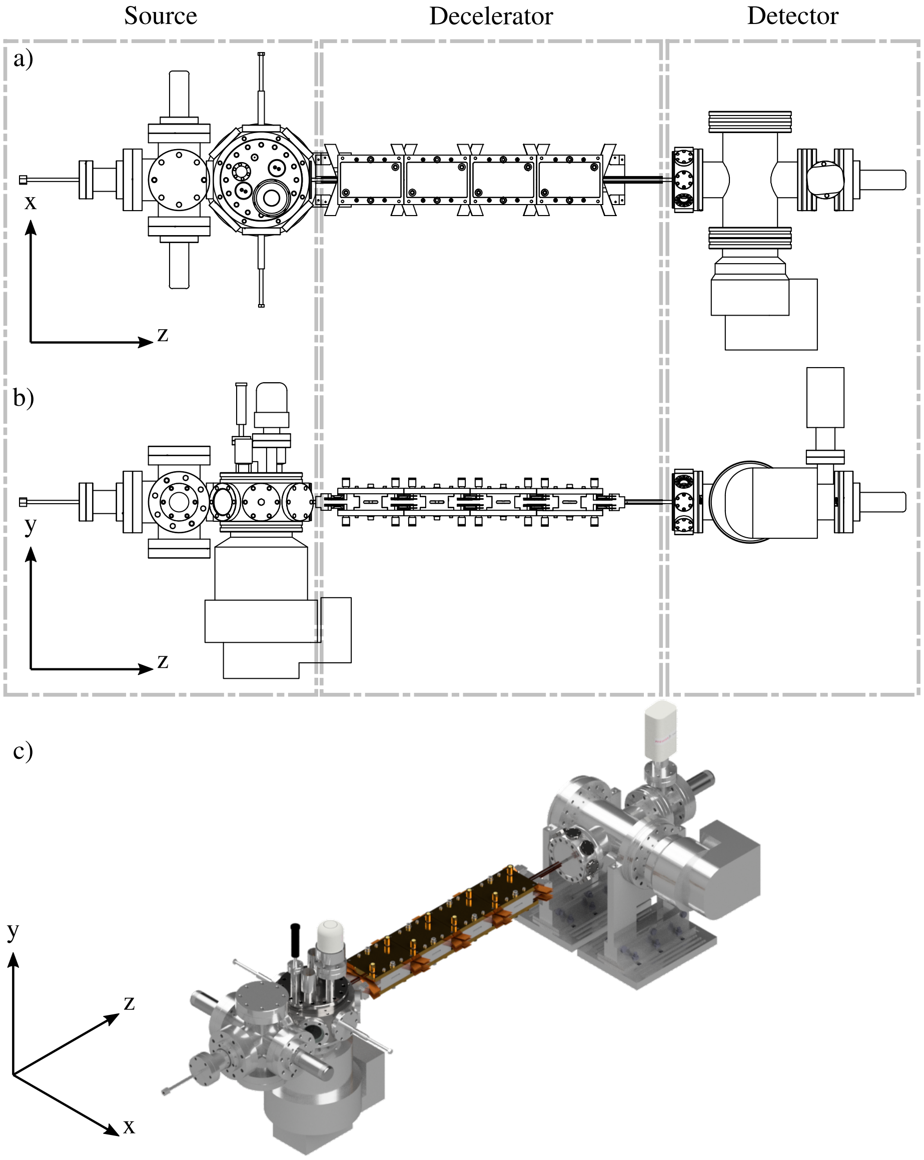

Figure 2.1: A complete view of the decelerator including the vacuum system and other measurement equipment. The panels show three views of the decelerator. Views a) and b) are labelled and indicate the location of the three major components of the device. These include the source chamber, the decelerator stage and the detection chamber. The source and detection chambers are linked together with a stainless steel tube, around which the decelerator modules are centred.

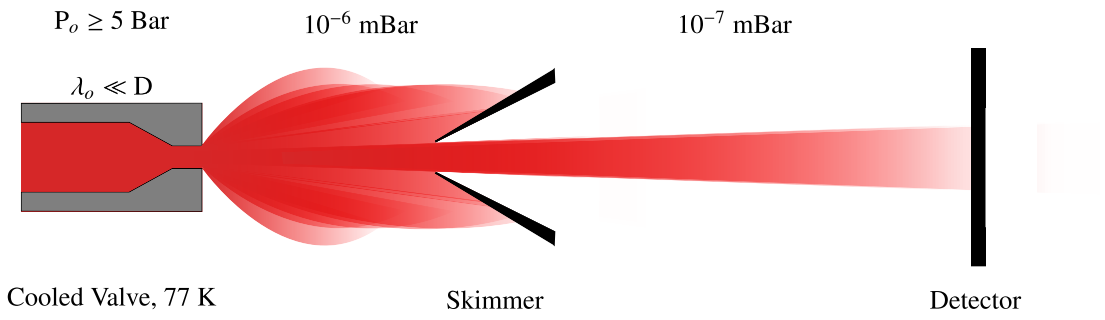

Figure 2.2: An illustration of supersonic expansion. The gas pulse is allowed to expand from a region of high pressure (typically 5 Bar or above) into a region of low pressure. Furthermore, it is assumed that the valve is cooled to 77 K. The drawing also includes the skimmer and detector.

2.1.1 Supersonic Expansion

Supersonic expansion occurs when a gas is allowed to isentropically expand from a region of high pressure, P_{o} into a region of vacuum at pressure, P. It is assumed that the high pressure reservoir is held at temperature T_{o}. Supersonic expansion is achieved if the mean-free path between collisions, λ_{o}, is much smaller than the diameter of the nozzle, D, that the gas expands through. An illustration of supersonic expansion can be seen in figure 2.2. The diagram shows a summary of the criteria necessary for supersonic expansion.

As the gas expands adiabatically, the initial stagnation molar enthalpy, H_{o}, is converted into kinetic energy and a rest molar enthalpy, H, by collisions taking place in the gas

$$H_{\mathrm{o}} = H + \frac{1}{2} N_{\mathrm{A}} m v_{\mathrm{s}}^{2}. \tag{2.1}$$

The kinetic energy of the new distribution, $\frac{1}{2} N_{\mathrm{A}} m v_{\mathrm{s}}^{2}$, for a particle of mass m and velocity v_{s}^{2} is gained in the direction of the particle flow. Using the relationship between enthalpy and specific heat capacity at a constant pressure, c_{P}, $\left(m N_{\mathrm{A}} c_{\mathrm{p}} = (\partial H/\partial T)_{P}\right)$ it is possible to calculate the stagnation velocity, v_{s}. Assuming that temperature dependence of c_{p} is negligible then

$$v_{\mathrm{s}} = \sqrt{2 c_{\mathrm{P}} \left(T_{\mathrm{o}} - T\right)}. \tag{2.2}$$

In an ideal gas $c_{\mathrm{P}} = b_{\mathrm{B}}/m \times \gamma/\left(\gamma - 1\right)$. Here, γ is the ratio of heat capacities, $c_{\mathrm{P}}/c_{\mathrm{V}}$, for a particular form of particle. For monoatomic particles $\gamma = 5/3$ and $7/5$ for diatomic particles. The latter case holds only in the vibrational ground state. As the gas packet continues to expand, the density of the gas packet eventually becomes sufficiently low that the rate of the collisions between the particles is negligible. It should be noted that the thermodynamic arguments used to produce the equations presented below are strictly only true for continuous beam expansion rather than the pulsed expansion used in this experiment. A discussion of pulsed supersonic expansion can be found in reference [175]. The ratio of initial to final temperature of a expanding gas can be linked to the ratio of initial and final pressures, $\left(T/T_{\mathrm{o}} = (P/P_{\mathrm{o}})^{(\gamma-1)/\gamma}\right)$, it is possible to determine that the final or terminal temperature,

T_t, is much smaller than the initial stagnation temperature of the gas. The approximate form of the terminal velocity of a supersonic source is

$$v_{\mathrm{t}} \approx \sqrt{\frac{2k_{\mathrm{B}}T_{\mathrm{o}}}{m}\frac{\gamma}{\gamma-1}}. \tag{2.3}$$

The form of the terminal temperature is

$$T_{\mathrm{t}} = T_{\mathrm{o}}\left(1+\frac{\gamma-1}{2}M_{\mathrm{t}}^{2}\right)^{-1}. \tag{2.4}$$

This introduces the terminal Mach number. The Mach number is the ratio of flow velocity to the local speed of sound. The terminal Mach number can be varied by altering the initial density of the gas packet (or valve pressure for a fixed temperature) and the nozzle diameter. Further dependencies are introduced by the collision cross-section of the particles and the efficiency of the collisions within the expansion. Generally, the terminal Mach number can be expressed in terms of the Knudsen number and the collision efficiency of the gas, ϵ [176]. The Knudsen number is the ratio of the nozzle diameter, D, and the mean-free path between collisions, $K_{\mathrm{N}} = D/\lambda_{\mathrm{o}}$. The terminal Mach number has the form

$$M_{\mathrm{t}} = G\left(\frac{\epsilon}{K_{\mathrm{N}}}\right)^{\frac{\gamma-1}{\gamma}}. \tag{2.5}$$

The constant G depends only on γ and the value of this takes can be found in table 1 in reference [175]. The distribution of velocities of a gas packet following the adiabatic expansion, is very different to a Maxwell-Boltzmann distribution. Integrating over the entirety of velocity space results in the 3D Maxwell-Boltzmann speed distribution

$$f_{\mathrm{v}}(v) = 4\pi\left(\frac{1}{2\pi\sigma_{\mathrm{v}}^{2}}\right)^{\frac{3}{2}} v^{2}\exp\left(\frac{-v^{2}}{2\sigma_{\mathrm{v}}^{2}}\right). \tag{2.6}$$

The velocity spread σ_{v} for an ensemble of particles of mass m and temperature T is given by $\sigma_{\mathrm{v}} = \sqrt{k_{\mathrm{B}}T/m}$. Following supersonic expansion, however, the distribution is modified, and now has the form

$$f_{\mathrm{v}}(v) = 4\pi\left(\frac{1}{2\pi\sigma_{\mathrm{vt}}^{2}}\right)^{\frac{3}{2}} v^{2}\exp\left(\frac{-(v-v_{\mathrm{t}})^{2}}{2\sigma_{\mathrm{vt}}^{2}}\right). \tag{2.7}$$

Equation 2.6 is now modified to include the terminal velocity and the terminal temperature [177]. The terminal velocity spread, σ_{vt}, for an ensemble of particles of mass m, is $\sigma_{\mathrm{vt}} = \sqrt{k_{\mathrm{B}}T_{\mathrm{t}}/m}$. In general, is it often convenient to normalise equations 2.6 and 2.7 to ensure $\int_0^{\infty} Nf_{\mathrm{v}}(v)\,dv = 1$. This allows the direct comparison of the speed distributions of a Maxwell-Boltzmann distribution and of a supersonic expansion. Figure 2.3 shows such a comparison for argon at a reservoir temperature, T_{o}, of 77 K. The supersonic expansion has a reservoir pressure of 5 Bar with a nozzle diameter of 0.2 mm. As a result of the collisions, the gas packet is adiabatically cooled and the velocity spread of the gas packet is very narrow, the intensity of the gas pulse is also much greater than the Maxwell-Boltzmann distribution. This is all, however, at the expense of a high mean velocity typically in the region of several hundred m s^{-1}. To achieve lower terminal velocities it is often beneficial to dilute

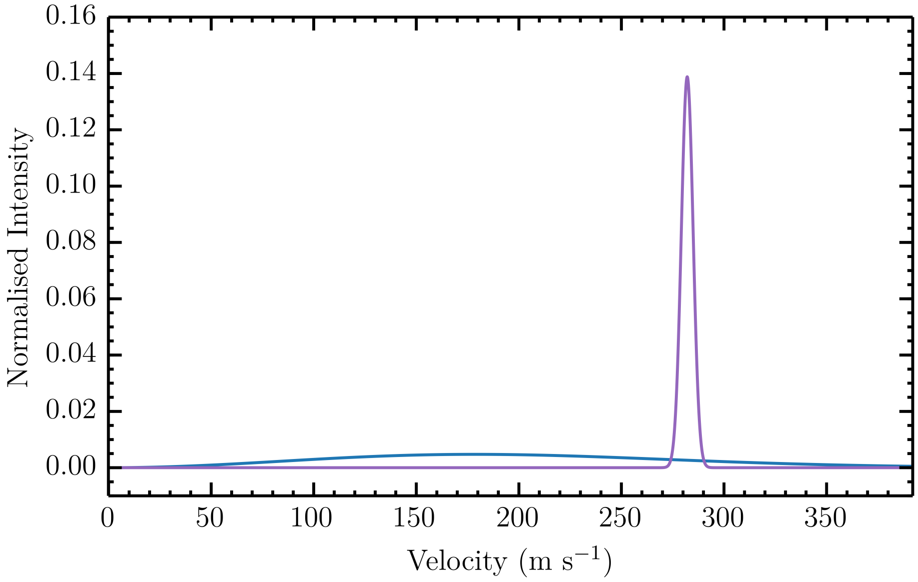

Figure 2.3: A comparison between the velocity distributions of argon in a supersonic beam (purple, equation 2.7) and a Maxwell-Boltzmann distribution (blue, equation 2.6). Both distributions were calculated at 77 K, the supersonic expansion was assumed to originate from a reservoir at 5 Bar. The curves are normalised by their areas.

the species of interest in a heavy carrier gas such as Kr or Xe. The characteristics of the expansion is then determined by the heavier carrier gas. Furthermore, this helps achieve denser gas packets and the more effective cooling of the additional degrees of freedom in molecular samples.

2.1.2 The Excitation Scheme: Dielectric Barrier Discharge

Supersonic expansion can be combined with some form of electrical discharge to produce ions, radical molecules, and metastable atoms. Previous iterations of the decelerator source have employed pulsed electric discharge stabilised with a filament placed close to the electrodes. The excitation would occur across two high voltage electrodes if a gas is present within the discharge volume. Conduction only occurs once the applied voltage exceeds the breakdown voltage of the gas. Collisions between the plasma formed and the gas particles redistribute the energy through the ensemble. A gas packet consisting of ions and excited atomic states or molecular radicals is formed as a consequence. With this configuration, the excitation of the argon atoms would occur some 4 mm away from the nozzle of the valve where the gas density has already begun to fall rapidly. Since the collision rate decreases with density, the energy transfer from the plasma to the gas particles is less efficient as a result.

The technique used currently is dielectric barrier discharge (DBD) and occurs in the nozzle itself. Here, two electrodes are separated by a thin insulator layer. The discharge is initiated by applying a series of high voltage RF pulses to the external electrode. The properties (such as the current, frequency and number of pulses of the RF pulses) are set using a pulse generator *FES - DBD 4000P High voltage RF pulse generator*. This generator is also capable of driving the valve as well. The advantages of the DBD over the previous glow discharge is that firstly the discharge through the gas occurs uniformly. The reasoning is two-fold in the Even-Lavie valve. Firstly, the high voltage is applied around a cylindrically symmetric dielectric. Furthermore, the discharge current through the dielectric is 'self-limiting'. This occurs because of the high mobility of the electrons in the dielectric which initially quenches the field below the breakdown voltage as the current uniformly charges the dielectric [178]. Therefore this method prevents the production of 'hot spots' within the gas packet [179]. Secondly, the DBD allows for the excitation of the high densities of the gas packet without arcing. Thirdly, the excitation results in more intense pulses of metastable gases since the electron energy distribution is much narrower than in glow discharges. Finally, the gas pulse and, more importantly, the valve are not heated to the same extent as the glow discharges.

2.1.3 Source Design

In order to produce pulses of gas, the expansion is controlled with a pulsed valve. The Even-Lavie valve (*SS, unmounted cryogenic valve*) is used in this experiment. The advantage of the Even-Lavie valve over other valves previously used in the experiment is simply higher intensity. This is a direct result of the nozzle shape, which produces a far more directional beam. Additionally, the solenoid action allows backing pressures of up to 100 Bar to be used without compromising the opening and closing of the valve [180]. Typically, the 0.2 mm diameter valve can be opened and closed in around 30 μs. The valve is mounted in a copper cooling jacket through which liquid nitrogen is fed in order to cool the valve. From the equations previously discussed in section 2.1.1, it is clear that this temperature reduction results in a slower, colder gas packet. The temperature of the front and rear faces of the valve body can be monitored with thermocouples.

The final component of the source is the skimmer. Skimmers are used to extract the central spatial region of the gas packet therefore removing the higher transverse velocity components. As a result the beam remains more collimated. In the limit of high densities, the skimmer may interfere with the beam which may result in heating or reduced transmission [180]. The location, shape and sharpness of the skimmer is an important consideration in the dense gas packets produced by the Even-Lavie valve. Somewhat unconventionally, it is necessary to place the skimmer aperture several hundred nozzle diameters away from the valve. In this experiment the skimmer is placed 150 mm away from the valve. The skimmer (*Model 5.8 CU molecular beam skimmer*) has an orifice diameter of 4 mm and is conical in shape. This should help reduce skimmer interference.

A labelled diagram of the source can be seen in figure 2.4. The upper part of the figure shows the geometry of the valve and skimmer, annotated to include relevant dimensions. Additionally the z axis is chosen as the molecular beam axis. The lower half of the drawing shows a cut-through of the source and the vacuum chamber. The parts of the vacuum chamber have been labelled. The extension (a customised *Lewvac FL-5X63CF* 5-way cross with an additional CF40 half nipple) was necessary to accommodate the large valve-to-skimmer separation into the original chamber (*Kimball Physics Inc., MCF600-SphOct-F2C8-A*). Despite this, the vacuum system of the source chamber is largely unchanged from the previous design [172]. The drawing is labelled to show the mounting points for the electrical feedthrough, pressure gauges and the turbopump. The turbopump is placed close to where expansion occurs and therefore ensures low background pressures between pulses. A zoom on the valve is included. This shows the valve mounted in its cooling jacket formed from 1/8 inch copper tubing. The liquid nitrogen can then be passed through from a pressurised dewar (see [172] for further details). The vacuum feedthroughs for the liquid nitrogen and some other electrical connections are normal to the page.

A final point to make regarding the source is the typical characteristics of the metastable argon produced by the combination of the Even-Lavie valve and the DBD. A summary of the main properties is given in table 2.1. The table includes both data collected from various pieces of literature for metastable argon and some values acquired in this experiment (after the valve has been cooled) where applicable. It should be stressed that the properties obtain in this experiment are not necessarily the limiting values of this particular setup. It should also be noted that firstly, the gas density given here is based a simulations of noble gases rather than direct measurement and secondly that the literature regarding the excitation process was presented for metastable neon.

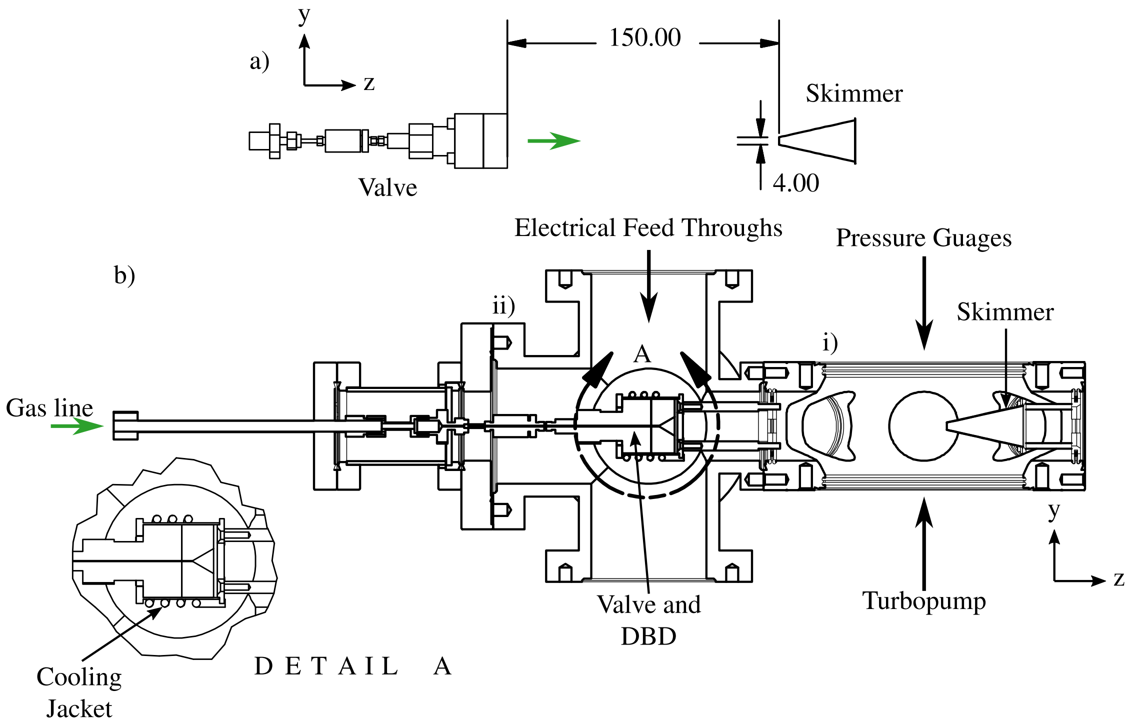

Figure 2.4: A diagram of the source assembly. View a) shows a simplified schematic of the Even-Lavie valve and the skimmer. The nozzle of the valve is located 150 mm away from the skimmer aperture. The skimmer is conical shaped with a 4 mm diameter orifice. These precautions should reduce skimmer interference of the beam. The molecular beam axis is chosen to point along the z direction. View b) shows the cut-through of the source chamber assembly. The original chamber (i) and the extension (ii) are labelled. The drawing includes the mounting locations of the electrical feedthroughs, pressure gauges and the turbopump. Some feedthroughs, such as the liquid nitrogen feedthroughs are normal to the page. Detail A shows a close-up of the valve mounted in the cooling jacket.

Parameter	Typical observed range, Ar	Gas	Extracted values	Reference
Longitudinal temperature (K)	3-4.5	Ar	~1.5 (Valve temperature 130 K)	[180]
Mean longitudinal velocity ($\mathrm{m\,s^{-1}}$)	330-370	Ar	~320 (Valve temperature 130 K)	[180]
Density ($\mathrm{atoms\,cm^{-3}}$)	-	Ne, Ar	1×10^{15} to 1×10^{17} (a few tens of mm from the nozzle).	[180]
Metastable excitation	-	Ne	100% into the $^3P_2$	[181]
Metastable fraction	-	Ne	~6.1×10^9 atoms/valve pulse after the skimmer.	[179]

Table 2.1: A Summary of the parameters expected for an expansion of a noble gas such as argon using the combination of Even-Lavie valve and DBD.

2.2 Decelerator Stage

The first step in producing a cold gas of molecules or atoms from a supersonic source is to reduce the mean velocity of the gas packet to a standstill. Conservative fields, such as magnetic fields, cannot be used to cool a sample. One can narrow the velocity distribution at the expense of the density of the sample. This link between density and temperature is known as Liouville's theorem. A more generalised version of this principle states that in conservative fields the phase space density must remain constant [182]. Therefore, cooling in the strictest sense can only be achieved with a dissipative field, such as a light field, or by loss of particles, in evaporative cooling. The goal of any conservative field decelerator is to bring the mean longitudinal velocity to zero while maintaining the high density of the supersonic pulse. The fraction of the gas packet accepted by the decelerator is dependent on the depth and extent of the field. This concept is illustrated in figure 2.5. The diagram shows a supersonic distribution with a highlighted central region, this represents the fraction of the gas packet accepted by the decelerator. In this example, the decelerator is used to extract the high density central region of the gas packet.

The design of the decelerator is based upon that developed by Trimeche *et al.* [75] although the variant developed in Durham has been scaled up. Firstly, the original coils were constructed from 345 μm diameter cable which limited the current which can be passed through the coils and consequently, the depth of the trap. The coils discussed here are wound from AWG 18, kapton wrapped, copper wire (1.2 mm diameter). This allows the maximum current of 1000 A to be used. The spatial acceptance was also limited by the 1 mm internal diameter of the tube that the decelerator was constructed around. The Durham decelerator is constructed around a 5.35 mm internal diameter (6.35 mm external diameter) stainless steel tube to further increase the spatial acceptance of the decelerator. This section will describe the decelerator coils and the quadrupole coil that produce the decelerator field. The geometry of each coil module and the field that is produced will also be examined. Finally, the layout of the current iteration of decelerator will be presented.

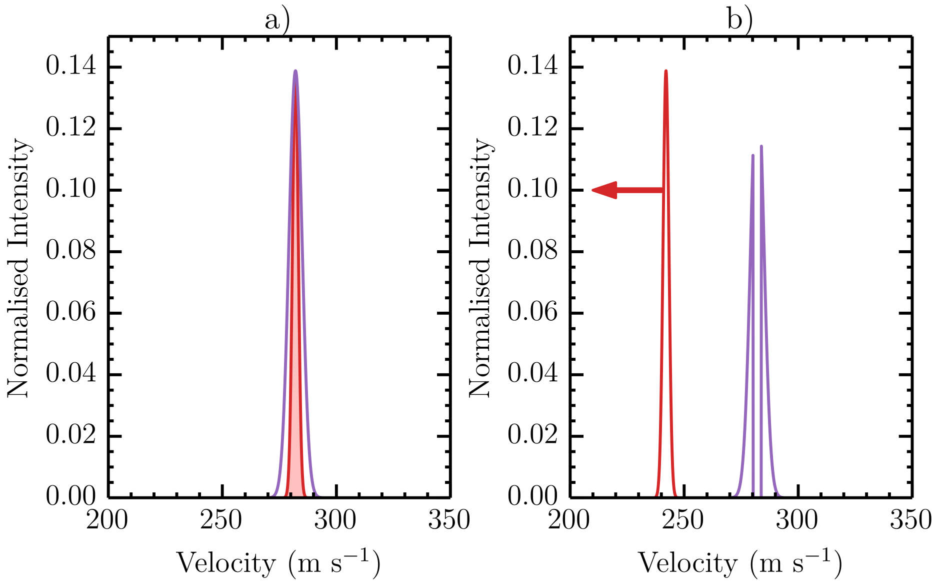

Figure 2.5: A schematic representation of the deceleration process. The longitudinal velocity distribution of a supersonic expansion (purple) is shown in panel a) with the fraction that is accepted by the decelerated highlighted (red). Panel b) shows the same velocity distribution some time later during the deceleration process. Once again, the slice of the velocity distribution accepted by the decelerator has been highlighted. This phase-stable region then has the mean longitudinal velocity removed while conserving the density of the slice.

2.2.1 The Decelerator Coils

The coils that produce the decelerator field are planar, helical coils. Figure 2.6 shows a pair of simplified coils each consisting of 2 wires. The first thing to note is that a decelerator module is formed from two sets of coils. These coils are equidistantly spaced around the z (or molecular beam) axis. The coils below the z axis are wound with the opposite handedness to those above the axis. The coils are also periodic and have a spatial periodicity of λ, this implies that the field produced by these coils is also periodic. Hence, why the field is often referred to as a wave. Figure 2.6 also shows the current flow through each wire element. By tracing the current around a single coil it is possible to see how a trap is formed. The wires that form a coil periodically cross each other. This geometry can be approximated to a set of separate rhombus shaped rings. The current in the lower set of rings flows in the opposite direction to that through the upper rings, forming an anti-Helmholtz coil array. Therefore, the field produced by these coils is quadrupole in nature.

In order to produce deep traps, Trimeche *et al.* constructed each coil from two sets of 16 wires similar to the coil shown in figure 2.7a). The period length is dependent on the diameter of the wire, d_{w}, and the half angle the wires cross at, α. The period of the coil, λ, has the form

$$\lambda = \frac{32 d_{\mathrm{w}}}{\sin(\alpha)}. \tag{2.8}$$

The choice of half angle in the Durham decelerator was chosen to be 70°. It has been previously found that this angle is near optimum in terms of decelerator efficiency while still possessing fairly large longitudinal traps. The period of the coils in this thesis is therefore 40.9 mm. The wires in each period are divided into blocks to form separate current phases. The Trimeche *et al* coil consisted of 2 × 8 wire blocks. This helps keep the motion of the trap smooth since the additional phases add more effective current loops to each coil. Two phases, however, result in spatially large traps. To

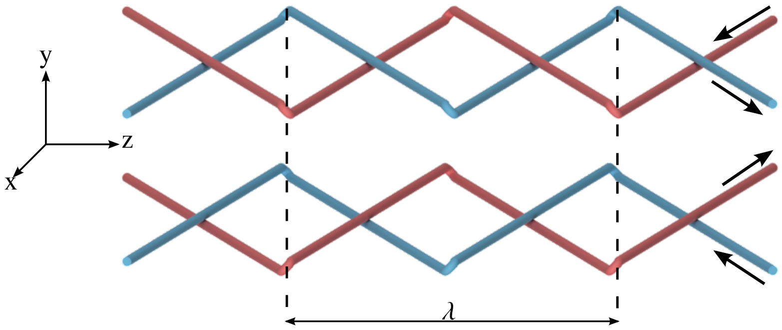

Figure 2.6: A simplified pair of flattened helical coils consisting of just four wires. The coils are offset in the y direction while remaining symmetrically spaced around the z axis. The lower set of coils is wound with the opposite handedness to the upper coils. The arrows represent the direction of the current flow in the wires. The spatially periodic nature of the coils is clearly shown in this representation, the period, λ has been labelled.

limit the spatial extent of the trap the coils employed in this thesis are divided into 4 wire blocks. In addition, each coil was paired with another coil thereby constructing wire blocks consisting of 4 × 4 wires. The advantage of this configuration is that for a particular current the field gradient is roughly doubled. Moreover, more effective traps results in the smoother translation of the moving trap. Figure 2.7b) shows the 4 coils that produce a decelerator module. The diagram is an exploded view of the coil module, in reality the coils that form a pair are in contact.

A single decelerator coil has three periods and is 12.3 cm in length. This was chosen based on the resistance and inductance of the coil, more details can be found in chapter 3. The coils are wound on a motorised jig which wraps the wires around a die. The coils can then be pressed flat and set in thermally conductive epoxy (*Stycast 2850FT with catalyst 9*). The construction process is detailed fully in appendix C. The outer coils are not impressed entirely flat. Through trial and error, it was found that the electrical properties of the coil were better if the coil has a small loop at the edges rather than being crushed flat as shown in figure 2.7. However, such a loop could not be formed on the inner coils. This is partially due to lack of space but, more importantly, the advantage of this type of coil is that it allows for optical access along the x axis. This would be beneficial for additional vacuum pumps for instance but would be obscured by such a loop.

The simulated DC field produced by the decelerator coils is shown in figure 2.8. In this example, a coil of three periods has been simulated with the current magnitude of 1000 A. The face-to-face spacing of the coils is 7.9 mm. As can be seen from figure 2.8a), the field produced in the z direction is very deep, almost 1.4 T. From figures 2.8b) and 2.8c), it is clear that the transverse confinement is somewhat weaker. This is particularly problematic in the x direction and , as such, it is necessary to introduce further transverse confinement within the decelerator. This is achieved by including an independently driven quadrupole coil which runs along the entirety of the decelerator.

The decelerator field can be made to move along the molecular beam axis by applying the correct time dependent current to a coil phase. The way the trap moves is similar to the anti-Helmholtz coil arrays used to transport ultracold atoms to different regions of the experiment [183]. In this decelerator it is necessary to apply a sinusoidal current to each of the coil phases. It therefore follows that the phase difference between the sinusoidal currents is $\pi/4$. The velocity of the trap is dependent on the frequency, ω, of the applied current and the period length of the coil,

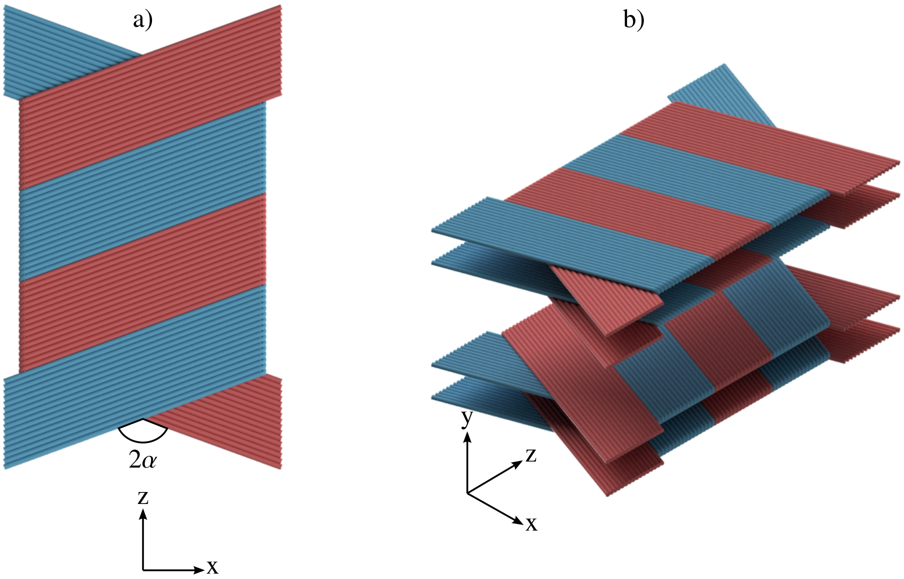

Figure 2.7: The schematic representation of the flattened helical coils. Panel a) shows a two period coil constructed from two sets of 16 wires (coloured red and blue). The half angle at which the wires cross, α is also shown. Panel b) shows the exploded view of the coil module used in this thesis. The module is formed by a total of four coils, two above the z axis and two below. The coils upper and lower coils are wound with opposite handedness in order to form the periodic anti-Helmholtz array.

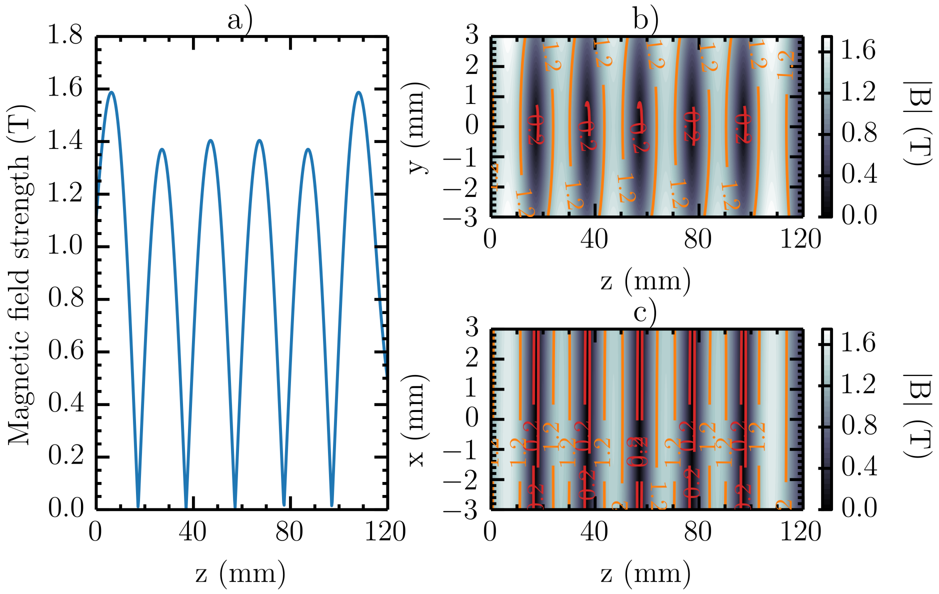

Figure 2.8: Simulations of the decelerator field generated by a three period coil operating at 1000 A. Panel a) shows the field along the z axis. The trap depths beyond the edges of the coil is roughly 1.4 T and the periodic nature of the potential is clearly visible. Panels b) and c) show the contour fields along the x and y axes respectively. These plots illustrate the weaker transverse confinement provided by the decelerator coils. This is particularly problematic in the x direction where the trap is fairly open.

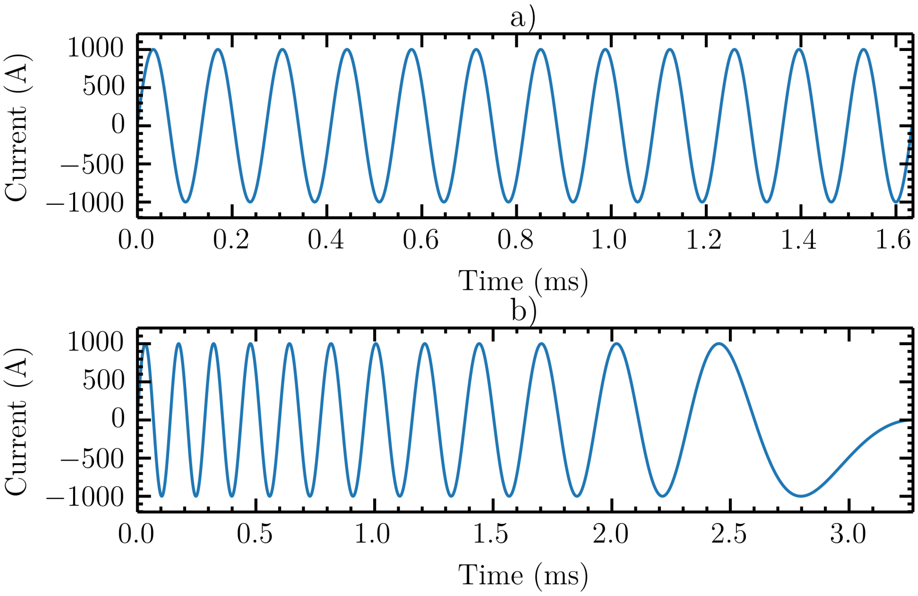

Figure 2.9: The two forms of current waveform required for the decelerator coils. In both examples, the initial frequency of the waveform corresponds to 300 $\mathrm{m\,s^{-1}}$, the relationship is given in equation 2.9. The waveforms will allow a trap to travel across 4 coil modules. Panel a) shows a sinusoidal current wave at a constant frequency, this is required for 3D guiding. Panel b) shows a chirped-down current waveform. In this particular example the trap velocity will linearly decrease to 0 $\mathrm{m\,s^{-1}}$

$$v_{\mathrm{z}} = \frac{32 d_{\mathrm{w}}}{\sin(\alpha)} \cdot \frac{\omega}{2\pi}. \tag{2.9}$$

This relationship shows that a constant frequency results in a constant trap velocity. By tuning the initial velocity of the trap to match that of the centre of mass velocity of the gas pulse, one is able to capture part of the gas packet. The width of this slice in velocity space depends on the trap depth. Once captured, the trap can be kept at this velocity to prevent the captured gas packet from spreading out due to its finite temperature. This will be referred to as 3D guiding or velocity bunching. Alternatively, chirping-down the frequency linearly results in the linear decrease in trap velocity and thus the deceleration of the captured gas packet. The trapping potential is modified while decelerating the gas packet since the gas packet is no longer in an inertial reference frame. An example of both waveforms is given in figure 2.9. The waveforms correspond to the current pulse required to a) guide and b) decelerate a trap with the initial velocity of 300 $\mathrm{m\,s^{-1}}$. The chirp waveform is linearly decreased in frequency to reach a DC value (0 $\mathrm{m\,s^{-1}}$).

The two pictures that can be used to describe the modifications of the field will be discussed. For simplicity this explanation will be limited to 1D. In the first picture, it is convenient to borrow nomenclature used in conventional Zeeman decelerators. In this case the synchronous particle is defined as the particle that initially possesses the same velocity and position as the trap minimum. Thus if the trap were to be kept at a constant velocity, the synchronous particle would always coincide with the trap minimum and will not sample the potential. A non-synchronous particle will experience the potential and will oscillate around the trap minimum, provided they remain trapped. If the trap velocity were to be reduced, the position of the synchronous particle moves further along the z axis since the instantaneous trap velocity is less than that of the synchronous particle. A non-synchronous particle will still oscillate around the synchronous particle, however, the effective trap depth of this leading edge is lower. The height of the barrier is dependent on the deceleration of the trap. A sketch of this can be seen in figure 2.10a). Alternatively, this affect can be described in terms of the non-inertial

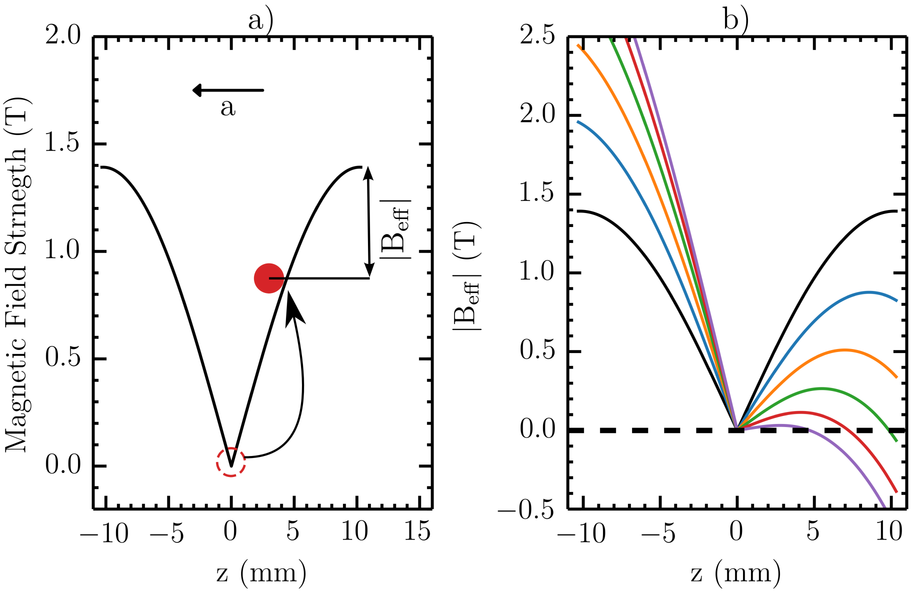

Figure 2.10: Two representations of the consequence of the deceleration on the potential experienced by a particle. Panel a) shows a representation of the synchronous particle of the trap. The trap as viewed in an inertial frame is shown in black. At a constant trap velocity the synchronous particle will coincide with the trap minimum (red dashed dot). The deceleration results in the synchronous particle rising up the trap edge resulting in a lower effective potential depth. Panel b) shows an alternative view expressed in terms of a pseudo force experienced by the particles. The example shows how the field in the inertial frame (black) generated at 1000 A travelling at 300 m s^{-1} is modified by the deceleration. Here metastable argon (in the $m_J = 2$) is considered. The curves show the effective field for a series of final trap velocities of 260 m s^{-1} (blue), 220 m s^{-1} (orange), 180 m s^{-1} (green), 140 m s^{-1} (red) and 100 m s^{-1} (purple). Again demonstrating the lowering of the front potential edge.

frame introducing a pseudo potential. The potential can be expressed in terms of magnetic field and has the form

$$B_{\text{pseudo}} = \frac{-am\hat{z}}{\mu'}. \tag{2.10}$$

In this form it possible to see the linear form of the modifying potential and that the magnitude scales with deceleration, a, and the mass to magnetic moment ratio, m/μ', of the species being decelerated. The modification of the field occurs in the direction that the trap is decelerated, in this case along the z axis. Additionally, this view demonstrates that the back edge of the trap is greater in depth. Figure 2.10b) shows the effect of the pseudo potential on metastable argon (in the $m_J = 2$) initially travelling at 300 m s^{-1}. The modified field is also shown for reference and was calculated at a current of 1000 A. In this example, the decelerator length was fixed to 4 modules long and the final velocity of the trap varied. In both pictures it is the effective barrier height that governs the phase space acceptance of the trap. Therefore an important consideration of a moving trap decelerator is the interplay between trap depth and the magnitude of the deceleration.

2.2.2 The Quadrupole Coil

As mentioned previously, the transverse field of the decelerator is fairly weak, particularly in the x direction. It is, therefore, necessary to supplement this lack of field to ensure the traps are closed in 3D. This is achievable with a quadrupole guide that runs along the entirety of the length of the

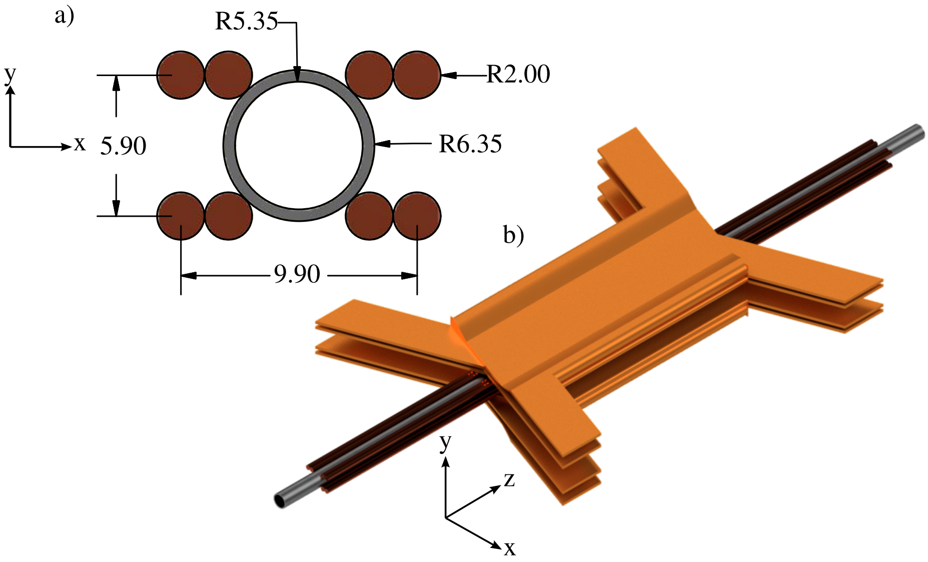

Figure 2.11: View a) shows an annotated drawing of the quadrupole view in the xy plane. This view shows the two windings of 2 mm diameter copper wire the quadrupole is constructed from and also includes the stainless tube. This geometry of quadrupole allows the decelerator coils to sit relatively close together. View b) shows a coil module and the quadrupole guide. The combination of fields forms a 3D magnetic trap. This view demonstrates the optical access (or potential access for side pumping) in the x direction allowed by this coil design.

decelerator. The quadrupole produces a linear field which ensures that the low-field-seeking atoms or molecules are focused back towards the centre of the decelerator in the transverse directions. Each pole consists of two 2 mm solid copper wires which were straightened after being cut to length. The form of the quadrupole can be seen is figure 2.11a). The quadrupole is centred around the stainless steel tube which links the source and detection chambers together. Figure 2.11b) shows the form of the decelerator coils in combination with the quadrupole. It is worth noting the optical access allowed by this coil design. The geometry of the quadrupole was selected to minimise the separation of the decelerator coils, thus maximising the decelerator field depth. The number of poles and wire diameter was chosen through the consideration of magnetic field gradient that the quadrupole produced and the voltage required to drive 700 A DC through a 1 m long quadrupole. The search was constrained by the supplies commercially available. For the selected supply, the maximum gradient achievable was produced by a quadrupole formed from two windings of 2 mm wire. Figure 2.12 shows the contour field plots and the axial fields for the quadrupole guide. The field gradient was found to be $46.7 \pm 0.1\ \mathrm{T\,m^{-1}}$ in the x direction and $43.3 \pm 0.3\ \mathrm{T\,m^{-1}}$ in the y direction at 700 A. Figure 2.13 shows the total field generated by the quadrupole and decelerator field combined. In this example the decelerator field was generated at 500 A to emphasise the need for the quadrupole field. Once again, the quadrupole field was calculated at 700 A. This plot shows that in the x direction, particularly at low current, it is the quadrupole that provides the majority of the transverse confinement.

2.2.3 A Comparison of the Travelling Wave and Moving Trap Zeeman Decelerators

It is worth comparing the design of the travelling wave decelerator presented here to the moving trap decelerator of Narevicius and co-workers. The beauty of the moving trap decelerator is the relative simplicity of the design of the coils and power electronics. Since the coils are ultimately solenoids, they can be produced efficiently with a commercial winder or simply purchased. The solenoids can

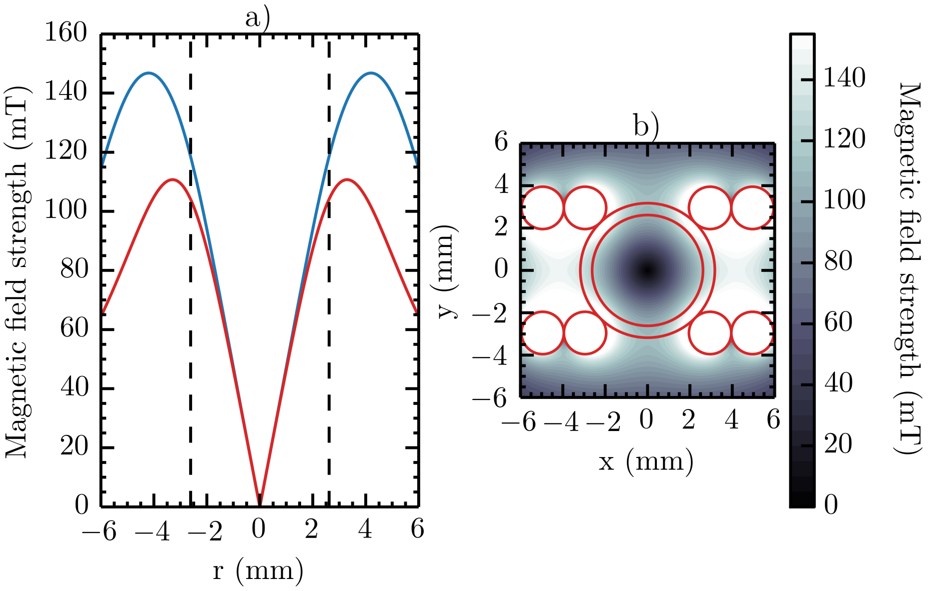

Figure 2.12: The calculated transverse magnetic fields at 700 A produced by the quadrupole. Panel a) shows the axial field components in the x (blue) and y (red) directions. The dashed lines represent the inner radius of the stainless steel tube. The field gradients are 46.7 ± 0.1 $\mathrm{T\,m^{-1}}$ and 43.3 ± 0.3 $\mathrm{T\,m^{-1}}$ in the x and y directions respectively. Panel b) A contour plot of the magnetic field. The location of the wires and the tube have been plotted for reference.

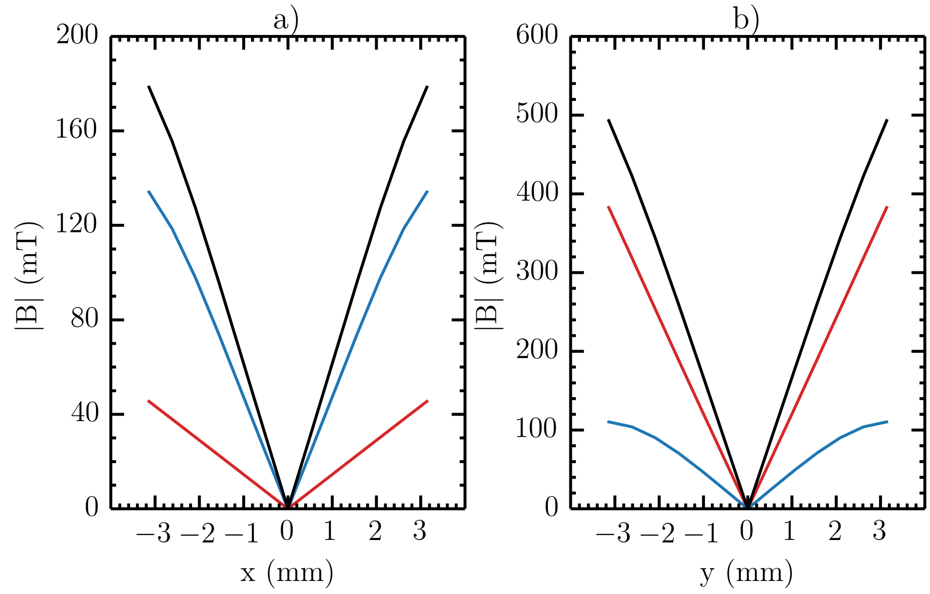

Figure 2.13: The calculated combined transverse fields of the quadrupole and decelerator coils. The quadrupole was operating at 700 A while the decelerator field was calculated at 500 A. Panel a) shows the field components in the x direction and panel b) of that in the y direction calculated at the longitudinal trap minimum. In both graphs the total field (black), decelerator field (red) and quadrupole field (blue) are plotted.

be independently driven which dramatically reduces the power requirements of the electronics. The helical coils described here are unquestionably more difficult to wind and do not allow any means to individually control each period separately. This means that the power electronics needed for the travelling wave decelerator must be able to deal with higher powers to compensate for the higher resistance of the helical coils. Additionally, this means that the power electronics must produce a longer current pulse where the decrease in peak amplitude across each period is negligible. This is not an issue for the moving trap decelerator. Finally, the solenoid coils are able to produce a deeper trap for a similar peak current to that employed in this thesis. This is impressive as the internal diameter of the tube used by the Narevicius group is almost double the size of that used in the travelling wave decelerator (10.2 mm compared to 5.35 mm) [168]. This results in a greater transverse acceptance over the travelling wave decelerator. Despite this, there are some advantages to the travelling wave decelerator. It has previously been shown that the travelling wave decelerator divided into four phases (rather than two phases demonstrated by Trimeche *et al.*) while operating with a pure sine wave results in much smoother motion of the trap and far less variation of the trap depth than that of the moving trap decelerator. Additionally, the ability to independently tune the transverse confinement in the travelling wave decelerator is an advantage. The means the decelerator presented here can be used for a variety of experiments from collisions in beams (where a small transverse velocity spread is required [153]) to trapping experiments. The optical access in the x direction could potentially be useful as the decelerator becomes longer. Ports would facilitate the pumping of the tube connecting the source and detection chambers to maintain a high-quality vacuum without removing the 3D confinement. Finally, the optical access would also allow for transverse cooling in the x direction.

2.3 Detection Schemes

The detection apparatus discussed are mounted in the detection chamber. Since the detection chamber is linked to the source chamber, differential pumping is therefore provided by the source vacuum system. Again, the complete design of the chamber and vacuum system has been previously detailed in reference [172]. This chamber has been designed to accommodate a selection of detection methods, however, only the micro-channel plate (MCP) will be discussed here. This detector is used to extract the time of flight (TOF) profile of the gas pulse.

Owing to the high internal energy of the $^3P_2$ state of metastable argon (11.54 eV [147]), it can be detected using a MCP detector without the need for additional excitation into an ionised state. The MCP consists of several million, closely packed, channels with typical diameters of 12 μm in a chevron configuration. The operation and the schematic view of a MCP can be seen in figure 2.14. If a particle with a large enough energy enters one of the channels, it will eventually strike the wall. This causes the release of an electron which is accelerated towards the rear of the MCP due to the high voltage (typically a couple kV) on the front plate. The electron will also strike the surface of the channel which liberates additional electrons, further amplifying the signal. This is known as a cascade effect. The MCP is located some 30 mm away from the end of the quadrupole guide. This relatively short difference is in part due to the compact design of the MCP (*Hamamatsu compact MCP assembly F12334-11*). In order to pass the MCP signal to an oscilloscope it is necessary to fit a unity gain buffer or voltage follower to impedance match the high output impedance of the MCP to the low input impedance of the scope. This circuit simply consists of a high-speed operational amplifier and additional information on the development of this device can be found in reference [172].

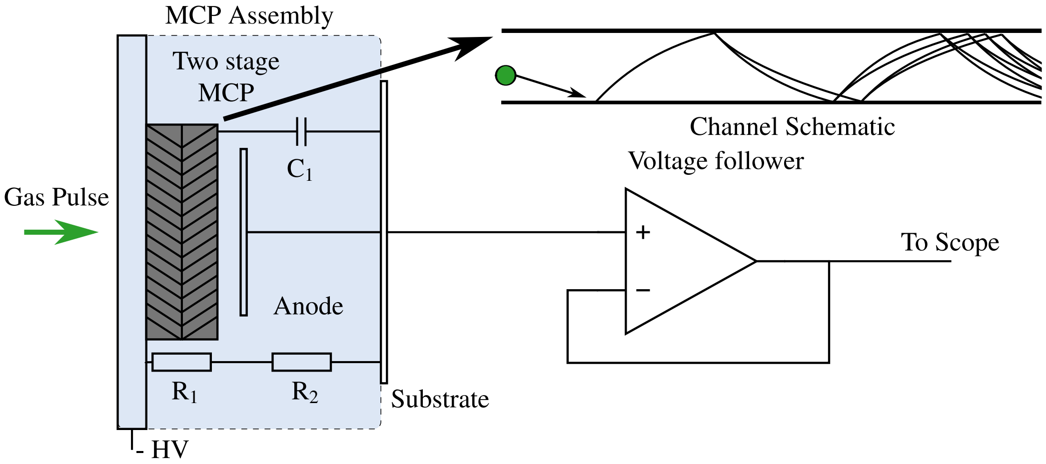

Figure 2.14: A simplified circuit schematic of the MCP and voltage follower. The MCP circuit shows the connections to the high voltage power supply and the chevron configuration of the channels of the MCP. The diagram also illustrates the basic concept of the cascade effect that amplifies the signal from a single particle.

2.4 The Design of the Four Stage Decelerator

At this stage all aspects of the decelerator have been explained, thus to conclude this chapter the design of the current four module decelerator will be presented. Figure 2.15 shows a simplified view of the experiment with the vacuum components removed. Panels a) and b) show two views of the entire decelerator consisting of the source, the decelerator modules and, in this instance, the MCP. Panel b) has been annotated to include relevant dimensions. The decelerator coils are shown in the mounts and cooling plate. The cooling plates are made from brass and are channelled to allow the flow of water. This active cooling is necessary while operating at high currents. Each module consists of two cooling plates located above and below the coils. The plates are held in place with aluminium blocks which also keep the decelerator coils and the quadrupole in place around the stainless steel tube. The design of the mounts are modular in nature and additional modules can be added by simply slotting the modules together.

The first decelerator coil sits 279 mm away from the valve nozzle whereas the quadrupole sits some 249 mm away. The quadrupole is 630 mm long to ensure that there is very little no field region along the decelerator. The end of the quadrupole is roughly 30 mm away from the MCP detector. The four modules of the decelerator are approximately 490 mm in length and sit 140 mm away from the MCP. Figure 2.15 also includes c) a drawing of the apparatus described above and d) a similar view of the decelerator stage. The latter image shows the construction process of the coil modules. The mounts are built from separate parts which form a solid structure once the cooling plates are attached. The mounts are designed with a slotted access point if additional vacuum pumping was required.

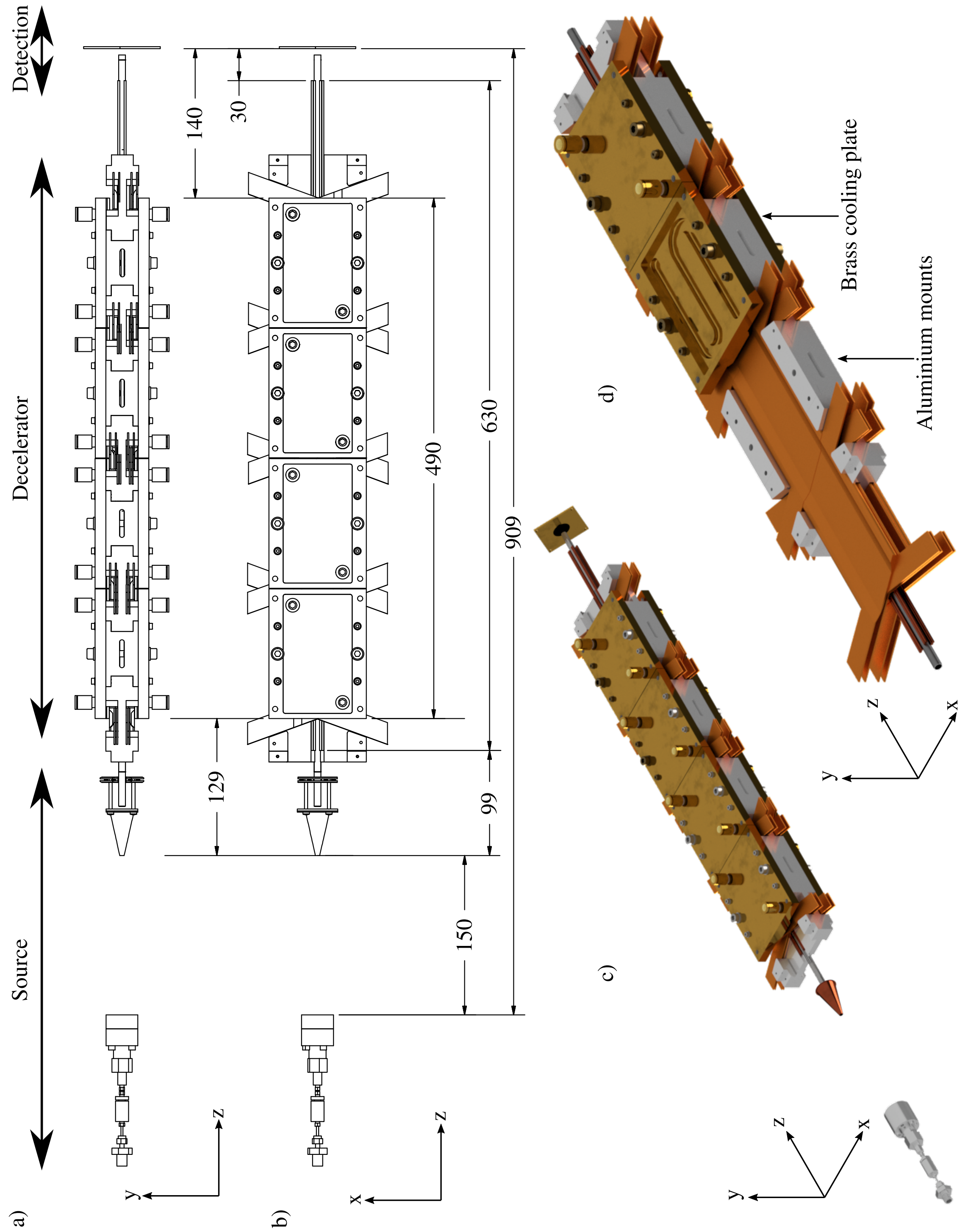

Figure 2.15: Drawings of the complete 4 module decelerator assembly. Panels a) and b) show sketches of the decelerator viewed in the yz and xy planes respectively. The diagrams are labelled showing the source, deceleration and detector regions of the experiment. Furthermore, the relevant dimensions have been annotated. Panel c) shows a render of the parts described in the main text. Finally panel d) shows a render of the decelerator stage. This diagram is intended to show the construction process of the coil modules. Both the quadrupole and helical coils are supported by aluminium blocks. The coils are cooled with water which flows through the brass plates above and below the coils. The modules are designed to be slotted together if the decelerator were to be extended further.

2.5 Chapter Summary

This chapter has provided an overview of the various parts of the decelerator. The source of the decelerator is built around supersonic expansion. A brief introduction of the theory behind supersonic expansion has been provided. When coupled with a pulsed valve, supersonic expansion of a gas is a convenient starting point since the gas packet is cold, and dense. The disadvantage is that the gas packet has a mean velocities typically in the region of a few hundred $\mathrm{m\,s^{-1}}$. The Even-Lavie valve offers a commercial solution to ensure short gas pulses, which are both highly collimated and dense. In addition to this, the built in excitation scheme (a dielectric barrier discharge) provides a method of producing both metastable atomic states and molecular radicals used within this thesis. Owing to the high densities of the gas packet from the Even-Lavie valve, it has been necessary to adapt the source chamber. To ensure the minimisation of skimmer interference it has been necessary to place the valve 150 mm away from the skimmer orifice. This ensures that the density of the gas pulse is sufficiently low such that the skimmer does not interact significantly with the gas. The design of the current source chamber was explained and the modifications from the previous design described. The motivation behind these changes was to accommodate the new source layout.

The operation of the decelerator has also been reported. The decelerator does not cool the gas packet in the strictest sense. Instead, it selects a fraction of the gas packet produced by the source and decreases the mean longitudinal velocity to zero while maintaining the high density of the accepted packet. The decelerator relies upon the combination of flattened helical coils and a quadrupole guide. The former is periodic and generates the deep, moving potential in the longitudinal direction. This requires the application of high magnitude sinusoidal currents (up to 1000 A peak) to each phase of the coil. Compared to the coils originally proposed by Trimeche *et al.* the coil design has been modified. More wire blocks create more effective current loops, allowing for a smoother translation of the trap. While the extra coils improves the field gradient produced by the coils.

The velocity that the trap moves at is determined by the frequency of the applied current. Therefore, if a linearly chirped down sine wave were applied, the trap can be decelerated. This deceleration tilts the trap, lowering the front edge of the potential which limits the effectiveness of the deceleration process. A compromise between efficient deceleration (i.e. the final particle number density) and the final mean velocity of the packet must be made. The quadrupole guide is required in order to supplement the weak transverse confinement of the decelerator coils, particularly in the x direction. The design of the quadrupole was selected to maximise the field gradient of the quadrupole without compromising the field produced by the decelerator coils.

The detection scheme used to measure the TOF profile of metastable argon was described. The micro-channel plate detector is a convenient method since the large internal energy of metastable argon means that additional excitation schemes are unnecessary. The longitudinal temperature and mean velocity of the gas pulse can then be extracted from the TOF profile.

Chapter 3

The Development of the Power Electronics

This chapter will describe the development of the control circuitry and the power electronics for the quadrupole and decelerator. Section 3.1 begins with a brief explanation of the low level electronics that produce the pulses that drive the power electronics. This mainly focuses on the development of the multiplexing and fibre-optic coupling used for control of the power electronics. Sections 3.2 and 3.3 explain the specification of the quadrupole and decelerator power electronics. In both cases the electronics had to be built specifically for the decelerator project and thus the development of the electronics will be described in detail. Additionally, these sections will conclude with an evaluation of the performance of the electronics. These sections will present the current waveforms generated and compare the fields measured to that obtained through theory. Section 3.3, also explains the software that was developed to generate the pulse sequences used to trigger the decelerator power electronics. Figure 3.1 should be used for reference to illustrate how the various elements of the circuitry are linked together. This figure shows the work-flow of the control system from left to right. The trigger pulses (one each for the decelerator and quadrupole) are supplied by the pulse generator (*BNC Model 575 Digital delay/ pulse generator*) which activate the quadrupole and decelerator protocols. The fibre-optics then relay the pulses from the control electronics to the driver cards which ultimately enable the power electronics.

3.1 Low Level Electronics

The section describes the development of the control system for the power electronics. Generally, it is most convenient to buy commercial control units when setting up an experiment, however, this largely was not possible in this experiment. The control system for the power electronics is based around a Field-Programmable Gate Array (FPGA) (*DE0-Nano-Altera cyclone IV EP4CE22F17C6*). This device can be configured by the user after the manufacture of the device and therefore offers versatility. FPGAs tend to also possess many input and output pins and enough memory to make them an attractive basis for an experiment control system. During the prototyping phase, it became clear that systems with supply voltages of 5 V or below close to the power electronics are highly susceptible to AC noise generated while the power electronics are operating. The effects on the low-level electronics include the devices locking up or sporadically triggering. These are qualities that are somewhat problematic for a control system. Typically, the control system for power electronics

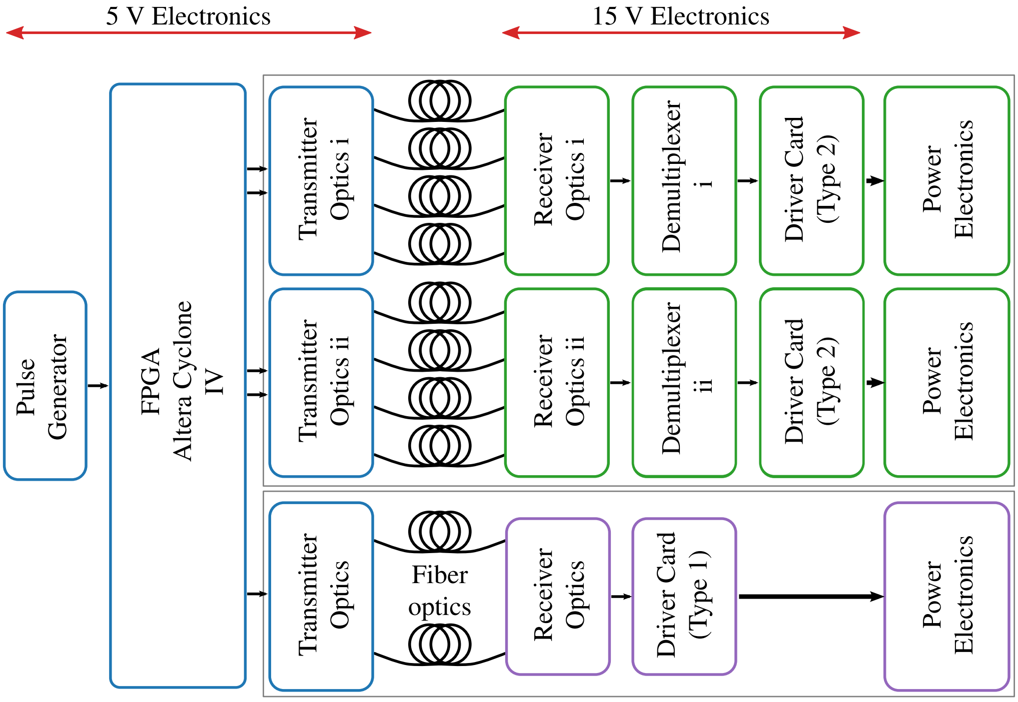

Figure 3.1: The work-flow diagram of the electronics. The pulse generator is used to trigger the quadrupole and decelerator protocols. In both cases the relevant time duration of each pulse is loaded from memory and sent to the appropriate transmitter optics. Fibre-optic cable are then is used to link the low voltage system the to high voltage control electronics. This consists of the receiver optics and the driver cards. The decelerator receiver board has an input for each coil phase, however, in order to minimise the number of components required, the receiver is multiplexed. This is possible provided the coils are grouped into even and odd numbers and given separate channels.

operate at 15 V to ensure immunity to the noise generated but, modern chips tend to operate on low voltages. The initial strategy was to shield as much of the control electronics as possible, however, this simply was not enough to protect them. It seems that the addition of long signal and supply leads coupled with the possibility of earth loops [184] provided other means to introduce noise into the system. It was decided to separate the control system from the power electronics using a fibre-optic coupler. This was a home built system such that the receiver optics would generate a 15 V signal. This section will be broken into the specification of the FGPA board and of the fibre-optic coupler. Next, the description of the multiplexing procedure of the electronics will be given. Finally, the control system will be analysed in terms of the signal pulses produced. This discussion intends to evaluate the precision of the control system and to demonstrate the negligible effects it has on the timing of the circuit.

3.1.1 Development and Operation of the Control System

Before describing the control system, it is first necessary to describe some of the issues that occurred during the prototyping of the decelerator. This ultimately formed the specifications that the control system would have to conform to. It became clear during the prototyping phase that the electrical noise generated during the switching of the high currents was going to be problematic unless preventative steps were taken. The suppression of electrical noise can be divided into two groups: containment of the electronics that generate the noise or shield sensitive equipment. Only some of the methods implemented in the experiment will be discussed here as the topic of noise suppression is vast. The ideas adopted in the experiment can be found in references [184, 185, 186, 187].

The first step in noise suppression is to shield as much of the electronics as possible. The power electronics are, however, unfortunately very bulky and thus difficult to effectively enclose them to contain the electrical noise they produce. The control electronics can be shielded in Electro-magnetic Interference (EMI) enclosures to attenuate the electromagnetic noise. Since the FPGA operates on a 5 V supply, it should be located as far from the power electronics as possible. This introduces the problem of long signal cables, which increases the susceptibility to electrical noise. Perhaps a less obvious problem this causes is the introduction of earth loops. Earth cables are susceptible to electrical noise pickup from AC sources such as power lines. As the earth cable has finite resistance, the current induced results in an induced voltage. The magnitude of this voltage is dependent on the properties of the conductor and its local environment. When two circuits are connected this can lead to multiple paths to reach ground and provide a means to introduce noise into the system [184]. This type of configuration forms a loop which acts as an antenna inducing a current in the cables altering the voltage between two connections. Earth loops can be eliminated, in principle, in the design phase. For instance by designing circuits with a single earth point (often referred to as a star configuration) rather than multiple earth points. Other techniques can be fitted after development, which include breaking the shields, fitting ferrite rings or the installation of fibre-optics [185]. To overcome the problems listed above, the FPGA was connected to the power electronics via a fibre-optic system. The combination of these preventative measures allows the FPGA to operate normally.

The VDHL code used by the FPGA to generate the sequence of timing pulses for the power electronics was developed by John Scott. The code loads a memory file for each channel, each containing the duration for the series of pulses which will be delivered to the power electronics. The transmitter of the optical coupler is connected directly to the output pins of the FPGA and therefore operates at 5 V. A fast switching transistor buffer is used to protect the FPGA from excessive current draw needed to power the LED. A schematic of the opto-coupler can be found in figure 3.2. The casing of the LED (*Avago Technologies SFH757V*) and the photodiode (*Avago Technologies SFH250V*) allows the fibre-optic cable (*Avago Technologies HFBR-RNS005Z*) to be fitted directly to the front of the emitter and receiver. The receiver electronics consists of a transimpedance amplifier and a fast

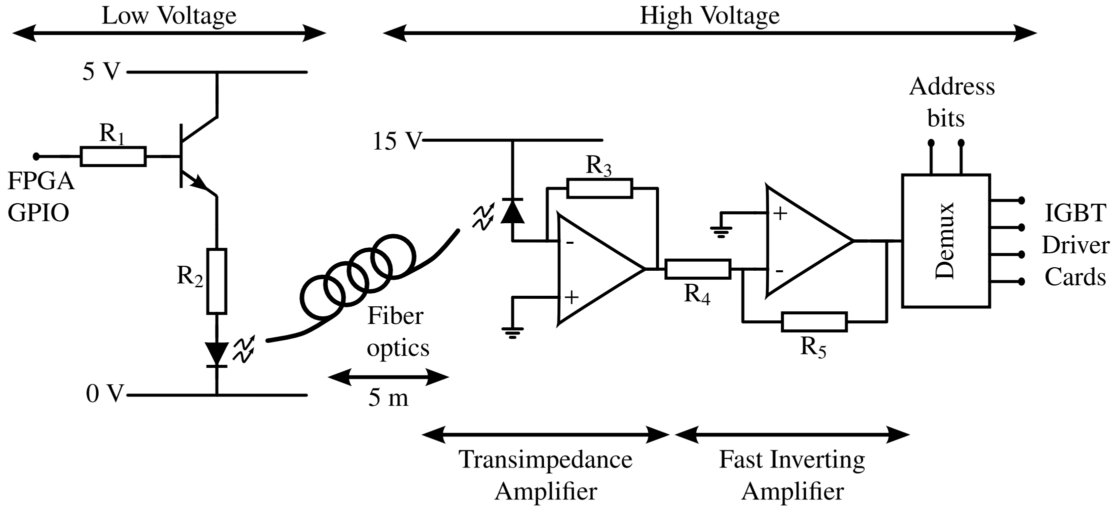

Figure 3.2: The circuit diagram for the opto-coupler. The FPGA output is protected from the LED with a fast transistor switch. The LED is linked to the photodiode through a 5 m long fibre-optic cable. The receiver board is fitted with a transimpedance amplifier and a fast inverting amplifier in order to amplify the sequence of pulses to 15 V. The decelerator receiver card is fitted with a two-bit demultiplexer to direct the pulse sequence to the correct coil phase.

inverting amplifier. The former converts the current produced by the photodiode into a voltage. The latter amplifies this low voltage to the 15 V required to trigger the driver cards. It should also be noted that each phase of each coil module requires a separate input channel as well as the channels for the quadrupole power electronics. In order to reduce the number of these circuits, the receiver card that controls the decelerator power electronics is multiplexed. The demultiplexer directs the output of the fast inverting amplifier to one of the driver cards depending on the address. The demultiplexer is a two bit device, hence, each channel can drive four coils. Since adjacent coils must be active simultaneously, the coils are divided into two groups. Where channel i from the FPGA drives the odd numbered coils and channel ii the even. Each coil in the group has an address associated with it which is sent to the demultiplexer via a separate optical circuit. A typical timing sequence is shown in figure 3.3. The figure shows the location of each coil and the coil's address. The boundary between each coil is shown to highlight the overlap of the current waveforms between adjacent coils so that the trap moves uniformly.

The optical coupler was developed to minimise the response time of the circuitry. It was important to ensure that the discrepancy between the duration of the pulses calculated and measured were minimised. This can be achieved through careful choice of components and the values of resistors shown in figure 3.2. Initially, it was found that the average deviation between the pulses measured at the output of the driver cards and the calculated pulses was 255 ns. This seemed likely due to a combination of board and component capacitance. The error was consistent across all pulses; a correction term could then be included in the software used to produce the pulse sequence. The average variation of the pulses after this correction was 30 ns, which is equivalent to a couple of clock pulses of the FPGA.

3.2 The Quadrupole Power Electronics

As stated before, the quadrupole is required to supplement the lack of transverse confinement. This is achieved by placing current carrying wires along the length of the stainless steel tube. The connec-

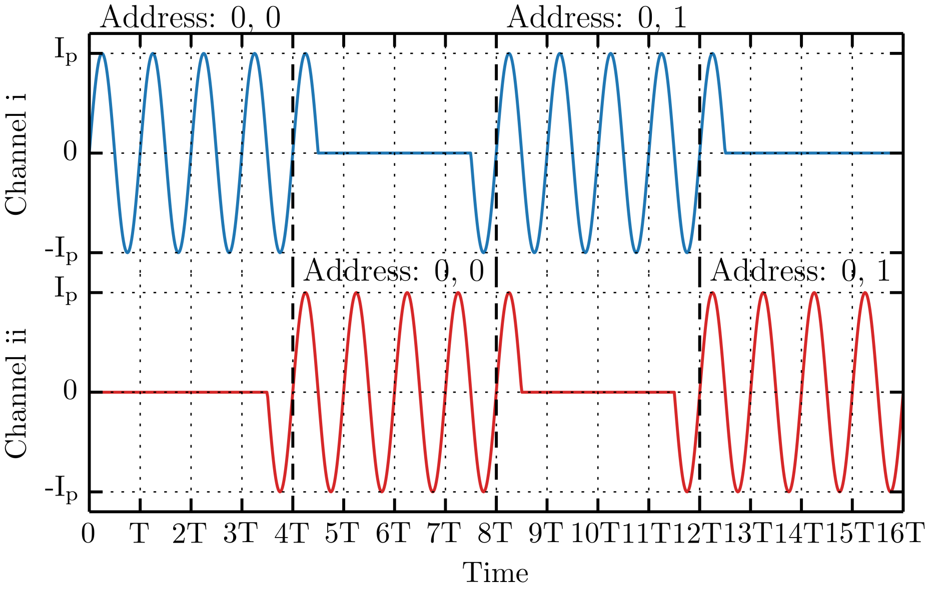

Figure 3.3: A pictorial view of the coil module multiplexing showing an example of a guiding waveform split across four coils. The boundary of each coil module is shown as a dashed line. In order for the field to vary smoothly across the boundary it is necessary for each coil to overlap by one time period. Furthermore, this diagram shows the multiplexing of the decelerator fibre-optics. The coils are divided into groups depending on its position in the decelerator. Each coil in the channel is given an address which is used by the demultiplexer.

tions between the poles are similar to an Ioffe Pritchard baseball trap (i.e. the poles are connected in series). This section explains the operation of the power electronics needed to drive the 700 A current through the quadrupole. These high currents are necessary to generate field gradients up to 46.7 ± 0.1 $\mathrm{T\,m^{-1}}$ in the x direction and 43.3 ± 0.3 $\mathrm{T\,m^{-1}}$ in the y direction. An ideal quadrupole, in the context of this experiment, should not produce a force in the z direction. This, however, is not the case close to the ends of the quadrupole. The poles of the quadrupole are connected using 3 mm copper bar which ensures that the connections between the poles are made normal to the bars. This kept the load inductance low. Moreover, it makes modelling the fields at the edges of the quadrupole easier to quantify. Figure 3.4 shows a simplified model of the fringe fields generated by the quadrupole at 700 A. The fields were produced using the Radia plug-in for Mathematica. The upper panel shows the field along the z axis, while the lower panel shows a colourmap of the fields in the yz plane. The large field at the end of the quadrupole is caused by the supply leads. These fields are often difficult to model and to account for, however, this simplified model of the quadrupole suggests that these fields are certainly not negligible. Additionally, the effect of the fringe fields on the motion of the molecules in the transverse and longitudinal directions were investigated with a prototype decelerator. This demonstrated the severity of these fields as it was found that the quadrupole fringe fields could alter the arrival time of the gas packet up to 40 µs.

To avoid the regions with fringe fields it is beneficial to apply the quadrupole field while the gas packet is well within the quadrupole. However, it is necessary to maximise the interaction time of the atoms or molecules with the field. Ideally, once the gas packet moves either sufficiently far enough away from the entrance or becomes close to the exit of the quadrupole, the current would be instantaneously switched on or off. The atoms or molecules will avoid the fringe fields while the transverse confinement is maximised. Instantaneous switching cannot, however, be achieved in a realistic circuit. This is because producing a square pulse of current of 700 A is limited by the finite inductance and resistance of the coil. This results in an associated rise and fall time of the current, thus producing a near-square current pulse. Another issue is that the overall period of time that the quadrupole needs to be active for is the order of a few milliseconds. Generally, capacitors can be

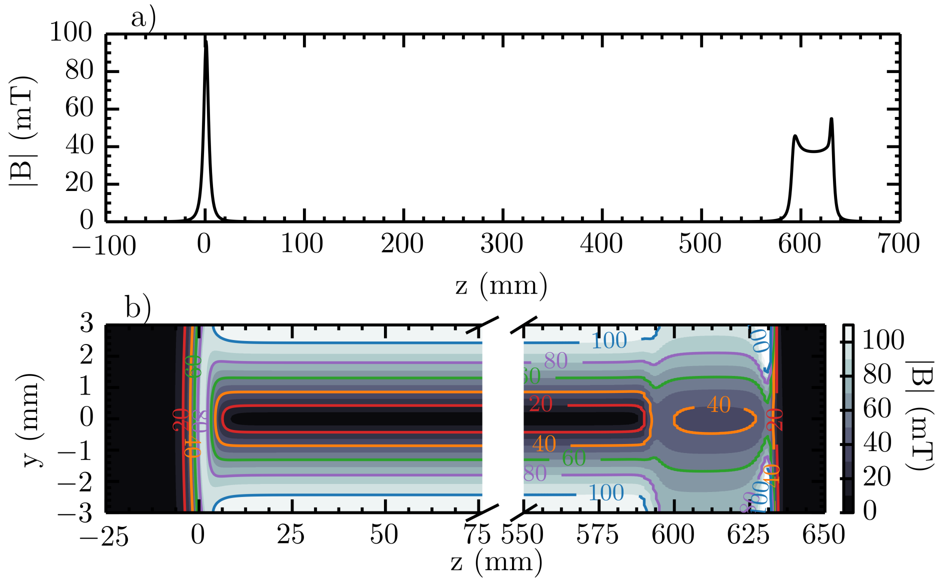

Figure 3.4: A simplified model of the quadrupole fringe fields. The upper panel shows the magnetic field produced along the z axis. The lower panels show a zoomed in view of the fields at the beginning and the end of the quadrupole in the yz plane. The large spatial extent of the end field is due to the location of the supply leads to the quadrupole.

employed to supply high magnitude pulses of current in applications such as this. The pulse duration makes this method infeasible due to the sheer size of the capacitor bank required. Another possible source of high current are DC supplies. Supplies can produce a current pulse of an arbitrary duration, however, the most significant problem is the intrinsically long rise and fall times of the current. To overcome this problem, an additional circuit is needed to improve the rising and falling edges of the current pulse. This section will report the development of the quadrupole power electronics. The operation of the electronics will then be evaluated and, finally the field generated compared to theory.

3.2.1 Development and Operation of the Quadrupole Power Electronics

The core component of the quadrupole power electronics is the high current DC supply. Two power supplies (*Ametek Sorensen SGA40-375D 15kW*), each capable of delivering 375 A at 40 V, are connected in parallel. This arrangement can provide a hold current up to 750 A. With the 63 cm long quadrupole described in chapter 2 connected, the rise and fall times of the supply can be investigated. The rise time (defined here as the time to reach 90 % of the maximum current from 0 A) was found to be 209 µs. The fall time (defined as the time to fall from 100 % to 10 % of the supply current) was 362 µs. These times do not meet the specification described above. A convenient method of producing large current quickly is simply discharging capacitors initially charged to a high voltage. The rate of which current is drawn is dependent on the properties of the load and capacitor. Not only can capacitors be used to drive current quickly through the coil, they can be used to drive the decay of current once the supply voltage is removed. The rate of the free inductive decay of the current through a coil is dependent on the inductance and resistance of the coil. A large voltage can be applied across the coil to drive the decay of current, resulting is faster decay rates. By combining the desired characteristics of a capacitor circuit with the power supply a near-square current pulse can be produced. This circuit was inspired by that used by Wiederkehr *et al.* [159] which produces short, low magnitude current pulses to the coils of a conventional Zeeman decelerator.

LTspice was used to simulate the current pulse from a capacitor discharging through a quadrupole.

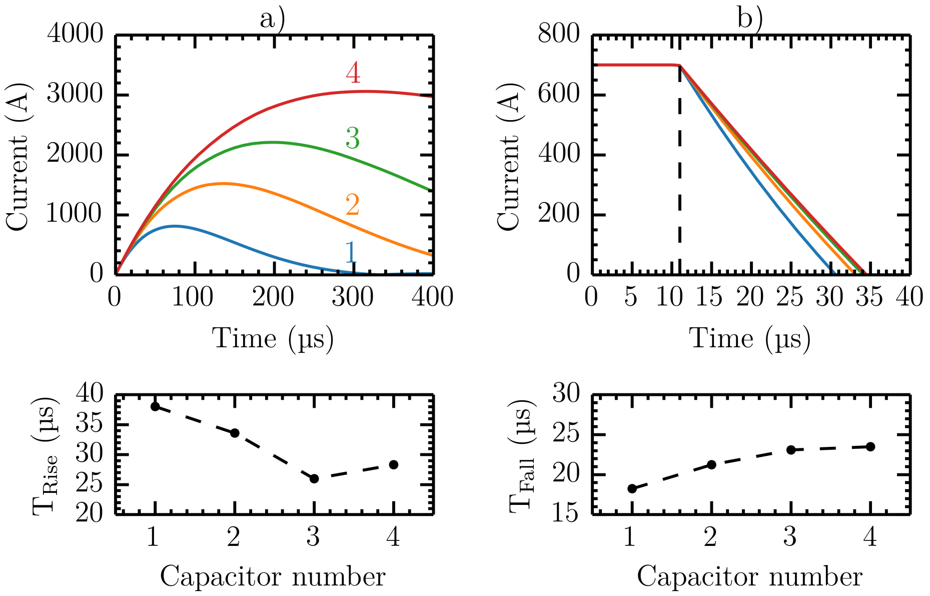

Figure 3.5: The simulated rise and fall times through the quadrupole with different capacitors. Capacitor 1 (blue) C = 1.5 mF, ESR = 52 mΩ. Capacitor 2 (orange) C = 4.7 mF, ESR = 18 mΩ. Capacitor 3 (green) C = 10 mF, ESR = 7 mΩ. Capacitor 4 (red) C = 33 mF, ESR = 3.3 mΩ. Panel a) shows the current through the quadrupole as a function of time in the rise phase while panel b) shows the same but during the decay phase. Plots c) and d) show the rise and fall time of the current through the quadrupole respectively. The rise time is defined as the time required to reach 90 % of the maximum current from 0 A. The fall time is defined as the time to fall from 100 % to 10 % of the supply current.

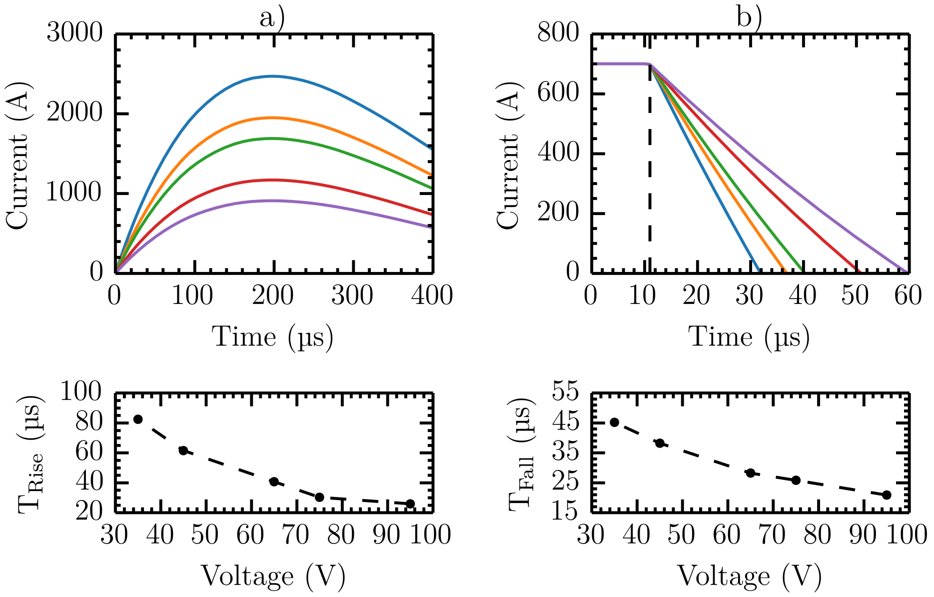

Figure 3.6: The simulated rise and fall times through the quadrupole with the 10 mF (capacitor 3 from figure 3.5). The voltages applied were 95 V (blue), 75 V (orange), 65 V (green), 45 V (red), and 35 V (purple). Panel a) shows the current through the quadrupole as a function of time for each voltage in the rise phase while panel b) shows the same but during the decay phase. Plots c) and d) show the rise and fall time of the current through the quadrupole respectively. Again, the rise time is defined as the time required to reach 90 % of the maximum current from 0 A. The fall time is defined as the time to fall from 100 % to 10 % of the supply current.

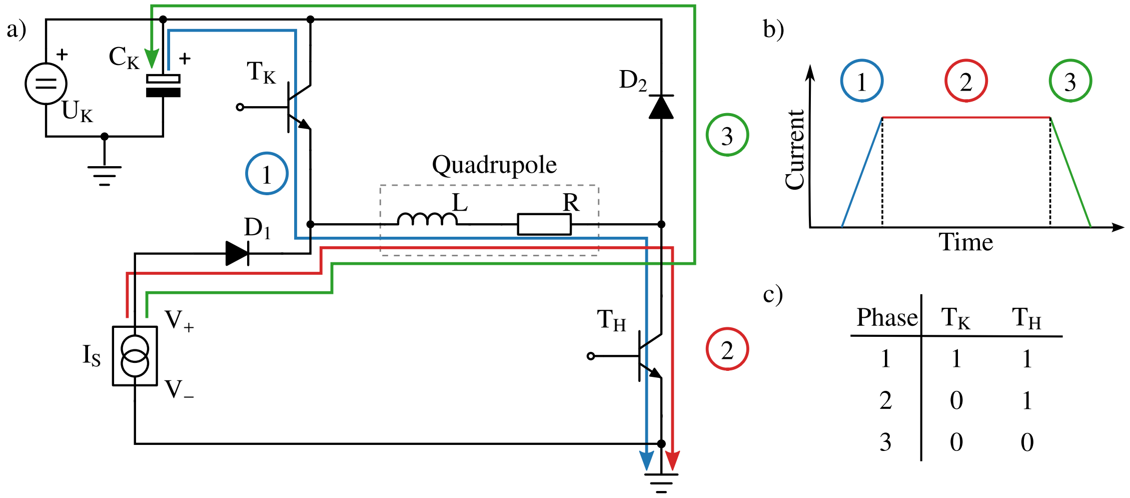

Phase	T_K	T_H
1	1	1
2	0	1
3	0	0

Figure 3.7: The operation of the quadrupole power electronics. A drawing of schematic of the quadrupole electronics in shown in panel a). Where the quadrupole itself is broken into the inductive and resistive components of the coil. The current flow through the quadrupole is broken into three phases. The flow of the of the current pulse in each phase has been sketched on the circuit. Furthermore, the temporal flow of current through the quadrupole and the phase it corresponds to is shown in panel b). The kick supply, U_K, is used to charge the kick capacitor C_K. The IGBTs, T_K and T_H, are used to select which phase the circuit is in. A summary of the logic states the IGBTs are in is shown in the table in panel c). Here, 1 means active thus acting as a closed switch and 0 means the switch is in an open position. The hold supply is labelled I_S. The three phases are the kick (blue), hold (red), and decay (green).

It should be noted that this was used as a toy model as spice modelling is ideal for low level applications but with power electronics, board properties and layout have a non-negligible effect. These simulations were useful to examine the effects on the rise and fall of the current due to the properties, such as the Equivalent Series Resistance (ESR), of different capacitors. The rate that current is drawn is proportional to the capacitance and the ESR of the capacitor. Higher capacitance or high voltage tolerance is necessary to store greater amounts of energy in order to reach higher peak currents and longer durations of the current. An optimum rise and fall time is achieved with a capacitor with low ESR and a fairly large capacitance while being able to tolerate high voltages. Unfortunately, there is a limited number of capacitors which fulfill these criteria. Figure 3.5 shows the simulated current flow through the quadrupole for a few example capacitors. The quadrupole used during this design phase was found to have an inductance of 3.14 µH and a resistance of 16.6 mΩ. The upper plots show the current through the quadrupole either as it rises, assuming the capacitor is charged to 80 V (left), or falls from 700 A (right) for different available capacitors. The rise and fall times for each capacitor has been plotted in the lower panels. The best compromise between the peak current achieved and the rates of the rise and fall in current is given by the 10 mF (*EPCOS B41580A9109M000*) capacitor. The effect of the initial voltage can then be studied for this capacitor, this is shown in figure 3.6. Again, the lower panels of this plot show the rise and fall times of the current. Faster rise and fall times are achievable with larger voltages across the capacitor. The applied voltage across the capacitor should, however, be limited to 90 V. This allows adequate tolerance in case of large induced voltage spikes.

Figure 3.7 shows the schematic for the quadrupole power electronics. The schematic also shows the current flow coloured to indicate which of the three phases is in effect. In order to transition between the three phases of the current pulse, a pair of Insulated Gate Bipolar Transistors (IGBTs) were employed (*Semikron SKM600GB066*). The state of the IGBTs is summarised in the table included in figure 3.7. Unseen in the figure is the low level electronics consisting of the driver cards

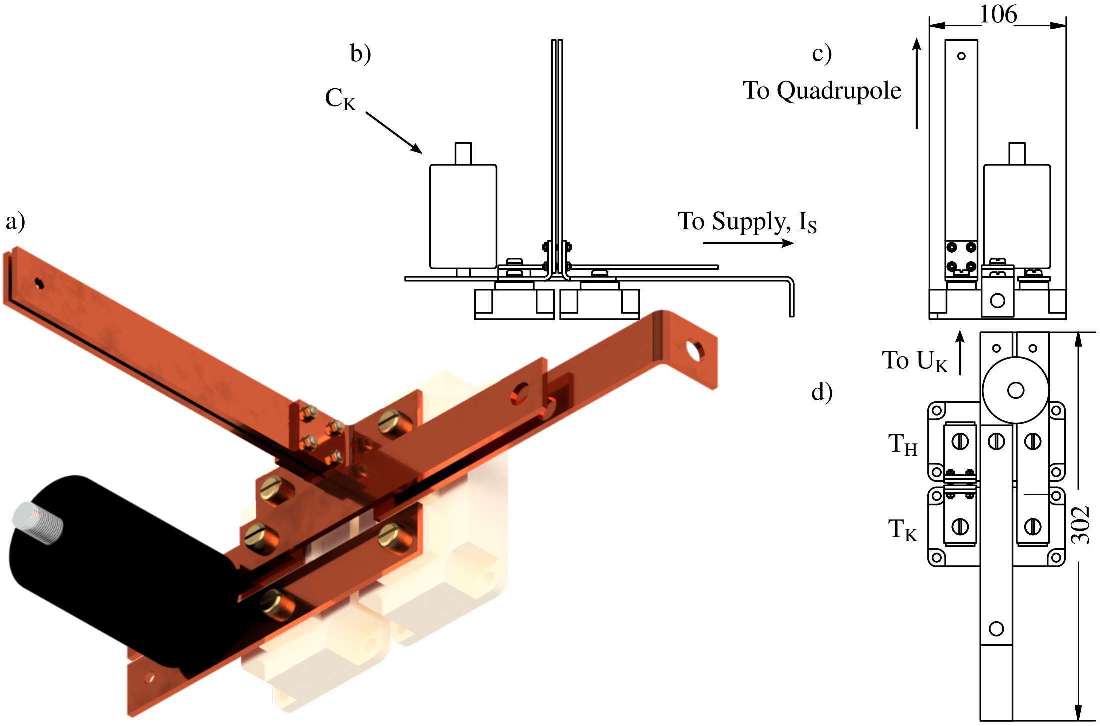

Figure 3.8: Drawings of the quadrupole power electronics. View a) shows a rendered image of the layout of the circuit. The connections between the terminals are made using 3×25 mm copper busbar, the orientation of which is chosen to keep the inductance of the system low. Views b) to d) show the orthographic views of the circuitry labelled to show the placement of the components in figure 3.7. These diagrams also include where the connections are made to the kick capacitor supply, U_K, the current supply, I_S, and to the quadrupole. The quadrupole connection busbar point normal to the plane of the electronics because the electronics are suspended above the quadrupole in order to save space. Some dimensions of the electronics have also been annotated. These power electronics are mounted on a heat sink which is actively cooled with a fan.

(*Semikron SKHI 10/12 (R)*) and the previously described fibre-optic coupler and FPGA. The first part of the current pulse is the kick phase. Since both IGBTs, T_K and T_H, are in an 'on' (or closed) state, current is drawn from the kick capacitor. The kick capacitor is charged by the supply U_K (*TDK Lambda 202A-3kV-POS-PFC*). The current passes through T_K, followed by the quadrupole and finally through T_H to earth. The diode D_1 prevents current flowing to the lower voltage power supply. As shown in figure 3.6, the current extracted from the kick capacitor may exceed the nominal rated current of the IGBT switch. The circuit has been designed such that the current can be limited by rapidly switching the transistor T_K to maintain an average current which can be set using the FPGA control programme. This also limits the discharge of the capacitor, allowing for a quicker fall time of the current. The second stage of the current pulse is the hold. In this phase only T_H is open allowing current to flow from the power supply. As described previously, the power supply will allow current to flow indefinitely. Finally, phase three is the removal of energy stored in the quadrupole once T_H is in the off (or opened) state. The quadrupole will try to maintain the field produced by the current following Faraday's law. The rate of decay of current is dependent on the resistance and inductance of the coil. In order to enhance the rate of inductive decay, the load is biased by the kick capacitor which drives the decay. The current flows through diode D_2 back into the capacitor, partially charging it for the next cycle. The circuit is constructed from copper busbar (25×3 mm cross section) which forms the electrical connections between components. The busbar layout is such that the positive and negative supply rails run in parallel which helps keep the mutual inductance between the bars low [188]. Furthermore, busbar which is thin yet wide tends to have lower inductance than square cross-section busbar [189]. The circuit is intended to hang above the quadrupole so that the two busbar that supply the quadrupole are short and normal to the plane of the rest of the electronics. A drawing of the electronics can be seen in figure 3.8. The diagram is labelled to include the parts of the circuit shown in figure 3.7. The IGBT modules are mounted on a heat sink which is actively cooled with a fan. These components are not shown on the diagram. The active cooling of the electronics will allow the quadrupole electronics to be operated at high repetition rates.

The two limits of operation of the kick circuitry will now be evaluated. In the example below, the quadrupole was 0.63 m long requiring the kick to maintain a current of 700 A for 650 μs. The kick circuitry is limited to an initial voltage of 90 V, although in the examples below the initial charge was set to 60 V. This allows adequate tolerance in case of large induced voltage spikes. Figure 3.9 compares the current waveform through the coil with and without the kick circuitry measured using an open-Hall effect current probe (*Pico technology TA167 AC/DC current probe*). Figure 3.9a) shows the how the current drawn from the power supply is modified with a single pulse from the kick capacitor. The peak current drawn here is 963 A with the kick capacitor charged to a mere 60 V. This reduces the rise time to 58.4 μs. Figure 3.9b) shows the other extreme of the kick circuitry, when the capacitor is not allowed to discharge from the initial 60 V. The driven decay reduces the fall time to 178 μs. This mode of operation has been used during the acquisition of the experimental results present in chapter 5 because the rear fringe field is more detrimental to the metastable argon signal detected on the MCP. Since the FPGA is used to supply the trigger voltages to the IGBTs, it is possible to operate the kick in a switched mode. In this third mode of operation, once the kick current reached the target hold current, the rise in current can be interrupted, by opening transistor T_K. This IGBT would then be pulsed such that the average current through the quadrupole is equal to the target hold current. The duration of these pulses can be determined through knowledge of the resistance and inductance of the quadrupole and can be calculated in advance much like the pulse width modulation technique described in section 3.3.1. This would produce a fairly square pulse, while ensuring that the kick capacitor is not fully discharged in the process. To date, this technique has not been implemented in the experiment. Since the rear fringe field has such a large effect on the metastable gas packet, the kick circuitry has only been used to increase the decay of current through the quadrupole to minimise the interaction with this region of fringe field.

Another consideration is the heat load of the quadrupole. During an experimental run, the quadrupole itself must be actively cooled with fans. This ensures that the resistance of the poles does not dra-

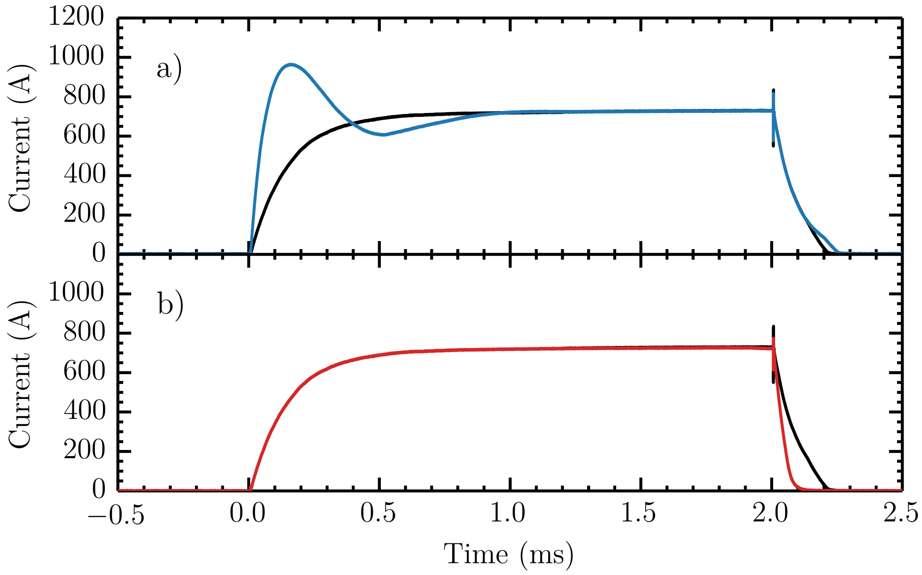

Figure 3.9: Comparison of the current measured through the 0.63 m long quadrupole under different kick conditions. In each case, the power supply delivered a 700 A holding current. Panel a) shows the current measured through the quadrupole after a single pulse from the kick capacitor initially charged to 60 V. This reduces the rise time by approximately a factor of four. Panel b) shows the resultant current waveform is the kick capacitor is not discharged from the initial 60 V. This reduces the fall time by a factor of two. In both cases, the current measured through the quadrupole delivered by the hold power supply have been plotted for reference (black).

matically increase over the course of an experiment. This is particularly important while operating at high repetition rates. Figure 3.10 shows the temperature increase of the quadrupole measured using a thermocouple. The figure shows the increase in temperature with and without cooling. In this example, the quadrupole, of length 0.63 m, was pulsed on for 2.3 ms at a repetition rate of 5 Hz. The quadrupole was active for a total time of 230 ms. Without the fan the quadrupole heats to a maximum temperature of 20.7 °C above room temperature. Even with the presence of the fan, the quadrupole heats up to 11.5 °C above room temperature, moreover, the quadrupole takes 5 minutes to return to room temperature. This raises the question whether is it possible to increase the trapping gradient while minimising the power consumption of the experiment and reducing the heat load of the quadrupole? With these considerations, it may be desirable to exchange the wire quadrupole for one constructed using permanent magnets. This maybe particularly useful near the region of the experiment where sympathetic cooling takes place.

The final aspect of the quadrupole to investigate is the field that is generated. This is useful in order to confirm the theoretical field used to model the decelerator. The Hall probe used to make the field measurements was based around a commercially available chip (*Honeywell SS39ET*). The compact nature of the chip allows the axial field to be measured between the poles of the quadrupole. The probe was calibrated by measuring the axial field of a ring magnet of known residual magnetisation. The measured points could then be compared to the theoretical field of the magnet generated using the Radia plug-in for Mathematica. The theoretical field was verified with a commercial Hall probe (*GM04 Hall probe Hirst Magnetic instruments Ltd.*). The measured and theoretical quadrupole fields are plotted in figure 3.11. The fields were measured in the central region of a test quadrupole (of length 30 cm) with 700 A flowing through the coil. Overall the theory agrees well with the measured data. The discrepancies are likely due to the undulations in the wires introduced by the original winding process.

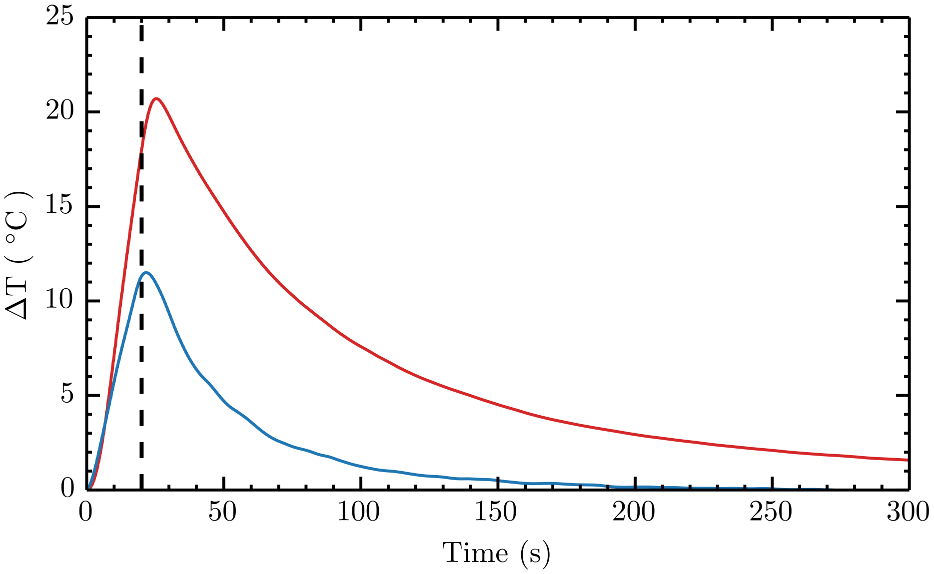

Figure 3.10: The heating of the wire quadrupole while being pulsed at 5 Hz. During the experiment the total time that the quadrupole spent conducting was 230 ms. The end of the experimental run has been plotted for reference (black dashed). The temperature plotted is relative to room temperature. Without a fan (red) the quadrupole heats to a maximum of 20.7 °C. With the fan (blue) the quadrupole heats to a maximum of 11.5 °C. The quadrupole length was 0.63 m.

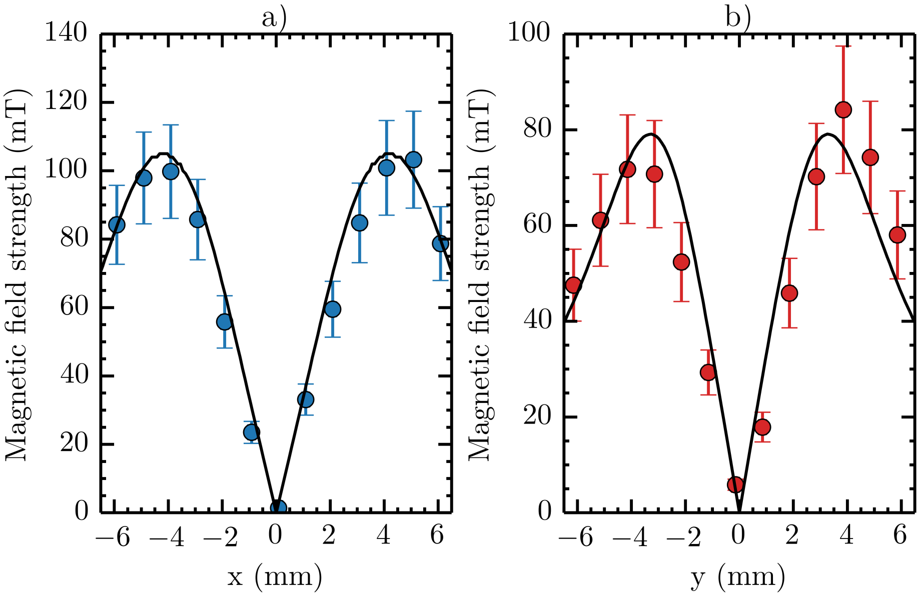

Figure 3.11: A comparison of the theoretical (black line) and measured (coloured points) fields of the quadrupole along the x and y axes. The fields were measured in the central region of a 300 mm long quadrupole operating at 700 A.

3.3 Decelerator Power Electronics

The power electronics required for the decelerator are more complex than those of the quadrupole. Firstly, the electronics needs to deliver a sinusoidal waveform up to 1000 A peak from roughly 10 kHz to DC. Secondly, the decelerator coils pose a much larger load for the electronics because the power electronics must power four coil phases. Additionally, each phase must be controlled independently since each requires a sinusoidal current offset by $\pi/4$ radians. Commercial units that meet these specifications do not exist, therefore it was necessary to design and build the power electronics for this particular task. The difficulty of this task arises from generating a pure sine wave. To achieve this, the impedance of the switching devices would have to be varied over time, however, any device with a finite resistance will undergo Joule heating. With the currents required in this application the heating will be significant and, after prolonged use, will damage or destroy the device. Therefore, it is beneficial to choose a switching device that has two states. The first state has zero resistance (an ‘on’ state) while the second has infinite resistance (an ‘off’ state) in order to minimise power dissipation. Although this method minimises the heating effects of the devices it introduces additional problems. All electronic components have some inductance, additionally electrical connections also introduce some small inductance. The values are often hard to quantify in the design phase and are usually denoted as the stray inductance of the device. The problem occurs when current passes though the circuit and energy is stored due to this stray inductance. When the current supply is removed a voltage is generated across the device to maintain the current as described by Faraday’s law. Faraday’s law states that the voltage, V generated to oppose the change in current, I, is

$$V = -L\frac{\mathrm{d}I}{\mathrm{d}t}. \tag{3.1}$$

Even though the inductance, L, may be in the order of picoHenries, the voltage generated may be several hundred volts. This combined with the supply voltage has the potential to exceed the nominal voltage that the switching device is rated to. Repeated use under these conditions will eventually destroy the device. The circuit layout is important in order to minimise the stray inductance. This may include placing the supply rails in parallel to reduce the mutual inductance [188], and careful consideration of the orientation of additional connections [190, 191]. It is also possible to include additional passive or active circuits, known as snubber networks, to suppress these voltage spikes [192, 193]. The best practice, however, is to optimise the circuit design to keep the stray inductance low. To aid with this, Barry Moss, a highly experienced power electronics engineering consultant, was recruited to layout the circuit. This section explains the development of the driver electronics for the decelerator coils. This section is broken down in to the development of the power electronics followed by an evaluation of the electronics. The former will describe the method used to produce a AC waveform from a DC source and present the design of the power electronics. The latter will investigate the effects that the design of the power electronics have upon the operation of the coils and the fields they produce.

3.3.1 Development and Operation of the Decelerator Power Electronics

In order to fully describe the operation of the decelerator electronics, it is convenient to consider a simplified circuit then build up to the full circuit. Firstly, the concept of synthesising a sinusoidal waveform from a DC voltage applied to a coil will be discussed. After, it is possible to describe the requirements for the switching circuit that will apply the voltage to the coil. Finally, the circuit elements required to provide the high peak current can be reported.

Synthesising a Sinusoidal Current

To reduce the number of components (thus maximising the voltage drop across the coil) it was decided that the sine wave should be generated by making use of the way a coil draws current. Coils are generally modelled as a perfect resistor, with resistance R, in series with a perfect inductor, with inductance L. When a DC voltage, $V_{\rm o}$, is applied to such a circuit current exponentially rises to the Ohm's law value. The time dependence of the current, follows from Faraday's law and is therefore

$$I\left(t\right) = \frac{V_{\rm o}}{R}\left[1 - \exp\left(-\frac{t}{\tau}\right)\right]. \tag{3.2}$$

When the voltage is removed, the current exponentially decays to zero. The free inductive decay has the form

$$I\left(t\right) = \frac{V_{\rm o}}{R}\exp\left(-\frac{t}{\tau}\right). \tag{3.3}$$

In both equations the time constant is defined by the ratio of the inductance and resistance, $\tau = L/R$. This defines the time scale that current can rise and fall through the coil. Therefore, if the properties of the coil are known it is possible to use these analytic expressions to predict the current through the coil. This finite response time has the potential to be problematic. Lets take the example of a coil which has a time constant of 100 µs. Additionally lets further assume that the magnitude of the reference waveform is equal to the maximum current that a coil can draw (i.e. the value set by Ohms law for given voltage). The coil will reach the peak current in approximately 5τ or 500 µs whereas the sine wave reaches the peak current at time equals T/4 (where T is the period of the waveform). This means that this particular coil can only be driven at 500 Hz which is well below the specified value given earlier. Fortunately, the rate that current is drawn is also voltage dependent. Thus, by applying a large supply voltage (such that the current derived through Ohms law is much greater than the peak current of the sine wave) it is possible to ensure that the current is driven through the coils faster than in the case previously described. To prevent the current overshooting significantly, it is necessary to switch the applied voltage in order to generate the desired sine wave. It must therefore be stressed, however, that this method of synthesising a sine wave is dependent on the frequency and amplitude of the target waveform as well as the voltage applied to the coil and the implications of this relationship will be discussed later in this chapter. In the example described below it is assumed that the coils are operating in the regime where the response time is sufficiently enhanced to accurately capture the properties of the reference sine wave.

To synthesise the current waveform in the experiment, it is first necessary to calculate the voltage pulses in advance using python code. The starting point of this is to first produce a target waveform. In the example discussed below, a sine wave of a single coil phase will be created with a frequency equivalent to a trap velocity of 300 m s^{-1} and an amplitude of 500 A. Figure 3.12 shows the process of synthesising the current waveform. From the reference waveform generated, an envelope is produced by offsetting the target waveform vertically by a fraction of the target peak current. This stage of the code is shown in figure 3.12a). Next, a voltage is applied allowing a current to rise. This continues up to the point the current meets the upper part of the envelope. At this point the voltage is removed and the current decays. It continues to decay until the current meets the lower envelope. Once again a voltage is applied allowing the current to rise. By repeating this process the complete sine wave can be generated. Additionally, switching devices tend to have a recovery period before they can be switched again. The code also accounts for this and will not allow the current to switch until this recovery time as elapsed. The negative cycle of the sine wave is generated in the same way, however, the voltage applied across the coil is now in the other direction. Figure 3.12b) shows the current waveform generated while panel c) shows the voltage pulses required to generate the current. This

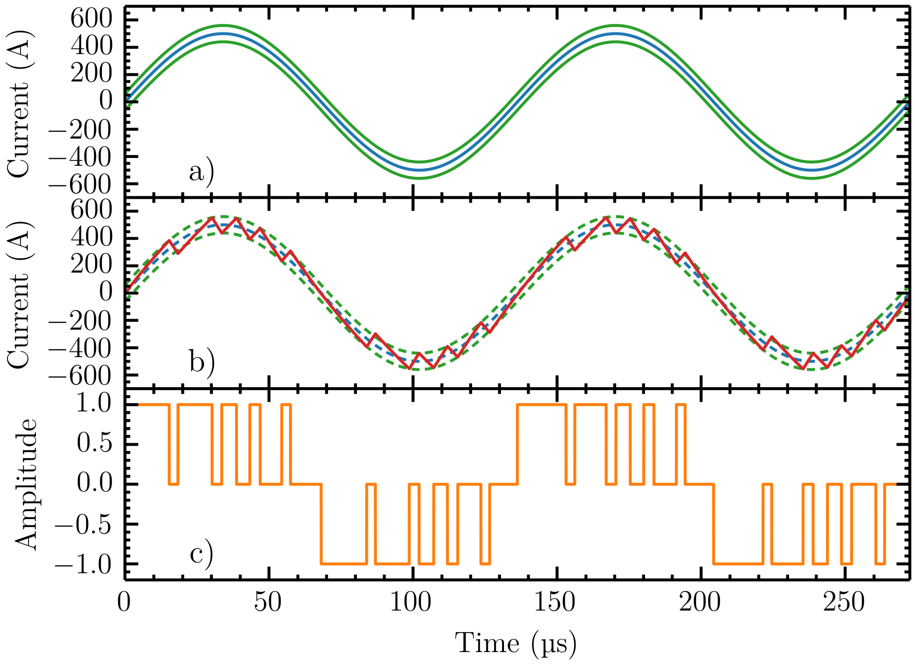

Figure 3.12: The process used to synthesise a sinusoidal waveform, this example is of a sine wave with a frequency equivalent to a trap velocity of 300 m s^{-1} and an amplitude of 500 A. Panel a) shows the first step in generating the waveform. A reference waveform (blue) is generated from which an envelope (green) is created by offsetting the target waveform vertically by a fraction of the target peak current. Panel b) shows the synthesis of the current waveform (red). By applying a voltage to the coil the current rises, this ceases once the current meets the upper part of the envelope. The voltage is then removed and the current decays until the current meets the lower envelope. Once again the voltage is applied allowing a rise in current. The negative cycle of the sine wave is generated in the same way, however, the voltage applied across the coil is now in the other direction. Panel c) shows the voltage pulses required to generate the current. This technique is a form of pulse width modulation which encodes the analogue target signal as a set of digital pulses.

technique is known as Pulse Width Modulation (PWM) and is a method of encoding the analogue target signal as a set of digital pulses; these pulses are sent to the power electronics. It is worth mentioning that each coil phase requires two signal channels (one for the positive half cycle and the other for the negative half cycle). The low level electronics described previously were built with a eight module long decelerator in mind. Therefore multiplexing of the channels reduces the number of outputs from 64 individual outputs to 20 outputs (two sets of 8 signal channels and 2 sets of 2-bit address channels). This dramatically reduced the size and cost of the control electronics.

Although other methods can be employed to produce a sine wave, this method reduces the number of components required. The obvious issue with this method is the imperfection of the sine wave. The effect this has on the decelerator field will be discussed in chapter 4 whereas the effects this has on the efficiency of the decelerator will be discussed in chapter 5. The other issue with this method is that the quality of the waveform is highly dependent on the initial velocity of the trap. A high trap velocity requires the current to vary much faster, however, it is the combination of the resistance and inductance of the coil phase that determines the time in which the current rises. If the time constant is too long, either the waveform will contain only a few pulses (therefore is an lower quality) or it maybe impossible to synthesise the target waveform. Consideration of the properties for different length coil modules are also important. The following discussion will describe the circuit design, properties and operation of the decelerator power electronics.

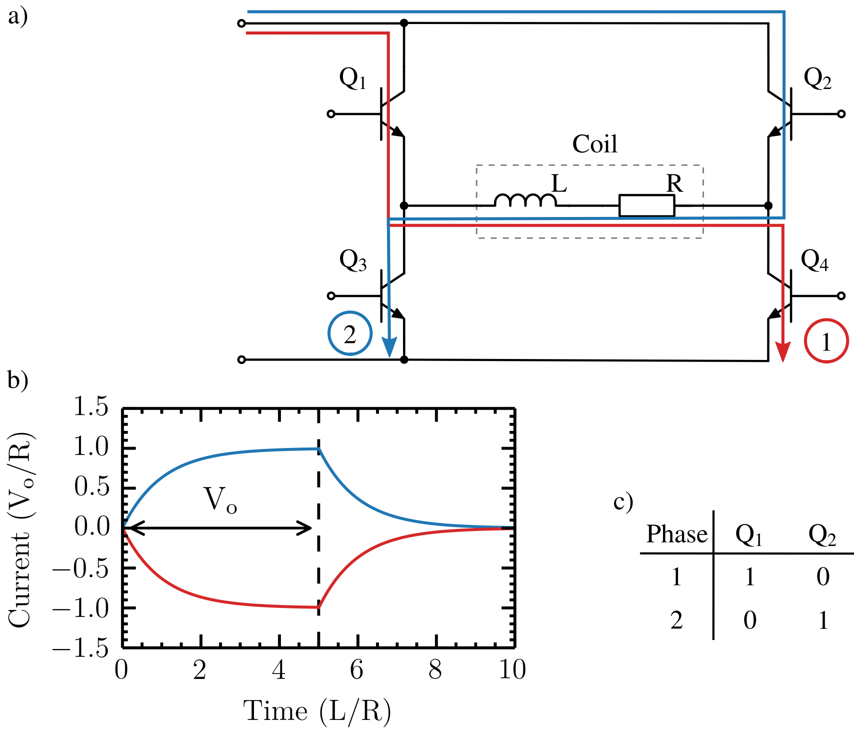

c)

Phase	Q_1	Q_2	Q_3	Q_4
1	1	0	0	1
2	0	1	1	0

Figure 3.13: The operation of a H-bridge. Panel a) shows a schematic of a typical H-bridge constructed from IGBTs. The switches are paired to allow the direction of the current across the load to be alternated. The decelerator coil is broken into the inductive and resistive components. When switches Q_1 and Q_4 are closed current flows through the coil left to right (red). The direction of the current flow is alternated when Q_2 and Q_3 are closed. Since the load has inductive and resistive components, when a voltage, V_o, is applied across the coil the current drawn is time dependent and rises exponentially to the current given by Ohm's law. When the voltage is removed the current exponentially decays. The characteristic time associated with the rise and fall time of the current is the time constant of the circuit which is the ratio of the inductance and resistance. This time dependence is shown in panel b). A summary of the logic states of the IGBTs is shown in the table in panel c). Here, 1 means active thus acting as a closed switch and 0 means the switch is in an open position.

Circuit Design and Operation

With the technique used to encode the analogue waveform into a set of digital pulses described, the switching circuit can be reported. The simplest form of switching circuit is the H-bridge. The benefit of this circuit over similar setups is that the entirety of the supply voltage is dropped across the load. Figure 3.13a) shows the schematic of the H-bridge. In this instance, the circuit is constructed from IGBTs (*Semikron SKM400GB12T4*). The H-bridge is constructed from pairs of the switching units. Q_1 and Q_4 are triggered simultaneously as are Q_2 and Q_3. The current flow through the coil in both phases has been annotated. Figure 3.13b) shows the current drawn through the coil in phase 1 (when Q_1 and Q_4 are triggered) and phase 2 (when switches Q_2 and Q_3 are triggered). The supply voltage in the first phase is dropped from left to right across the load and is reversed in phase 2. This diagram also shows the current through a coil as a function of time as previously described. Once the supply voltage V_o has been removed the current decays to zero. For reference the IGBTs active in each phase have been shown in figure 3.13c).

The next part of the circuit to consider is the voltage supply, however, knowledge of the electrical properties of the coils was first required. The development of the power electronics occurred simulta-

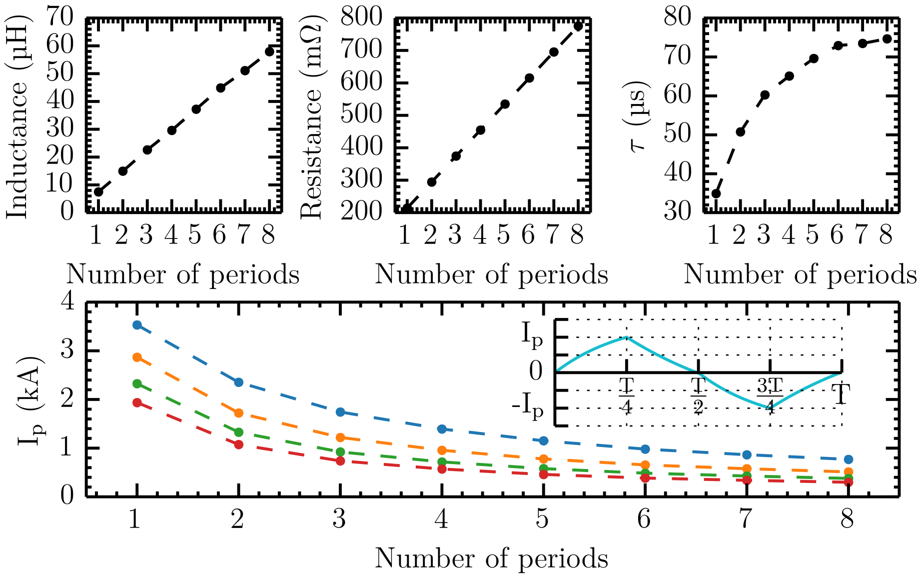

Figure 3.14: The idealised calculated electrical properties of the decelerator coils used to inform the decision of coil length. The upper panels show the resistance, inductance and time constant of the coils as a function of number of coil periods. The lower panel then shows the peak current that is achievable from a supply voltage of 800 V. To find the peak current it is assumed that the current waveform is generated from a single voltage pulse, resulting in a near triangular waveform as shown in the inset. The curves plotted correspond to different trap velocities of 100 m s^{-1} (blue), 200 m s^{-1} (orange), 300 m s^{-1} (green), and 400 m s^{-1} (red).

neously as the development of the method used to wind the coils. Without access to the actual coils, a theoretical approach was required to determine the properties of the coils. Each of the coil blocks are wired in series which ensures the current through the wires in the coil phase are all equal. Additionally, this simplifies the connections at the expense of the maximum current drawn. Calculating the resistance is a simple task, while predicting the inductance is more difficult. Using the method of partial inductance it is possible to estimate the inductance of a helical coil [194]. This method sums the mutual inductance between current carrying wires as well as the self-inductance of each wire. Estimating these properties is somewhat more complicated because of the connections between the wires and supply busbar and therefore any calculated value is a lower limit. Additionally, it was assumed the mutual inductance between the lower and upper coils is negligible compared to that of the wires which are in contact. Nevertheless, estimates of the inductance, resistance and the time constant for different lengths of coils are shown in figure 3.14. The lower panel in figure 3.14 shows the peak current (with a supply voltage of 800 V) obtained using a coil of a particular length for a series of trap velocities. The plot assumes that the lowest quality approximation to the sine wave is achieved, which is essentially a triangular waveform. An example of this waveform is shown as an inset and the definition of peak current, I_p, has been labelled. This figure further emphasises the link between sine wave quality and the trap velocity. From these plots, a three period coil gave the best compromise between the electrical properties, the heat load, and the number of coils required to make a 1 m long decelerator. While the power electronics were being developed, the source of the decelerator was slightly different. While a General Valve Series 9 was employed, the mean velocity of the gas pulse was found to be between 350 and 400 m s^{-1}. From the lower panel of figure 3.14, the 3 period long coil would be able to reach close to the 1000 A peak current with the beam velocity measured at that time.

As stated before, capacitors are the logical starting point for a high current DC supply. The characteristics of the capacitor, as shown previously with the quadrupole, must be considered in order to achieve the optimum current drawn by the load. Moreover, these capacitors must be rated to several hundred volts due to the relatively high resistance of the coils. Barry Moss designed this circuit and opted to place two 2.2 mF (450 V) capacitors (*BHC ALS30A222F420*) in series, although the total capacitance is halved, this allows 900 V to be dropped across the pair. Additionally, these capacitors have a low ESR, the benefits of this have been discussed previously. Three of these pairs are placed in parallel to increase the overall capacitance by a factor of three (3.3 mF total per power electronics module). The layout of the capacitors also allows for the driven decay of the current from the coils, rather than relying on free inductive decay. The principle behind this has been described previously in section 3.2. The benefit of this layout is that the fall in current occurs on a shorter time scale than free inductive decay, therefore allowing more PWM per cycle. As stated before, the simplicity of the power electronics comes with the issue of transient voltage spikes. These are generated while switching the high currents. To aid with the suppression of these spikes small filter 1.5 mF (850 V) capacitors (*Vishay MMKP386*) are placed across the IGBT package. These film capacitors rapidly charge and discharge and therefore initially provide a small kick in current. To further suppress these voltage spikes, the circuit layout is such that the positive and negative supply rails are placed close together to lower the total inductance of the circuit. From equation 3.1 the magnitude of the voltage spike can be altered by varying the rate of change of the current. This can be altered by varying the switching speed of the IGBTs. The switching time of the IGBT is proportional to the value of resistor connected to the gate of the IGBT which can be fitted directly on the driver card (*Semikron SKHI 23/12*). A larger gate resistance slows the rate of decay of the current resulting in a smaller transient spike, however, this means that the IGBT spends more time switching between the ‘on’ (saturation) state and the ‘off’ state. In this region the IGBT has a finite resistance and thus is heated by the current. A compromise must be reached between the magnitude of the voltage spike and the amount of heating. Figure 3.15 shows the voltage measured across one of the IGBT units during a switching event. In this particular example the supply voltage was 750 V and the IGBT was active for 20 μs. This plot clearly shows the effect of gate resistance on the rise time of the voltage and the magnitude of the voltage spike. As a result of good circuit layout and component choice, the transient spikes are only a couple of hundred volts peak. Furthermore, the peak voltage reached does not vary greatly over the range of gate resistance trialled. The figure also clearly shows that the total voltage across the IGBT does not exceed its rated voltage of 1200 V. The gate resistance selected was 4.5 mΩ, since this minimises the heating of the IGBT while having little effect on the transient voltage. Although the amount of heating will be minimised, the IGBTs were mounted on a water cooled plate. This precaution should help prolong the lifetime of the devices.

The full schematic of the decelerator power electronics is shown in figure 3.16. The schematic shows the four switching units (one for each coil phase) in parallel supplied from the same supply capacitors. Not shown are the driver cards connected to the gate of the IGBTs nor is the safety circuit consisting of normally closed relays to short the capacitors (for details on the latter see appendix D). The 10 kΩ bleed resistors (*TE Connectivity HSA50 50 W*) are fitted to ensure that the capacitors are completely discharged after use. Additionally, the circuit is designed such that the capacitors are charged and discharged uniformly, this technique is known as load balancing. The layout ensures that the load does not preferentially draw current from one set of capacitors. This is achieved by placing the terminals that connect to the power supply at opposite ends of the circuit. This technique helps prolong the lifetime of the capacitors. Figure 3.16 also shows the coil phases as a single inductor and resistor. The wires that form a phase are connected in series to ensure that equal current is drawn through each wire. The connections between the wires are made by inserting the wires into brass pins, the former are then held in place with grub screws. Finally, the pins are held in place with a PEEK mount. The connector assembly was designed by Ed Hinds and Jon Dyne (see appendix E for details). This compact design allows for multiple coil modules to be placed adjacent to one another while keeping the wire lengths to a minimum. Typically, a coil phase (including the connectors and busbar) has an average resistance of 520 ± 1 mΩ and an inductance of 41.6 ± 0.5 μH, leading to a time constant of 80 ± 1 μs. The four power electronic modules are connected in parallel, however, each module is fitted with a diode on the positive rail to prevent the modules discharging.

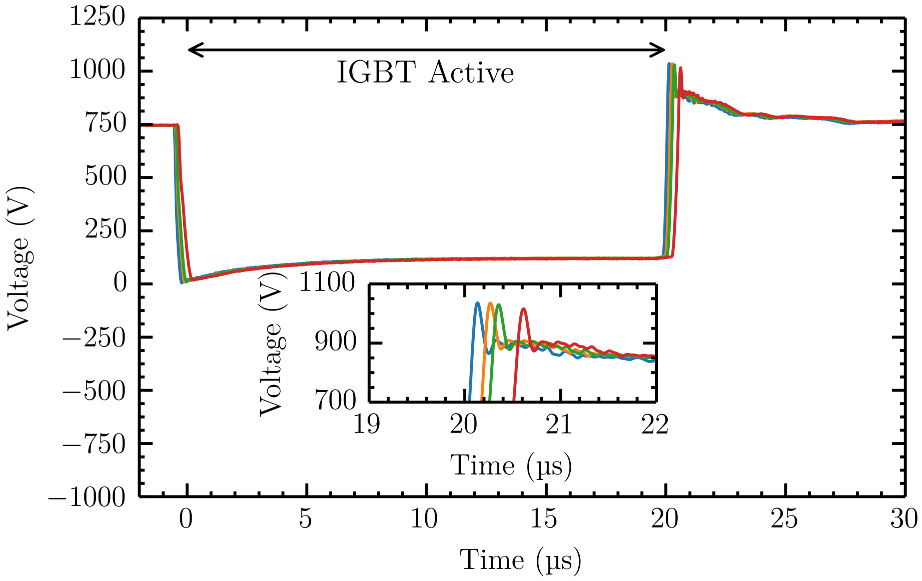

Figure 3.15: The voltage measured across one of the IGBT units during a 20 µs long switching event. In this example the supply capacitors were charged to 750 V. The plot shows the effect of the gate resistance of the IGBT on the switching rate. In the resistors shown are 4.5 mΩ (blue), 6 mΩ (orange), 6.9 mΩ (green), and 10 mΩ (red). The inset plot shows a zoomed in view of the transient voltage spike generated as a result of switching the high current. The magnitude of the spikes are only a couple of hundred volts peak and do not vary greatly over the range of gate resistances shown here. The total voltage across the IGBT does not exceed its rated voltage of 1200 V.

This configuration simultaneously charges the modules with a high voltage power supply (*Elektro-Automatik EA-PS 81500-30*). The diode keeps the power electronic module isolated which prevents the capacitors from a partially discharged module from drawing current from a fully charged module. A separate discharge rail had to be included to allow the capacitors to be rapidly discharged in the case of an emergency. Further explanation of this circuitry can be found in appendix D.

Drawings of the decelerator electronics can be found in figure 3.17. The drawing a) shows the cooling plate that the IGBTs are mounted on. The plate is made from copper pipe pressed into grooves milled into an aluminium plate. Drawings, b), c) and e) show the orthographic views of the decelerator power electronics while view d) shows a rendered image of the electronics. The parts of the electronics in the orthographic drawings are labelled to correspond to the components shown in figure 3.16. The IGBT modules (i) are used to pulse and orientate the current supplied by the supply capacitors, C_S, (ii). The filter capacitors, C_F, (iii) help to suppress the transient voltages produced while switching the IGBTs. The bleed resistors, R_B, (iv) are also labelled, these ensure the discharge of the capacitors after use. To make the electronics more compact, the circuit is folded in half. Therefore half of the IGBT modules are located on the underside of the cooling plate and thus cannot be seen in view d). For the same reasons listed in section 3.2, the busbar is constructed from 25 × 3 mm copper strip arranged in antiparallel. The driver cards (v) that drive the IGBTs modules have also been shown in image d). Finally, the orthographic views include annotations of some dimensions and where the connections are made to the power supply and to the coil phases. Once again, the latter are placed in antiparallel to keep the inductance of the load low.

The operation of the decelerator electronics can now be evaluated. To begin, the current waveform will be investigated. Figure 3.18 shows the current measured through the coils at a) 350 $\mathrm{m\,s^{-1}}$ and b) 150 $\mathrm{m\,s^{-1}}$. The waveforms were measured using a solenoid (*Honeywell CSNK500M*). The reference waveform and the pulses supplied to the driver cards have been included in both cases. Both examples are limited to roughly 500 A and generated from 650 V supply. As explained previously, it is the

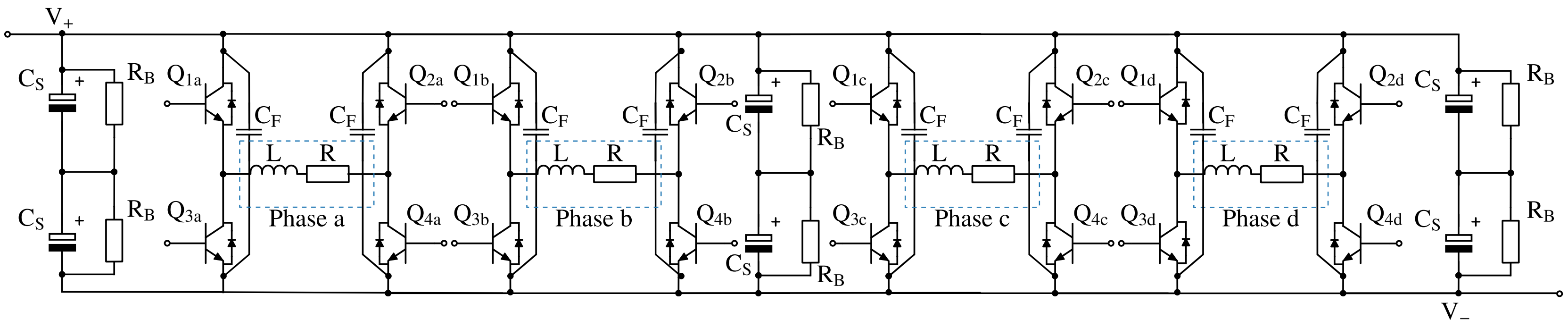

Figure 3.16: The complete circuit schematic of the decelerator electronics. The four coil phases and the IGBT units associated with that phase have been labelled (a to d). Each phase has a resistance and inductance associated with it. The IGBTs are labelled depending on their position in the H-bridge (see figure 3.13). For example IGBT Q_{1a} is in position 1 and controls coil phase a. The supply capacitors, C_S, consist of two capacitors (each 2.2mF rated to 450 V) in series to allow the full 800 V to be dropped across them. The filter capacitors, C_F, (1.5mF rated to 850V) are used to suppress the transient voltage spikes generated while switching the IGBTs. The bleed resistors, R_B used to discharge the capacitors after use have also been included. The positive and negative terminals are also shown. The configuration of these rails balances the current drawn by the load.

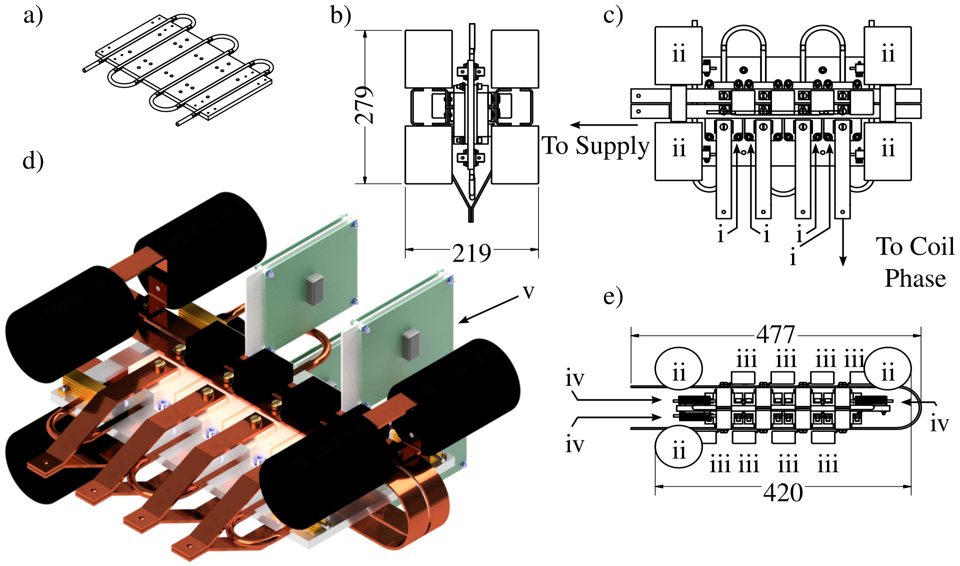

Figure 3.17: Drawings of the decelerator power electronics. View a) shows the cooling plate that the power electronics are mounted on. Views b) to e) are of the power electronics. Views b), c) and e) are orthographic drawings which are labelled to correspond to the components shown in figure 3.16. The IGBT modules (i) are used to pulse and orientate the current supplied by the supply capacitors, C_S, (ii). The filter capacitors, C_F, (iii) help to suppress the transient voltages produced while switching the IGBTs. The bleed resistors, R_B (iv) , have also been included. The circuit is folded in half to make the electronics more compact, thus half of the IGBT modules are located on the underside of the cooling plate and thus cannot be seen in view d). View d) also shows the location of the driver cards (v).

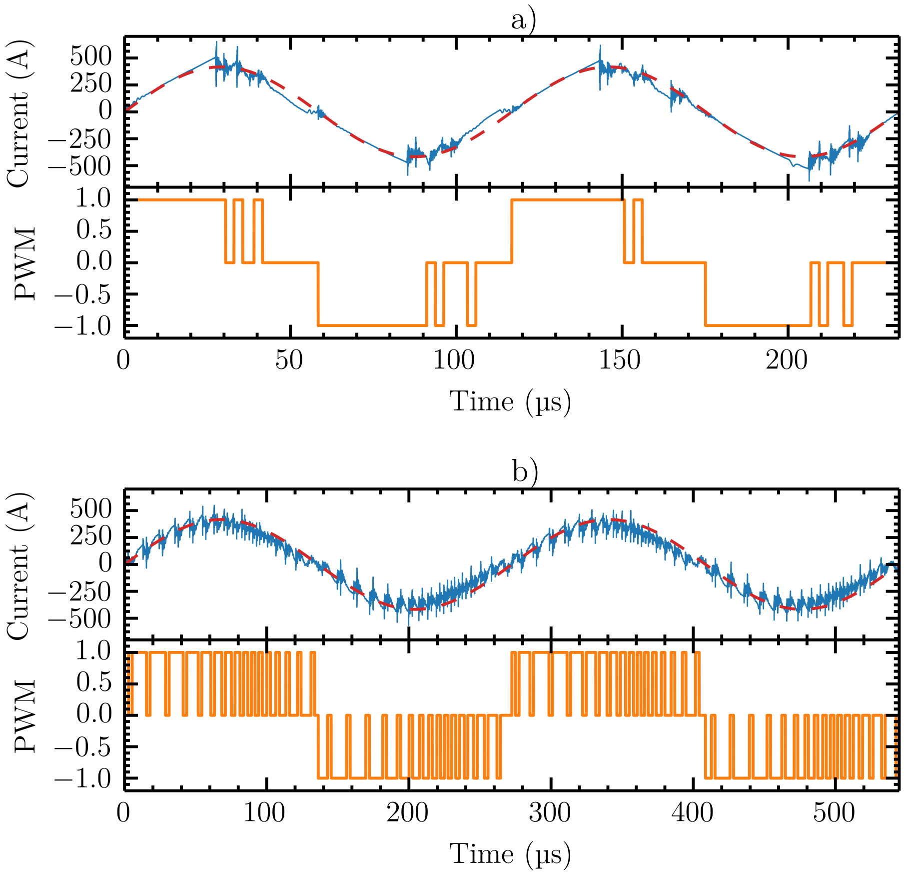

Figure 3.18: Examples of the measured current waveform through one of the coil phases (blue). The two examples shown are at frequencies corresponding to a) 350 m s^{-1} and b) 150 m s^{-1}. In both cases the reference waveform has been plotted (red dashed). The lower panels of each example gives the PWM signal sent to the driver cards.

combination of resistance and inductance of the coil which limits the rise of the current through the coil and therefore the peak current reached in a certain time. This relationship limits the quality of the sine wave which is clearly shown in the upper panels of figure 3.18. The relatively close agreement of the reference and target waveforms can only be achieved with accurate measurement of the properties of the coils and the precise timing of the FPGA. The heating of the coils was also studied. For instance with the switching sequence shown above, the coils experienced little heating. This may seem surprising as the root-mean-squared (RMS) power is fairly high, however, the coils are only activate for a short amount of time so the amount of heating is minimised. Despite this, the water cooling is still applied to ensure that the properties of the coil (particularly the resistance) does not vary between experimental runs.

The time dependence of the magnetic fields can also be compared to that generated theoretically. The Hall probe, previously described in section 3.2, can be used to perform such measurements. The Hall probe was fixed to the end of a plastic tube. The outer diameter of which was chosen to fit tightly in the internal portion of the stainless steel tube that the decelerator coils are mounted around. This ensures that the field being measured is along the z axis of the coil module. Due to the Hall probe's low saturation field the decelerator electronics was charged to 30 V to limit the current through the coils to 20 A. Figure 3.19 shows the measured and theoretical fields along the z axis of two coil modules at different times. This test allowed the evaluation of the overlap between two coil modules and for adjustments in the location of the coils to be made if necessary. To evaluate the simulations of the magnetic fields, the plots shown in figure 3.19 also includes the total calculated field of the coils and the separate field contributions of each coil. The first noticeable characteristic of the syntheised current waveform is that the depth of a trap is no longer constant over the two coils. In fact the trap depths vary across each of the times shown in 3.19. This shall be further studied in chapter 4. The magnitude of the fields, however, exhibit deviations due to the low voltage performance of the power electronics. This altered the characteristics of the power electronics and made accurately determining the synthesised current difficult. To overcome this issue, the measured current was imported into the field simulations in order to generate the theoretical fields. Despite this, the fields are not in complete agreement possibly due to artifacts (such as large transient spikes) introduced by the current probe at certain times. Finally, the overall agreement in the spatial extent of the magnetic fields are fairly high.

The velocity at which the trap moves through the coils can also be measured. As shown in figure 3.18, although the measured current waveforms are in close agreement with the target waveform there are slight discrepancies. This results in a difference between the target and measured velocities of the trap. The velocity of the trap can be determined by tracking the magnetic field minima over time while fixing the hall probe at a point along the z axis. In the example shown in figure 3.19, the magnetic field was intended to travel at 330 $\mathrm{m\,s^{-1}}$. The measured trap velocity suggests that the trap was actually moving at 334 ± 2 $\mathrm{m\,s^{-1}}$. Similar deviations can be observed as the trap velocity is varied from 50 to 450 $\mathrm{m\,s^{-1}}$. The percentage deviation is generally less than 1 % provided at leat four pulses form the current waveform. Unsurprisingly, the deviation of the trap velocity is larger for higher target velocities. This limits the ability to fine tune the trap velocities and may pose to be problematic when decelerating to very low final velocities.

One final consideration is the transformer effect between coils. Although not necessarily a limiting factor, these stray fields may further manipulate the beam if the gas packet expands significantly. In some of the panels shown in figure 3.19, the magnetic field does not always return to zero in the region of the coil which is not drawing current, despite careful calibration of the Hall probe. Furthermore, when a single coil is active, current through adjacent inactive coils can be measured. This effect is likely due to the alternating currents in the adjacent coil inducing a small current in the other coil module. This effect is exploited in transformers, although the current in this instance is less efficiently induced. Although direct Hall probe measurements have not been made in the high current regime, induced currents on the order of 15 A peak have been measured while the coils are operating at 500 A peak over a range of frequencies. The induced currents are on the order of a few percent of the applied current waveform, so will be ignored in the following Monte Carlo simulations.

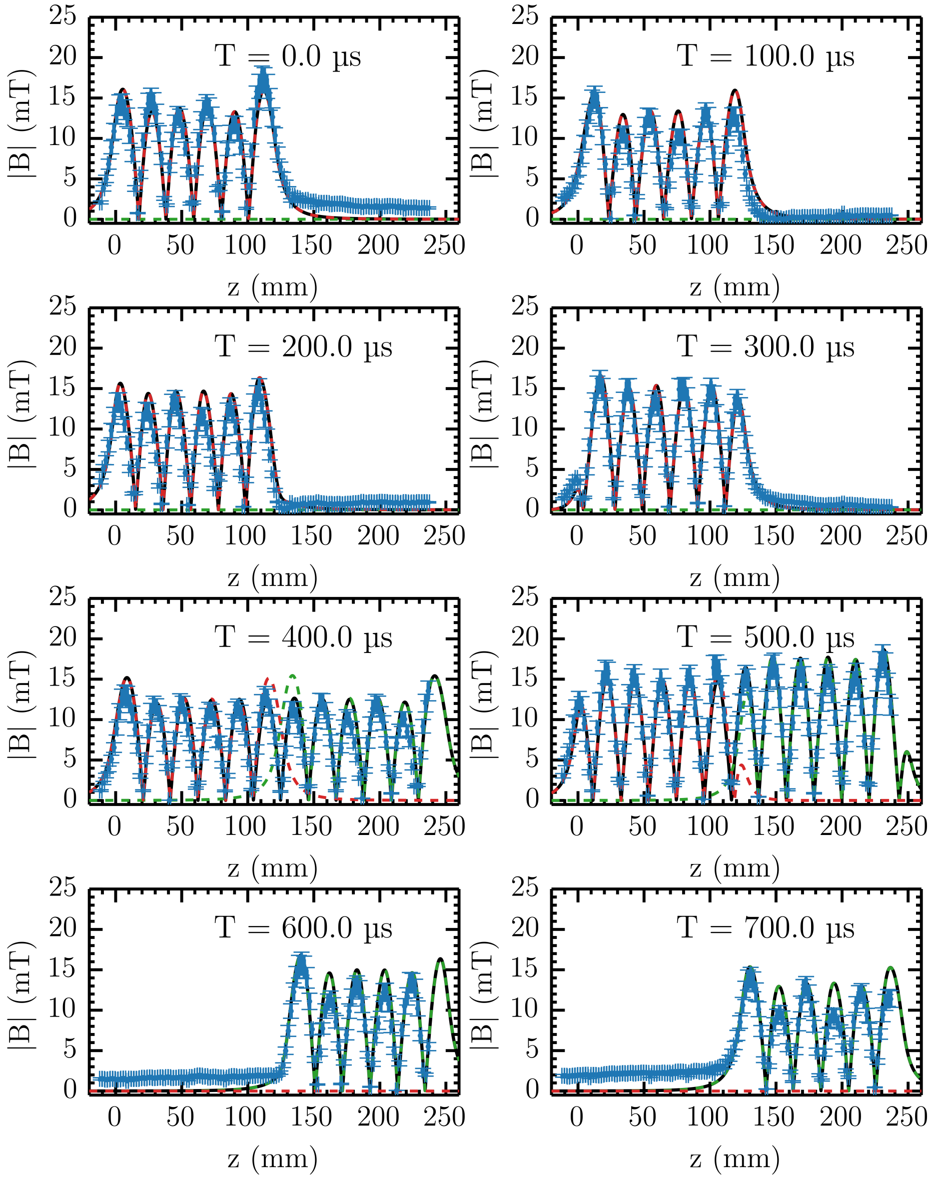

Figure 3.19: The evolution of the magnetic field measured through two adjacent coil modules along the z axis as a function of time. The measured field (blue) was generated by a 20 A peak current. To allow comparison of the measured field to theory, the field generated by coil 1 (red) and coil 2 (green) as well as the total field (black) have also been plotted.

3.4 Chapter Summary

This chapter has presented the design specification and the evaluation of the components electronics. The design of the low level electronics have been briefly described. The FPGA is used as the control unit for the power electronics. Devices such as this have an adequate number of outputs for address bits, the triggers for the positive and negative parts of each coil phase and the quadrupole triggers required for the project. The optical-coupler is beneficial as it not only breaks a significant number of potential earth loops, it also reduces the length of signal conductors which further decreases the amount of noise introduced into the control circuit. The disadvantage of this circuit is that it introduces additional PCBs which increases the power consumption, cost and size of the electronics. Multiplexing the control electronics has kept both the size and cost low. The multiplexing unit has been designed around a 1 m (8 modules) long decelerator. In order to multiplex the circuitry, the coils are divided into two groups depending on the coil's position in the decelerator. The even number coils are in one group while the odd numbered coils are in the other. It is important to note that coils in the same group are never on simultaneously. This reduces the number of outputs from 64 to 20 (two sets of 8 signal channels and 2 sets of 2-bit address channels).

The quadrupole electronics must be able to produce a constant current of 700 A for a few milliseconds. Furthermore, the pulse must avoid the fringe field regions of the quadrupole. These regions of magnetic field are produced at the ends of the quadrupole where the various electrical connections are made. The duration and magnitude of this current pulse requires a power supply, however, supplies of this type intrinsically possess large rise and fall times associated with the currents. Therefore, an electronics circuit is required to modify the current from the power supply to add fast rising and falling edges. The design of the electronics circuit has been described and evaluated. The electronics are capable of producing a current pulses with a rising edge of 58.4 μs and a falling edge of 178 μs with the kick circuitry charged to 60 V. The hold supply, in contrast, produces current pulses with a rising edge of 362 μs and a falling edge of 209 μs. The fields generated by the quadrupole were compared to theory and the heat load of the coil investigated. The latter may prove problematic, particularly with longer length quadrupoles.

The decelerator power electronics were described. Each decelerator coil phase requires a sinusoidal waveform up to 1000 A peak from 10 kHz to DC. Additionally, each module should be able to control each phase individually since each requires a sinusoidal current offset by $\pi/4$ radians. The technique used to generate the AC waveform from a DC supply has been explained. This relies on a bank of capacitors to supply a current while a H-bridge is employed to alternate the direction of current flow. The AC waveform is syntheised by making use of the inductance and resistance, and hence the finite rise time, that each coil phase possesses. Pulse width modulation is used to encode the target analogue waveform into a series of digital pulses. The digital pulses are calculated in advance with knowledge of the inductance and the resistance of the coil. These, along with analytic expressions for the rise and the decay of the current through the coil, can then be used to synthesise a current waveform with characteristics similar to the ideal target waveform. The digital pulses calculated can then be sent from the FPGA to the power electronics via the fibre-optic link. The disadvantage of this technique is that the peak current drawn by the coil and the quality of the sine wave is dependent upon the electrical properties of the coil. The design of the power electronics was presented and the justifications for the layout and choice of components made. Finally, the performance of the power electronics was evaluated. A measured current waveform generated by the power electronics for two frequencies was presented. This proved that the PWM technique has the ability to generate a waveform with an arbitrary frequency and peak magnitude. A low current study of the magnetic fields produced by the decelerator coils was then reported. This allowed the motion of the traps through the coil to be investigated. This highlighted two consequences of the PWM technique: firstly, that the field depth varies over time and secondly, the difference in the target trap velocity and the measured trap velocity. Measurements of the trap velocity vary from the target by no more than 1% provided at least four pulses went to synthesise the current waveform. This technique, however, limits the ability to fine tune the trap velocity which may be problematic at the very low velocity regime. These measured fields were also compared to theory. This demonstrated the ability to simulate the fields within the decelerator and generally showed excellent agreement. Finally, the transformer effect between the coils was considered. Since the current induced between adjacent coils is low the effect will be ignored throughout any theoretical treatment of the decelerator.

Chapter 4

Simulating the Decelerator

This chapter describes some key aspects of the simulation procedure used in the decelerator project. Most of the algorithms used are fairly well known, however, a number had to be developed specifically for this project. Section 4.1 begins by explaining a computationally efficient way to capture the major elements of the geometry of the source. Section 4.2 describes the technique used to calculate the field produced by the quadrupole and decelerator fields. The methods discussed here were largely developed by Ulrich Krohn, although as the project developed the code had to be updated to accommodate changes introduced. Section 4.3 goes on to explain the tricubic method of interpolation implemented to determine the acceleration experienced by the paramagnetic species within the decelerator field. Finally, section 4.4 justifies the simplification used in the simulation process, and rigorously evaluates the effects that the synthesised current waveforms have on the motion of the trap.

4.1 Emulating the Source

Certain simulations require the source of the decelerator to be simulated. Ideally, a full direct Monte Carlo simulation of the gas expansion would be performed in order to completely capture the velocity and density of the gas pulse. Additionally, interference from the skimmer could be built in for completeness. This type of simulation is computationally expensive. As such it is advantageous to simulate the valve without the need to perform these calculations for different conditions the valve is subjected to. Instead, a geometric argument is made and a schematic view of this can be found in figure 4.2.

The first step of this process is to set a supersonic velocity distribution in z, such that

$$v_{\mathrm{z}} = f\left(v_{\mathrm{z}}, \mu_{\mathrm{vz}}, \sigma_{\mathrm{vz}}\right) = \sqrt{\frac{2}{\pi}} \frac{v_{\mathrm{z}}^2}{\sigma_{\mathrm{vz}}^3} \exp\left(\frac{(v_{\mathrm{z}} - \mu_{\mathrm{vz}})^2}{2\sigma_{\mathrm{vz}}^2}\right). \tag{4.1}$$

The standard deviation, σ_{vz} and mean, μ_{vz}, can be set after fitting the time-of-flight profiles to the experimental data (see chapter 5). If necessary, an initial spatial spread in z can also be set using a Gaussian distribution. In most cases, however, a point source centred at the valve nozzle is a sufficient approximation. This option allows further tuning of the source by setting the values of σ_{z} and μ_{z}, the standard deviation and mean location of the initial spatial distribution respectively. The x and y distributions can be determined geometrically from the skimmer aperture, the valve nozzle, and their

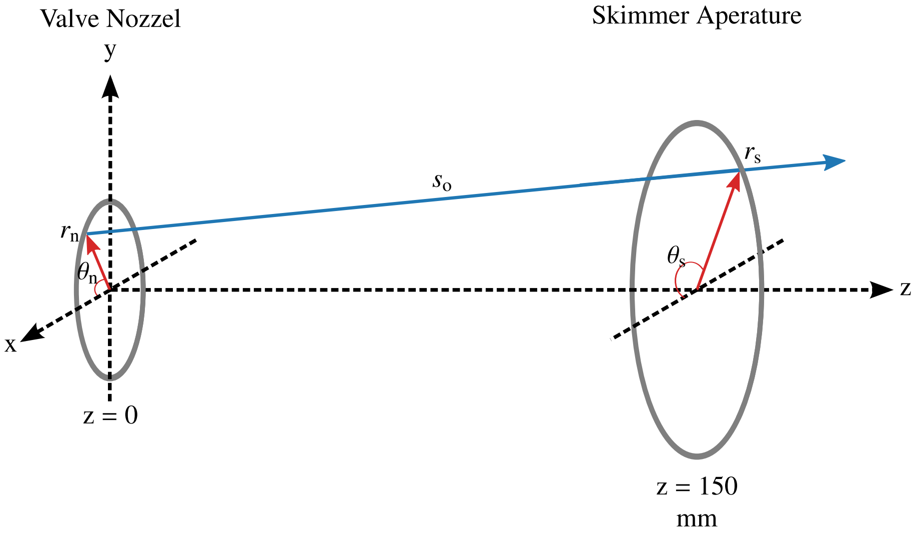

Figure 4.1: A schematic view of the nozzle aperture (z = 0 mm) and skimmer aperture (z = 150 mm). The simulation begins by randomly setting a velocity in the z direction from a supersonic velocity distribution. The mean and standard deviation is set by the fitting of the time of flight profiles produced by the experiment. A Gaussian spatial function can also be applied in z, however, a point source centred at the nozzle is sufficient in most cases. The particles are uniformly given points at the nozzle and skimmer apertures, producing a vector $\mathrm{s_o}$. Given these constraints, it is possible to calculate the transverse velocities of each particle.

separations. To achieve this, all particles are given a random point at the nozzle aperture. Each point has a random radial position, r_n, and a random angle, θ_n, relative to the x axis. Next, the particles are given another random point at the skimmer aperture located at z = $\triangle_\mathrm{ns}$. Once again, the particles receive a random radial position, r_s, and a random angle, θ_s.

At t = 0, the particles are uniformly distributed around the valve aperture. The initial spatial vector of any particle is therefore

$$\begin{pmatrix} x_\mathrm{o} \\ y_\mathrm{o} \\ z_\mathrm{o} \end{pmatrix} = \begin{pmatrix} r_\mathrm{n}\cos\left(\theta_\mathrm{n}\right) \\ r_\mathrm{n}\sin\left(\theta_\mathrm{n}\right) \\ f\left(z, \mu_\mathrm{z}, \sigma_z\right) = \frac{1}{\sigma_z\sqrt{2\pi}}\exp\left(\frac{\left(z-\mu_\mathrm{z}\right)^2}{2\sigma_\mathrm{z}^2}\right) \end{pmatrix}. \tag{4.2}$$

For completeness, it is assumed that the packet initially also possesses a Gaussian spatial spread along the z axis. A vector, s_o, can be drawn between the nozzle and skimmer points. Using the known z and v_z values, the transverse velocity components can then be calculated provided the nozzle to skimmer separation is known. It follows that the initial velocity vector of any particle is

$$\begin{pmatrix} v_\mathrm{x} \\ v_\mathrm{y} \\ v_\mathrm{z} \end{pmatrix} = \frac{v_\mathrm{z}}{\triangle_\mathrm{ns} - z_\mathrm{o}} \begin{pmatrix} r_\mathrm{s}\cos\left(\theta_\mathrm{s}\right) - r_\mathrm{n}\cos\left(\theta_\mathrm{n}\right) \\ r_\mathrm{s}\sin\left(\theta_\mathrm{s}\right) - r_\mathrm{n}\sin\left(\theta_\mathrm{n}\right) \\ \triangle_\mathrm{ns} - z_\mathrm{o} \end{pmatrix}. \tag{4.3}$$

This method ensures that the particles simulated are all accepted by the skimmer which prevents unnecessary particle loss due to the skimmer aperture. It is necessary to create the temporal broadening caused by the excitation scheme. To achieve this, the particles are given a new position along the z axis such that the particle distribution uniformly fills the excitation region. Since the velocity distribution remains unchanged, the time taken for each particle to reach this new longitudinal position can be calculated and the transverse coordinates can then be evolved accordingly. This spatial broadening was found to be less important for the Even-Lavie valve than it was for the previous setup consisting of a General Valve and an electric discharge. As the simulation begins, each particle is given a starting time which uniformly gives the distribution a temporal spread, the width of which is set by the experimental parameters. This is justified because the time of flight measurements are relative to the creation of the excited gas not the opening of the valve. Finally, the distribution of states after excitation of the metastable argon are assumed to be identical to those of metastable Neon. When using the DBD, it has been shown that 100 % of the Neon is excited to the $^3P_2$ state [181]. Furthermore, it is assumed here that each of the five m_J states are initially uniformly populated.

4.2 Calculating the Decelerator Fields

The total magnetic field at time t is the sum of the fields from each of the wires in the decelerator. The decelerator coils will be modelled as a series of current carrying elements of length d. This length is dependent on the angle which the wires cross α and the diameter of the wire, d_w. The form this length takes is

$$d = \frac{16 d_\mathrm{w}}{\sin(\alpha)\cos(\alpha)}. \tag{4.4}$$

The k$^\mathrm{th}$ wire of the decelerator will have the current $I^{(k)}$ flowing through it and the wire centre will be located at $\mathbf{v}^{(k)}$ relative to the origin. The total magnetic field vector at an arbitrary point, P, described by vector $\mathbf{r}$ relative to the origin, can be calculated using the Biot-Savart law

$$\mathbf{B} = \frac{\mu_0}{4\pi} \sum_k I^{(k)} \int \frac{\mathbf{R}^{(k)} \times d\mathbf{s}}{\left|\mathbf{R}^{(k)}\right|^3}. \tag{4.5}$$

Where $d\mathbf{s}$ is the current element of the wire and $\mathbf{R}^{(k)}$ is the separation between point P and the k$^\mathrm{th}$ wire. Hence $\mathbf{R}^{(k)} = \mathbf{r} - \mathbf{v}^{(k)}$. The Biot-Savart law can be solved for conductors of finite length the equation has the form

$$\mathbf{B}_\mathrm{w} = \frac{\mu_0}{4\pi} \sum_k \frac{I^{(k)}}{\left|\mathbf{R}^{(k)}_\mathrm{w}\right|} \hat{e}^{(k)}_t \left[\sin\left(\phi^{(k)}_\mathrm{u}\right) - \sin\left(\phi^{(k)}_l\right)\right]. \tag{4.6}$$

The angles $\phi^{(k)}_\mathrm{u/l}$ arise from the limits of the integrated cross product and are used to set the finite length of the wire. The tangent unit vector, $\hat{e}^{(k)}_t$, sets the direction of the field originating from the k$^\mathrm{th}$ wire. Figure 4.2 shows an illustration of the field calculation. The upper panel shows a simplified version of a decelerator coil constructed from two wires. Depending on the wire orientation, the wires cross the z axis at an angle of α or $\pi - \alpha$. The lower panel shows a cut-through of a coil module in the yz plane. The colour of the wires depends on the direction and magnitude of the current through the wire. This diagram forms the basis for the field calculations.

The solution of the Biot-Savart law given in equation 4.6 is only strictly applicable for an array of parallel, straight wires. Moreover, the coordinate system of the calculation is defined as the system where the wire lies in parallel to a coordinate axis and point P along another axis. In this coordinate

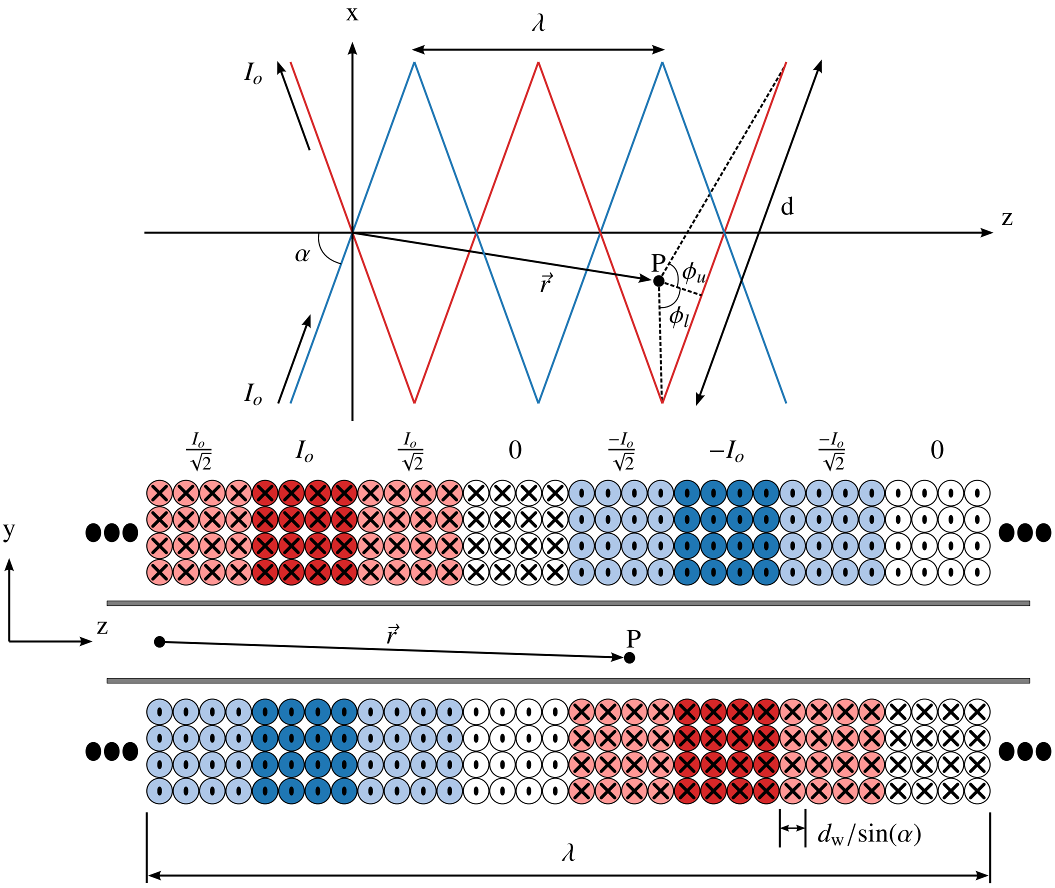

Figure 4.2: An illustration of the method used to calculate the magnetic field generated by the decelerator coils. The upper panel shows a simplified version of a decelerator coil. The wires cross the z axis at an angle of α or $\pi - \alpha$. To calculate the magnetic field at point P, the field due to a finite length current carrying wire must be computed. The lines that join point P to the end of the wire element and the normal vector of the wire are also sketched. These lines enclose the angles ϕ_u and ϕ_l. The vectors representing the current flow through the wires are also shown. The lower panel shows a cut-through of a coil module in the yz plane. The wire elements are coloured depending on the direction and magnitude of the current. The current values through the coil phase have been labelled.

system the separation of point P and the k$^{\text{th}}$ wire is $\mathbf{R}_{\text{w}}^{(k)}$. To transform point P from the laboratory frame into the frame of the wire, a rotation in the y axis is required. The rotation is dependent on the crossing angle of the wire and the z axis, thus $\theta = \{\alpha,\ \pi - \alpha\}$ and

$$U = \begin{pmatrix} \sin(\theta) & 0 & \cos(\theta) \\ 0 & 1 & 0 \\ -\cos(\theta) & 0 & \sin(\theta) \end{pmatrix}. \tag{4.7}$$

The rotation matrix has been modified from the standard form to ensure the wire runs along the x direction in the new coordinate system. Point P must then be translated relative to the k$^{\text{th}}$ wire to calculate $\mathbf{R}_{\text{w}}^{(k)}$ and the angles $\phi_{\text{u/l}}^{(k)}$. For instance, the vector $\mathbf{r} = (x, y, z)^{\text{T}}$ pointing towards P in the laboratory frame is now given by

$$\mathbf{R}_{\text{w}}^{(k)} = U \begin{pmatrix} x \\ y \\ z \end{pmatrix} - \begin{pmatrix} z^{(k)}\cos(\theta) \\ y^{(k)} \\ z^{(k)}\sin(\theta) \end{pmatrix}. \tag{4.8}$$

In the frame of the k$^{\text{th}}$ wire with coordinates $\left(x^{(k)}, y^{(k)}, z^{(k)}\right)^{\text{T}}$. The translation term redefines the location of the wire such that the wire crosses the origin of the new coordinate system. In this frame the angles $\phi_{\text{u/l}}^{(k)}$ have the form

$$\phi_{\text{u}}^{(k)} = \arctan\left(\frac{d/2 - x_{\text{w}}^{(k)}}{\left|\mathbf{R}_{\text{w}}^{(k)}\right|}\right), \quad \phi_{\text{l}}^{(k)} = \arctan\left(\frac{-d/2 - x_{\text{w}}^{(k)}}{\left|\mathbf{R}_{\text{w}}^{(k)}\right|}\right). \tag{4.9}$$

Where $x_{\text{w}}^{(k)}$ is the x coordinate of the k$^{\text{th}}$ wire in the frame of the wire. In this frame, equation 4.6 can now be applied. The magnetic field of the decelerator in the laboratory frame, $\mathbf{B}_{\text{D}}$, can be returned following another rotation

$$\mathbf{B}_{\text{D}} = U^{\text{T}}\mathbf{B}_{\text{w}}. \tag{4.10}$$

The quadrupole field can be generated in a similar fashion. It is a reasonable approximation to consider the poles of the quadrupole to be infinitely long. Furthermore, the rotation of the frame is unnecessary because the wire already is parallel to the z axis. In this treatment, the j^{th} pole carrying a current $I^{(j)}$ is located $R^{(j)}$ from point P. Hence the total magnetic field from the quadrupole is

$$\mathbf{B}_{\text{n}} = \frac{\mu_0}{2\pi}\sum_j \frac{I^{(j)}}{R^{(j)}}\hat{e}_t^{(j)}. \tag{4.11}$$

This can be added to the decelerator field to obtain the complete magnetic field generated by the decelerator

$$\mathbf{B} = \mathbf{B}_{\text{D}} + \mathbf{B}_{\text{n}}. \tag{4.12}$$

The fields are calculated on a cuboid grid which must be interpolated to find the potential at an arbitrary point. It is also necessary to determine the field gradients at such a point in order to calculate the force exerted on the magnetic dipole by the potential.

4.3 3D Field Interpolation

The trajectories of atoms or molecules through the decelerator are built up over the course of many discrete time steps. This can be achieved using a fourth order Runge-Kutta algorithm. In order to calculate a position at the next time step knowledge of the force, $\mathbf{F} = -\nabla U$, experienced by the atom or molecule in the potential U is required. Rather than calculating the magnetic field at each time step it is convenient to interpolate the grid of field points previously calculated and employ a third-order polynomial interpolator to determine the acceleration at an arbitrary point. The method implemented here was developed by Lekien *et al.* [195]. The interpolated potential can be expressed as a sum of polynomials given by

$$U_{\mathrm{I}}\left(x,y,z\right) = \sum_{i,j,k=0}^{N} \alpha_{ijk} x^i y^j z^k. \tag{4.13}$$

For a third order polynomial the interpolation coefficients, α_{ijk}, can be determined with knowledge of the following derivatives

$$\left\{ U, \frac{\partial U}{\partial x}, \frac{\partial U}{\partial y}, \frac{\partial U}{\partial z}, \frac{\partial^2 U}{\partial x \partial y}, \frac{\partial^2 U}{\partial x \partial z}, \frac{\partial^2 U}{\partial y \partial z}, \frac{\partial^3 U}{\partial x \partial y \partial z} \right\}. \tag{4.14}$$

Where the other second and third order derivatives can be shown to be a linear combination of the other constraints. For a regular mesh constructed from rectangular cells, the field data is provided on 8 points, which is shown in figure 4.3a). It is necessary to calculate the 8 derivatives at each point thus, the total number of calculations is $N = 64$. It should be noted that the method developed is a local interpolation routine so the field data can be calculated from the corners of each cell individually. Global interpolation requires knowledge of the derivatives of the field over all cells including the derivatives at the faces of the cell. The local interpolation allows for the interpolation of a sparsely populated grid. This avoids the accumulative error of the spline due to measurement or calculation errors of the field. Furthermore, this method does not require knowledge of the boundary conditions, such as the step size of the grid.

The interpolation coefficients, α_{ijk}, can be assembled in a vector, $\boldsymbol{\alpha}$, such that

$$\boldsymbol{\alpha} = \left(\alpha_{000}, \alpha_{100}, \alpha_{100}, \alpha_{300}, \alpha_{010}, \alpha_{110}, ..., \alpha_{233}, \alpha_{333}\right)^{\mathrm{T}}. \tag{4.15}$$

Additionally, a vector, $\mathbf{b}$, containing the spatial derivatives given in equation 4.13 on each of the 8 corners of the cell has the form

$$\begin{aligned} \mathbf{b} = \Bigg(& f|_1, ..., f|_8, \left.\frac{\partial f}{\partial x}\right|_1, ..., \left.\frac{\partial f}{\partial y}\right|_1, ..., \left.\frac{\partial f}{\partial z}\right|_1, ..., \\ & \left.\frac{\partial^2 f}{\partial x \partial y}\right|_1, ..., \left.\frac{\partial^2 f}{\partial x \partial z}\right|_1, ..., \left.\frac{\partial^2 f}{\partial y \partial z}\right|_1, ..., \left.\frac{\partial^3 f}{\partial x \partial y \partial x}\right|_1, ..., \left.\frac{\partial^3 f}{\partial x \partial y \partial z}\right|_8 \Bigg)^{\mathrm{T}}. \end{aligned} \tag{4.16}$$

The interpolation coefficients can be converted into the derivatives by a suitable matrix,

$$\boldsymbol{\alpha} = \mathfrak{B}^{-1}\mathbf{b}. \tag{4.17}$$

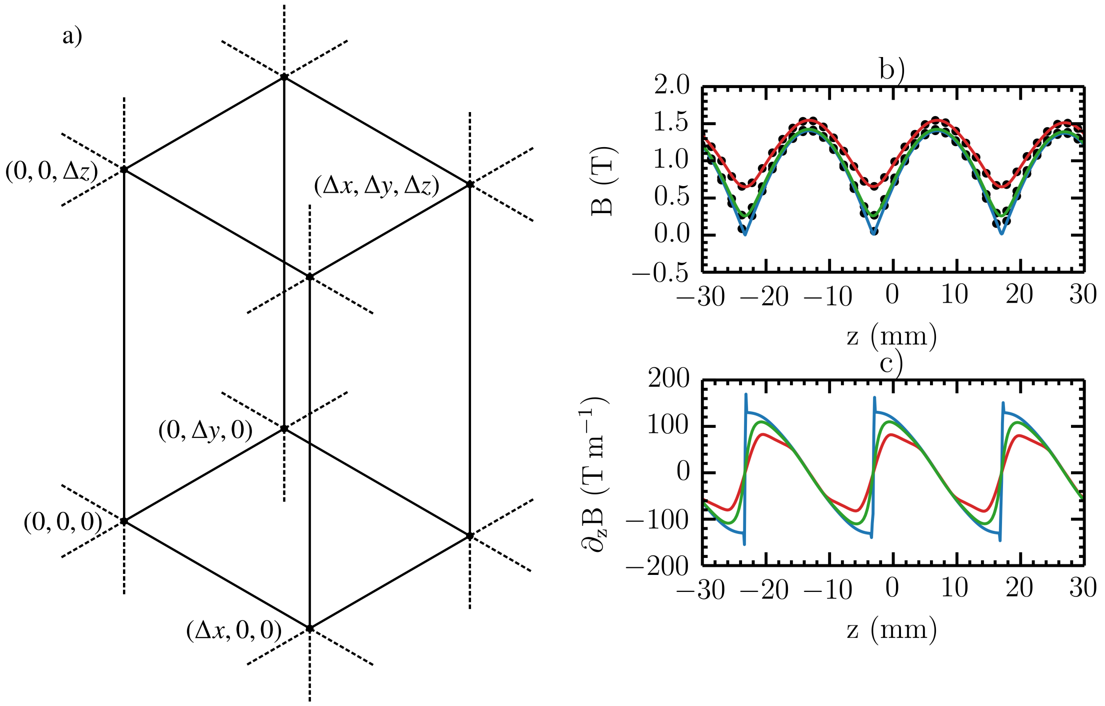

Figure 4.3: Illustration of the tricubic interpolation unit cell and interpolation results. Panel a) shows a sketch of the cuboid unit cell that forms the grid on which the field components are calculated. The values of the potential and acceleration can be calculated from this information. Panel b) shows an example of the interpolation of the potential at x = 0 mm, y = 0 mm (blue), x = 0 mm, y = -2.62 mm (red), and x = -1.05 mm, y = 1.05 mm (green). The points represent the calculated values. Fianlly, panel c) shows the interpolated gradient in the z direction constrained by the same x and y coordinates.

m	i	j	k
1	0	0	0
2	1	0	0
3	2	0	0
4	3	0	0
5	0	1	0
...	...	...	...
64	3	3	3

Table 4.1: The partial table showing the relationship between the m^{th} column and the indices i, j, k.

Where $\mathfrak{B}$ is a 64×64 matrix with integer entries. If the cuboid cell shown in figure 4.3 was taken to be non-uniform (such that $\Delta x \neq \Delta y \neq \Delta z$) then the m^{th} column of the matrix can be written as

$$\mathfrak{B} = \begin{cases} x(n)^{i(m)} \times y(n)^{j(m)} \times z(n)^{k(m)} & \text{if } 1 \leqslant r \leqslant 8 \\ ix^{|i-1|} \times y^j \times z^k & \text{if } 9 \leqslant r \leqslant 16 \\ x^i \times jy^{|j-1|} \times z^k & \text{if } 17 \leqslant r \leqslant 24 \\ x^i \times y^j \times kz^{|k-1|} & \text{if } 25 \leqslant r \leqslant 32 \\ ix^{|i-1|} \times jy^{|j-1|} \times z^k & \text{if } 33 \leqslant r \leqslant 40 \\ ix^{|i-1|} \times y^j \times kz^{|k-1|} & \text{if } 41 \leqslant r \leqslant 48 \\ x^i \times jy^{|j-1|} \times kz^{|k-1|} & \text{if } 49 \leqslant r \leqslant 56 \\ ix^{|i-1|} \times jy^{|j-1|} \times kz^{|k-1|} & \text{if } 57 \leqslant r \leqslant 64. \end{cases} \tag{4.18}$$

Where the notation $x(n)$ means the x-value of the n^{th} corner ($1 \leqslant n \leqslant 8$) of the cuboid. r is the row of the matrix and i, j, k are functions of the column index m. The brackets of the functions have been dropped from the second line onwards. The indices for the m^{th} column can be found in table 4.1 which shows a partially complete look-up table.

The potential U_{I} for any point in space (x, y, z) that lies within the cell can be obtained using the set of alpha coefficients, $\boldsymbol{\alpha}$, and computing the product

$$U_{\text{I}} = \boldsymbol{\alpha}.\left(\mathbf{x} \cdot \mathbf{y} \cdot \mathbf{z}\right). \tag{4.19}$$

Here, the in-line dot denotes a scalar product whereas the centre dot denotes a component-wise product. The position vectors $\mathbf{x}$, $\mathbf{y}$ and $\mathbf{z}$ are given by

$$\begin{aligned} \mathbf{x} &= \mathbb{I}_{16} \otimes \left(1, x, x^2, x^3\right)^{\text{T}} \\ \mathbf{y} &= \mathbb{I}_4 \otimes \left(1, y, y^2, y^3\right)^{\text{T}} \otimes \mathbb{I}_4 \\ \mathbf{z} &= \left(1, z, z^2, z^3\right)^{\text{T}} \otimes \mathbb{I}_{16}. \end{aligned} \tag{4.20}$$

The matrix of ones of length s is signified with $\mathbb{I}_s$ and $\otimes$ is the Kronecker product. The derivatives of the position vectors are

$$
\begin{aligned}
\partial_x \mathbf{x} &= \mathbb{I}_{16} \otimes \left(0, 1, 2x, 3x^2\right)^{\mathrm{T}} \\
\partial_y \mathbf{y} &= \mathbb{I}_4 \otimes \left(0, 1, 2y, 3y^2\right)^{\mathrm{T}} \otimes \mathbb{I}_4 \\
\partial_z \mathbf{z} &= \left(0, 1, 2z, 3z^2\right)^{\mathrm{T}} \otimes \mathbb{I}_{16},
\end{aligned}
\tag{4.21}
$$

can then be used to obtain the derivative of the potential at an arbitrary point

$$
\nabla U_{\mathrm{I}} = \begin{pmatrix} \alpha.\left(\partial_x \mathbf{x} \cdot \mathbf{y} \cdot \mathbf{z}\right) \\ \alpha.\left(\mathbf{x} \cdot \partial_y \mathbf{y} \cdot \mathbf{z}\right) \\ \alpha.\left(\mathbf{x} \cdot \mathbf{y} \cdot \partial_z \mathbf{z}\right) \end{pmatrix}.
\tag{4.22}
$$

This can then be used to find the acceleration of the particle in the field. An example of the interpolated field is shown in figures 4.3b) and c). An example of both the interpolation of the potential and the gradient of the field in the direction z have been plotted.

4.4 Justification of the Method to Emulate the Trap Dynamics

As already explained in chapter 3, the pulse width modulation used to generate the current waveform in this experiment has already experimentally been shown to alter, not only the trap depth, but also the motion of the trap through the decelerator coils. This section examines the differences between the magnetic fields produced using the synthesised and idealised waveforms. Understanding the extent of these differences is important to fully characterise the decelerator. Furthermore, the fields must be studied in order to find a computationally efficient method to simulate the trajectories of the particles. Ideally, an interpolator capable of generating spatial and temporal interpolation data would be employed, however, this is simply not practical. The problem is that the time for the interpolator to run scales non-linearly with the number of points calculated, which makes the interpolation a computationally intensive task. This limits the ability to interpolate the field every time step. In order to simulate the experiment in a reasonable time it has been necessary to reduce the level of simulation. This section will conclude with a justification of any approximations made.

4.4.1 Variation of the Magnetic Field

The magnetic field generated by the synthesised waveform has already been shown to modify the trap velocity and cause fluctuations in the trap depth. Using the simulation techniques presented above it has been possible to further investigate the motion of the trap. For the purpose of this investigation, the quadrupole field will be removed. To begin, two constant frequency waveforms will be examined with different frequencies. These correspond to 100 $\mathrm{m\,s^{-1}}$ (2.47 kHz) and 300 $\mathrm{m\,s^{-1}}$ (7.34 kHz). The waveforms considered here have an amplitude of 500 A generated from a supply voltage of 650 V. The upper panels of figure 4.4 show the generated sine wave along with the reference waveform. The lower panels show the required PWM input to generate them. The left column of figure 4.4 displays the 300 $\mathrm{m\,s^{-1}}$ waveform, while the right column shows the 100 $\mathrm{m\,s^{-1}}$ waveform. The switching events occur on average every 6.4 µs (300 $\mathrm{m\,s^{-1}}$) and 3.8 µs (100 $\mathrm{m\,s^{-1}}$).

To investigate further the motion of the trap the location of the field minimum can be observed. To accomplish this, the 1D simulations of the trapping potential will be examined. This was achieved by using synthesised current waveforms, shown in figure 4.4, as an input in the field calculations. Figure 4.5 shows the motion of the trap through one coil. Where figure 4.5a) corresponds to the 300 $\mathrm{m\,s^{-1}}$

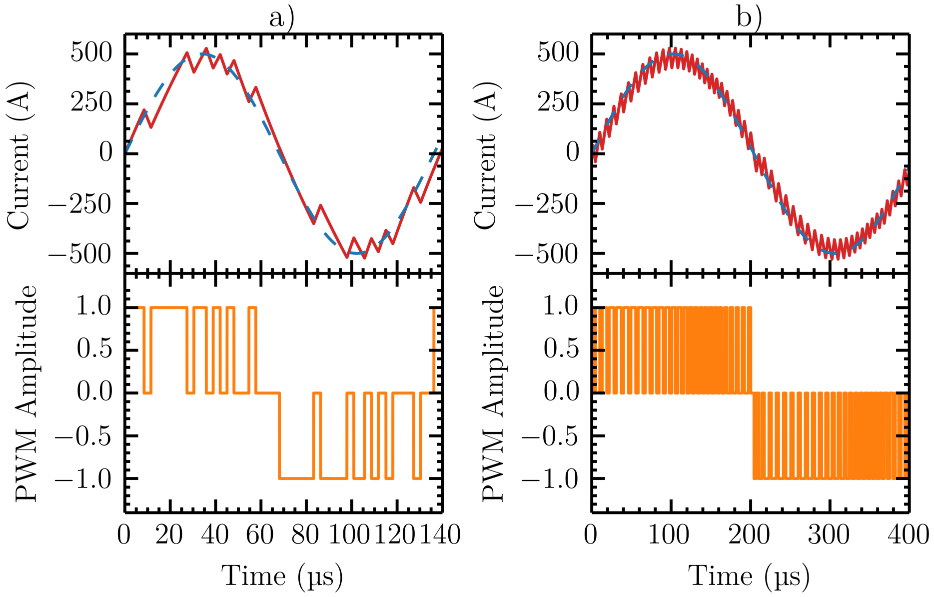

Figure 4.4: A single period of the waveforms required to generate a trap with a constant velocity of a) 300 m s^{-1} and b) 100 m s^{-1}. The upper panels show the expected current waveform (red) and the reference waveform (blue dashed). The lower panels shows the required voltage pulses to the coil in order to synthesise the sine wave.

waveform and figure 4.5b) corresponds to the 100 m s^{-1} waveform. The velocities obtained through fitting was 297.4 ± 0.2 m s^{-1} and 99.6 ± 0.4 m s^{-1} for the two waveforms. The lower panels of figure 4.5 show the difference in the fitted velocity of the trap and calculated field minima location. This result demonstrates that the field produced not only lags behind the pure current waveform but also oscillates rapidly. The magnitude of these oscillations in position decreases with target trap velocity while the frequency of these oscillations increases with target trap velocity.

These oscillations can be studied in much closer detail. The top row of figure 4.6 shows the location of the trap minimum as a function of time, but in this case for the pure and synthesised waveforms. Figures 4.6a) shows the simulation for 300 m s^{-1} whereas figure 4.6b) displays that of 100 m s^{-1}. Each graph consists of 75 time steps and examines the first quarter period of the coil (10.2 mm). The error bars plotted indicate half the grid size used to calculate the field. The graphs also show the fits of the position of the trap minimum for the synthesised current waveform. The lower panels of the graphs show the difference between the location of the trap minimum calculated from the simulations and using the fitted average velocity. These plots reiterate the two conclusions that were drawn previously: firstly, in general the trap generated by the synthesised waveform lags the pure waveform. This is simply because of the lower average trap velocity. Secondly, in order to accurately capture the trap oscillations the sample rate must be fairly high as figure 4.6 could not capture the true rate of the oscillations. The lower panels of figure 4.6 show that the trap oscillates back and forth as much as 1 mm and their occurrence is consistent with the switching events in the current waveforms used in the field calculations. The time averaged magnitude of the oscillations around the fitted trajectory (extracted from simulations across one coil) is 0.5 mm and 0.3 mm for the 300 m s^{-1} and 100 m s^{-1} waveforms. Interestingly, the pure current waveforms also causes trap oscillations, however, these occur on a scale smaller than a µm.

The variation of the longitudinal magnetic field depth shall now be investigated. This particular consequence of PWM has already been established, however, simulations of the field can further probe the effects that the current switching has on the trap depth. Figure 4.7 shows the variation of the depth of the front edge of the trap as a function of time. Once again, only the first quarter period of the simulation has been plotted to demonstrate the difference between the pure and synthesised

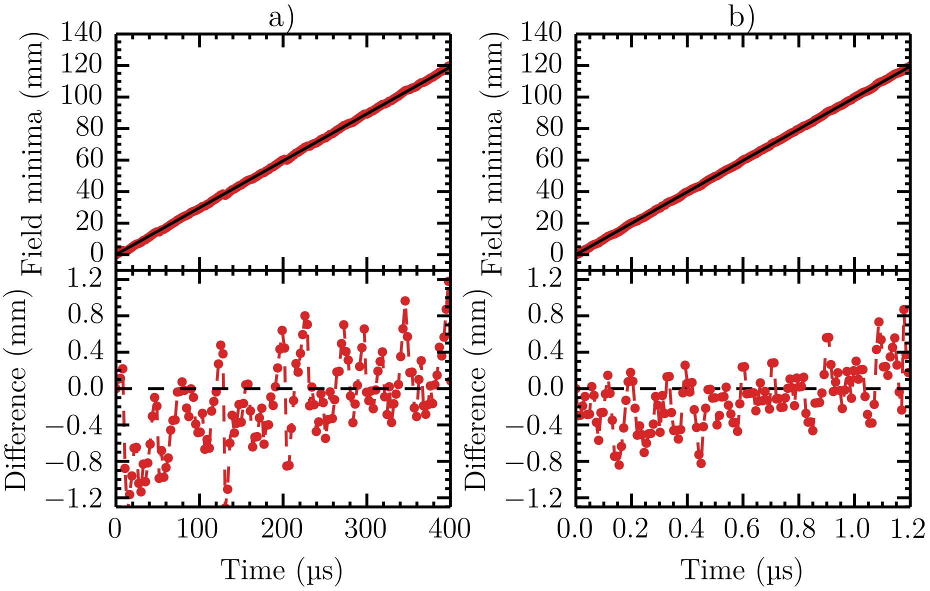

Figure 4.5: The motion of the trap minimum through one coil produced by a synthesised waveform. The upper panels show the location of the minimum of the trap in the longitudinal direction as a function of time. The motion of the trap is shown for a) a target trap velocity of 300 m s^{-1} and b) 100 m s^{-1}. The lower panels show the deviation of the trap minimum produced by the synthesised waveform from the fitted velocity.

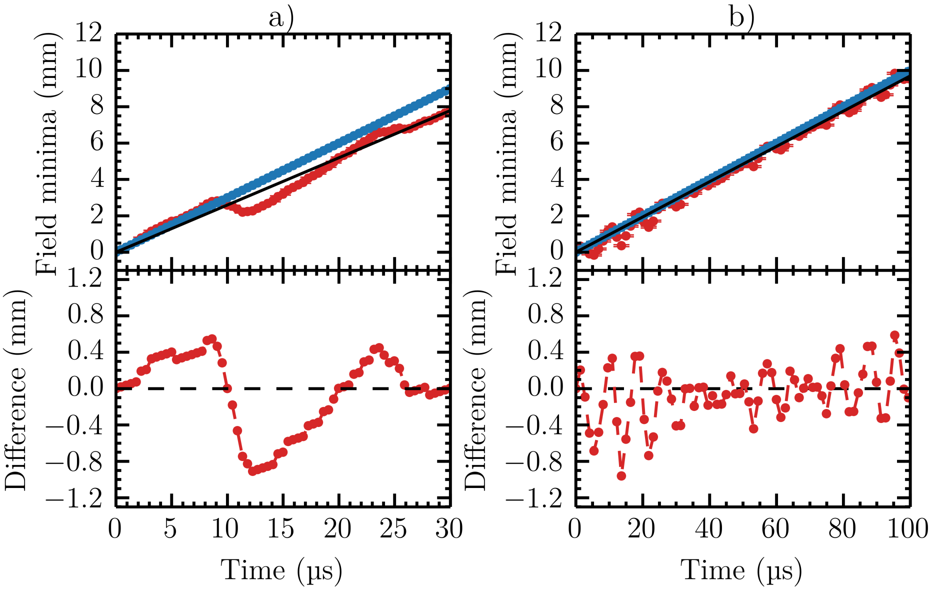

Figure 4.6: The motion of the trap minimum through one quarter period produced by a pure and synthesised waveform. The upper panels show the location of the minimum of the trap in the longitudinal direction as a function of time. The pure (blue) and synthesised (red) waveforms are plotted along with the fitted average velocity of the trap produced by the synthesised waveform (black). Panel a) shows the minimum location for 300 m s^{-1} while panel b) show that for the 100 m s^{-1} waveform. The lower panels show the deviation of the trap minimum produced by the synthesised waveform from the fitted velocity.

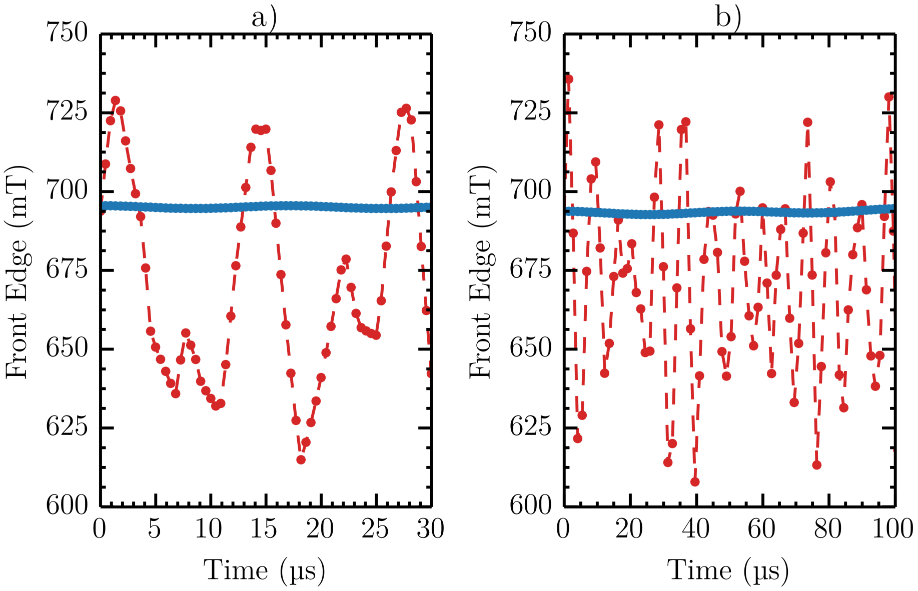

Figure 4.7: The variation of the magnetic field over time for a pure (blue) and synthesised (red) current waveform. The plots show the variation over a quarter period for a) the 300 $\mathrm{m\,s^{-1}}$ waveform and b) the 100 $\mathrm{m\,s^{-1}}$ waveform.

waveforms for the two frequencies investigated here. For both frequencies investigated (corresponding to a) 300 $\mathrm{m\,s^{-1}}$ and b) 100 $\mathrm{m\,s^{-1}}$), the pure waveform form results in little variation of the depth of the trap. Any variation that does occur is on the order of a fraction of a mT in both cases. The synthesised waveform introduced much larger variation and as a result, the average field depth of the synthesised waveform is roughly 20 mT lower than the pure waveform. The Root Mean Squared (RMS) variation of the field about the time averaged field is on the order of 30 mT for both frequencies studied here. Since the current is switched more rapidly in the 100 $\mathrm{m\,s^{-1}}$ waveform, the field variation occurs more rapidly. Interestingly, the trap depth of the front and back edges of the trap in the longitudinal direction waveforms vary independently. Although the front edge of the trap has been considered in this example, further investigation has shown that one side of the trap tends to be deeper than the other. Over the course of a period the average trap depth tends to the same value.

The trap depths of the 3D trap will also be examined. Unlike the previous simulations where only the field component in the z direction has been considered, the magnitude of the field will be considered here. As the 3D field calculations take more time to simulate, fewer time steps have been calculated. Figure 4.8 compares the variation of the magnetic field for the pure and synthesised waveforms. The plots show the variation of the field in the x and y directions at the longitudinal minimum for a) the 300 $\mathrm{m\,s^{-1}}$ waveform and b) the 100 $\mathrm{m\,s^{-1}}$ waveform. Again, the depth of the trap has been plotted over the course of one quarter of a period. As expected, the synthesised waveforms exhibit large fluctuations in the trap depth in each direction. More surprisingly, is the periodic change in the field in the transverse directions in the pure waveform. These are clearly visible in the y direction in both waveforms. These transverse oscillations have a uniform period and occur at a frequency of 58.8 kHz for the 300 $\mathrm{m\,s^{-1}}$ waveform and 19.6 kHz for the 100 $\mathrm{m\,s^{-1}}$ waveform. These frequencies are consistent in each direction with the total change in field of 0.5 mT in x and 25.0 mT in y for both velocities. The synthesised waveform, however, introduces larger fluctuations, on the order of 10 mT in x and 80 mT in y for both frequencies considered here. It is much the same story in z. The pure waveforms oscillates within a range of 11.4 mT whereas the synthesised waveform produces field depth changes on the order of 130 mT for both frequencies. Hence, the amplitude of the fluctuations for the synthesised waveform are on the order of approximately 5 % of the average field depth.

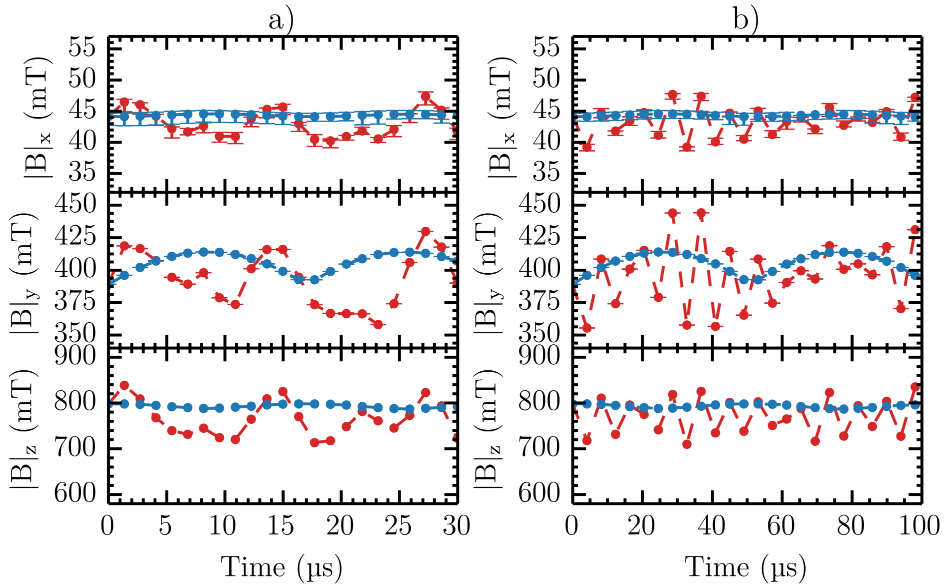

Figure 4.8: A comparison of the trap depths as a function of time for the pure (blue) and the synthesised (red) waveforms. The plots show the variation of the trap depths over a quarter of a period in the transverse directions at the longitudinal trap minimum for a) the 300 m s^{-1} waveform and b) the 100 m s^{-1} waveform.

4.4.2 Justification of the Trap Motion Emulation Method

It has been necessary to reduce the level of simulation complexity in order to maximise the speed of the simulations, it is therefore necessary to justify any approximations made. The interpolated potential cannot simply be scaled to include the effects of the PWM waveform because the potential is constructed from the four separate decelerator coil phases and the quadrupole field. Since the interpolation method is fairly computationally expensive a single trap is calculated and interpolated. Prior to the interpolation, the field is modified by a correction factor calculated from a 1D simulation of the field. These simulations can be completed fairly quickly with a fine enough time step to calculate a meaningful average. This correction factor modifies a 3D trap calculated to capture the lower field depth discussed previously. This is an approximation as the transverse and longitudinal fields evolve slight differently. For example, using the data presented in figure 4.8, the average discrepancy between the transverse and longitudinal fields is approximately 1.4 %, and 2.5 % in the x and y directions. Although this error is small, it is still a limiting factor in the method used to simulate the trap. As an aside, a more convenient method to calculate the correction factor would be to use the RMS current of the synthesised waveform, however, this does not provide such an accurate insight into the variation of the trap.

This average potential is acceptable as the oscillations of the potential occur at a much faster rate than the characteristic frequency of the particles in the trap [196]. This means the particles only respond to the relatively slow motion of the trap rather than the rapidly altering depth. Through extensive analysis, such as those presented above, the properties of the trap oscillate in a frequency range of 40 to 180 kHz depending on the number of switching events present in the current waveform. This range of frequencies has been derived through consideration of the rate of switching events and analysing the periodicity of the oscillations in position and trap depths. The characteristic frequency of the motion of the species investigated here does not exceed the order of a few kHz meaning that this approximation is valid. It is noted, however, that this technique becomes less reasonable for high target velocities where the number of switching events is small. To further capture the variation of the trap, the spatial oscillations of the trap have been included in the simulations. The oscillations are approximated to be sinusoidal and the frequency and magnitude of the oscillations are set from the frequency of the switching events and the 1D simulations respectively.

Once the modified potential centred around a trap minimum has been calculated the trajectory simulations can begin. The simulations are quasi-time dependent, meaning that the particles experience hard switching of the potential. The gas packet is allowed to freely expand until the temporal and spatial requirements of the quadrupole or the decelerator fields are met. Once in the region of the decelerator coils, the longitudinal spatial coordinates of the particles are transformed into the frame of the 3D trap at this particular time. The position of the trap at each time step is evolved using the equations of motion with the oscillating position superimposed. It was also necessary to construct the periodic nature of the decelerator field. This requires two traps to be interpolated because the quadrupole field adds with adjacent decelerator traps differently. When the particles enter the decelerator field, the code calculates which trap in the travelling wave the particle is in. It also calculates which type of trap the particle occupies. Furthermore, the code calculates when the decelerator coils are active prior to the start of the simulation. Thus, even if the particles are within the confines of a particular coil, they will not experience a force if that coil is not active at that particular time. Unless the current coil and the next coil in the sequence is active, the trap is terminated once the maxima of the trap reaches the edge of the coil. Again, the potential is instantaneously removed. Otherwise, the trap is allowed to cross the boundary between the two coils. Thus the simulation neglects any fringe fields and does not accurately capture the initial loading of the trap or the particle leaving the trap. Once the decelerator coils are deactivated, the gas packet is allowed to expand until it reaches the detector where the simulation is terminated.

4.5 Chapter Summary

The technique used to emulate the source within the Monte Carlo simulations of the decelerator was described. The method relies on geometric arguments in order to determine the transverse velocity of the gas packet from a longitudinal distribution. The simulation, therefore, requires only the peak velocity and the temperature of the gas packet as inputs to emulate the spread of velocities and spatial extent of the distribution. The particles are also broadened to introduce the slight temporal and spatial spread in order to emulate the excitation scheme. This is achieved by assigning a randomised starting time within the length of the excitation period and a starting longitudinal position within the excitation region. The technique used to calculate the fields generated by the decelerator and quadrupole coils were described. Since the wires that form the decelerator coils do not lie in parallel in the laboratory coordinate system, it is necessary to rotate the point into the coordinate system of the wire to perform the calculation. Once in the frame of the wires, the magnetic field can be calculated at an arbitrary point for a finite length wire. The field in the laboratory frame can be obtained through a second rotation. The quadrupole field can be calculated by approximating the poles as infinitely long wires. The tricubic interpolator used to calculate the field gradient at an arbitrary point was also described. The algorithm generates a 64×64 matrix describing the relationship between the derivatives of the potential and the coefficients of the tricubic interpolant at the corners of each grid element of the discrete potential calculated. The benefit of local interpolators, such as that described here, is that they do not require fitting to the entire data set.

The simulation method described above can then be used to evaluate the motion of the trap produced with the pulse width modulated current waveforms. As has been stated previously, the PWM results in the trap depth varying over time as well as a change in the velocity of the trap. Study of the field in 1D shows that the trap minimum oscillates around the trajectory of the average fitted velocity with an amplitude of approximately 1 mm. The occurrence of these oscillations are consistent with the switching events that produce the synthesised current waveform. Furthermore, the magnitude of these oscillations tends to be smaller for waveforms that contain more switching events. The pure waveforms considered here also show trap oscillations, however, these are on the order of μm. In each of the velocities presented here, the PWM resulted in a trap velocity lower than the target. For instance while trying to synthesise a trap with a velocity of 300 $\mathrm{m\,s^{-1}}$ the actual trap moves at an average velocity of 297.4 ± 0.2 $\mathrm{m\,s^{-1}}$. The trap depth in both one- and three-dimensions has been considered for the pure and synthesised waveforms. The synthesised waveforms introduce large fluctuations in the trap depth, on the order of 10 mT in x, 80 mT in y, and 130 mT in the z direction for both frequencies considered here. The amplitude of the fluctuations for the synthesised waveform in the z direction are on the order of approximately 5 % of the average field depth. Interestingly, the pure waveform also exhibits periodic oscillations in the trap, with uniform frequency of 58.8 kHz for the 300 $\mathrm{m\,s^{-1}}$ waveform and 19.6 kHz for the 100 $\mathrm{m\,s^{-1}}$ waveform. The difference in trap depth for the pure current waveform was approximately 0.5 mT in x, 25.0 mT in y, and 11.4 mT in z for both velocities studied.

The purpose of the final section of this chapter has been to justify the method used to emulate the trap dynamics as a consequence of employing the synthesised waveform created by the power electronics. The interpolated potential cannot simply be scaled to include the effects of the PWM waveform because the potential is constructed from the four separate decelerator coil phases and the quadrupole. The characteristic frequency of the trap does not exceed the order of a few kHz which is true for all the atoms and molecules studied in this thesis. The properties of the trap vary within a frequency range of 40 to 180 kHz depending on the number of switching events present in the current waveform. This range has been derived through consideration of the rate of switching events and analysing the periodicity of the oscillations in position and trap depths. This difference in frequencies is large enough that the particles do not respond fast enough to react to the rapidly changing field but instead feel the average potential. To create this potential, a single static 3D trap must be scaled by a correction factor which lowers the field depth from the ideal value. This correction factor is calculated from time-dependent 1D simulations which can calculated quickly while maintaining a high sample rate to accurately capture the changes in the field. Although the potential along the z axis contains many of the features of the transverse fields, the drawback is that the magnitudes of these features tend to differ. After scaling, the average difference is approximately 1.4 % in x, and 2.5 % in y. The oscillations of the trap around its average trajectory is added in the Monte Carlo simulations. This is approximated by modifying the trajectory of the trap with a sinusoidal oscillation in position. The magnitude is set through the 1D simulations while the frequency is set by the occurrence of the current switching events. The method to generate the average potential is as follows: firstly, the synthesised waveform is used as an input for a time dependent 1D field simulation with enough samples to generate the time averaged data required. This creates a correction factor that is then used to modify the 3D field generated at time zero using a pure waveform. The quadrupole field can be combined with the new decelerator field and the potential interpolated. This section concluded with an overview of the Monte Carlo simulation process which described the formation of the travelling magnetic wave from just two traps. The traps follow the fitted trajectory calculated in the 1D simulations with a sinusoidal variation in position superimposed. During the trajectory simulations, the code calculates which coil a particle is located in and whether that coil is active at that time. If the latter is true, the potential around the nearest trap minimum is used to apply a force to this particle. The limitations of this method, such as the fringe fields being ignored, were also discussed.

Chapter 5

Characterising the Decelerator with Metastable Argon

The aim of this chapter is to evaluate the operation of the decelerator and present the experimental results taken thus far. A convenient species to achieve this is metastable argon. The supersonic expansion of argon results in the production of a relatively cold, slow beam which can be readily excited into the metastable state by the DBD. Furthermore, due to the high internal energy of the metastable states, the gas packet can be detected using a MCP without the need for an additional excitation scheme. Finally, metastable argon in the $m_J = 2$ state has a reasonable magnetic moment to mass ratio of 0.0751 $\mu_B\,u^{-1}$, where u is the atomic mass unit. These properties make metastable argon an ideal candidate to test the decelerator. Section 5.1 explores the concept of phase space stability of the decelerator. The focus of this section will be to examine the effects of the synthesised waveform on the acceptance. Additionally, this section aims to highlight some of the limiting factors associated with the current design of the decelerator. Section 5.2 presents the experimental results of the four module long decelerator. The results are compared to the simulated results. This section will report the results of 2D and 3D guiding, and deceleration.

5.1 Phase Space Stability of the Decelerator

An important factor in the operation of the decelerator is the effect of the synthesised waveform on the phase space acceptance. In the following discussion, the acceptance of the decelerator will be simulated using metastable argon in the $m_J = 2$ state. To begin, the acceptance of the decelerator will be examined while 3D guiding. This eliminates any losses due to the deceleration process and will allow the examination of loss channels from the trap. In the following examples the particles are classified as lost if they reach either the internal wall of the tube or they cross over either of the maxima of the trap. The acceptance of the decelerator in the velocity bunching mode is shown in figure 5.1a) as a function of trap velocity. The acceptance is plotted for a pure and synthesised waveform for two lengths of decelerator. Here a comparison is made between a four (0.49 m) and a nine (1.10 m) module long decelerator. The acceptance was calculated from an initially uniform distribution (5.3 mm × 5.3 mm × 22 mm × 30 $\mathrm{m\,s^{-1}}$ × 45 $\mathrm{m\,s^{-1}}$ × 60 $\mathrm{m\,s^{-1}}$) consisting of 500,000 particles. In the examples shown, the decelerator was operating at 500 A peak while the quadrupole was running at 700 A. Ideally, the acceptance of the decelerator in the velocity bunching mode should be roughly constant. In reality, the particles with lower mean velocity have more time to explore phase space which allows the particles to find loss channels. This can be seen in the lower plot of figure 5.1 which shows the final distribution of particles in the longitudinal direction after 3D guiding across a nine module long decelerator. The phase space distributions are b) 50 $\mathrm{m\,s^{-1}}$, c) 250 $\mathrm{m\,s^{-1}}$, and d) 450 $\mathrm{m\,s^{-1}}$, where the upper row corresponds to a pure current waveform while the lower plots are that of the synthesised waveform. The 1D separatrix, which shows the boundary between stable and unstable regions of phase space, is only partially filled and in general the high velocity regions are empty. Additionally, for low mean velocities, it is clear that the particle distribution is unstable in the outer spatial regions of the trap. In these regions the transverse component of the trapping potential, particularly in the x direction, is non-existent or slightly defocusing. Consequently, the acceptance of the decelerator decreases as the guiding velocity is decreased simply because the particles spend more time in these unstable regions leading to loss. The same conclusion can be drawn for both the pure and synthesised waveforms regardless of decelerator length. In the case of the four module long decelerator, the acceptance of the trap is far greater than that of the nine module long decelerator particularly at high velocities. This difference arises because the particles do not have adequate time to fully explore the phase space and find the loss channels of the trap. This can be seen in the final phase space distribution particularly for high trap velocities as particles are found in the phase space regions outside the 1D separatrix. In general, the overall trend in acceptance, as shown in figure 5.1a), is similar for both types of waveform. The difference between the two waveform types is apparent at high velocities where the synthesised waveform consists of only a few current pulses. At low velocities, however, the acceptance of the synthesised waveform is slightly greater than that of the pure current waveform. This is a result of the PWM technique employed to synthesise the current waveform which means that the quality of the waveform depends on the electrical properties of the coil and the target trap velocity. This trend can be explained by the rapid oscillations in the position of the trap. These provide additional transverse confinement in the outer spatial region of the trap due to an averaging effect. At these high velocities the trap oscillations are slower, thus particles experience less net focusing. These conclusions are consistent for both the four and nine module long decelerator.

To explore the phase stability further, the potential produced in the xz and yz planes will be considered for a static trap. Figure 5.2 shows the 3D potential of a single well of the decelerator generated by a 500 A peak current pulse. The figure shows the fields with (in the upper row) and without (in the lower row) the quadrupole field, generated with a current of 700 A, present. As has been stated previously, the transverse field produced by the decelerator coils in the y direction is fairly strong even without the quadrupole. The confinement is, however, much weaker in the x direction. In general, the potential is strongly confining towards the centre of the trap but the transverse confinement is weaker towards the trap maxima. The projected contours of the field in the x direction shown in figure 5.2b) show the variation of the confinement of the field at constant values of z and x. Those in the x direction vary from weakly confining at the longitudinal minimum to defocussing towards the trap maxima. The addition of the quadrupole field, shown in figure 5.2d), enhances the transverse confinement in the x direction particularly close to the longitudinal minimum. Even at 700 A, the point at which the trap becomes defocusing is significantly closer to the edge of the trap. The major disadvantage of this form of decelerator is that, even with the quadrupole, the potential remains weakly defocusing at the edges of the trap in the x direction. Furthermore, apart from near the trap centre, the quadrupole has little effect to the transverse confinement in the y direction. These fields explain the phase space plots shown in figure 5.1. The 1D separatrix is not filled because the particles that spend time in the outer regions of the trap experience weaker transverse confinement and, given enough time, will ultimately be lost due to coupling of the transverse and longitudinal motions.

The acceptance of the decelerator while operating in the deceleration mode will now be discussed. The acceptance was calculated from an initially uniform distribution (5.3 mm × 5.3 mm × 22 mm × 20 $\mathrm{m\,s^{-1}}$ × 40 $\mathrm{m\,s^{-1}}$ × 60 $\mathrm{m\,s^{-1}}$) consisting of 1,000,000 particles. In this example, the decelerator was operating at 1000 A peak while the quadrupole field was generated by a current of 700 A. In order to explore the variation of the acceptance of the deceleration at low final velocities the

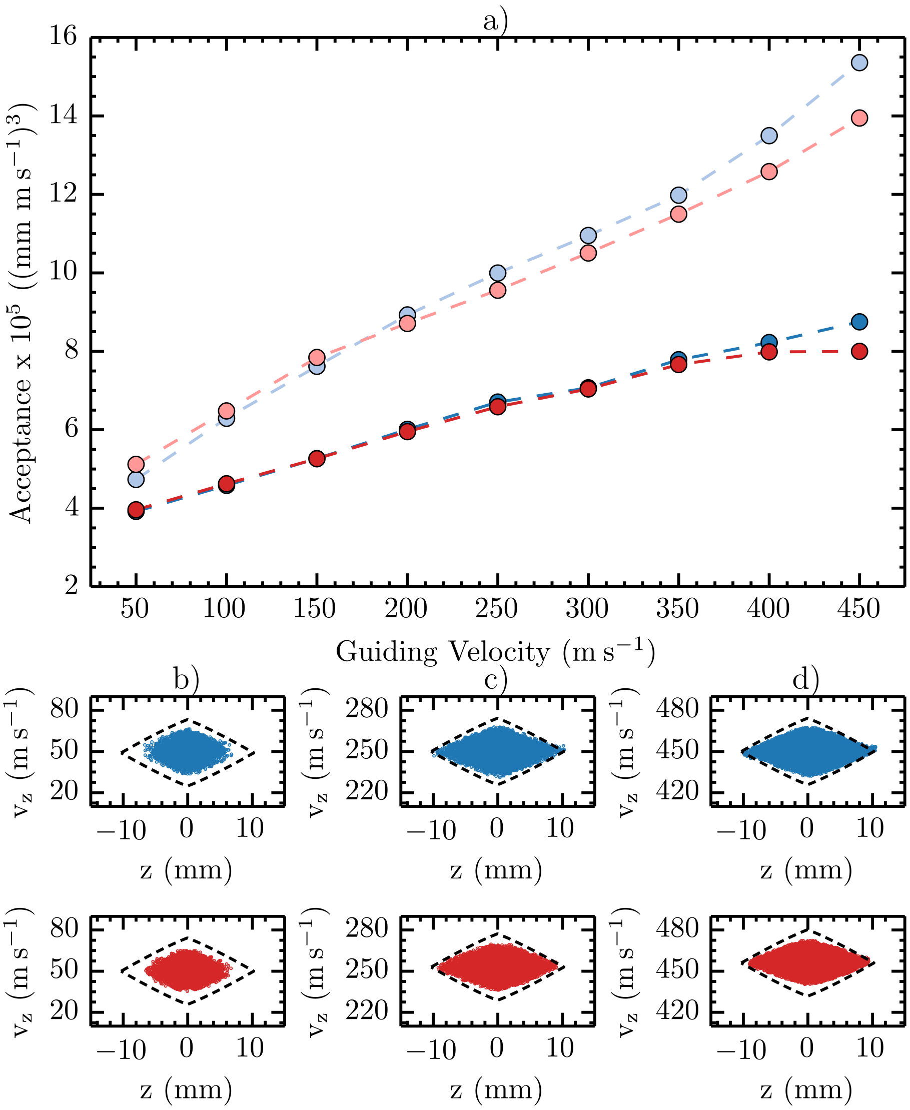

Figure 5.1: The acceptance of the decelerator as a function of velocity in the 3D guiding mode. Panel a) shows the acceptance of the decelerator for a pure and a synthesised current waveform. These are plotted for a four module long decelerator (pure waveform - light blue and synthesised waveform - light red) and a nine module long decelerator (pure waveform - blue and synthesised waveform - red). The lower panels show the longitudinal acceptance of the nine module long decelerator. The upper row (blue) shows the acceptance for the pure current waveform whereas the lower row (red) is that of the synthesised waveform. The columns of these plots are different trap velocities which correspond to b) 50 m s^{-1}, c) 250 m s^{-1}, and d) 450 m s^{-1}. In each case the 1D separatrix of the decelerator has been plotted (black dashed).

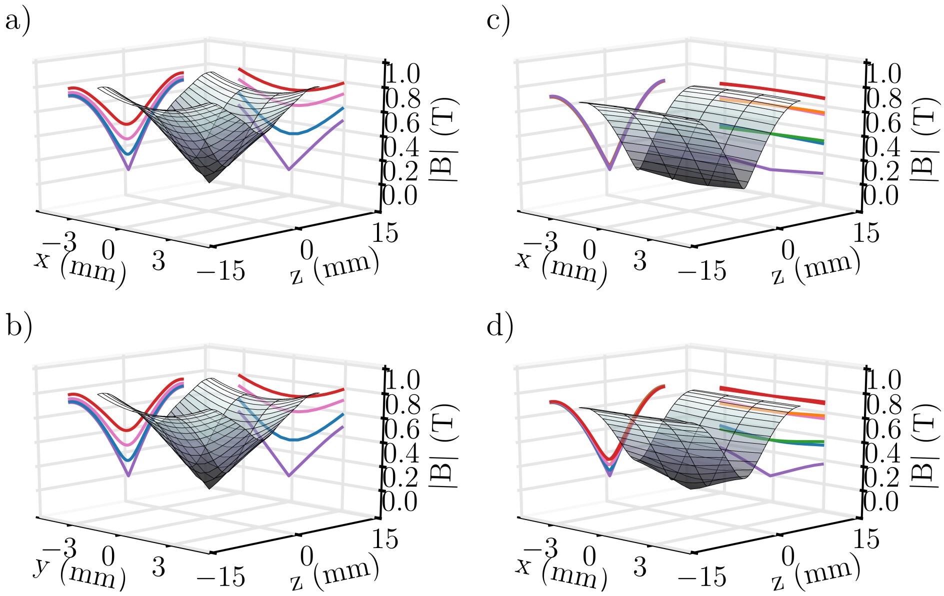

Figure 5.2: The 3D surface plots in the xz and yz planes showing a single trap of the decelerator field generated with a 500 A peak current waveform plotted and without the quadrupole field, generated at 700 A. Panels a) and c) show the xz and yz planes respectively of just the decelerator field while panels b) and d) show the xz and yz planes respectively of the combination of the decelerator and quadrupole fields. In each case the projected contours of the field in each direction have been plotted.

deceleration was simulated over a nine module long decelerator. Figure 5.3a) shows the acceptance of the decelerator as a function of final velocity for both the pure and synthesised current waveforms. In this example the mean longitudinal velocity of the gas packet was 350 $\mathrm{m\,s^{-1}}$. The initial trap velocity was set to 350 $\mathrm{m\,s^{-1}}$, thus the magnitude of the deceleration investigated here ranges from 0 to 5.56×10^4 $\mathrm{m\,s^{-2}}$. Unlike the 3D guiding mode, the acceptance with deceleration applied differs greatly for the pure and synthesised waveforms. The PWM causes the acceptance of the trap to fall rapidly compared to the pure current waveform. Moreover, for deceleration to 50 or 0 $\mathrm{m\,s^{-1}}$, the acceptance of the synthesised waveform is so small the points have been omitted. There are several factors that influence this trend. Firstly, the acceptance of the decelerator using the synthesised waveform is limited by the initial current that can be drawn by the coils. Despite the target of 1000 A peak being set in the PWM code, this can only be drawn by the last few coil modules. This combined with the lower trap depths inherent with the PWM technique results in the average trap depth being lower than the pure current waveform variant. This is possibly the most significant factor. Secondly, the difference in the final and initial velocities of the trap further contribute to the lower acceptance. As stated previously, there is no fine control over the velocity of the trap using PWM. In general, the magnitude of the deceleration for the synthesised waveforms tends to be greater than that of the pure waveform. This, coupled with the lower fields, results in the loss of more particles in the simulation. Finally, oscillations in the trap position proved to be the least significant factor in the difference in the acceptance. The acceptance of the ideal 1D decelerator is plotted in the inset of figure 5.3a). The difference in the acceptance between the 1D and 3D cases once again emphasises the need to improve the transverse confinement of the decelerator. The 1D acceptance of the decelerator decreases by less than an order of magnitude over the range of decelerations investigated here. In the 3D case the acceptance decreases by nearly four orders of magnitude. The lower panels of figure 5.3 shows the final longitudinal phase space distribution of particles for several final velocities examined here. The phase space distributions correspond to final velocities of b) 150 $\mathrm{m\,s^{-1}}$, c) 250 $\mathrm{m\,s^{-1}}$, and d) 350 $\mathrm{m\,s^{-1}}$, where the upper row corresponds to a pure current waveform while the lower plots are that of the synthesised waveform. In each case, the 1D separatrix of the decelerator with an ideal current waveform has been plotted. Like in the 3D guiding, the 1D separatrix is not completely filled.

Once again this is due to the lack of transverse confinement, particularly in the x direction, near the longitudinal maxima of the trap. During deceleration, the particles have more time to explore phase space than during 3D guiding, allowing the particles to find the stable 3D region of phase space. These affects are far more obvious during deceleration as the particles spend more time in the outer regions of the trap. As will be examined below, the application of the quadrupole field to a trap generated by 1000 A peak makes very little change to the transverse field near the edges of the trap. This results in transverse loss being a significant factor in the reduction of the acceptance of the decelerator.

The topology of the trapping potential produced in the xz and yz planes will be considered for a static trap to study the phase stability during the deceleration process. Figure 5.4 shows the 3D potential of a single well of the decelerator generated by a 1000 A peak current pulse. As before, the figures show the fields without (in the upper row) and with (in the lower row) the quadrupole field present. Again, the quadrupole field was generated with a current of 700 A. The magnetic field generated by the decelerator coils at 1000 A peak exhibits similar characteristics as that generated by the 500 A peak current waveform described previously. When the quadrupole field is included, however, the effects are far less noticeable. The projected contours of the field in the x direction in figure 5.4d) show that the field is only confining very close to the longitudinal minimum. The fields remain largely defocusing even with the quadrupole. This is somewhat problematic for large values of deceleration as the synchronous particle moves closer to the trap edge. As is reflected in the lower panels of figure 5.3 this causes the stable region of phase space to reduce thereby limiting the acceptance of the decelerator. This suggests that for larger regions of stability, it maybe worth running the decelerator at lower currents such that the quadrupole can contribute transverse confinement at the edges of the trap. This would require a much longer decelerator in order to maintain the same front edge trap depth and would come at the expense of the range of longitudinal velocities accepted into the trap.

One final aspect to investigate is the dependence of the acceptance of the decelerator on the initial trap velocity. To study this the acceptance was calculated from an initially uniform distribution (5.3 mm × 5.3 mm × 22 mm × 20 $\mathrm{m\,s^{-1}}$ × 40 $\mathrm{m\,s^{-1}}$ × 60 $\mathrm{m\,s^{-1}}$) consisting of 1,000,000 particles. Once again, the nine module long decelerator was operating at 1000 A peak while the quadrupole field was generated by a current of 700 A. Figure 5.5 shows the acceptance of a pure current waveform decelerator as a function of final trap velocity for a series of initial trap velocities. This figure shows that the decelerator has a strong dependence on the initial trap velocity and in fact benefits from a slow initial gas packet. Two distinct trends can be seen in the acceptance of the decelerator. For the initial velocities in the range of 350 to 450 $\mathrm{m\,s^{-1}}$ the acceptance is greatly limited by the lack of transverse confinement as described previously. In this regime, the maximum deceleration seems to be approximately 5×10^4 $\mathrm{m\,s^{-2}}$ before the trap becomes significantly lossy. Below an initial trap velocity of 350 $\mathrm{m\,s^{-1}}$, the trend in the acceptance behaves more like the 1D case. This indicates that the longitudinal and transverse motion of the particles in the trap remain uncoupled. The interaction time with the field also has an effect on the acceptance, the concept of which has already been explained earlier in this section. The consequence of this is that similar values of deceleration result in different relative changes in acceptance. For instance, 350 to 250 $\mathrm{m\,s^{-1}}$ has the same magnitude of deceleration as 250 to 50 $\mathrm{m\,s^{-1}}$, however, the acceptance of the latter is slightly less due to the longer interaction time with the field. Similarly, the relatively short interaction time of the deceleration of the 450 $\mathrm{m\,s^{-1}}$ beam results in much higher acceptance of the trap compared to similar decelerations with lower initial velocities.

The relationship between the acceptance of the decelerator and the transverse confinement of the quadrupole can be explored further. The geometry of the quadrupole will be kept the same in each case, however, the current will be varied from 0 to 5000 A for a decelerator operating at 500 and 1000 A peak. Again, to avoid the losses introduced through deceleration the device was simulated in the 3D guiding mode with the wave travelling at 50 $\mathrm{m\,s^{-1}}$ across nine decelerator modules. In this example only the effect on the pure waveform is investigated. The acceptance of the decelerator

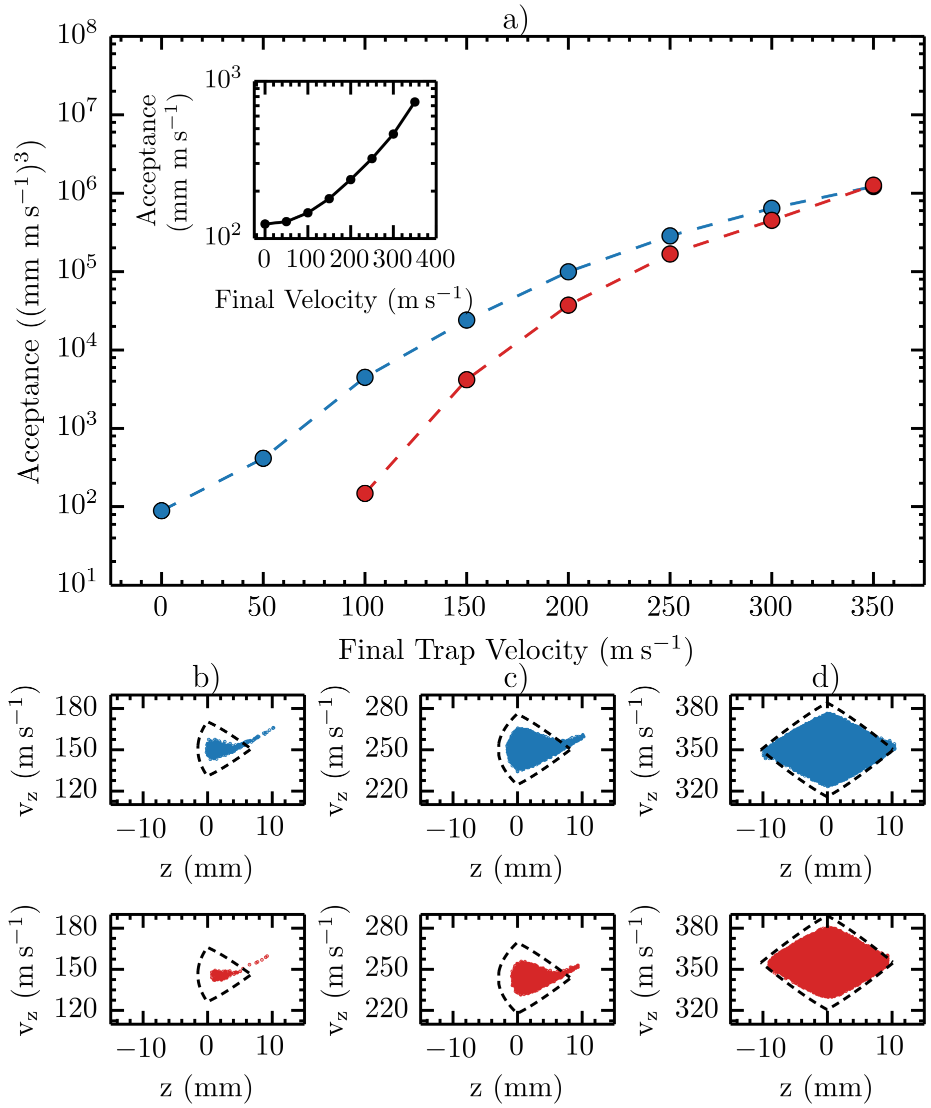

Figure 5.3: The acceptance of the decelerator as a function of final trap velocity in the deceleration mode. Panel a) shows the acceptance of a nine module long decelerator operating at 1000 A peak for the pure current waveform (blue) and synthesised current waveform (red). The mean longitudinal velocity of the gas packet was 350 m s^{-1}. Initially, the trap velocity was set to 350 m s^{-1}, thus the magnitude of the deceleration ranges from 0 to 5.56×10^4 m s^{-2}. The inset of panel a) shows the ideal 1D acceptance of the decelerator. The lower panels show the longitudinal acceptance of the decelerator. The upper row (blue) shows the acceptance for the pure current waveform whereas the lower row (red) is that of the synthesised waveform. The columns of these plots are different trap velocities which correspond to b) 150 m s^{-1}, c) 250 m s^{-1}, and d) 350 m s^{-1}. In each case the 1D separatrix of the decelerator has been plotted (black dashed).

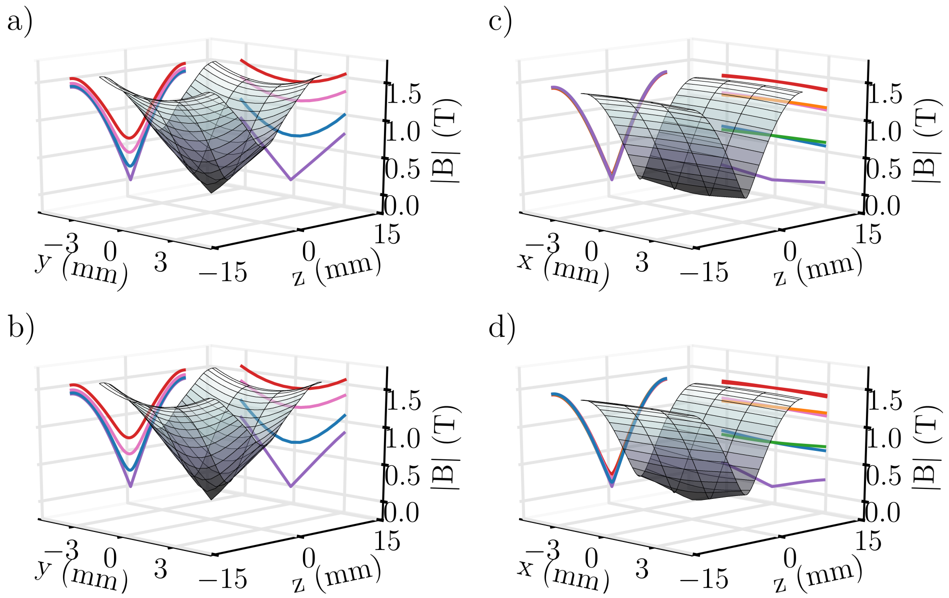

Figure 5.4: The 3D surface plots in the xz and yz planes showing a single trap of the decelerator field generated with a 1000 A peak current waveform plotted and without the quadrupole field, generated at 700 A. Panels a) and c) show the xz and yz planes respectively of just the decelerator field while panels b) and d) show the xz and yz planes respectively of the combination of the decelerator and quadrupole fields. In each case the projected contours of the field in each direction has been plotted.

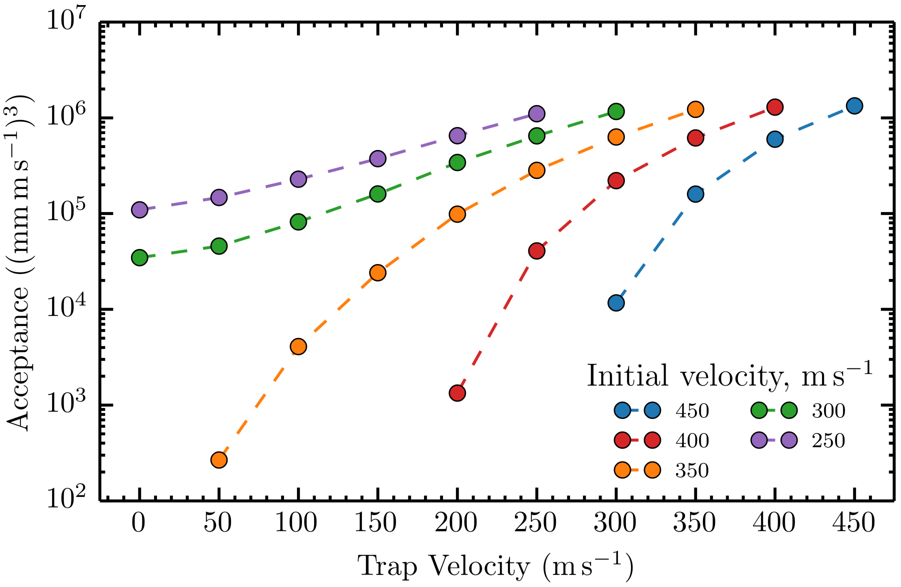

Figure 5.5: The acceptance of the decelerator operating at 1000 A peak with a quadrupole field generated with 700 A as a function of the final trap velocity for a series of initial trap velocities. Here an ideal nine module long decelerator has been used to highlight the dependence of the acceptance of the decelerator on the initial trap velocity. The packets of argon have an initial velocity in the range of 250 to 450 m s^{-1} and the 3D guiding data has been plotted in each case.

is shown as a function of quadrupole current in figure 5.6a). The initial phase space volume of the distributions were 9.27×10^7 (mm m s^{-1})^3 and 2.73×10^8 (mm m s^{-1})^3 for the 500 A and 1000 A peak waveforms respectively. This figure demonstrates the importance of the transverse confinement introduced by the quadrupole. In the case with no quadrupole, the acceptance of the trap is lowered dramatically even when compared to the next lowest value of quadrupole current. The plot shows that, at least over the range of quadrupole currents investigated, a peak acceptance has not been reached. In general, the acceptance of the trap increases with transverse current. The gain in acceptance is greater for the decelerator operating at 500 A peak as the field components from the decelerator and quadrupole coils are comparable in magnitude even for low quadrupole currents. The inset in figure 5.6a) shows the fraction of the total losses that occur in the trap in each direction for the decelerator operating at 500 A peak. In general, the majority of losses occur in the x direction. As the current through the quadrupole is increased, however, the fraction of losses that occur in the x direction decreases while those in the z direction increase. The losses in the y direction remain roughly constant despite additional transverse focusing. The phase space plots in figures 5.6 show the final particle distribution for quadrupole currents of b) 0 A, c) 1500 A, and d) 5000 A. The upper row of which shows the final distribution of particles as a result of the decelerator operating at 500 A peak while the lower row shows the final distribution of particles with the decelerator operating at 1000 A peak. The 1D separatrix (shown as the dashed line) shows the predicted region of stability. As in the example above, the central regions are uniformly filled once the quadrupole field is applied. In the case where the quadrupole field is zero, the particles occupy the region of the field near to the minima where the transverse fields are focusing. As the quadrupole current is increased, the particles begin to fill more of the 1D separatrix, however, the high velocity regions remain empty for all quadrupole currents investigated.

5.2 Experimental Results

So far the performance of the decelerator has been theoretically examined. The experimental results obtained from the decelerator will now be presented. This section will be split into the three modes of operation of the decelerator: 2D guiding, 3D guiding, and deceleration. To begin, the profile of the metastable argon gas packet, in the absence of any external fields, will be discussed. In order to extract information such as the mean velocity and longitudinal temperature of the gas packet, it is necessary to construct a suitable fitting equation to describe the time-of-flight (TOF) profile measured by the detector. The starting point of such an equation is the flux from a supersonic source, altered to include a time component. The flux of particles from a supersonic source within the speed interval v to $v + dv$ is $f(v)dv = Av^3\mathrm{exp}\left[-M\left(v - v_\mathrm{o}^2\right)/2k_\mathrm{B}T\right]dv$ [177]. Where the gas packet is assumed to have a peak velocity of v_o. This equation can be rewritten in terms of time for a source to detector separation, L, while assuming no acceleration. The length of the decelerator from the valve nozzle to the MCP was inferred to be 92.4 ± 0.2 cm. To include the effects of the finite valve time the valve is open for, as well as the effects that the DBD has on the gas packet, additional temporal and spatial terms, t_e and z_e respectively, are used to modify the distribution of arrival times. It is assumed that these additional terms are negligible. The signal at the detector is

$$f(t, t_\mathrm{e}, z_\mathrm{e}) = A\frac{L^4}{t^5}\mathrm{exp}\left[-4\mathrm{ln}2\frac{\left(t - t_\mathrm{o} - t_\mathrm{e} + \frac{z_\mathrm{e}}{v_\mathrm{o}}\right)^2}{w\left(t\right)^2}\right]. \tag{5.1}$$

Where $v_\mathrm{o} = L/t_\mathrm{o}$ and the temporal width (FWHM) is $w\left(t\right) = \sqrt{8\mathrm{ln}2\, k_\mathrm{B}T/mL^2}$ [197]. The height, A, the peak arrival time, t_o and temperature, T can therefore be used as fitting parameters. This allows the central velocity and the spread of velocities to be determined and fed directly into the simulations.

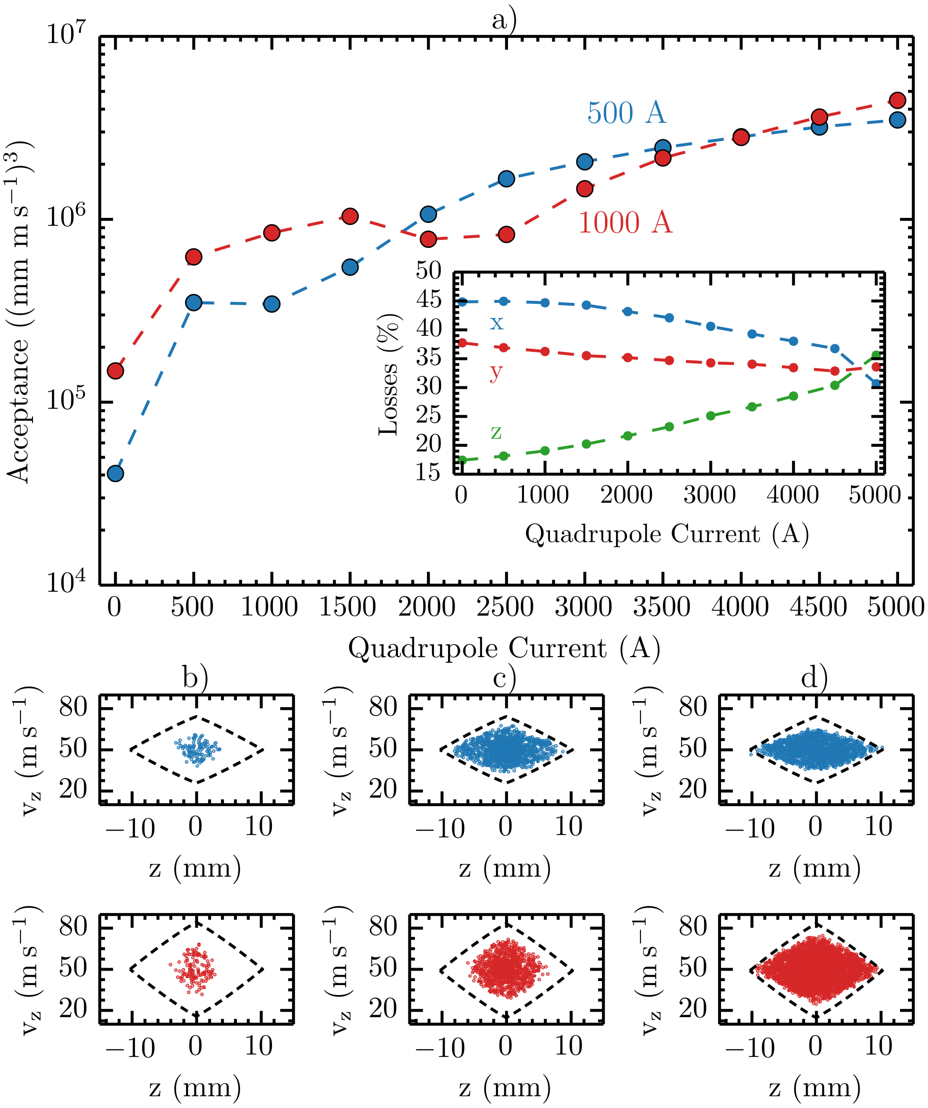

Figure 5.6: The acceptance of a nine module long decelerator as a function of quadrupole current for a set of decelerator coils operating at 500 A peak (blue) and 1000 A peak (red). Panel a) shows the variation of the decelerator as a function of quadrupole current while the decelerator is in the 3D guiding mode with the trap velocity of 50 m s^{-1}. The mean longitudinal velocity of the particle distribution was also 50 m s^{-1}. The inset of panel a) shows the fraction of the total losses that occur in the trap in each direction for the decelerator operating at 500 A peak. The lower panels show the longitudinal acceptance of the decelerator. The upper row (blue) shows the acceptance for the 500 A peak current waveform whereas the lower row (red) is that of the 1000 A peak waveform. The columns of these plots are different quadrupole currents of b) 0 A, c) 1500 A, and d) 5000 A. In each case the 1D separatrix of the decelerator has been plotted (black dashed).

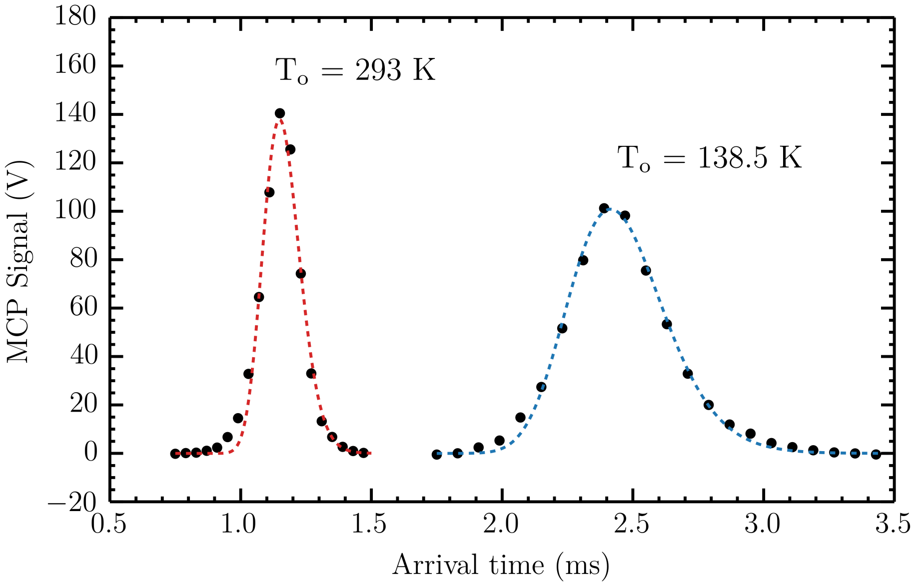

Figure 5.7: Time of flight measurements and fits of the metastable argon expansions with the valve held at two temperatures. In both cases the observed results (black dots) have been plotted at discrete intervals although the actual fitting was performed on the continuous data. The fitted time of flight curves have been plotted (red 293 K and blue 138.5 K).

Figure 5.7 shows fits to metastable argon TOF profiles collected from the MCP while the valve is maintained at 293 K and 138.5 K. In general, the profile of the fitting equation agrees fairly well with the data and captures the essential components of the gas packet. The fitted peak velocity of the gas packets were 813 ± 4 and 377 ± 2 $\mathrm{m\,s^{-1}}$ with longitudinal beam temperature of 13.0 K and 4.3 K for the room temperature and liquid nitrogen cooled valve respectively. It should be noted that although the observed results have been plotted at discrete intervals, the fitting procedure was performed on the continuous data. A final point to mention is the validity of the fitted parameters. Since the MCP has a fixed location, the parameters extracted from the fits gives an upper limit. Given the length of the decelerator these limits are, in all likelihood, fairly close to the true values. In the following discussion the valve temperature, measured at the cooling jacket, was measured to be 138.5 K.

5.2.1 Quadrupole Guiding

The first aspect of the decelerator to investigate is guiding the gas packet without the presence of the decelerator coils. Naively, one would expect that applying any transverse confinement would result in an increase in the integrated TOF profile. This is caused by the quadrupole field focusing back the low field seeking fraction of the gas packet within a velocity range back towards the molecular beam axis which otherwise would have been lost. This is at the expense in the number of high-field-seeking states that remain in the final distribution. In the prototyping phase of the decelerator, while using a General Valve, the more divergent source meant that the quadrupole made a marked increase to the integrated signal. While using the Even-Lavie valve, however, very little change in signal is observed even with the quadrupole operating at the full 700 A. This is likely because of the highly directional nature of the valve coupled with the geometry of the source. In addition, the large fringe field region of the quadrupole reduces the amount of time that the particles can interact with the quadrupole field. To confirm these assumptions, the TOF profiles observed experimentally can be compared to those created in particle trajectory simulations.

Figures 5.8a) and 5.8b) shows the experimental and simulated results of 2D guiding with the

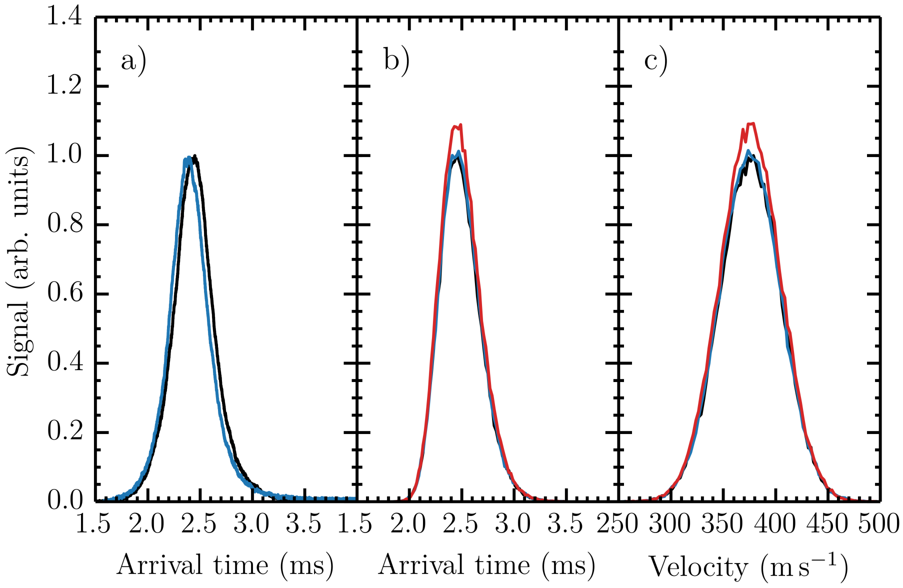

Figure 5.8: A comparison of the experimental and simulated time of flight profiles of metastable argon. Panels a) and b) show the experimental and simulated TOF profiles respectively. Both include the zero field TOF profile (black dashed) and the resultant TOF profile with the quadrupole field generated by 700 A applied (blue). The simulated data also shows the TOF profiles for an ideal quadrupole, which can be switched instantaneously and produces no fringe fields. Panel c) shows the longitudinal velocity distributions of each of the simulated regimes at the location of the MCP.

quadrupole operating at 700 A respectively. Fitting the expression shown in equation 5.1 to the zero field TOF profile gives a peak velocity of 371 ± 1 m s^{-1} and a temperature of 4.17 ± 0.02 K. To accurately capture the current flow through the quadrupole in the simulations, the measured current was fed into the trajectory simulations. The current was then interpolated and used to scale the magnetic field at each time step. Both the experimental and simulated TOF profiles exhibit little change in the integrated signal or longitudinal temperature of the beam with the application of the quadrupole field. Although the simulated data captures much of the experimental parameters, it does not replicate the 44 μs shift in the peak arrival time of the beam. It is unlikely that the fringe fields of the quadrupole simulated in chapter 3 are responsible for this. The shift in peak arrival time for the calculated fringe fields is on the order of a μs as such there must be other contributing factors to this large change in peak arrival time. Figure 5.8 also includes the simulated TOF profile in the case of an ideal quadrupole. In this case the quadrupole current is assumed to have instantaneous switching times and no fringe field regions. The increased interaction time of the gas packet with the quadrupole field results in a 1.2 times increase in the integrated signal. It is also worth commenting on the slight discrepancy of the simulated and experimental TOF profiles in the absence of any external fields. The simulation does not accurately capture the rising edge of the distribution; in the experiment this part of the distribution extends further back in time. Like in the expression used for fitting, this is likely a result of several factors such as the finite response time of the solenoid and the non-uniform nature of the excitation process, both of which alter the expansion characteristics of the gas. Figure 5.8c) shows the velocity distribution of the gas packet when it reaches the MCP. The simulated quadrupole produces zero magnetic field component in the z direction. As a result there is no acceleration experienced in the longitudinal direction and the overall shape of the velocity distribution remains unchanged when compared to the zero field example. Like the TOF profile, there is little difference between the zero field and the 700 A velocity distributions. In the case of an ideal quadrupole, the majority of the gain in signal can be attributed to the subset of velocities that are in the region of the peak velocity of the distribution.

The simulated data can be used to examine the phase space distribution of the metastable argon

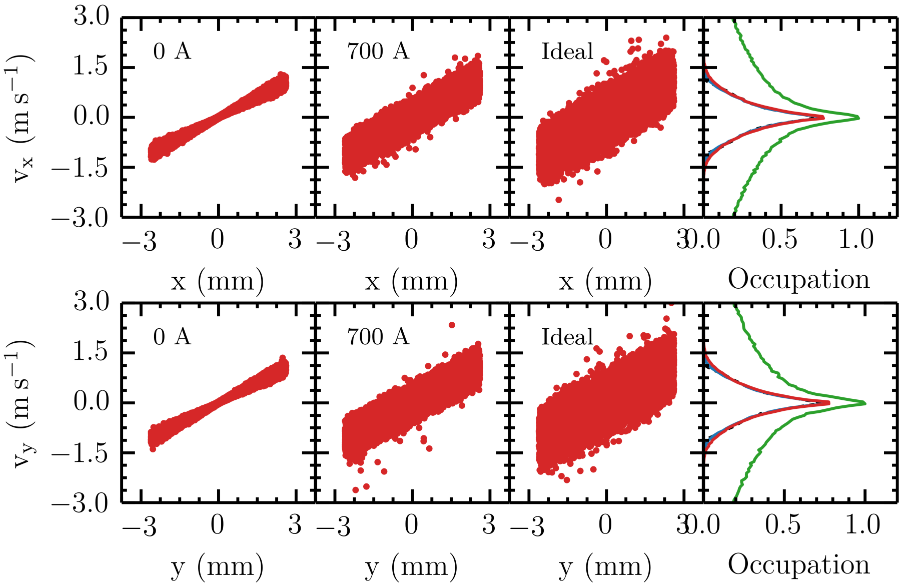

Figure 5.9: The final phase space distributions in the transverse direction at the detector for the quadrupole running at 0 A, 700 A and an ideal quadrupole also with 700 A flowing through the poles. The distributions are collected at the location of the MCP. The rightmost panel shows the histograms of the final spread of transverse velocities for the quadrupole running at 0 A (black dashed), 700 A (blue) and the ideal quadrupole operating at 700 A. The initial velocity distribution at the nozzle is also plotted (green).

through the experiment. Figure 5.9 shows the phase space distribution of the particles at the MCP for the three simulated regimes. The application of the quadrupole field causes the states with magnetic dipole moments to rotate in phase space. Due to the increase in the interaction time, this effect is far more noticeable in the case of the idealised quadrupole. In both cases with the quadrupole field applied, the high-field-seeking states are ejected from the quadrupole, although a small subset of m_J = -1 particles remain in the case of the actual quadrupole guiding. Additionally, the range of transverse velocities that reach the detector is slightly larger when the quadrupole is applied, however, most of the enhancement occurs in the central region of the velocity distribution. Figure 5.9 includes the binned transverse velocity spread of the phase space distributions. The initial spread of velocities at the valve nozzle has also been included for reference. These plots confirm that, despite a larger spread of transverse velocities reaching the detector, the loss of the high-field-seeking states results in little change to the TOF profile. Furthermore, given that the transverse velocities from the valve are calculated to make it through the skimmer, it seems that the geometry of the skimmer and the stainless steel tube results in further skimming of the beam. By comparing the broad transverse velocity at the nozzle with the far narrower spread that arrives at the detector, it is clear that the tubing removes the higher transverse velocity components, further skimming the gas packet.

5.2.2 3D Guiding

The operation of the decelerator will be evaluated in the 3D guiding mode. In this mode of operation, the presence of the longitudinal field prevents a subset of velocities, centred on the trap velocity, from spatially expanding. This results in an intense peak in the MCP signal. The operation of this 3D guiding and deceleration modes of the decelerator were suboptimal as the contactors which isolate the power electronics were faulty (see appendix D). Consequently, as one electronics module discharged two other modules were able to charge the partially discharged capacitors. This severely limited the peak current that could be drawn by three of the coils as the capacitors were never fully charged. During these particular experimental runs although a target of 500 A peak was set the coils could only draw in the range of 100 - 200 A peak depending on the particular set of parameters used. Despite this, experimental data from the four module long decelerator has been collected. Two features of 3D guiding shall be considered. Firstly, the capture of the gas packet by varying the time at which the decelerator coils are activated. Secondly, the effect of varying the velocity of the trap shall be presented.

1D Analysis

A unique problem of this form of decelerator is being able to load multiple traps. To investigate this aspect of the decelerator, a fully time dependent 1D simulation of the decelerator has been employed. This captures all aspects of the synthesised current waveform as well as the effects of the fringe fields generated by the decelerator. The delay between the activation of the DBD and the decelerator must be such that the trap which is loaded moves continuously through the decelerator, while combining with the quadrupole field in such a way that enhances the transverse confinement. The first requirement is a result of the temporal overlap between the decelerator coils only allowing two traps to cross the boundaries between modules. The second requirement is a direct consequence of the wave-like nature of the magnetic field. The travelling wave consists of two of traps; one where the quadrupole field enhances the transverse confinement and one where the quadrupole field attenuates the transverse confinement. The type of trap generated alternates over the potential wells generated. The 1D simulations ignore this and, as a result, show twice the number of peaks than what is observed in the full 3D simulations. The choice in the location of the peak in the experiment can be made by reversing the polarity of the quadrupole current. In principle, these simulations could also be used to optimise the experimental setup as they provide a quick means to test a set of experimental parameters. In addition to this, the 1D simulations have provided the means to help determine the location of the coil and the location of the first trap minimum. The information taken for these simulations can then be used to improve the more time consuming 3D simulations.

Figure 5.10a) shows a series of TOF profiles generated through the fully time dependent 1D simulations for a series of different delays between the DBD discharge and the point at which the decelerator coils are activated. The model calculates the field generated by the four coils using the current waveforms generated in the PWM software. The waveforms were based around a 500 A peak reference waveform with a frequency corresponding to 360 $\mathrm{m\,s^{-1}}$, although the average trap velocity was calculated to be 373 $\mathrm{m\,s^{-1}}$. In the example shown, the coils require an extra 43 µs in order for the current to reach its peak value. After this rise time, the traps begin to move through the decelerator. The zero field TOF profile has been calculated for a velocity distribution with peak velocity of 368 ± 2 $\mathrm{m\,s^{-1}}$ and a temperature of 4.16 ± 0.03 K. Additionally, the profiles contain all of the m_J states of the $^3P_2$ metastable state. The high field seeking states have manually been removed from the simulations where the external field is present. Figure 5.10a) shows that across the range of delays simulated here, multiple traps are loaded. The intensity of the resulting peaks vary in magnitude because of the possibility of velocity mismatching and that many of the traps that are formed do not cross the boundary between modules in a continuous fashion. Instead these peaks are occasionally loaded back into subsequent traps. By increasing the delay between the DBD and the activation of the decelerator coils the location of the optimally guided peak can be shifted into the more dense region of the gas packet. With the distances involved the ideal delay should be 756 µs (corrected for the rise time in current) to load the first trap. The wave-like nature means two additional loading points occurs between 600 and 700 µs. For instance, the delay of 600 µs loads the central region of the gas packet into the third trap. In each of the examples shown, three strong peaks are visible in the TOF profile.

Figure 5.10b) shows the velocity distribution at the location of the MCP. The plot also shows the calculated mean velocity of the trap through the 1D simulations. The origin of the additional peaks in the velocity distribution seems to be a function of decelerator length. One or two modules exhibit fewer peaks and therefore the origin seems to be caused by the opening and closing of traps that do not cross the coil boundary. Aside from the weaker longitudinal guiding, these particles will also experience fringe field effects. It is therefore likely that these peaks would eventually be lost in a longer decelerator if allowed adequate time to explore phase space. The strongest peak in velocity is formed with a delay of 700 μs where the central velocity of this peak is near to both the mean velocity of the trap and the peak velocity of the distribution of particles. However, inspection of the velocity profile at the end of the four coils suggests that a subset of velocities with a mean velocity of 356 $\mathrm{m\,s^{-1}}$ are accelerated to this mean velocity between the second and third coils. The delay of 600 μs, on the other hand, maintains the same peak velocity throughout the experiment.

Finally, figure 5.10c) shows the spatial extent of the gas packet 1 ms after the traps begin to move. The spatial coordinates are plotted relative to the mean longitudinal position of the gas packet in zero field at the same point in time. These plots show the effectiveness of the 3D guiding at different delays. Once again, the delay of 600 μs will be examined, although a similar argument can be made for the other delays. The spatial extent of the particles shows that the second trap formed in the decelerator is near ideal to load the most dense part of the beam. To reiterate, this trap is one which travels continuously across the coil boundaries. Surprisingly, despite the trap collecting from the densest region of the gas pulse, this is not the most prominent peak. This strong secondary peak located at roughly -32 mm (and the weaker peak located at -67 mm) seems to arise from spatially bunched particles over a wide range of velocities in a partially continuous trap. The latter seems to be the origin of the additional velocity peaks seen in figure 5.10b). The phase space distribution suggests that the particles are only partially trapped and are already beginning to leave the trap by the end of the third coil. In fact, the heights of the most intense secondary peak becomes comparable to the guided peak as they leave the decelerator. The conclusion that the particles are leaving these additional traps is supported by mapping the motion of the particles through the field and comparing this to the phase space plots. The evolution of these particles indicate that the centre of the bunched particles are approaching the maximum of this trap during the time in the fourth coil and seem to begin to be spilling into the adjacent traps. This result seems to imply that these secondary features would not be so prominent in a longer decelerator. As mentioned in the discussion of figure 5.10b) the function of length suggests that the cause of these features are symptomatic of the non-continuous nature of these traps.

Experimental 3D Guiding

Figure 5.11 shows the decelerator in the 3D guiding mode for the target velocities of 340, 360 and 380 $\mathrm{m\,s^{-1}}$. From the 1D field simulations the average trap velocity was actually found to be 351, 373 and 393 $\mathrm{m\,s^{-1}}$ respectively. Panels a) and b) compare the experimental and 3D simulated data. For reference the zero field TOF profile has been plotted. Fitting equation 5.1 reveals a peak velocity of 359 ± 2 $\mathrm{m\,s^{-1}}$ and a temperature of 5.16 ± 0.04 K. In this example the delay between the DBD and the activation of the decelerator coils has been fixed, thus each sample of the gas pulse is loaded into different traps. The experimental and simulated TOF profiles clearly exhibit the same general features, consisting of three strong peaks. The 351 $\mathrm{m\,s^{-1}}$ exhibits the greatest resemblance to the actual data, this is likely because the approximations used to simplify the simulations are more valid in this instance. Panel c) of figure 5.11 shows the velocity distribution of the particles as they reach the MCP. In each instance, a clear peak can be seen in the velocity distribution roughly centred on the velocity of the trap. The width of the peaks are consistent with the predicted range of velocities that can be trapped. A range between 9 and 20 $\mathrm{m\,s^{-1}}$ is necessary because the trap depth is dependent on whether the coil was operating at 100 or 500 A peak.

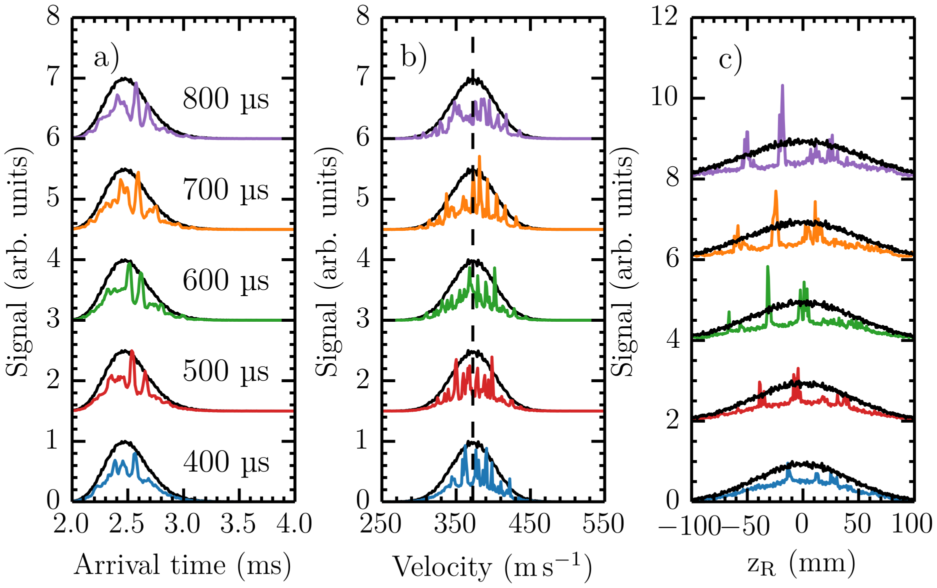

Figure 5.10: The effects of the wave-like nature of the TOF profiles generated through the fully time dependent 1D simulations. Panel a) shows a series of TOF profiles for a series of different delays between the DBD and the point at which the decelerator coils are activated. The resultant TOF profile has been plotted against the zero field variant (black). Panel b) shows the velocity distribution at the location of the MCP plotted against the velocity distribution in the zero field decelerator (black). Panel c) shows the spatial extent of the gas packet 1 ms after the traps begin to move. The spatial coordinates are plotted relative to the mean longitudinal position of the gas packet in zero field at the same point in time. In each case the spatial extent of the particles in zero field has been plotted (black).

The locations of the peaks vary slightly between the experiment and the simulations. For instance, the arrival time of the main guided peaks is 2.71 ms, 2.62 ms and 2.35 ms for traps travelling at 351, 373 and 393 $\mathrm{m\,s^{-1}}$ respectively. The simulations predict arrival times of 2.68 ms, 2.62 ms and 2.43 ms, consequently the experimental peaks arriving 21 µs, 3 µs, 79 µs earlier respectively. There are several possible factors which contribute to the difference in arrival times. Firstly, the errors associated with the measurements in parameters such as the location of the first coil in the actual experiment are fairly significant. Even standard errors in position on the order of 1 mm causes the peaks to shift up to 10 µs. Further to this, the point at which the first trap is formed is not well known. The trap begins to form near to the edge of the coil but does not reach the full trap depth until some time later. The location of the first trap is dependent on the geometry of the coil and the ratio of the currents through each of the four coil phases. Such dependencies are ignored in the simulations as a trap is only considered formed if its maxima reside within the confines of a coil. It is not possible to establish a value for this particular error without either direct measurement with a Hall probe or measurement of the current through each phase to infer the location of the minima using field simulations. Secondly, the spacing between the peaks in the experimental data varies for each of the trap velocities presented here. The difference ranges between 40 - 65 µs. This is not observed in the simulations which assume that the spacing between the minima is uniform. In reality, this is known to vary slightly between coils by a few millimeters from the ideal value of a period (40.8 mm). Taking the length of a single coil, one can deduce that the average period length is in fact 41.7 ± 0.6 mm. It was also found that the average period length measured across the four decelerator coil modules was 41.3 ± 0.7 mm in length. The latter is roughly 0.4 mm longer than the ideal period and is a consequence of the imperfections introduced in the coil winding process. Although this subtle difference has been built into the simulations, the deviations from period to period perhaps may have a greater effect than initially anticipated. Effects such as the shift in the peak arrival time caused by the quadrupole, as noted in section 5.2.1, may also have an influence on the arrival time which has not been taken into account. A final point to make is that the peaks in the simulations tend to be more intense than that of the experiments. This is likely due to the hard switching potential used in the simulations. This model is particularly problematic when crossing the boundary between two coils operating at different peak currents. The simulations use an instantaneous transition from one potential well to another whereas in reality the transition of the potential well across the boundary would not be so seamless and, as seen in the 1D simulations, these effects are clearly not negligible. One final limitation of the simulations is the initial velocity distribution and the resultant zero field TOF profiles. Once again, the deviation of the profiles, particularly at the rising edges seems to be particularly problematic.

5.2.3 Deceleration

Finally, the operation of the decelerator will be evaluated in the deceleration mode. In this mode of operation, the time dependence of the trap velocity can be used to decelerate the trapped particles. Again, the operation of the decelerator was suboptimal as described in appendix D. As a result, the deceleration process is far less efficient as the lower trap depth, combined with the pseudo potential generated through the deceleration, lowers the acceptance of the trap further. Despite this, figure 5.12a) shows the experimental results of the decelerator operating in the deceleration mode. The initial and final trap velocities obtained through the fitting of the 1D simulations have been labelled. The initial target velocity was intended to be 360 $\mathrm{m\,s^{-1}}$ which has been plotted for reference. Fitting of the zero field TOF profile gives a peak velocity of 364 ± 2 $\mathrm{m\,s^{-1}}$ and a temperature of 4.56 ± 0.03 K. Figure 5.12b) shows the simulated TOF profiles for the three trap velocities. The target deceleration of the traps in the two cases shown were from 360 to 340 $\mathrm{m\,s^{-1}}$ and 360 to 300 $\mathrm{m\,s^{-1}}$. The effects of loading secondary traps has already been discussed in the context of 3D guiding, the trap which is loaded is not the first but one of the subsequent traps formed after the wave begins to

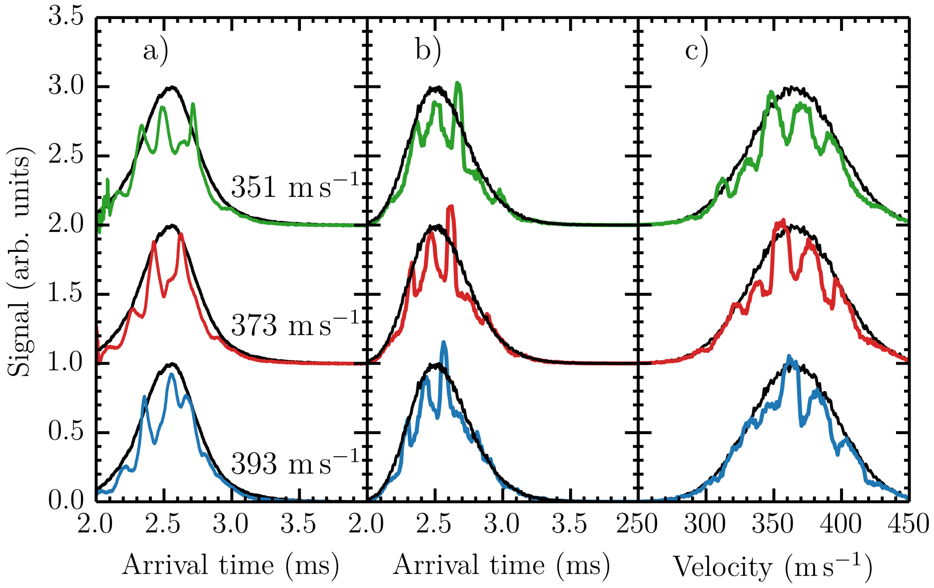

Figure 5.11: Comparison of the experimental and simulated TOF profiles while the decelerator is in the 3D guiding mode. Panels a) and b) show the TOF profiles for the experimental and simulated data respectively for average trap velocities of 351, 373 and 393 m s^{-1}. The zero field TOF profile has been plotted for reference in each instance (black). Panel c) shows the velocity distribution taken from the simulated data as the particles reach the MCP.

move. In the deceleration mode, the linear decrease in frequency begins as soon as the trap is formed. Consequently, the initial velocity of these particles will be lower than that loaded into the optimally loaded 3D guided peak. To phrase this another way, one can not compare the second trap, which is near optimally loaded, in the 3D guiding mode to that in the deceleration experiment as the velocity of these traps are already very different. The peaks of interest for two examples of deceleration shown here actually have a fitted initial and final trap velocities of 350 to 346 m s^{-1} and 342 to 304 m s^{-1}. The main guided peak in the experiment has an arrival time of 2.62 ms which is consistent with that of the simulations. The peak that will be examined here in the deceleration data with a final trap velocity of 346 m s^{-1} has an arrival time of 2.65 ms. The difference in arrival time is 32.6 µs. The corresponding peak in the simulated data arrives at 2.67 ms with a difference in arrival time of 55 µs. The peak in the deceleration data with a final trap velocity of 304 m s^{-1} has an arrival time of 2.71 ms. The difference in arrival time is 90 µs. The corresponding peak in the simulated data arrives at 2.68 ms resulting in a difference in arrival time of 60 µs. The differences between the experimental and simulated TOF profiles are on the order that can be described using the errors and deviations discussed in the context of 3D guiding. Comparing the difference in arrival times presented here and the idealised difference in arrival times it can be concluded that deceleration from the guided trap velocity of 373 m s^{-1} did not occur. Figure 5.12c) shows the velocity distribution of the particles at the MCP. The plots show further manipulations of the gas packet due to the deceleration of the potential. Peaks do however occur at 347.3 and 310.3 m s^{-1} for the final velocities of 346 and 304 m s^{-1} respectively indicating deceleration to some extent. The difference in final velocity is because in the simulations, the traps are only considered to be formed while the trap maxima are within the spatial confines of the coils, these final velocities are consistent with a shorter decelerator with the same magnitude of deceleration. Finally, it is unlikely that deceleration alone causes manipulation of the gas packet from the 3D guided example. Efficient deceleration occurs in the coils operating at the full 500 A peak, the other coils allow the particles to escape allowing the gas packet to expand out of the trap. This is likely more problematic for larger decelerations. As discussed previously, the overlap of the coils operating at different currents is the likely cause for the difference in the heights of the peaks in the experimental and simulated data.

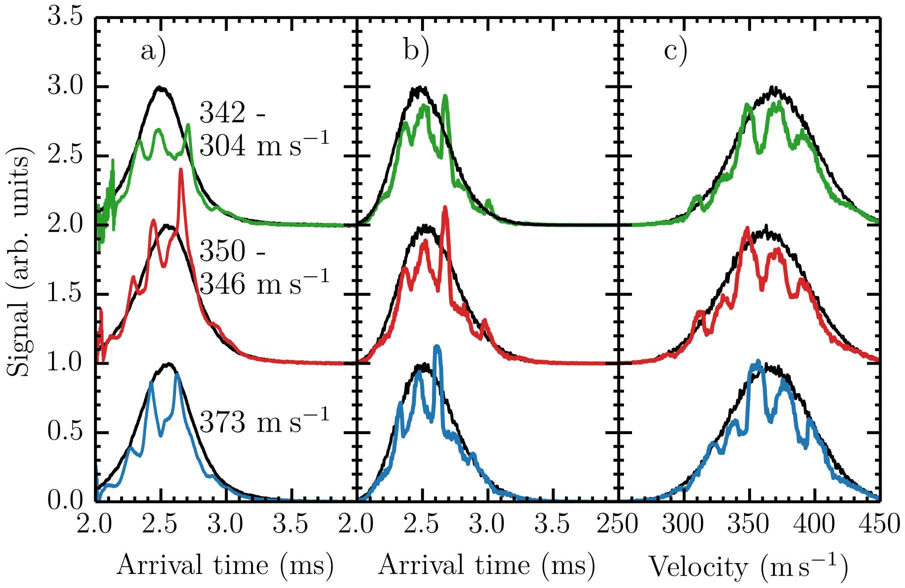

Figure 5.12: Comparison of the experimental and simulated TOF profiles while the decelerator is in the deceleration mode. Panels a) and b) show the TOF profiles for the experimental and simulated data respectively for final trap velocities of 346 and 304 m s^{-1}. The zero field and the 3D guided TOF profiles has been plotted for reference (black). Panel c) shows the velocity distribution taken from the simulated data as the particles reach the MCP.

There are a number of issues that hamper the experimental and simulated data sets which may cause these discrepancies. The differences between the experimental and simulated arrival times that have been discussed previously are certainly applicable here, however, a number of additional factors also must be considered. As explained earlier in this chapter, the magnitude of the deceleration is often very different than that expected because the velocity of the trap cannot be fine tuned particularly while trying to maximise the depth of the traps. As such, the simplified nature of the simulation process can only capture the essence of the true motion of the trap. Since the decelerator performed suboptimally there are a number of factors, such as the way the magnetic fields add together between coil modules operating at different peak currents, that cannot be captured in this type of simulation.

A final consideration is what the TOF profiles would look like while the decelerator was running under perfect conditions. Even with the trap depth scaled by an amount typical for the range of velocities explored, deceleration from 360 to 290 m s^{-1} should be possible if the full 500 A peak is reached. This is exciting because starting at a lower initial velocity (i.e. slower than the peak velocity of the distribution) while maintaining the same deceleration will allow the final velocity of the decelerated gas packet to be taken outside of the main distribution. The major difference between the idealised experiment and the experimental results presented earlier is the duration that the quadrupole field is active for. The intensity of the peaks is far greater with the quadrupole interaction time maximised. A possible solution to this will be described in chapter 6. Finally, a major flaw with the current setup of the decelerator is that the actual velocity of the trap is not known until after the data was collected. This, combined with the other problems described above often leads to suboptimal loading of the target region of the gas packet both spatially and in terms of velocity. Optimisation software, even in 1D, would be a useful tool to choose a delay and offer further information during an experiment rather than *post factum*.

5.3 Chapter Summary

Due to its magnetic characteristics and the properties of a gas pulse after supersonic expansion, metastable argon is an ideal candidate to test the decelerator. Metastable argon has been used to theoretically and experimentally characterise the design of the decelerator reported here. The phase stability and the acceptance of the decelerator has been analysed for the $m_J = 2$ state of metastable argon in both the 3D guiding and deceleration modes of operation using both the pure and synthesised current waveforms. In the 3D guiding mode, the acceptance of the decelerator decreases with the target trap velocity. This trend holds for the two types of current waveform employed and is also true for the four and nine module long decelerators considered. This seems to be a result of the extended interaction time with the field. This allows the particles to further explore the unstable regions of phase space and find loss channels from the trap. A surprising result is that the synthesised waveform has little impact on the acceptance of the trap in the 3D guiding mode of operation. At low target trap velocities, the acceptance tends to be slightly larger for the synthesised waveform, owing to the rapid longitudinal trap oscillations providing additional transverse confinement at the edges of the trap. The acceptance of the trap tends to be slightly smaller for higher target velocities which is probably a consequence of the lower trap depth that is produced by the synthesised current waveform. The acceptance of the decelerator in the deceleration mode has also been explored. The acceptance of a nine module long decelerator has been studied to further highlight the differences between the pure and synthesised current waveforms. The acceptance of the decelerator with a synthesised current waveform rapidly decreases because of the lower trap depth that the synthesised current waveform produces and the velocity of the trap cannot be fine tuned. The latter means that the magnitude of the deceleration tends to be greater than that of the pure current waveform variant. The general trend in the acceptance is very different for the 1D and 3D simulations, which means that there are additional transverse effects that limit the acceptance of the decelerator. The dependence of the acceptance of the decelerator on the initial trap velocity was investigated. It was found that the decelerator benefits from being loaded with a slow initial gas packet. For initial velocities above 350 $\mathrm{m\,s^{-1}}$ the limiting factor is the lack of transverse confinement near the longitudinal maxima. The maximum deceleration seems to be approximately 5×10^4 $\mathrm{m\,s^{-2}}$ before the trap becomes significantly lossy. Below an initial trap velocity of 350 $\mathrm{m\,s^{-1}}$, the acceptance behaves more like the 1D case which indicates that the longitudinal and transverse motion of the particles in the trap remain uncoupled. It was also shown that similar values of deceleration often result in different relative changes in acceptance, this was attributed to the longer interaction time with the field. Similarly, the relatively short interaction time of the deceleration of the 450 $\mathrm{m\,s^{-1}}$ beam results in much higher acceptance of the trap compared to similar decelerations with lower initial velocities. The simulations have shown that the limiting factor for the decelerator in its current form is certainly the lack of transverse confinement particularly in the x direction. This results in the longitudinal and transverse motion of the particles experiencing some coupling. The advantage of this form of decelerator is that the transverse field can be varied separately to the longitudinal field, allowing more complex arrangements of magnetic poles to be examined. It has been shown that even a modest increase in the transverse confinement can further enhance the acceptance of the decelerator in the 3D guiding mode.

The experimental results from the four module long decelerator have been reported. The fitting function used to extract parameters such as temperature and the peak velocity of the metastable argon gas packet was explained and contrasted to the time-of-flight profiles measured for the valve at two temperatures. The effects on the metastable argon gas packet produced by the Even-Lavie valve held at 138.5 K were studied and the experimental and simulated TOF profiles were presented. Due to the highly directional nature of the valve, the measured and calculated TOF profiles exhibited little increase in the integrated signal due to the presence of the quadrupole field even at 700 A. A modest increase in signal could be achieved in an ideal quadrupole where the entirety of the quadrupole could be utilised and the current source could be instantaneously switched. The results of the decelerator operating in the 3D guiding mode were presented. The effects of the delay between the activation of the DBD and the decelerator coils have been examined in 1D. This was used to highlight the unique problem associated with trap loading due to the wave-like nature of the magnetic field. Due to the temperature of the gas pulse, it is possible to fill multiple traps; the choice of the delay alters which traps are efficiently loaded. Since only two traps continuously move across the boundary between adjacent coils, the choice in delay becomes an extremely important concept in these experiments.

Both the experimentally and numerically produced TOF profiles for three trap velocities were presented. From the 1D field simulations the average trap velocity was actually found to be 351, 373 and 393 $\mathrm{m\,s^{-1}}$. This difference for the target trap velocities is a consequence of the PWM technique while trying to maximise the peak current to 500 A. Nevertheless, peaks in the velocity distribution at these trap velocities were observed in the simulated data. The difference in the arrival time of the peaks in the simulated and experimental data were discussed. Errors associated with the measurements in parameters such as the location of the first coil and where the first trap is considered to be formed are fairly significant. Even standard errors in position on the order of 1 mm causes the peaks to shift up to 10 µs. Another consideration was the differences between the ideal coils and the actual coils. The average period length of the decelerator was measured to be 41.3 ± 0.7 mm in length, which is approximately 0.4 mm longer than the ideal period. This subtle difference has been built into the simulations, however, the deviations from period to period perhaps may have a greater effect than initially anticipated. Limitations of the simulation techniques such as the hard switching of the potentials and the model of the supersonic expansion were also discussed. The ability to 3D guide and decelerate were severely hampered by the failure of the contactors used to isolate the power electronic modules (see appendix D). The deceleration results in particular are limited as the coils operating at 100 A peak will lower the acceptance of the decelerator as these coils allow the particles to expand out of the trap. Due to the delay between the DBD and the activation of the deceleration coils, the initial velocity of these decelerated particles will be lower than expected. It is already known that in the experiments presented here the trap which is loaded is one of the secondary traps. The linear decrease in frequency begins as soon as the trap is formed which means that one cannot compare the optimally loaded trap in the 3D guiding mode to that in the deceleration experiment as the velocity of these traps are already very different. The peaks of interest for two examples of deceleration shown here actually have fitted initial and final trap velocities of 350 to 346 $\mathrm{m\,s^{-1}}$ and 342 to 304 $\mathrm{m\,s^{-1}}$. The final peaks in the velocity distribution occur at 347.3 and 310.3 $\mathrm{m\,s^{-1}}$ respectively which indicates deceleration to some extent. The difference in final velocity is because, in the simulations, the traps are only considered to be formed while the trap maxima are within the spatial confines of the coils, these final velocities are consistent with a shorter decelerator with the same magnitude of deceleration. A comparison of the difference in the arrival times of the peaks presented here and the idealised difference in arrival times leads to the conclusion that deceleration from the guided trap velocity of 373 $\mathrm{m\,s^{-1}}$ did not occur.

Finally, the limitations in the current experiment were discussed. These included the suboptimal peak currents achieved as well as the usage of the quadrupole and the delay between the DBD and the activation of the decelerator. Addressing the former as well as achieving the full 500 A peak through the decelerator would allow the deceleration from 360 to 290 $\mathrm{m\,s^{-1}}$. Furthermore, with the issues associated with the quadrupole addressed, the intensity of the guided or decelerated peaks could be maximised. Optimisation software could be used to find a suitable starting set of parameter particularly for the delay between the DBD and the activation of the decelerator. This will reduce the size of the parameter space to be searched to find the variables that leads to the optimal loading of the target trap. The current experiment is severely limited by only being able to examine the trap dynamics *post factum*, therefore, even 1D optimisation software would be an invaluable tool to inform the operator of the experiment on their choice of parameters.

Chapter 6

Outlook: A Hybrid Molecular Trap and Atomic MOT

The objective of this final chapter is to explain the steps necessary to achieve the aims of the decelerator project that were outlined in chapter 1. The chapter will be split into the short and long term outlooks for the decelerator project. The travelling wave Zeeman decelerator provides a method to produce cold molecules, however, short term improvements to the decelerator must be made in order to produce cold, slow molecules. These improvements will be discussed in section 6.1, where the changes to the source of cold molecules and quadrupole guide will be described. This section will also explain why the decelerator must be extended. The long term goal of this project is to use the decelerator as the first stage to produce molecules over a range of temperatures as low as the ultracold regime. A method to achieve this is sympathetic cooling. This involves creating an ultracold sample of atoms and allowing it to coalesce with an ensemble of cold molecules. Elastic collisions between the two species rethermalise the molecules, cooling them to the ultracold regime. A potential system is calcium monohydride and lithium, which will be the focus of this chapter. Section 6.2 provides an overview of sympathetic cooling and the collision studies into the CaH-Li system that have been undertaken to date. Section 6.3 explains how sympathetic cooling with atoms can be used to transition the molecules from the cold to the ultracold regime. This provides a way to study inelastic and reactive collisions in atom-molecule systems and, moreover, offers a way to even explore the ability to control the outcomes of such collisions through selection of the state the particles are in. The design of a trap capable of the simultaneous loading of the decelerated atomic and molecular species which also facilitates the cooling of the atomic sample will be described in section 6.4. The cooling of the atoms relies on the formation of an atomic Magneto-optical Trap (MOT) which will be described in section 6.5. The method used to load the trap and a description of any additional coils will be explained in section 6.6. This section will conclude with a one dimensional model to evaluate the efficiency of the loading procedure.

6.1 Short Term Outlook

The short term goals of the decelerator will be outlined in this section. Given the set-backs with the power electronics, the immediate objective is to study the decelerator while operating at its full potential with metastable argon. The goal after that would be to decelerate a molecule. The most likely candidate is the methyl radical. As stated previously, the detection chamber is designed to accept a number of detection techniques including a quadrupole mass spectrometer (QMS). In order to ionise the methyl radical, resonance enhanced multi-photon ionisation (REMPI) would be employed. The radical would be excited using a 2 + 1 REMPI scheme via the 4pA_2'' Rydberg state [164]. The methyl radical has a mass to magnetic moment similar to that of metastable argon and can be seeded in a heavy carrier gas such as Krypton. Even with the four module long decelerator, it should be possible to decelerate the methyl radical by a similar amount as metastable argon. This section will focus on the challenges that, as yet, still need to be overcome. The focus shall be achieving molecular packets with zero velocity in the longitudinal direction. This requires the decelerator to be extended and possibly a change to the method used to produce the molecules initially. Finally, a potential improvement to the quadrupole guide will be discussed and will be compared to the existing wire quadrupole currently used in the decelerator.

6.1.1 Extending the Decelerator

The first step towards achieving the goal of the sympathetic cooling of molecules is to at least double the length of the decelerator. As was described previously in chapter 2, there are two methods to view the effect of the deceleration on the potential. The pseudo potential is generated by the deceleration, this lowers the front edge of the inertial potential while increasing the trapping gradient of the rear edge. The modified potential experienced by a metastable argon atom, in the $m_J = 2$ state, is shown in figure 6.1. The plot shows the pseudo potential in 1D for a series of different length decelerators. In each case the decelerator is operating at 1000 A peak and has an initial trap velocity of 300 $\mathrm{m\,s^{-1}}$ and a final trap velocity of 0 $\mathrm{m\,s^{-1}}$. The length of the decelerator is given in terms of number of modules. The 4 module long decelerator is insufficient to decelerate metastable argon to a standstill. It is therefore necessary to increase the length of the decelerator in order to minimise the effect of the pseudo potential. The final length of the decelerator should be a compromise between the efficiency of the deceleration process and the properties of the final distribution of molecules such as the final longitudinal temperature. Sympathetic cooling experiments with molecules and atoms look feasible from an initial molecule temperature of 20 mK [198]. Using this as a basis, it can be determined that the minimum length of decelerator required is 1.18 m which corresponds to at least 9 modules operating at 1000 A peak. Metastable argon has a favourable mass to magnetic moment ratio, however, a molecule such as CaH travelling in excess of 300 $\mathrm{m\,s^{-1}}$ would not be decelerated efficiently. In order to keep the decelerator versatile, one option is to simply continue extending the decelerator, however, it may be advantageous to alter the source of the molecules as well.

6.1.2 Buffer Gas Sources

Further to extending the decelerator it would be desirable to exchange the supersonic source for a buffer gas source. The advantage of this technique over supersonic expansion is the gas packet possesses much slower mean velocities. The temperature of the gas packet is also similar to that produced by a supersonic source. The modification of the potential, due to the deceleration, is reduced by the combination of the 9 module long decelerator and this type of source. The idea of a buffer gas source has been outlined previously in chapter 1. These sources tend to be bright, however, the caveat to this claim is that the initial input of molecules must be intense. Generally, laser ablation or capillary filling are common techniques used to deliver the high molecule numbers to the cell. The mean velocity of buffer gas source is dependent on the species and the design of the cell. Typically, one may expect mean velocities between 50 - 200 $\mathrm{m\,s^{-1}}$ and temperatures between 2-5 K [92]. Due to the slow extraction of the gas packet and the not insignificant temperature, the drawback to the buffer gas source is that the temporal extent of the packet tends to be fairly large [199]. Therefore, it will be particularly important to place the first decelerator coil as near as possible to the buffer

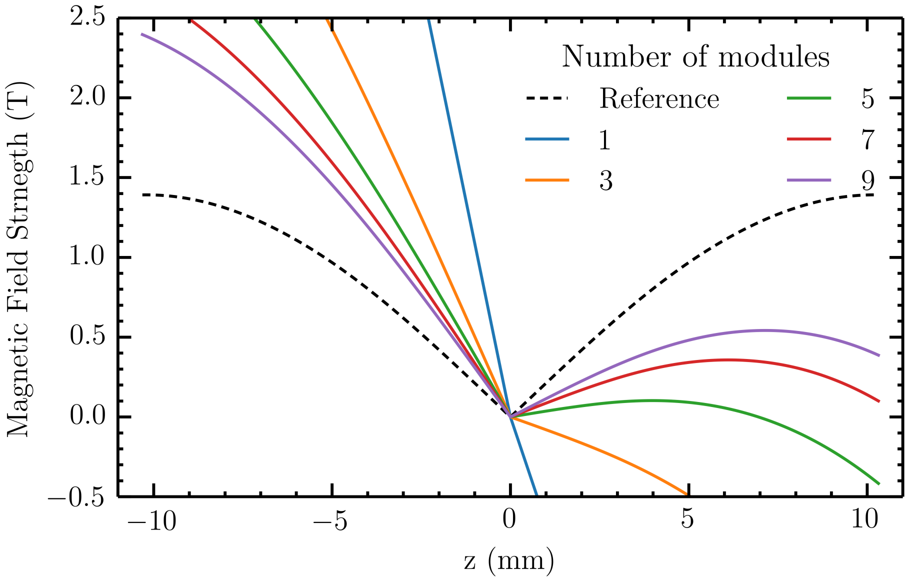

Figure 6.1: The calculated 1D pseudo potential experienced by metastable argon ($m_J = 2$) for a series of different length decelerators. In each case, the decelerator is operating at 1000 A peak and initial and final velocities of the trap were 300 and 0 $\mathrm{m\,s^{-1}}$ respectively. The length of the decelerator is given in terms of number of modules, where one module is 122 mm long. The potential in the inertial frame is shown for reference (black dashed). This pictorial view of the modification to the trapping potential shows that the current decelerator is incapable of decelerating metastable argon to a standstill from a supersonic source.

gas cell to ensure maximal loading of the trap. The design of the cell is likely be similar to that of Bulleid *et al.* [200]. The cell is likely to be mounted on a two-stage cryocooler and the helium fed into the cell via a capillary. The species to be decelerated will be loaded into the cell by laser ablation from a solid Li target and a solid CaH precursor. The design of the cell itself will need to be carefully considered to allow the maximum extraction of the sample. This requires consideration of the density and the flow rate of the of helium in the region of the ablation plume. The aim is to stop the ballistic expansion of the ablated material before it reaches the cell walls. Further modelling of the gas flow would allow the geometry of the source to be tailored to the species being cooled and the acceptance of the decelerator.

6.1.3 Improving the Quadrupole Guide

The decelerator is limited by the ability to capture molecules in the transverse direction. This is particularly problematic in the x direction where the helical coils produce a weak field. Although the quadrupole is able to supply a relatively strong confining potential, channels for a significant proportion of particles to escape still exist. The power requirements are also a concern. The power supplies were originally chosen to supply 700 A through a 1 m long quadrupole, therefore greater transverse confinement cannot be achieved without additional power supplies for a 9 module long decelerator. Moreover, as mentioned in chapter 3, the quadrupole must be actively cooled with fans to ensure that the resistance of the quadrupole does not dramatically increase. Even with a quadrupole of moderate length, the temperature of the quadrupole rapidly increases over the course of an experimental run. With these considerations it seems reasonable to modify the quadrupole to increase the trapping gradient while minimising the power consumption of the experiment and the heat load of the quadrupole. It would be preferable to exchange the wire quadrupole for one constructed using permanent magnets.

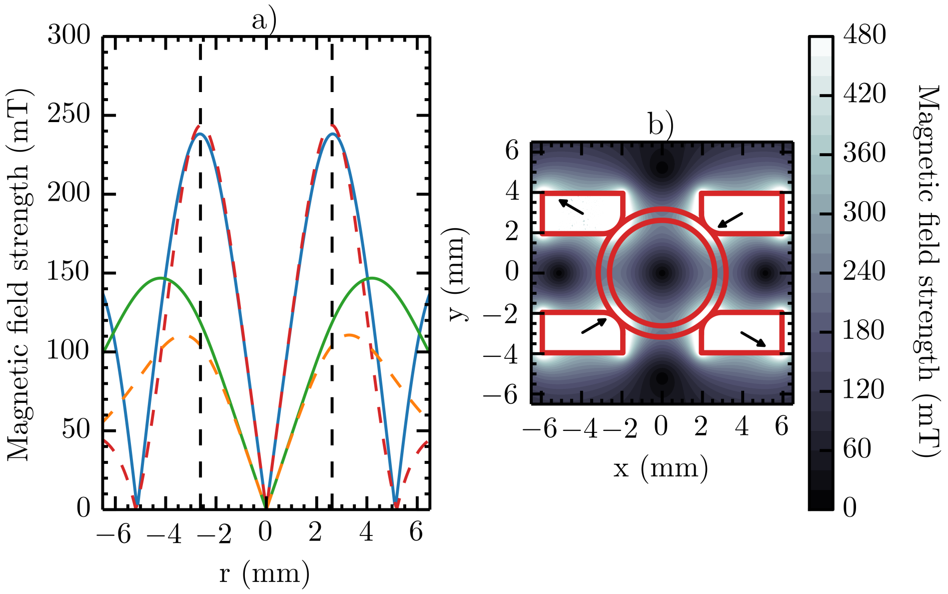

Figure 6.2: The comparison of the axial fields of the wire quadrupole and those of the permanent magnet quadrupole and the 2D potential generated by the permanent magnet quadrupole. Panel a) shows the x (y) field of the wire quadrupole plotted as the green solid (orange dashed) line. The x (y) field of the permanent magnet quadrupole is shown by the solid blue (dashed red) lines. The inner radius of the delivery tube also plotted (black dashed lines). Panel b) shows the colourmap image of the permanent magnet field. The outline of the magnet poles and the steel tube are shown for reference. The arrows within the magnet poles represent the direction of the magnetisation of that magnet.

The permanent magnet design was developed using the Radia plug-in for Mathematica. The starting point for the design was to ensure that the magnet poles would fit into the existing mounts for the quadrupole. In order to maximise the trapping gradient, N50 grade NdFeB was selected as the residual magnetisation of this material is 1.43 T. The residual magnetisation vector was chosen to point ±30 ° from the x axis of the magnet. As a result, the maximum of the axial field occurs outside the inner radius of the delivery tube. Figure 6.2a) shows a comparison of the fields along the x and y axes generated from the original wire quadrupole (at 700 A) and the permanent magnet variant. The trapping gradients in the x and y direction are 106 ± 1 Tm^{-1} and 109 ± 1 Tm^{-1} respectively. This is more than a factor of two greater confinement than with the wire quadrupole. Figure 6.2b) shows the colourmap of the magnetic field generated by the permanent magnet quadrupole in the xy plane. For reference the cross section of the magnets and the stainless steel tube are also sketched. Also shown is the magnetisation direction of the magnet poles, it should be noted that the angle of 30° from the x axis results in an absolute field where the maxima occur outside the internal radius of the tube. The resulting field is similar in terms of gradient in both the x and y directions. Finally, it is worth mentioning the fields generated in the z direction. The wire quadrupole generates fairly large fields in the z direction. This is unavoidable because electrical connections must be made between each pole. It can be estimated that the fields are on the order of hundreds of mT. This has driven the need to develop the fast switching circuitry employed by the quadrupole power electronics. Unlike the wire quadrupole, the fringe fields generated in the z direction are less of a problem with the permanent magnet quadrupole. In fact, the fields are on the order of µT and are generally difficult to distinguish from numerical noise.

The overall gain in the acceptance in 4D phase space can be examined. Figures 6.3 and 6.4 show the phase space plots of the wire quadrupole at 700 A and the N50 permanent magnet quadrupole respectively. The 1D separatrix is plotted in both instances. In the simulations, the trajectories of 10^5 metastable argon atoms in the $m_J = 2$ state were examined. The upper panels show the initial uniform

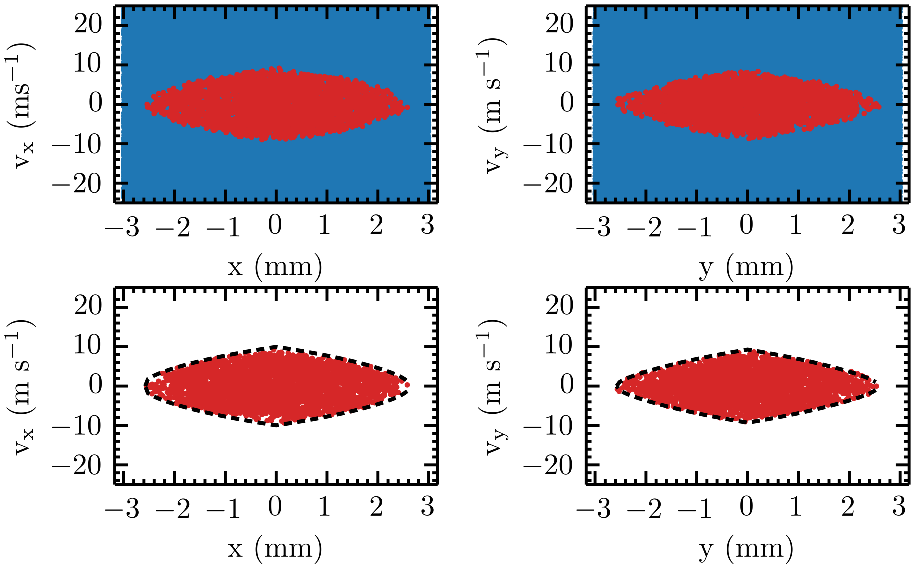

Figure 6.3: The 4D phase space acceptance of metastable argon (m_J = 2) of the wire quadrupole at 700 A. The upper panels show the initial phase space distribution of particles in the x and y directions. Each point represents a particle and is coloured to show which are accepted (red) and which are lost (blue). The lower panels show the emittance after the gas packets travels 1.18 m through the quadrupole field. The 1D separatrix in each direction is also plotted (black dashed).

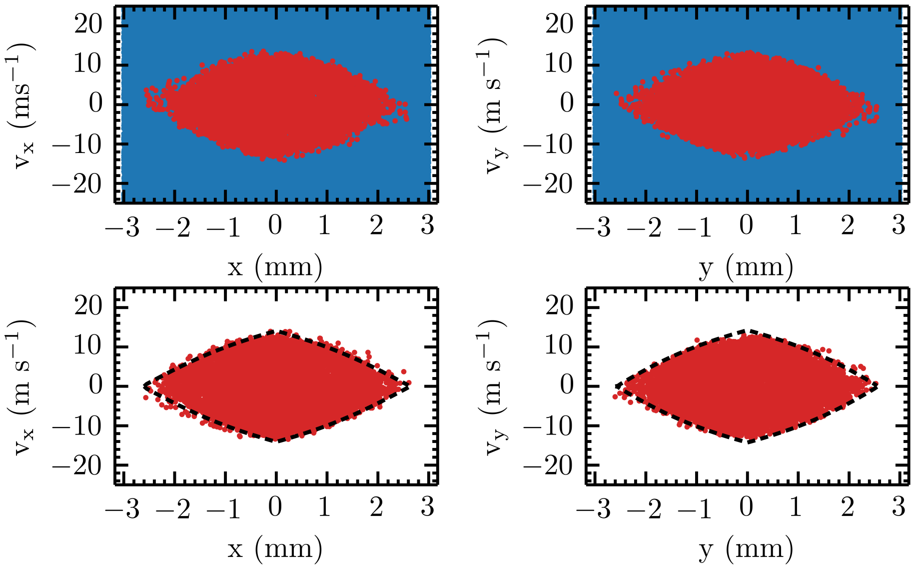

Figure 6.4: The 4D phase space acceptance of metastable argon (m_J = 2) of the permanent magnet quadrupole. The upper panels show the initial phase space distribution of particles in the x and y directions. Each point represents a particle and is coloured to show which are accepted (red) and which are lost (blue). The lower panels show the emittance after the gas packets travels 1.18 m through the quadrupole field. The 1D separatrix in each direction is also plotted (black dashed).

distribution of particles. The particles are coloured depending on whether or not they make it through the 1.18 m long quadrupole. The lower panels plot the final distribution of the particles after reaching the end of the quadrupole guide. An initial uniform distribution was used, with a phase space volume of 9.0×10^4 $(\mathrm{mm\,m\,s^{-1}})^2$. The acceptance of the wire and permanent magnet quadrupole are 2.72×10^3 $(\mathrm{mm\,m\,s^{-1}})^2$ and 5.14×10^3 $(\mathrm{mm\,m\,s^{-1}})^2$. Almost a factor of two increase. The effect on the 6D acceptance will be examined for Li and CaH in section 6.3.

6.2 Overview of Sympathetic Cooling and the CaH-Li System

The sympathetic cooling of molecules using an ultracold atomic species is a promising method of cooling as it brings together many well established techniques such as laser cooling of atoms and the ability to co-trap species. Suitable systems of atoms and molecules must be found which meet the rule-of-thumb condition for sympathetic cooling. This states that the rate of elastic collisions is at least 100 times faster than that of the inelastic collisions. Therefore the most important consideration in a sympathetic cooling experiment is the choice of atomic and molecular partners. In the following discussion, the properties that an atom-molecule system should have in order to facilitate sympathetic cooling in the same magneto-static potential will be examined. A static potential is only able to trap low-field-seeking states, however, the absolute ground state is always a high-field-seeking state. This potentially can be problematic during the sympathetic cooling process as inelastic collisions can transfer the particles from a trapped to an untrapped state. Besides trap loss, inelastic collisions can also result in the heating of the sample. As inelastic collisions are a limiting factor in sympathetic cooling, the rule-of-thumb ratio of elastic to inelastic collisions was introduced as a means of determining the likelihood of efficient sympathetic cooling. Theoretical studies have determined three desirable characteristics that an atom-molecule system should possess for sympathetic cooling [201]. Firstly, when trapping in a low-field-seeking state (i.e. not the absolute ground state) it is favourable to choose a light atomic species. This has been investigated for Mg [202], Li [198], and H [203] all with NH. Notably, hydrogen atoms seem to be a likely candidate for a universal coolant. Light collision partners result in large centrifugal barriers which suppress any low energy and low field losses. Secondly, the atom-molecule system should have weakly anisotropic interaction potentials. The closed-shell structure of the alkaline earth metals might fulfill this criterion, however, later studies have shown that this is only true for beryllium and magnesium. Additionally, the lack of orbital angular moment also reduces the likelihood of inelastic collisions. Unfortunately, these systems are limited by the strong ion-pair interactions [204] and, moreover, they have no ground state magnetic moment. More pragmatically, these species are regarded as being difficult to cool experimentally. An alternative atomic refrigerant, which still satisfies the first criterion, is Li. In the spin-stretched state, spin-exchange interactions and interactions involving ion-pairs are suppressed. The final characteristic that the system should have is that the molecules should have weak electron coupling to the intermolecular axis. In other words these molecules are best described by Hund's case b. A final consideration for the choice of an atom-molecule system can be made through extrapolation from buffer gas experiments. Molecules that have large rotational splitting and weak spin-spin and spin-rotational coupling tend to have fewer loss channels. Therefore such a system tends to benefit from a more favourable ratio of elastic to inelastic collisions [205]. This may also to be true for sympathetic cooling.

Another consideration for sympathetic cooling is the trap design, which effects the density and phase space trajectories of the trapped species. For instance, CaF, trapped in a microwave trap, along with ^{87}Rb held in a magnetic trap has been studied by Lim *et al* [206]. It was shown that one consequence of using potentials where the formation of circular orbits is possible is that a subset of molecules with large angular momenta circulate around the centre of the trap. As a result these particles do not interact with the refrigerant species located at the trap centre. This limits the overall cooling efficiency, the extent of which is dependent on the initial temperature of the molecules. The most efficient cooling occurs with initially colder samples of molecules.

The calcium monohydride ($^2\Sigma^+$) and lithium (^{2}S) system fulfills the criteria listed above. This particular system has already been investigated both experimentally and theoretically as a potential system that will exhibit sympathetic cooling. Collisions within the sample maybe elastic, inelastic or result in a barrierless, exothermic reaction. This would result in the production of LiH($^1\Sigma^+$) and Ca(^1S),

$$\mathrm{Li}\left(^2\mathrm{S}\right) + \mathrm{CaH}\left(^2\Sigma^+\right) \rightarrow \mathrm{Ca}\left(^1\mathrm{S}\right) + \mathrm{LiH}\left(^1\Sigma^+\right). \tag{6.1}$$

Tscherbul *et al.* have performed a theoretical study that indicates that the spin stretched state on the triplet surface has a favourable ratio of elastic and inelastic collisions for sympathetic cooling. Scattering calculations have also been able to identify a mechanism of collisional spin relaxation which potentially would be problematic at low temperatures. The rate of this relaxation, however, occurs slowly, and therefore is not a problem in this particular system [207]. Furthermore, the group have determined that the ratio of elastic-to-inelastic cross sections were in excess of 100 over a temperature range of 10 μK to 10 mK. Collisions that can result in reactions have been studied experimentally by Singh *et al.* [30] and have been theoretically examined by Warehime *et al.* [208]. Although the reaction is endothermic and is energetically forbidden at low collision energies, non-adiabatic transitions between the triplet and singlet surfaces maybe induced by spin-orbit coupling. The resulting reaction is exothermic. This study has shown that the triplet-to-singlet transition rate is negligibly small [208]. The rate constant of this reaction has been measured at 1K to be 3.6×10^{-10} cm^3 s^{-1} [30].

Finally, both species have a magnetic moment of 1 μ_B (while Li is in the $|F = 2, m_F = 2\rangle$ state), allowing the species to be co-decelerated by the decelerator. The conclusion drawn from these studies is that the CaH-Li system seems an ideal starting point for both sympathetic cooling and controlled chemistry experiments. It is worth noting, however, the limitations of any theoretical analysis into the prospects of sympathetic cooling. Recently, Frye *et al.* have investigated the dependence of the atom-molecule *ab-initio* potential energy surfaces on environmental factors such as the magnetic trapping potential [209]. The group have shown that even a small change in the magnitude of the magnetic field can lead to dramatic changes in the potential energy surfaces. Since these are required to calculate parameters that form the basis for any scattering simulations, such as the collision cross sections, these results therefore possess a large uncertainty. This reduces the confidence that a particular choice of atom-molecule system would actually undergo sympathetic cooling.

6.3 The Co-Deceleration of CaH and Li

The long term goal of the decelerator project is to study the collisions between atomic and molecular species with particular focus on controlling the collisions or reactions of the atomic and molecular species. Using sympathetic cooling these dynamics can be studied over a range of temperatures. Since moving trap decelerators are capable of the co-deceleration of different species, the decelerator presented in the proceeding chapters is then a good starting point to produce the initial cold ensemble. In the following sections an ensemble of Li and CaH produced by a buffer gas source will be considered. It will be assumed that the initial mean velocity of the atoms and molecules will be a conservative 200 m s^{-1}. Unless stated otherwise, the decelerator described below will be nine modules in length (1.18 m).

The 6D acceptance plots for CaH with the wire quadrupole can be seen in figure 6.5. In this simulation the quadrupole was operating at 700 A while the decelerator ran at 1000 A peak. It was further

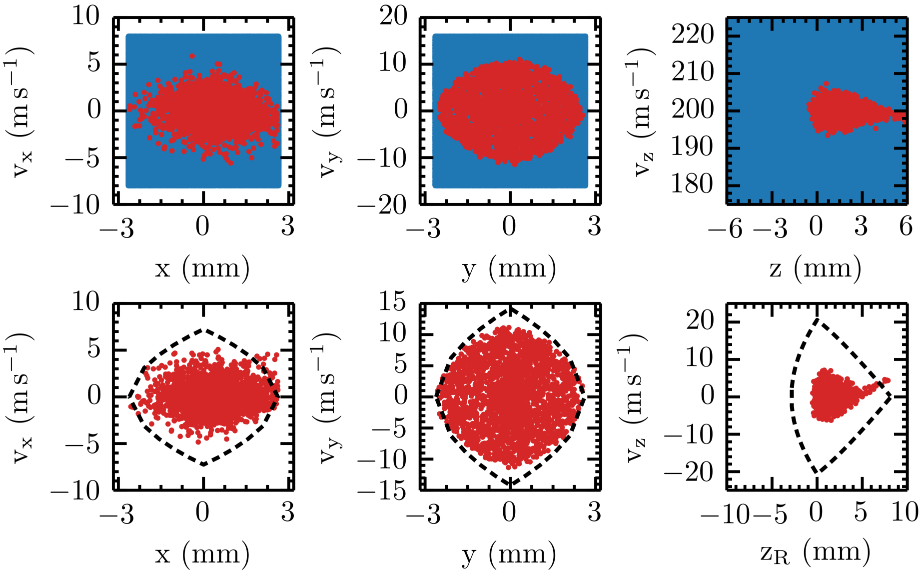

Figure 6.5: The 6D phase space acceptance of CaH after deceleration from 200 m s^{-1} to 0 m s^{-1} with the wire quadrupole operating at 700 A. The upper panels show the initial 6D uniform phase space distribution of particles. The particles are coloured depending on whether they are lost (blue) or accepted by the decelerator (red). The lower row shows the final distribution of particles after the deceleration to a mean velocity of 0 m s^{-1}. The 1D separatrix of the decelerator is plotted (black dashed).

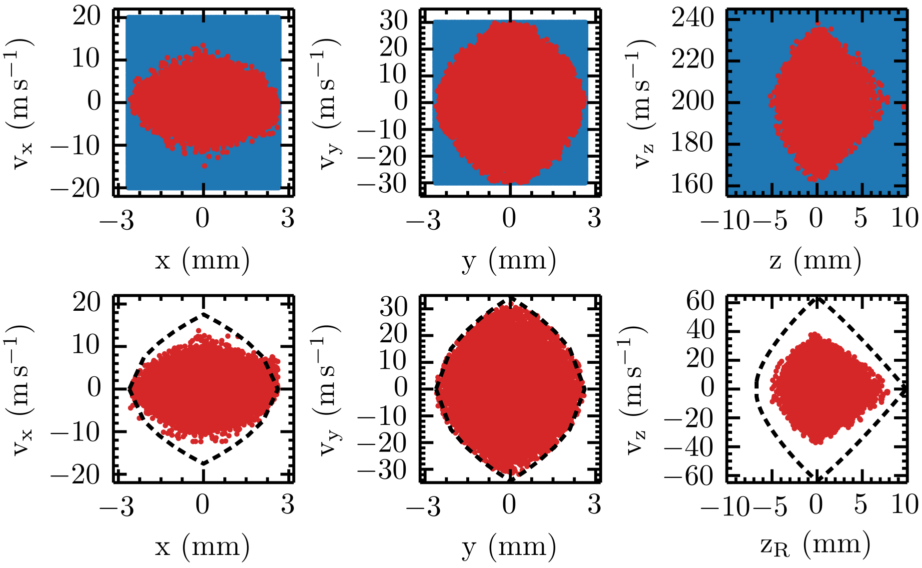

Figure 6.6: The 6D phase space acceptance of Li after deceleration from 200 m s^{-1} to 0 m s^{-1} with the wire quadrupole operating at 700 A. The upper panels show the initial 6D uniform phase space distribution of particles. The particles are coloured depending on whether they are lost (blue) or accepted by the decelerator (red). The lower row shows the final distribution of particles after the deceleration to a mean velocity of 0 m s^{-1}. The 1D separatrix of the decelerator is plotted (black dashed).

assumed that a pure sine wave is a reasonable approximation. This will provide an upper bound for the size of the final distribution of particles to be loaded into the trap. The initial uniform distribution in each direction is shown in the upper row. The particles are coloured depending on whether or not they make it through the decelerator. The lower row of figures show the final distribution in phase space of the molecules. The 1D separatrix of the decelerator is also included in this plot. The final temperature in the longitudinal direction is 19.3 ± 0.6 mK for the wire quadrupole and 29 ± 1 mK for the permanent magnet variant. Finally, the acceptance of the decelerator is decreased by a factor of two. The acceptance of the decelerator with the wire and permanent magnet quadrupoles are 1.9 $\times 10^4$ $(\mathrm{mm\,m\,s^{-1}})^3$ and 9.2 $\times 10^3$ $(\mathrm{mm\,m\,s^{-1}})^3$ respectively. The story is similar with Li. The 6D acceptance plots for Li with the wire quadrupole can be seen in figure 6.6, the same current parameters as previously stated were used in this simulation. The initial and final distributions are plotted as before, the 1D separatrix of Li is also plotted in the lower set of figures. The final temperature of the Li in the longitudinal direction is 142 ± 6 mK for the wire quadrupole and 192 ± 6 mK for the permanent magnet variant. The trend in acceptance is similar to that of CaH. The acceptance of the decelerator with Li is decreased with the permanent magnet quadrupole. The 6D acceptance is 2.1 $\times 10^6$ $(\mathrm{mm\,m\,s^{-1}})^3$ for the wire quadrupole and 4.5 $\times 10^5$ $(\mathrm{mm\,m\,s^{-1}})^3$ for the permanent magnet quadrupole. This is almost a factor of 5 times smaller.

A better understanding of the changes in phase space can be seen with a histogram of the final distribution of particles which can be seen in figure 6.7. The plots show the spread of particles spatially and in velocity due to the two types of quadrupole. It is clear from these plots that the accepted range of velocities are particularly altered for Li in the y direction. The greatest change is the reduced spatial size of the final gas packet particularly in the transverse directions. The explanation of these changes can be seen by following the trajectories of the particles in the trap and by contrasting the shape of the potentials. The trajectory of the particles in the yz plane are very similar for the two quadrupoles. Both undergo smooth oscillations in the trap. The motion in the xz plane, where the quadrupole field dominates the transverse confinement, is very different. The permanent magnet quadrupole alters the trajectory, creating elongated turning points near the edges of the potential in the x direction. Figure 6.8 compares the potential generated by the combination of the decelerator coils operating at 1000 A peak with both the wire quadrupole (upper row of figures) and the permanent magnet quadrupole (lower row of figures). The figures show the trapping potential in the yz and xz planes. The potentials are similar in the yz plane as the decelerator coils provide the most confinement in this direction. The major difference arises in the xz plane. The permanent magnet quadrupole provides a greater trapping gradient which causes the field to be less defocusing at the edges of the trap. The lower acceptance arises from the potential not being completely linear across the inner radius of the steel tube. This configuration of magnets creates a turning point just outside the inner radius of the steel tube which can clearly be seen seen in the xz plane and, to a lesser extent, the yz plane. Hence, the particles that reach the region near the inner radius of the tube experience a weaker force than those near the centre of the tube. This lack of confinement provides a loss channel for a subset of molecules which oscillate close to the inner radius of the steel tube. This often results in the amplitude of the oscillations in the xz plane growing over time, suggesting that the longitudinal and transverse motion becomes coupled. This effect is not seen with the wire quadrupole as the potential is completely linear within the steel tube. It seems unlikely that a permanent magnet quadrupole with the same geometry as the current quadrupole will increase the acceptance of the decelerator. The clear advantages of the permanent magnet quadrupole certainly warrants further study.

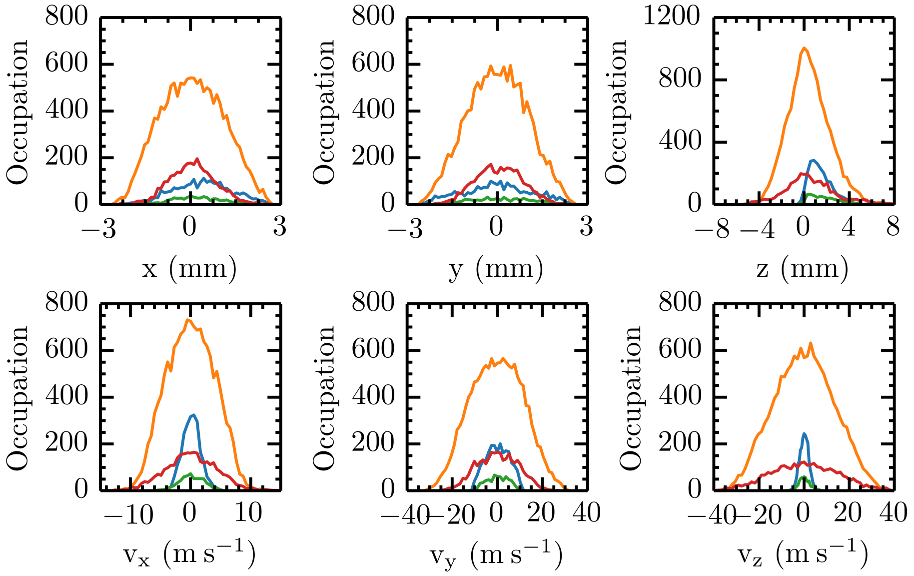

Figure 6.7: Histograms of the final distributions of CaH and Li for the wire quadrupole running at 700 A and the N50 NdFeB permanent magnet after deceleration. The CaH distribution of the wire quadrupole (blue) occupies a larger spatial region to that of the distribution of the permanent magnet quadrupole (green) after deceleration. Similarly, Li with the wire quadrupole (orange) and the permanent magnet quadrupole (red) is also shown.

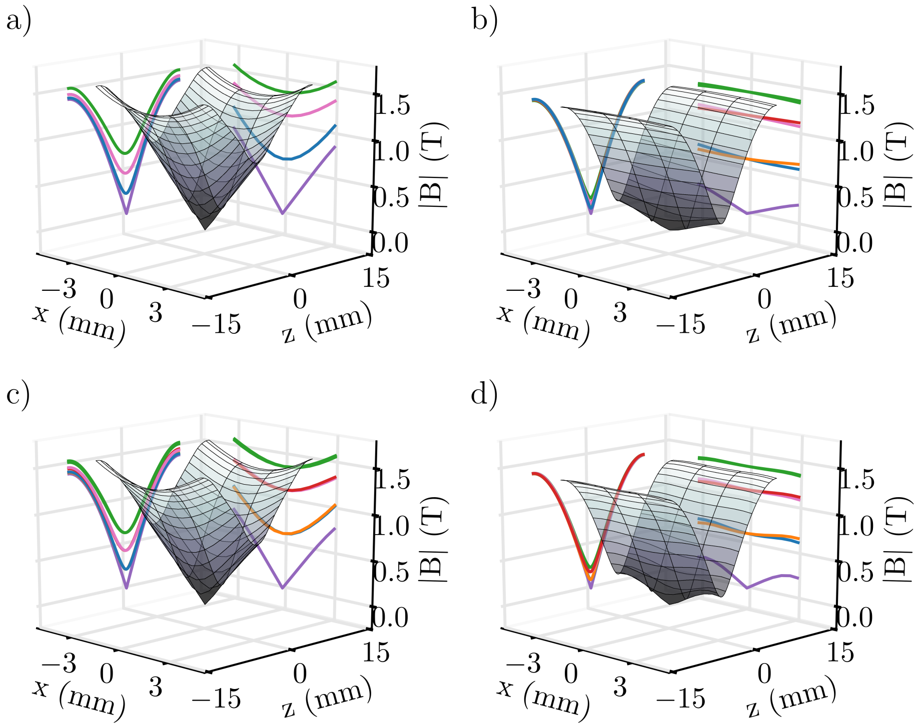

Figure 6.8: The 3D surface plots in the xz and yz planes showing a single trap of the decelerator field generated with a 1000 A peak current waveform with the wire and permanent magnet quadrupole. The combination of the decelerator field and wire quadrupole field, generated by a current of 700 A, is shown in the yz and xz planes in panels a) and c) respectively. Panels b) and d) show the xz and yz planes respectively of the combination of the decelerator and permanent magnet quadrupole fields. In each case the projected contours of the field in each direction has been plotted.

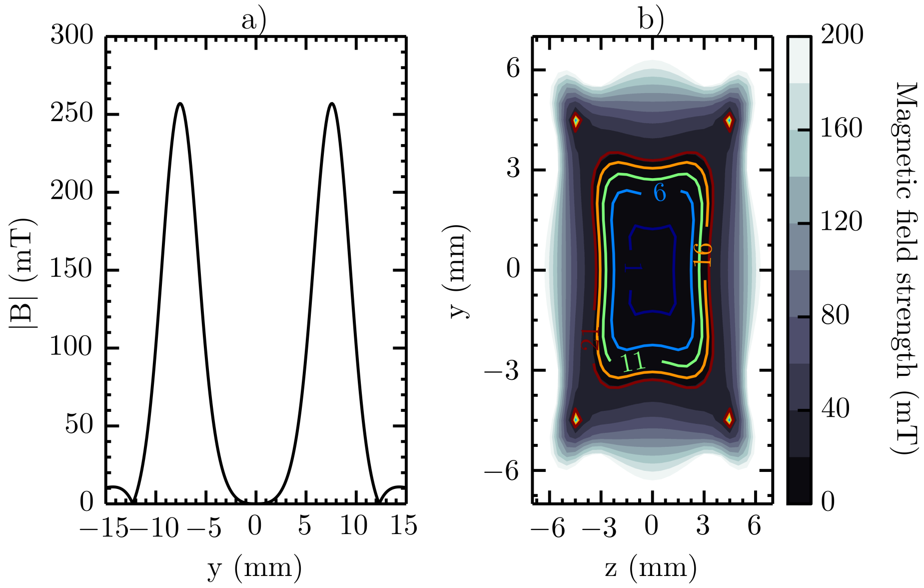

Figure 6.9: The magnetic field generated by the hexapole magnet configuration. Panel a) shows the field generated by the magnets along the y axis. The field is 257 mT deep with a particularly steep gradient. Panel b) shows the colourmap image of the field in the yz plane. The contour lines have been added to further illustrate the flat bottom nature of the trapping potential.

6.4 Designing a Hybrid Atom Molecule Trap

The basis of the trap is a hexapole permanent magnet configuration similar to Nohlmans [210]. The Radia plug-in for Mathematica was used to produce the potentials of the trap. The magnets chosen are NdFeB grade N27, with a pole to pole separation of 12 mm, which gives a trap depth of 257 mT. This large separation between the poles maximises the optical access into the trap. Additionally, the hexapole magnets have a wide bore with an ID of 6 mm which allows adequate space to load the decelerated packet through the magnet itself or for lasers for imaging and cooling. The magnets are also chamfered at an angle of 35° to ensure maximum optical access while maintaining a deep trapping potential. This provides an opening at the corners with a diameter of 5.38 mm, again allowing adequate space for optical access. The field produced by this particular arrangement of magnets scales strongly as r^4 and thus exhibits a relatively steep trapping gradient. Figure 6.9a) shows the trapping potential along the y axis while figure 6.9b) shows the colourmap of the trapping potential in the yz plane. These plots both demonstrate the steep trapping potential and the relatively flat bottomed potential close to the trap centre. A desirable quality of the potential would ensure that all of the molecules trapped eventually sample the centre of the trap where the ultracold sample of atoms will reside. The steep sided potential seems ideal to fulfill such a criterion. An example of CaH trajectories are depicted in figure 6.10. The trajectories are of five randomly selected CaH molecules from an initial distribution that initially uniformly fills the trap and has a temperature of 20 mK. Furthermore, the molecules that are displayed are all accepted into the trap. The points represent the starting location of the molecule and the line represents its trajectory over the course of 10 ms. The two panels of the figure show the motion in both the xy and yz planes and the colour of the particle is common to both plots. As is clear from the figure, the steep potential means that a particle will rebound much like a billiard ball. This ensures that over the course of a sympathetic cooling experiment, the hot molecules will eventually sample the region of space the ultracold atoms occupy.

The zero field of the trap is likely to be problematic during sympathetic cooling experiments. In the region of zero field, non-adiabatic transitions to untrapped states can occur, resulting in loss from

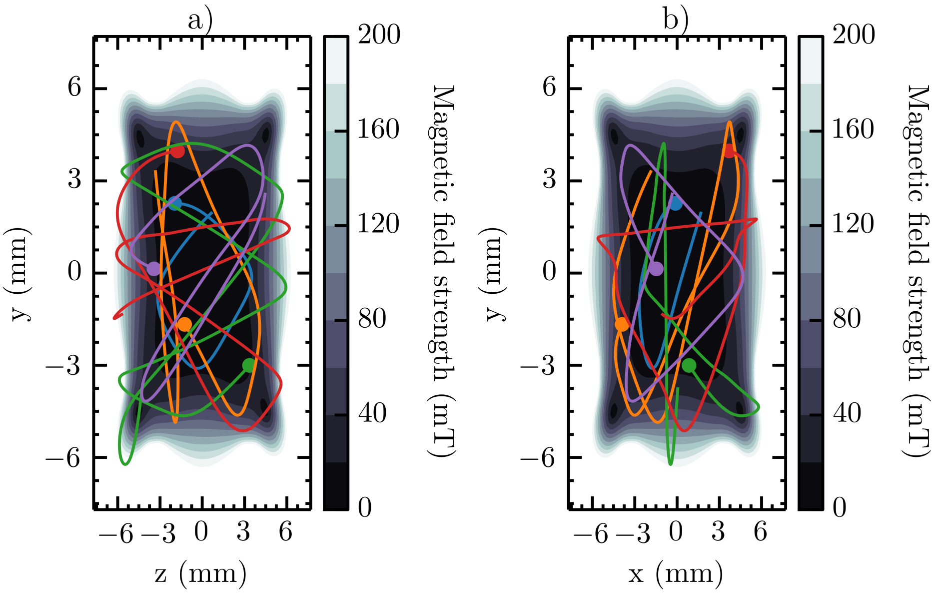

Figure 6.10: Examples of trajectories of CaH in the trapping potential. The trajectories are randomly selected from the accepted distribution of molecules. Initially, the packet had a temperature of 20 mK that spatially filled the trap. The starting positions of the molecules have been plotted as a point while the resulting trajectories, over the course of 10 ms, are plotted as the lines. The colour of the molecule is common to the two panels.

the trap. Such transitions are known as Majorana transitions. A simple modification to the trap can be made to minimise this loss rate. By applying a dipole magnet with a pole-to-pole separation of 30 mm along one of the [1,1,1] axes, a weak quadrupole gradient can be imposed in the central region in each plane. A render of the complete trap geometry is shown in figure 6.11. The image contains extra features that will be described in the sections below. These features include the coil assemblies and laser beams necessary for the six beam magneto-optical trap (see section 6.5) and the optical pump (see appendix F). A view of the central region of the modified field along the y axis is shown in figure 6.12. Also plotted is the fitted linear region of the trap as well as the unaltered hexapole field. Figure 6.13 shows the colourmap of the fields produced in the xy and yz planes. Contour lines have been added to highlight the quadrupole field. By placing the magnets along the (-1,1-1) axis the vector field particularly in the xy plane looks similar to a standard quadrupole field suitable for a MOT. Therefore this trapping configuration would be capable of not only trapping the co-decelerated atoms and molecules, but moreover, will simultaneously allow the cooling of the atoms into the ultracold regime. The trapping gradient was tuned to 87 G cm^{-1} to ensure a linear region greater than 1 mm. Although this gradient is large compared to fields generally used for Li MOTs, high field gradient 2D MOTs have been demonstrated [211].

6.5 Lithium Magneto-Optical Trap

The first lithium MOT was demonstrated in 1991 [212] and was followed quickly with the realisation of the first lithium Bose-Einstein condensate in 1995 [213]. MOTs provide the means to simultaneously trap and cool a species due to the presence of the dissipative light field and the weak magnetic potential. A full description of the operation of a MOT can be found in reference [214]. Lithium-7 has an abundance of 92.5 % [215] and, with a nuclear spin of I = 3/2 and is a bosonic species. Lithium-6 is fermionic in nature and has an abundance of 7.5 %. Lithium-7 can be evaporatively cooled and can be employed as the refrigerant species in sympathetic cooling.

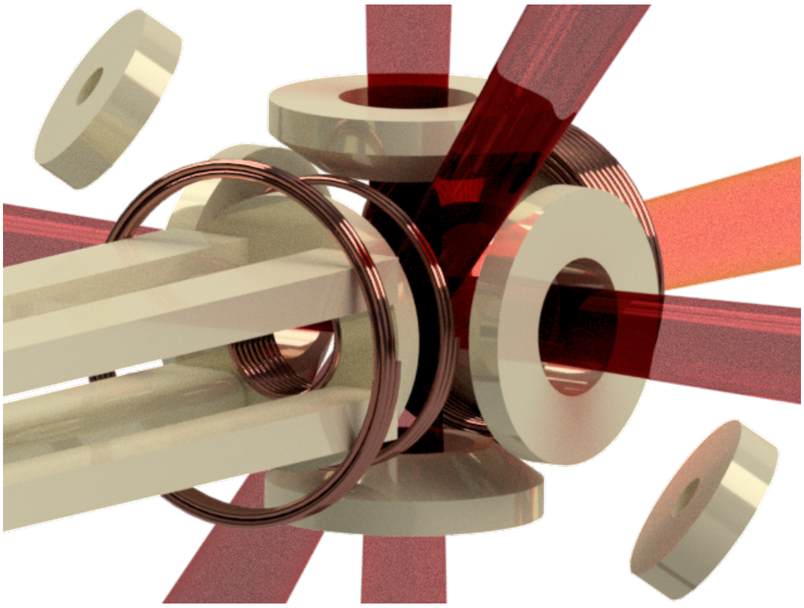

Figure 6.11: The complete hybrid trap and quadrupole guide including the beams used for the lithium MOT and the optical pumping. The coils described later in this chapter have also been included. The shaped hexapole magnets generate the strong confining potential. The dipole magnets along the (-1, 1, -1) axis provides a weak quadrupole potential in the centre of the trap. This will aid in preventing Majorana transitions. The goal is to build a MOT to further cool the atomic species. The MOT lasers (red) are shown in the diagram for reference. Some of the coil assemblies described in the main text and the optical pump laser (orange), which is discussed in appendix F, have also been included.

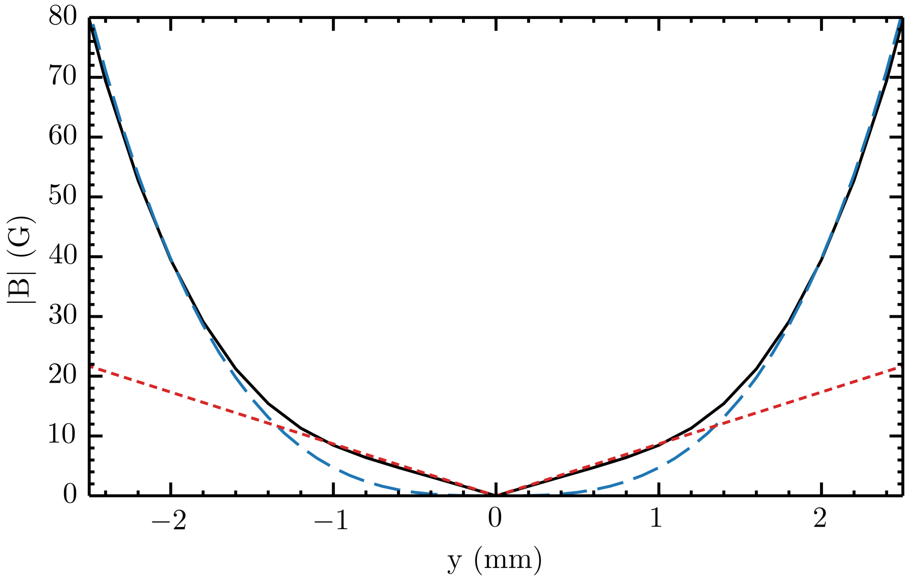

Figure 6.12: A close-up of the field generated in the trap centre due to the dipole magnets (black). The weak quadrupole gradient (87 G cm^{-1}) should be sufficient for a Li MOT. The linear fit of the central region is plotted (red dotted). For comparison, the unmodified hexapole field has also been included (blue dashed).

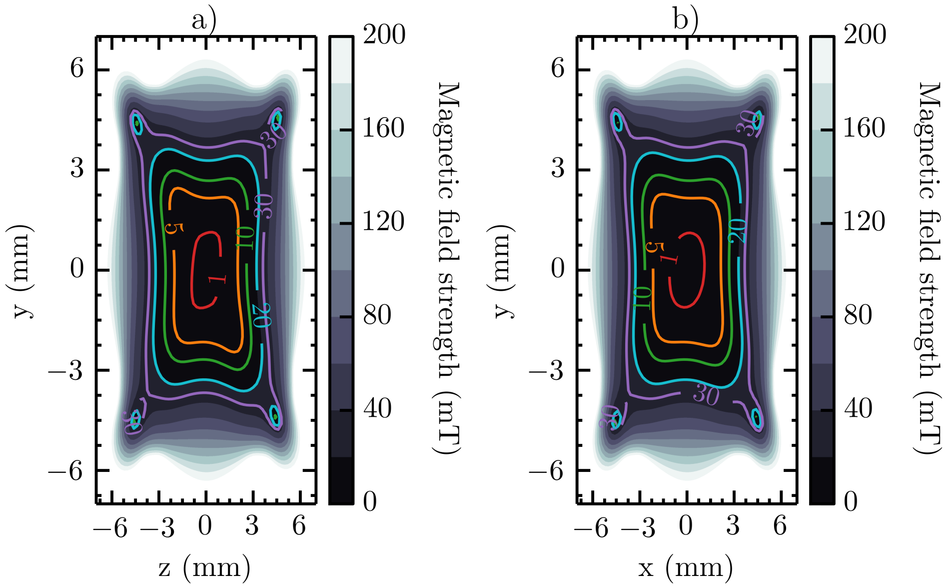

Figure 6.13: The magnetic field generated in the central region of the trap by the combination of the hexapole and the dipole magnets in a) the yz and b) xy planes. Contour lines have been added to further illustrate the modification to the flat bottom nature of the original trapping potential.

The main cooling transition in lithium-7 is on the D2 line between the F = 2 and F′ = 3 states. This is labelled in figure 6.14 which shows the energy level diagram for lithium-7. The natural linewidth of the D2 transition is $\Gamma/(2\pi) = 5.29$ MHz, hence the hyperfine states of the excited state are only partially resolved. It is therefore necessary to apply a repump laser for the F = 1 to F′ = 2 transition. This is also labelled in figure 6.14. This ensures that closed cycling transitions are maintained during the cooling process. The Doppler limit of lithium-7 is 140 μK but tends to be experimentally limited to roughly 300 μK. Through further consideration of the energy structure of the species being cooled, sub-Doppler cooling techniques have been developed to attain temperatures much colder than the Doppler limit. Such techniques maybe necessary if atom number becomes an issue. An example of a sub-Doppler cooling technique is Sisyphus cooling. Sisyphus cooling combined with adiabatic expansion has been shown to result in final temperatures as low as 40 μK at the expense of atom number [216]. Another approach to cool below the Doppler limit is the Λ-enhanced grey molasses on the D1 line which can cool lithium-7 to 60 μK [217].

The 1D properties of the MOT shall now be described. The laser frequency experienced by a particle in a MOT is affected not only by the Doppler shift, due to the velocity of the particle, but also the Zeeman shift due to the inhomogeneous field B(x). The total MOT detuning is

$$\delta_{\mathrm{MOT}} = \delta \mp kv \mp \frac{\Delta\mu_{\mathrm{eff}} B(x)}{\hbar}. \tag{6.2}$$

The total detuning is dependent on the laser detuning from the resonant frequency, ω_o, hence $\delta = \omega - \omega_o$. kv is the Doppler shift of a particle moving at velocity v in the presence of a light field with wavenumber k. Finally, the total detuning is dependent on the Zeeman shift in the magnetic field. The parameter μ_{eff} is the effective Bohr magneton between the lower and excited states of the cooling transition. Hence, in this example $\mu_{\mathrm{eff}} = \mu_{\mathrm{B}}$. The capture radius is defined as distance from the trap centre where the detuning caused by the Zeeman shift equals the laser detuning for a particle at rest. The capture radius, R_{Cap}, is therefore

$$R_{\mathrm{Cap}} = \frac{\hbar\delta}{\Delta\mu_{\mathrm{eff}} B'}. \tag{6.3}$$

The assumption is made in this step that the field is linear with a gradient of B'. Finally, the capture velocity can be defined. This is the largest velocity that can be slowed to a standstill within the trapping volume. Taking the maximum acceleration provided by the spontaneous force and applying it along a distance of R_{Cap}, provides an upper limit to the velocities that can be trapped. For particles of mass m and a natural linewidth of Γ, the capture velocity is

$$v_{\mathrm{Cap}} = \sqrt{\frac{\hbar k \Gamma R_{\mathrm{Cap}}}{m}}. \tag{6.4}$$

For a detuning of -3.5Γ the capture radius of the MOT is estimated to be 1.7 mm, thus the capture volume is limited by the extent of the linear portion of the trap and not the capture radius. The capture velocity is therefore 73.4 $\mathrm{m\,s^{-1}}$. This estimate suggests that the entirety of the transverse velocity spread of the Li from the decelerator can be captured. It should be noted that the expression for the capture velocity is particularly optimistic, in reality the measured capture velocity tends to be much smaller [218]. In terms of cooling efficiency, it should be stressed that because the beams are not orthogonal, the cooling rate in the z-direction is much less than that in the transverse directions. The full dynamics of any MOT formed in this trap are difficult to predict because of the interplay between the steep and shallow field gradients.

This design will allow the sympathetic cooling of the molecules while the Li is cooled by the MOT. Any atoms which are heated during the sympathetic cooling process can be cooled again by the MOT. The cooling trajectory could be tailored such that the cooling rates of the Li and the molecules are similar. This will keep the clouds comparable in size and maintain a good overlap of the two species. This should maintain a reasonable cooling rate of the molecules. Alternatively, if such a trajectory can not be accomplished, the molecules will sample the central region of the trap where the cold Li is located by virtue of the steep sides of the potential. This will no doubt lower the cooling rate of the molecules due to the slow oscillation frequency of the trap. Trajectory simulations can be used to estimate the time taken for the molecules to enter the MOT volume. Approximating the binned entrance time as a decaying exponential it is possible to fit a time constant. After neglecting the atoms that happen to start in the MOT volume, it takes approximately 18.2 ms for 63 % of molecules to enter the MOT volume, which is modelled as a sphere with radius of 1.5 mm. In order to reach the ultracold regime it may be possible to further cool the Li through evaporative cooling. This, in principle will reach temperatures on the order of 1 μK. Alternatively, it may be possible to directly evaporatively cool the molecules, which in itself is an exciting possibility.

6.6 Components for Trap loading

In order to load the decelerated packet of molecules and atoms into the trap, the trap must first be opened. In addition to this, the packet must also be decelerated to zero mean velocity. This section describes the proposed geometry of coils necessary to fulfill these two specifications. For reference, figure 6.15 has been included which provides an annotated drawing of the trap. The figure can be broken down into parts: the drawings of the hexapole and dipole magnets are given in views a) and b) which include the dimensions of each type of magnet. Panels c) and d) show two views of the trap and also include a series of labelled coils. These include the moving trap coil, the cancellation assembly, and the slowing coil. The function of each coil will be described below, a summary of the geometry of the coils can be found in table 6.1.

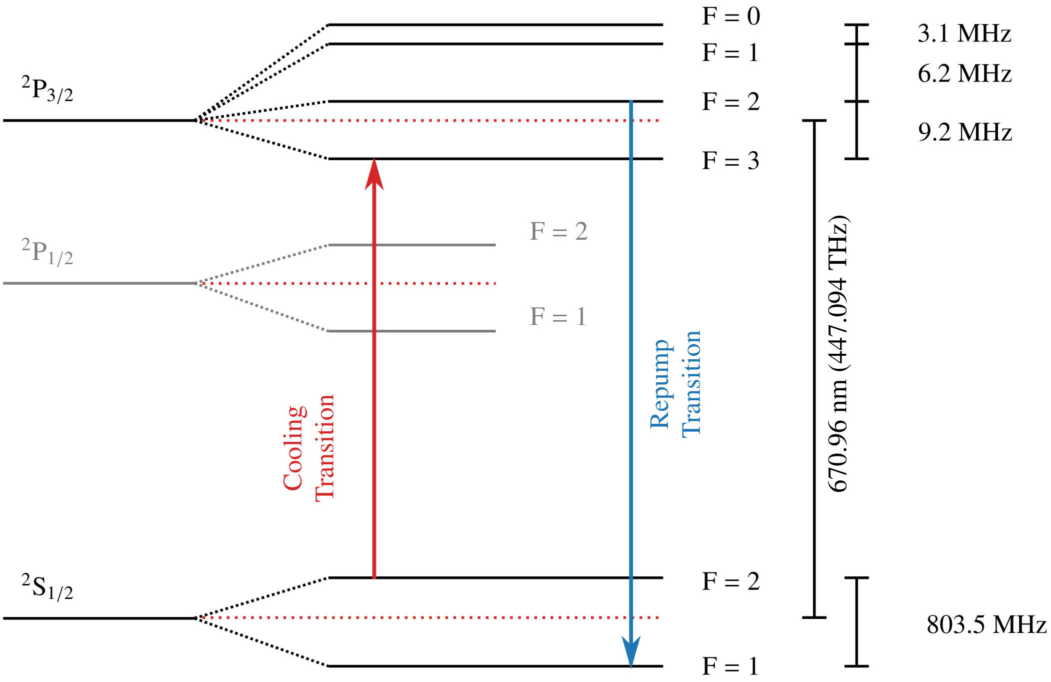

Figure 6.14: The energy level diagram of lithium-7. The relative difference in energy levels have been labelled as well as the cooling and repump transitions [2].

Coil	Wire Diameter (mm)	Windings	Coil centre to trap centre (mm)	Internal radius (mm)	Current (A)
Moving trap coil	0.5	6 × 6	17	7.4	500
Cancellation coil	0.4	2.5 × 1	7.6	5.6	190
Front trimming coil	0.4	2.5 × 1	5.6	6.0	60
Rear trimming coil	0.4	8 × 2	12.2	7.2	135
Slowing coil	0.4	8 × 3	7.6	6	200

Table 6.1: Properties of the coil elements that form the final moving trap, the cancellation field, and the final stage of deceleration into the trap.

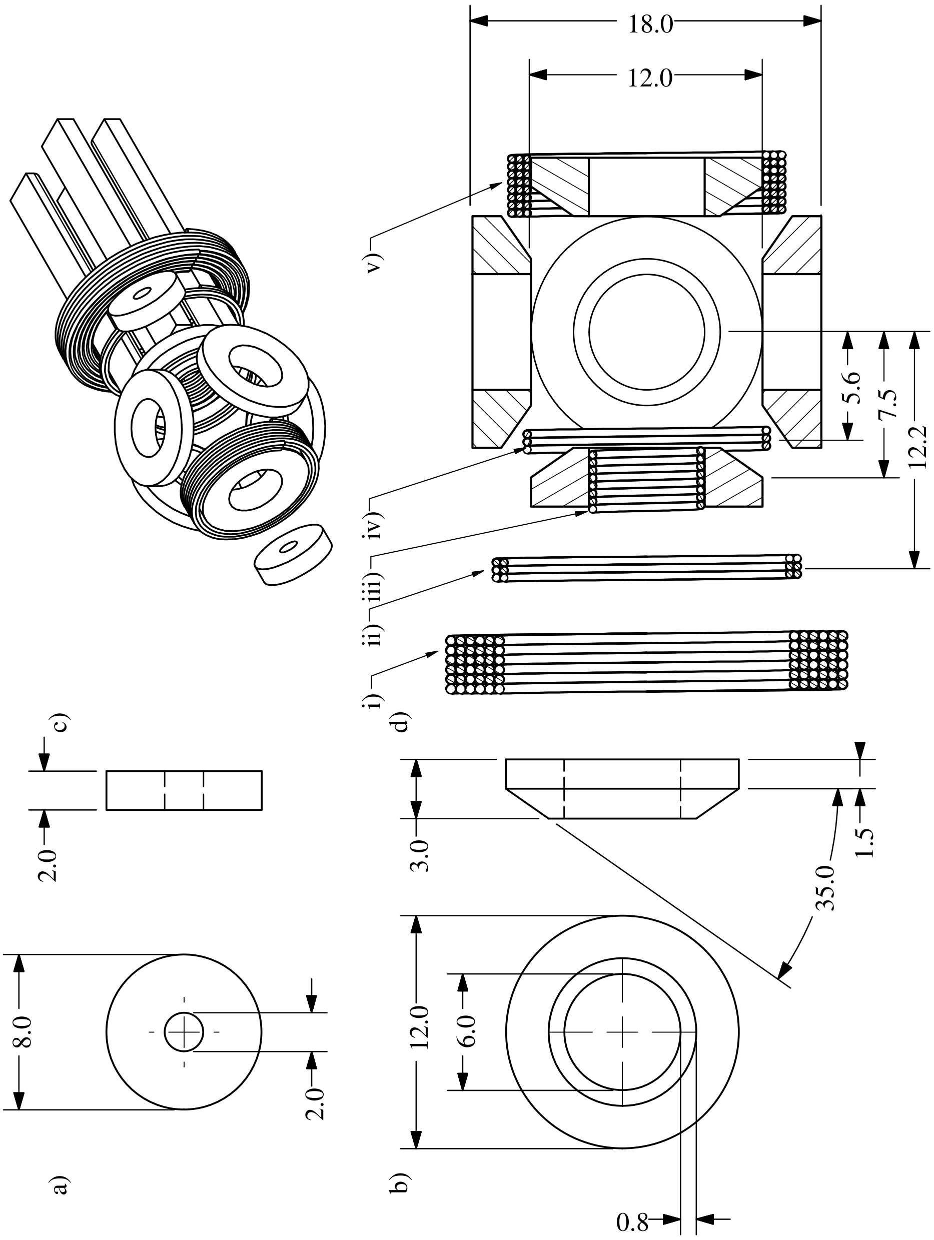

Figure 6.15: Annotated drawings of the magnets and coils required to build the hybrid trap. View a) shows an annotated drawing of a dipole magnet. View b) is the annotated drawing of a hexapole magnet. View c) show an isometric drawing of the complete trap assembly including coils and permanent quadrupole guide. Finally drawing d) is a labelled drawing of the hexapole magnets and various coils. i) The moving trap coil which, along with the helical coils, forms the last part of the travelling wave potential. The trap is designed to open close to the edge of the trap such that the spatial expansion in a field free environment in the z direction is minimised. ii) and iv) the front and rear trimming coils. These coils shape the field generated by the cancellation coil iii) to cancel the fields generated by the hexapole magnet closest to the quadrupole guide. v) the secondary slowing coil. This modifies the field generated by the back hexapole magnet to allow Zeeman deceleration to load the gas packet into the trap.

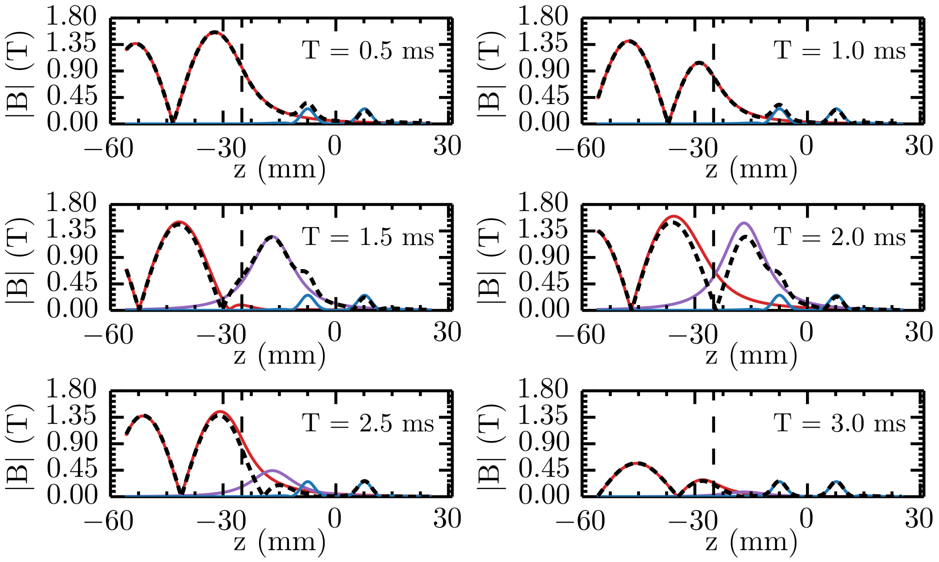

Figure 6.16: A series of time captures of the decelerator field (red) merging with the moving trap coil field (purple). The decelerator coil sits 25 mm away from the centre of the trap, the field of which is shown for reference (blue). The combination of these fields (dashed) form another stage of the travelling wave potential. The shape and velocity of this final trap is affected by the geometry of the solenoid and the shape of the current pulse used.

6.6.1 Moving Trap for 3D Guiding and Deceleration

The purpose of this coil is to close the final trap produced by the decelerator coils so that the gas packet does not expand beyond the spatial extent that is accepted by the trap. The coil consists of six by six windings in the radial and longitudinal directions. Since the coil will need to carry 500 A, the wire used is 0.5 mm in diameter. This coil sits around the quadrupole guide such that there is still net transverse focusing of the beam. The final decelerator coil sits 25 mm away from the trap centre as shown in figure 6.16. The coil is centred 17 mm from trap centre, providing space for a thin flange between the two types of coils. The current profile used relies on an exponential growth and decay of current to match that of the decelerator coil. The current through the final decelerator coil module will need to be linearly decreased to produce the correct field profile. This is possible using the PWM technique. Figure 6.16 shows the series of time captures of the fields produced by the decelerator coils, the moving trap coil field and the permanent magnet field. The plot shows how the fields add together in order to form another stage of the moving trap potential beyond the end of the decelerator (shown as a black dashed line). Due to the shape of the solenoid field, the merging of the fields from the two coils results in some change to the velocity of the trap; it may be possible to match the trap velocity by exploring other geometries of the coil and the shape of the current pulse. Finally, the transverse field produced by this coil and quadrupole is, in general, strongly focusing. This means that transverse loss is only an issue if the packet is able to travel over the maxima before the current through this coil is ramped towards zero.

6.6.2 Cancellation and Trimming Coils

The main cancellation coil is located inside the bore of one of the hexapole magnets. It consists of 8 turns along the z axis with only a single radial turn. The centre of the coil is located 7.57 mm away from the trap centre. The solenoid is constructed from 0.4 mm wire and is designed to have relatively low resistance and inductance to ensure fast switching times of the current. This is potentially crucial as the trap needs to be closed rapidly. The additional trimming coils modify the field generated by the cancellation coil to match that of the hexapole magnet. In this first iteration of the design, there are two trimming coils located near the front and back edges of the hexapole magnet. The front and rear coils are constructed from 0.4 mm diameter wire. The front coil consists of 2.5 windings in the z direction with no additional transverse loops. The coil is centred 5.6 mm from the trap centre with an internal radius of 6 mm. The rear coil consists of 2.5 longitudinal windings and has two transverse windings. It is centred 12.2 mm away from the trap centre and has an internal radius of 7.4 mm to allow the coil to fit around the quadrupole guide.

Figure 6.17 shows the total field generated from the cancellation and trimming coils along with the permanent magnets (which is also shown for reference). The plot is further broken down to illustrate the field generated by each current carrying coil. The current through the main cancellation coil is 190 A while the trimming coils are held at 60 A and 135 A for the front and back respectively. Figure 6.17a) shows the field along the z axis for each of the elements described above. Figures 6.17 b) and 6.17c) show the colourmap of the fields in the yz and the xy planes respectively. The field in the xy plane remains closed, however, the central region of the trap is only slightly modified. These figures confirm that the trap is indeed only open in the region of the bore of the magnet. A final, more pragmatic, point to make is the switching of the current. In order to achieve fast switching times of high currents a circuit similar to that which drives the quadrupole guide can be used. Depending on the load, such a circuit can easily reach several hundred Amps in the order of µs.

A final point to investigate is the effect the cancellation coil has on the transverse field. The loading process will undoubtedly become inefficient if the field becomes significantly defocusing. The cancellation coils leave a maximum residual field of 19.6 mT along the z axis which is small in comparison to the field maximum in the transverse direction. Studying the potential in the transverse direction as a function of longitudinal position shows that the field remains at least as confining as the quadrupole field whereas the transverse field within the magnets becomes more confining with a field depth of approximately 400 mT.

6.6.3 Slowing Coil

The final coil to discuss is the slowing coil. This solenoid is used to bring the molecules to rest close to the trap centre. This should optimally load the trap without large oscillations of the packet while in the trap. A fairly high mean velocity is chosen to be a compromise between loading times and expansion of the gas packet. The caveat of this co-loading is that the different masses mean that the two species are brought to rest in spatially different locations. This in itself could be problematic if the majority of the Li comes to rest outside the trap. For instance, in order to bring the co-decelerated packet to rest from 11 $\mathrm{m\,s^{-1}}$ requires a field of 463 mT for CaH. Li on the other hand is brought to rest by a mere 79 mT. Therefore the shape of this field must be considered. Another concern with this method of trap loading is that while one species is optimally loaded the other species will undergo large trap oscillation. This will be addressed later in section 6.7. The field must be tailored such that both the atoms and molecules are brought to rest inside the confines of the trap volume.

In order for the field produced by this solenoid to reach the centre of the trap, with minimal current, the coil is formed around the hexapole magnet. Additionally, choosing the direction of current flow is important. Naively, one might assume that the optimal direction of current flow would produce a vector field that results in an amplification of the field produced by the hexapole magnets in the z direction. The transverse field, however, becomes very divergent in the region of the centre of the trap. The resultant field will undoubtedly provide a loss mechanism in the transverse direction. If the current direction produces a field which attenuates the field of the hexapole the field remains far less divergent and even focusing near the trap centre. In addition, the extent of the longitudinal field

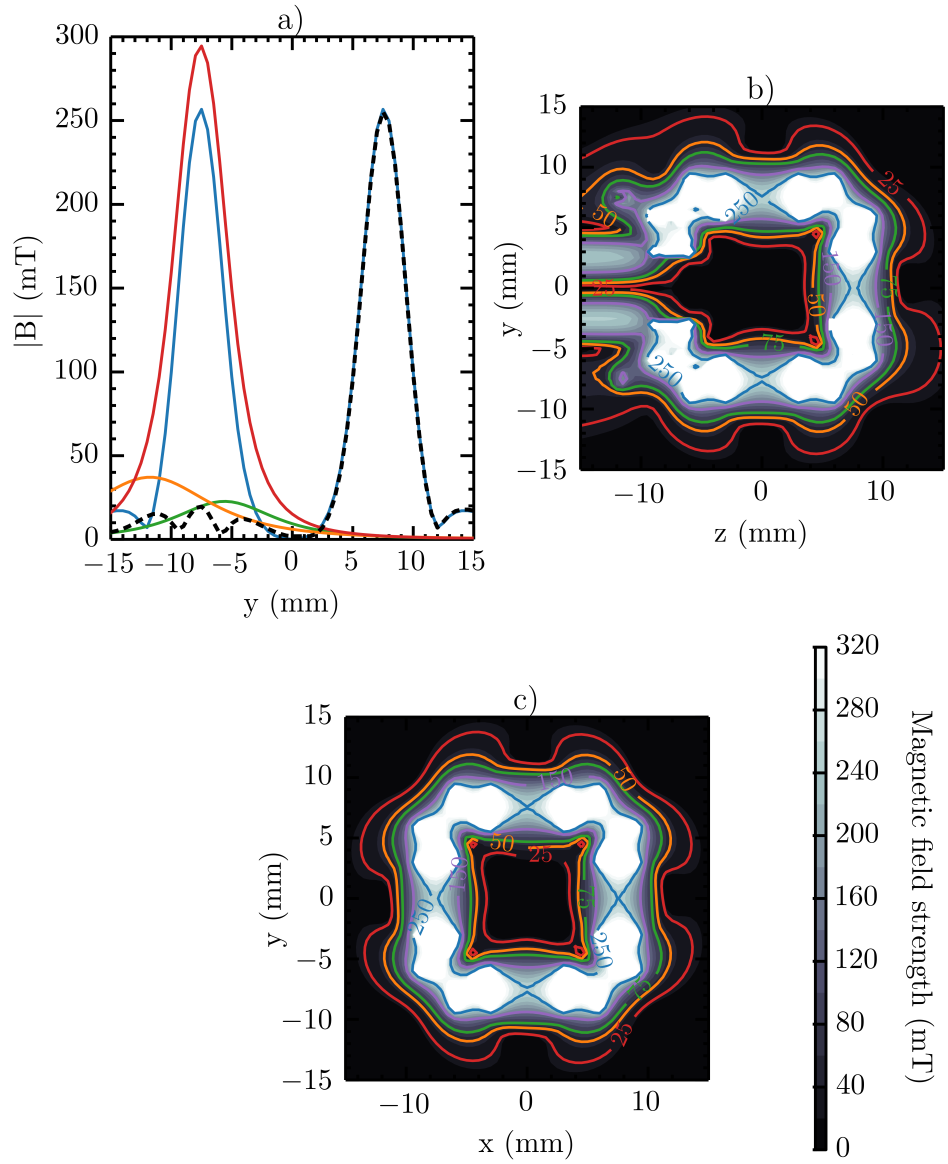

Figure 6.17: Plots of the magnetic field produced with the cancellation coil assembly active. Panel a) shows the fields produced by each element along the z axis. The fields generated include: the permanent magnets (blue), the cancellation coil (red), the front and rear trimming coils (green and orange respectively), and finally the total field (black dashed). Panel b) shows the colourmap image of the fields in the yz plane, clearly demonstrating the opening in the field generated by the cancellation coils. The permanent magnet quadrupole guide can also be seen. Panel c) shows the field generated in the xy plane at the trap centre. Contour lines (with units of mT) have been added for reference.

shape is limited to the trapping region which reduces the number of particles brought to rest outside of the trap.

The solenoid that forms the slowing coil is made from 0.4 mm wire. It is constructed from 3 radial windings and 8 longitudinal windings and is centred 7.57 mm away from the trap centre. The field produced by this coil is generated by a current of 200 A flowing through it. The internal radius of the coils is 6 mm, allowing it to sit around the hexapole magnet. Figure 6.18 shows the total field generated from the complete cancellation coil assembly and the slowing coils. Figure 6.18a) shows the field along the z axis for each of the elements described above. Figures 6.18b) and 6.18c) show the colourmap of the field in the yz and xy planes respectively. The field in the xy plane remains closed, however, the central region of the trap is modified. Despite this, the field remains largely focusing until close to the trap centre, thereby minimising the region where transverse loss might occur. Since the coupling between longitudinal and transverse motion may result in losses from the trap, the current through the slowing coil was kept low to minimise the transverse defocusing. It would, however, be beneficial to further investigate the trajectory simulations in 3D in order to determine the effect of the transverse field. It maybe possible to increase the current through the slowing coil without detriment to the transverse acceptance.

6.7 Trap loading of CaH and Li in 1D

6.7.1 Trap Acceptance

A method to determine which part of phase space of the atoms and molecules are trapped is to calculate the acceptance of the trap. This can be approximated by placing a 6D, uniformly distributed group of particles in the trap and numerically determining the trajectories. In the example shown in figure 6.19, a particle that remains in the trap volume for 100 ms is considered trapped. Each point in figure 6.19 represents the initial phase space coordinates of a CaH molecule. The red points indicate which molecules remain in the trap for 100 ms. The three panels correspond to the x, y and z coordinates in panels a), b), and c) respectively. The near-symmetric nature of the trap is reflected in these acceptance plots. The distribution of the CaH molecules after 100 ms is shown in figure 6.20. This clearly illustrates the effect of the steep potential on the arrangement of the molecules. The sharp cut-off in the spatial distribution at approximately 5 mm from trap centre is a direct result of this. The calculated maximum trapped velocity is 8.34 $\mathrm{m\,s^{-1}}$, which is also reflected in these numerical simulations. The acceptance of the trap is 2.09×10^6 $(\mathrm{mm\,m\,s^{-1}})^3$ for CaH and 2.56×10^7 $(\mathrm{mm\,m\,s^{-1}})^3$ for Li.

A final point to consider is the comparison of the emittance of the decelerator to the acceptance of the trap. This will indicate, to some extent, the efficiency of the trap loading process. Since the emittance of the gas packets of Li and CaH are smaller than the acceptance of the trap this indicates that, at least in principle, the entirety of the gas packet should be loaded. However, after examining the spread of emitted and accepted velocities it is clear that without further phase space manipulation the Li packet is too hot for the trap in both the y and z directions. The same conclusion can be drawn for both types of quadrupole discussed. Therefore, it is likely that the loading of the Li packet will be less efficient than the CaH. This implies that the buffer gas source of Li must be brighter than that of the CaH in order to load more atoms than molecules for sympathetic cooling.

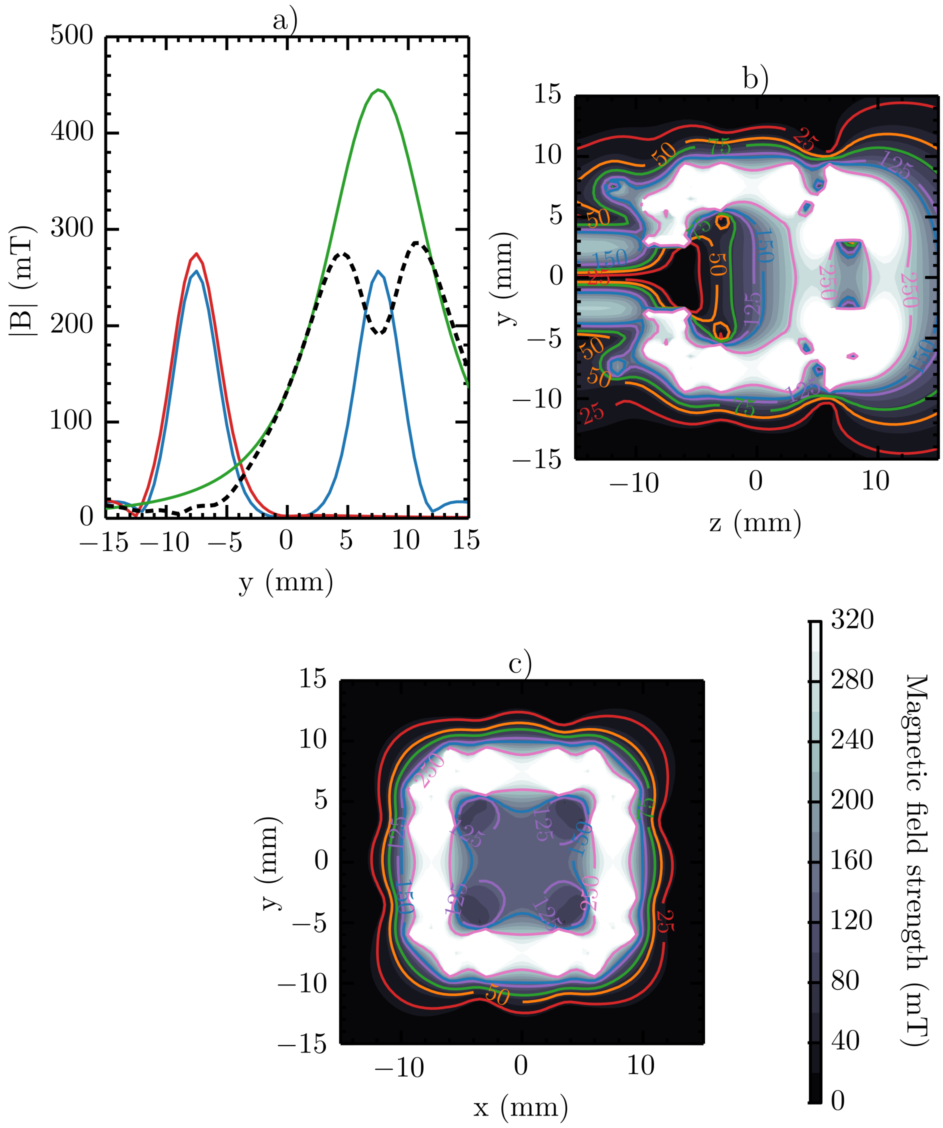

Figure 6.18: Plots of the magnetic field produced with the cancellation coil assembly and slowing coil active. Panel a) shows the fields produced by each element along the z axis. The fields generated include: the permanent magnets (blue), the cancellation coil assembly (red), the slowing coil (green), and finally the total field (black dashed). Panel b) shows the colourmap image of the fields in the yz plane, once again showing the open nature of the trap with the modification of the potential gradient along the z axis. The permanent magnet quadrupole guide can also be seen. Panel c) shows the field generated in the xy plane at the trap centre. Contour lines (with units of mT) have been added for reference.

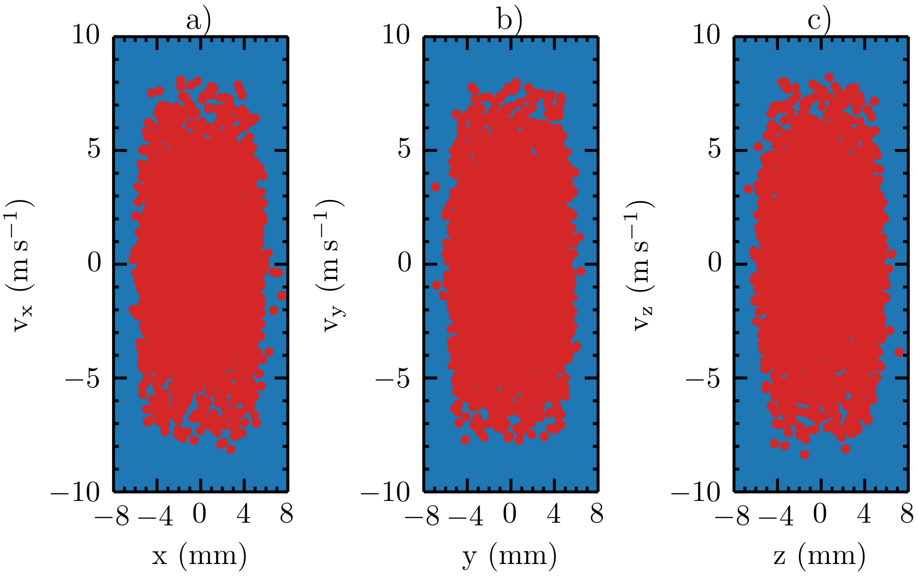

Figure 6.19: The acceptance into the permanent magnet trap for CaH. The plots show which of the molecules from the initial distribution remain in the trap after 100 ms. Each point represents the initial phase space location of the molecules. The red points represent which of these remain in the trapping volume after 100 ms and are regarded as accepted by the trap. The particles that are lost are shown in blue. The accepted distribution of molecules in each direction is similar due to the near-symmetric nature of the trap.

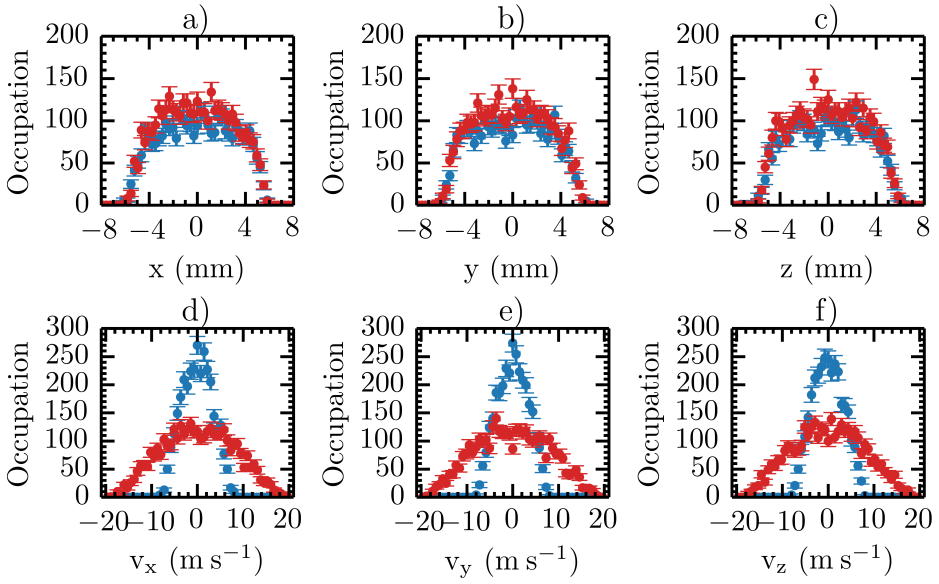

Figure 6.20: Histograms of the final distribution of CaH (blue) and Li (red) after 100 ms in the trap. The upper row shows the spatial distributions of the particles. The sharp edge of both these distributions clearly reflects the steep edge of the trap. The lower row displays the final velocity distribution of the two species.

6.7.2 Modelling the Loading of the Trap

The loading process is described below and was designed by considering solely the CaH molecule and altering parameters to load more Li atoms. This is a fairly limited approach and thus future work will continue to find a compromise between the loading of the Li and CaH. In the following discussion 100,000 particles were simulated. Their initial distributions were obtained through fitting Gaussian distributions of the previously discussed 3D deceleration simulations. The loading procedure begins after the deceleration process is complete. The final trap continues to 3D guide the atomic and molecular packets until the centre of the distributions are 16 mm away from the trap centre. Although the final decelerator trap is not completely open, some expansion of the packet will occur in the 4 mm region before it reaches the trap edge. This can be seen in the final panel of figure 6.16 where the trap becomes fairly flat bottomed in the longitudinal direction. There is additional 2D confinement in this region due to the quadrupole.

Once the packet reaches the edge of the trap it possesses a mean velocity of 11 $\mathrm{m\,s^{-1}}$. This is above the capture velocity of the trap and thus must be removed for efficient loading. This value of mean velocity was chosen as a compromise. A fast mean velocity is beneficial as it minimises the heat load from the coils and the expansion of the gas packet. It also results in a Li packet which has fewer atoms with a negative velocity when the trap opens. On the other hand, high mean velocities require large fields in order to Zeeman decelerate the packet. The CaH packet is first decelerated by the outside edge of the trap, this stage removes approximately 2.6 $\mathrm{m\,s^{-1}}$. The cancellation coil is then activated, nullifying the field and removing a portion of the kinetic energy of the packet. This is ultimately the same technique employed by conventional Zeeman decelerators. To load more Li, this process needs to occur twice, once for the CaH packet and once approximately 1 ms earlier for the Li packet which expands rapidly beyond the CaH. This results in loading almost twice as much Li.

Immediately after this first deceleration process the second phase begins by activating the slowing coil. Yet more kinetic energy is removed using this coil. The molecular packet is slowed until the synchronous particle has a mean velocity of 1.5 $\mathrm{m\,s^{-1}}$. This places the packet close to the trap centre at the expense of small amplitude bulk oscillations. The entire loading process is completed within 4.5 ms. Since the Li will be decelerated to a standstill much sooner than the CaH it is necessary to apply additional fields to accelerate the Li back towards the trap centre. Pulsing the moving trap coil briefly more than triples the Li loading efficiency. During the later stage of deceleration this can be achieved by deactivating the cancellation coil to prevent the Li from leaving the trap volume. A summary of the time dependence of the magnetic potential in 1D can be seen in figure 6.21.

Figure 6.22 illustrates the sequence of current pulses required for the the loading process described above. Three times have been selected and the field along the z axis plotted at that time. The shape of the current pulses for the cancellation and slowing coils were assumed to have a rise and fall time which is on the order of tens of μs and hence are not visible on this time scale. At time point i) the decelerator and moving trap coils are 3D guiding the gas packet towards the centre of the trap. Time point ii) shows the second phase of deceleration where both the slowing and cancellation coils are active. The moving coil also becomes briefly active to accelerate Li with a negative velocity back towards the trap. Finally, time point iii) shows that after the deactivation of the cancellation coil the rear trap edge is restored preventing escape of the Li.

The trajectories of a gas packet in 1D can be investigated. In this simulation, a 2D interpolator was employed to incorporate the time dependence of the fields. Column a) of figure 6.23 shows a series of time captures of the potential experienced by the CaH molecules. The initial phase space distributions of the molecules were taken from the 3D Monte Carlo simulations described in section 6.3. The molecules have a mean velocity of 11 $\mathrm{m\,s^{-1}}$ and experience the potential mapped in figure 6.21. Column b) of figure 6.23 shows the phase space distribution of the molecules at the time displayed. The 1D separatrix of the trap is also plotted. The model evolves the system for 100 ms after which 52.2 % of the original molecules remain in the trap. In the simulations the packet was

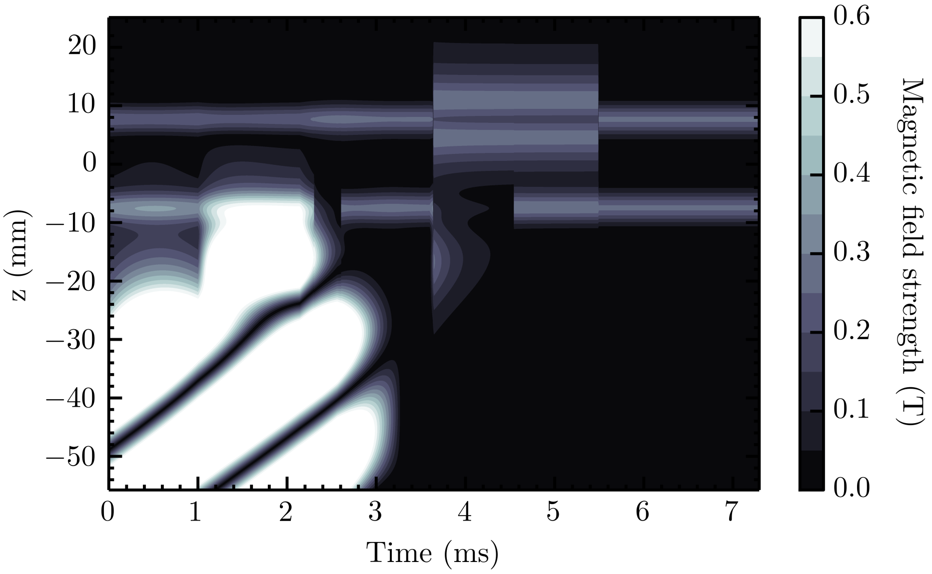

Figure 6.21: The loading sequence of particles into the magnetic trap. The time dependent field is shown along the z axis. The plot shows how the combination of coils are used to open, slow, and eventually load the trap. In this example the last phase of transport of the molecular and atomic packets are 3D guided at a constant velocity into the trap.

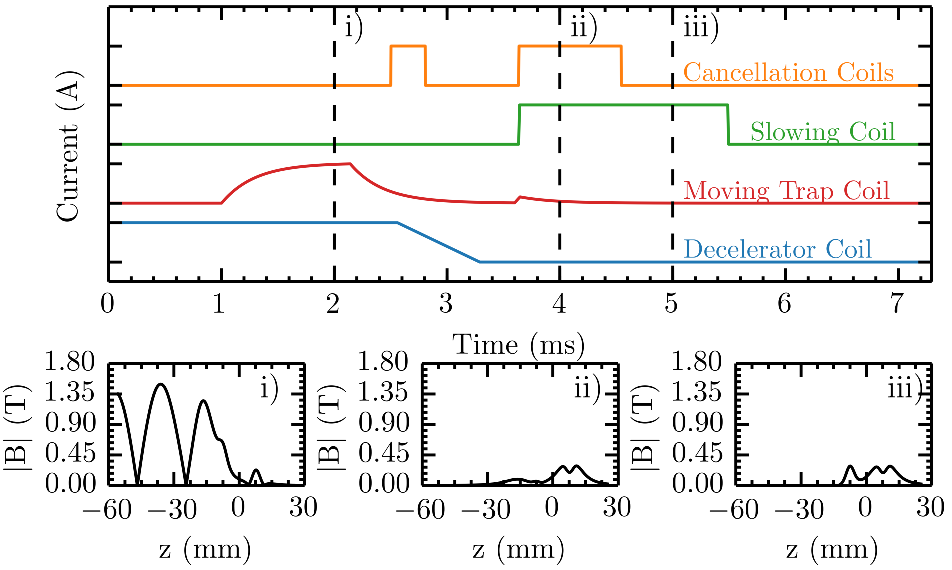

Figure 6.22: A schematic view of the magnitude of the current pulses through each coil. Each pulse has an associated rise and fall time, although not visible on this scale for the cancellation and slowing coils. The lower panels show the potential along the z-axis at 2, 4, and 5 ms as marked on the diagram.

3D guided to the edge of the trap, however further simulation would be beneficial to investigate decelerating up to the trap edge. A similar study can also be conducted with Li. As expected the loading is not nearly as efficient, only loading a mere 7.3 %. For efficient sympathetic cooling, the atomic number should exceed the molecular number by at least a factor of 100 [206]. Given the larger number of Li atoms decelerated the source of lithium will need to be 130 times brighter than the CaH source to meet this specification, which seems achievable with buffer gas sources [30]. The capture efficiency of the trap can be used to estimate the density of CaH and Li in the trap. A buffer gas source of CaF in the $N = 0$ state of both the electronic and vibrational ground states was used as a basis for these calculations. This has a flux of 1.9×10^{11} molecules sr^{-1} pulse^{-1}. Combining the simulations described above results in a trap density of 4.98×10^{6} molecules cm^{-1} in the spin stretched $|N = 0, F = 1, m_{\text{F}} = 1\rangle$ state. The density of Li should therefore have to be at least 100 times greater in order for sympathetic cooling to take place. In general, 1D models are useful to give an idea of the broad picture of a system, however, as mentioned previously, a full 3D time-dependent model will be necessary to obtain a true picture of the loading process. It is clear from figure 6.23 that there are a large proportion of molecules which are not sufficiently decelerated by the slowing coil and clearly a stronger deceleration field is required. This once again emphasises the need to explore the effects of the transverse field, particularly while the slowing coil is active.

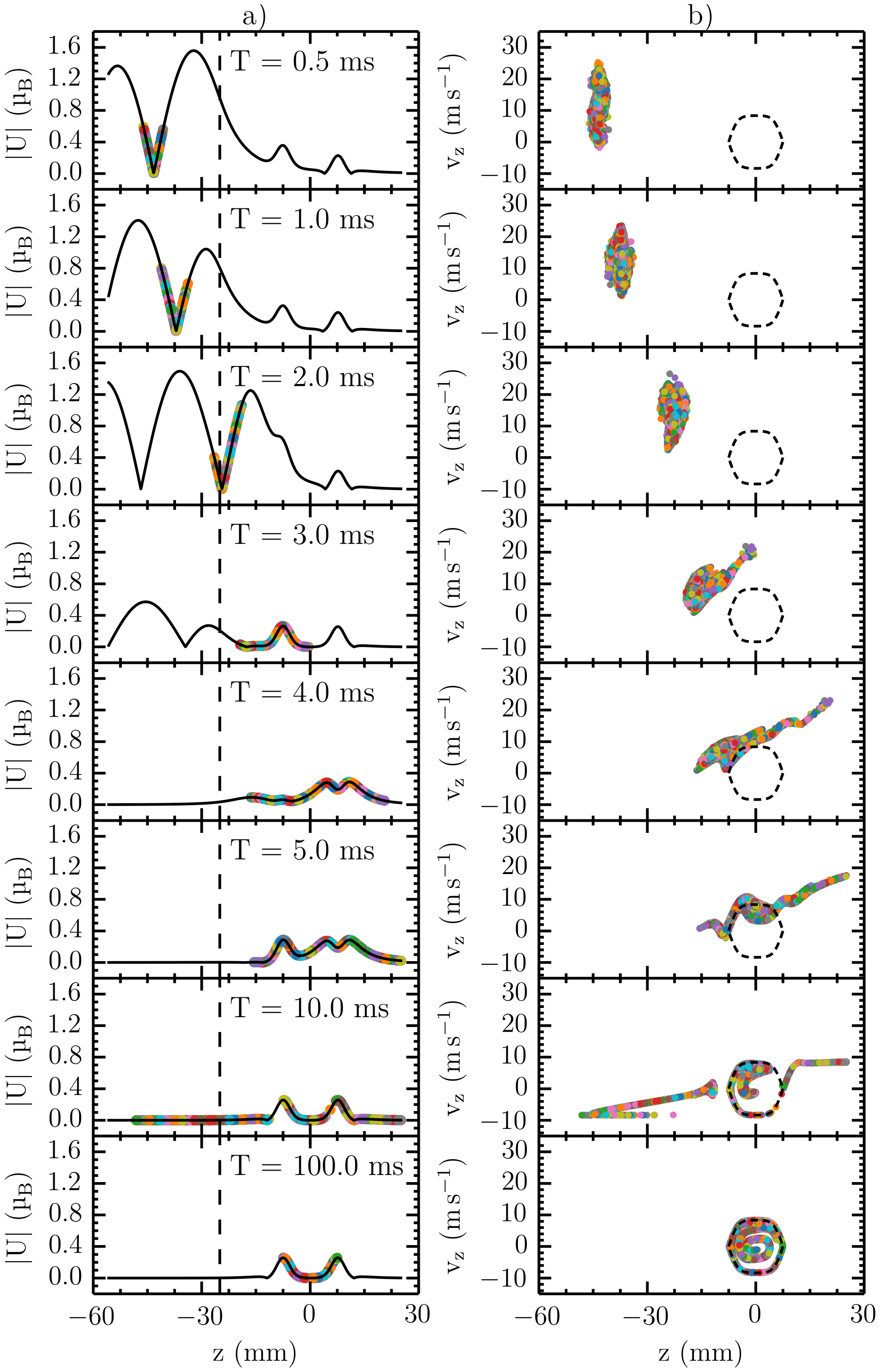

Figure 6.23: Time captures of the loading process of CaH into the trap. Column a) shows the total potential experienced by the CaH. The location of the molecules is represented by the points. For reference, the end of the decelerator coils is shown (dashed line). Column b) shows the phase space distribution of the molecules at each of the times shown in the left column. The 1D separatrix of the trap is also displayed (dotted line)

6.8 Chapter Summary

In this chapter the short and long term goals of the decelerator project have been presented. The immediate objective is to study the decelerator while operating at its full potential with metastable argon. The goal after that would be to decelerate the methyl radical. The long term goal of the project is to decelerate large ensembles of cold molecules. In order to increase the efficiency of the deceleration process, it is advantageous to extend the decelerator to nine coil modules. Combining this with a buffer gas source, producing molecular packets with a mean velocity below 200 m s^{-1}, the magnitude of the pseudo potential would be minimised. This will allow a wide range of molecules to be decelerated to the cold (mK) regime. To reach the ultracold regime (μK) an additional cooling method will need to be introduced. One promising technique is sympathetic cooling, where an ultracold sample of atoms cool the cold molecules. A system which already has received experimental and theoretical attention is CaH and Li. Furthermore, the CaH-Li system offers the possibility to investigate the dependence of reaction and collision cross-sections on the molecular orientation (in the presence of an external field) and the quantum state that the molecules and atoms occupy. Furthermore, the experiment will provide a means to investigate the characteristics of atom-molecule collisions over a range of temperatures.

Using a permanent magnet quadrupole certainly has advantages. Notably, the lack of fringe fields and negation of the need to dissipate heat. With an N50 NdFeB magnet, the field gradient is a factor of two greater than the wire quadrupole at 700 A. The trade off, however, for a decelerator of length 1.18 m, is that the 6D acceptance decreases. It was found that the acceptance fell from 1.9×10^4 (mm m s^{-1})^3 to 9.2×10^3 (mm m s^{-1})^3 of CaH and from 2.1×10^6 (mm m s^{-1})^3 to 4.5×10^5 (mm m s^{-1})^3 for Li. The explanation of this is that the potential generated by the combination of the decelerator coils and the permanent magnet quadrupole has a turning point near the inner edge of the steel tube. This is particularly problematic in the x direction. The weaker transverse confinement couples the longitudinal motion of the particles in the trap leading to an increase in losses in the x direction. Although it is unlikely that a permanent magnet quadrupole with the same geometry as the current quadrupole will increase the acceptance of the decelerator, the clear advantages of the permanent magnet quadrupole merits further work. It seems likely that a different geometry of poles could be tailored to produce a linear field throughout the diameter of the steel tube while increasing the trapping gradient further.

The concept of a trap suitable for capturing the co-decelerated packets of Li and CaH has been described. The combination of the steep hexapole potential and the weaker dipole field produce a potential that should allow the formation of a 3D MOT. Moreover, the weak quadrupole field lifts the flat bottom of the potential which should keep the rate of Majorana transitions low. The MOT will allow the further cooling of the Li, and with the combination of evaporative cooling of the Li or even the molecular sample, the 1 μK limit can be reached. The simplified characteristics of the MOT were explained and suggests that the MOT should be able to capture the Li loaded into the trap. It has also been possible to estimate that 63 % of the molecules will enter the MOT volume in approximately 18.2 ms, assuming that the MOT volume is a sphere with radius of 1.5 mm. The design of a series of coils has been discussed and how they are applied in the loading sequence described. The purpose of these coils is to guide the gas packet to the edge of the trap from the decelerator coils. Additional coils open the trap and bring the molecules to near rest within the trap. The efficiency of the loading process in a 1D model is 52.2 % for CaH and 7.3 % for Li. This will require a Li source at least 130 times brighter than the CaH source. Estimates of the trap density of CaH was found to be 4.98×10^6 molecules cm^{-1} in the spin stretched $|N = 0, F = 1, m_\mathrm{F} = 1\rangle$ state. Further work must be undertaken to find the effect of the transverse field. The model presented here kept the current through the slowing coils low to minimise the defocussing nature of the transverse field. Understanding the effect this has may allow the loading of the trap to be optimised, particularly for Li.

Chapter 7

Conclusion

Due to the wide range of possible applications of cold and ultracold molecules, great efforts have been made to produce large ensembles of molecules at very low temperatures. An overview has been given of the techniques developed to produce cold and ultracold molecules and several important applications that molecules can be employed in have also been discussed. Zeeman decelerators have be used for a decade to produce samples of atoms and molecules which can be trapped for further experimentation. These devices depend on the Zeeman effect, which describes the interaction between an external field and a paramagnetic atom or molecule. Despite the success of these conventional Zeeman decelerators, they offer limited phase space acceptance due to their design. The fields produced allow the transverse and longitudinal motions to couple, providing loss channels through both defocusing and over-focusing of the low-field-seeking states. One way to overcome this problem is to create a 3D moving magnetic potential to decouple the transverse and longitudinal motions. One such scheme is the travelling wave Zeeman decelerator presented here. The goal of this project is to use the decelerator as a first stage to produce molecules over a range of temperatures as low as the ultracold regime. The inelastic and reactive collisions in atom-molecule systems can then be controlled to empirically study collisions in these systems. The motivation behind this pursuit is that the theoretical prediction of the cross-section for collisions and reactions are typically computationally intensive. The Zeeman decelerator developed here is a versatile tool for the deceleration of a wide range of atoms, molecules, and radicals. Sympathetically cooling the molecules with ultracold atoms would allow for the examination of the dependence of reaction and collision cross-sections on the molecular orientation (in the presence of an external field) and quantum state of both the molecule and atomic species.

An overview of the various parts of the decelerator has been presented in chapter 2. This began with details of supersonic expansion which is the initial source of cold atoms, molecules, and radicals. A brief introduction of the theory behind supersonic expansion has been provided as well as some of the technical details of the Even-Lavie valve and the dielectric barrier discharge used as the excitation scheme. To accommodate this valve, the layout of the source chamber was explained such that effects like skimmer interference was minimised. The operation of the decelerator has also been reported. The decelerator does not cool the gas packet in the strictest sense but instead selects a fraction of the gas packet and decreases the mean longitudinal velocity to zero. This occurs while maintaining the high density of the accepted packet. The design of this decelerator was originally proposed by Trimeche *et al.* and relies upon the combination of flattened helical coils and a quadrupole guide. The former is periodic and generates the deep, moving potential in the longitudinal direction. This requires the application of high magnitude sinusoidal currents (up to 1000 A peak) to each phase of the coil. The multiple coil phases create more effective current loops, allowing for a smooth translation of the trap, while the extra coils improve the field gradient produced by the coils. The quadrupole guide is required in order to supplement the weak transverse confinement of the decelerator coils, particularly in the x direction. The design of the quadrupole was selected to maximise the field gradient of the quadrupole without compromising the field produced by the decelerator coils. The velocity that the trap moves at is determined by the frequency of the applied current. Therefore, if a linearly chirped down sine wave were applied, the trap can be decelerated. The deceleration causes the trap to tilt, lowering the front edge of the potential. This limits the effectiveness of the deceleration process. A compromise between efficient deceleration and the final mean velocity of the packet must be made. Finally, the MCP used as the detection scheme to measure the TOF profile of metastable argon was described. The MCP is a convenient detection scheme as metastable argon can be detected without additional excitation schemes owing to the high internal energy of the metastable state.

Chapter 3 presented the design specification and the evaluation of the components of the control and power electronics. The control electronics are based around a FGPA unit which has an adequate number of outputs for address bits, the triggers for the positive and negative parts of each phase and the quadrupole triggers required for the project. These pulses are sent to the power electronics through an optical-coupler. This is beneficial as it not only breaks a significant number of potential earth loops, it also reduces the length of the signal conductors which further decreases the amount of noise introduced into the control circuit. Multiplexing the control electronics for the decelerator coils has kept both the size and cost of the circuitry low. To achieve this, the coils are divided into two groups depending on the coil's position in the decelerator. This is only possible as coils in the same group are never active simultaneously. The even number coils are in one group while the odd numbered coils are in the other. This circuitry reduces the number of outputs from 64 (demultiplex) to 20 consisting of two sets of 8 signal channels and 2 sets of 2-bit address channels.

The quadrupole electronics must be able to produce a constant current of 700 A for a few milliseconds. It is also necessary to avoid the regions of magnetic field that are produced at the ends of the quadrupole where the various electrical connections are made. The duration and magnitude of this current pulse requires a power supply, however, supplies of this type intrinsically possess large rise and fall times associated with the currents. Therefore, an electronic circuit is required to modify the current from the power supply to add fast rising and falling edges. This circuit relies on the fast rising current pulses obtained through shorting a capacitor to earth. The same capacitor can also be used to reduce the fall time in current by driving the decay of the energy stored in the quadrupole. The electronics are capable of producing a current pulse with a rising edge of 58.4 µs and a falling edge of 178 µs with the kick circuitry charged to 60 V. For reference, the hold supply alone produces current pulses with a rising edge of 362 µs and a falling edge of 209 µs. The fields generated by the quadrupole were compared to theory and the heat load of the coil investigated. The latter may prove problematic, particularly with longer length quadrupoles.

The specification and evaluation of the decelerator power electronics were also presented in chapter 3. Each decelerator coil phase requires a sinusoidal waveform up to 1000 A peak from 10 kHz to DC each offset by $\pi/4$ radians. The technique used to generate the AC waveform from a DC supply constructed from capacitors was described. The direction of the current flow through the coil phase is alternated using an H-bridge. The AC waveform is syntheised by making use of the inductance and resistance, and hence the finite rise time, of each coil phase. Pulse width modulation is used to encode an analogue waveform into a series of digital pulses which are calculated in advance with knowledge of the inductance and the resistance of the coil phase. These properties, along with analytic expressions for the rise and the decay of the current through the coil, can then be used to synthesise a current waveform with characteristics similar to the ideal target waveform. The disadvantage to this technique is that the peak current drawn by the coil and the quality of the sine wave is dependent upon the electrical properties of the coil. As well as describing the design of the power electronics, the justifications for the circuit layout and the choice of the components made. This included considerations of circuit inductance, resistance, and transient voltage spikes. Several aspects of the performance of the power electronics have been evaluated. Firstly the measured current waveform generated for two frequencies was presented. This proved that the PWM technique has the ability to generate a waveform with an arbitrary frequency and peak magnitude. A low current study of the magnetic fields produced by the decelerator coils allowed the motion of the traps through the coil to be investigated. This highlighted that the PWM technique causes the field depth to vary over time and that there is a difference in the target trap velocity and the measured trap velocity. Measurements of the trap velocity vary from the target by no more than 1% provided that at least 4 pulses are used to produce the current waveform. This technique does in fact limit the ability to fine-tune the trap velocity which may be a problematic factor at the very low velocity regime. The measured fields were then compared to theory which demonstrated the ability to simulate the fields.

The algorithms developed in order to simulate the decelerator were described in chapter 4. The method used to emulate the source within the Monte Carlo simulations of the decelerator was described. The method relies on geometric arguments to determine the transverse velocity of the gas packet from a longitudinal distribution. The simulation only requires the peak velocity and the temperature of the gas packet as inputs. This technique determines a range of transverse velocities accepted by the skimmer without the need for complex direct Monte Carlo simulations of the valve. The procedures used to calculate the fields generated by the decelerator and quadrupole fields were described. Since the wires that form the decelerator coils do not lie in parallel in the laboratory coordinate system, it is necessary to rotate the point where the field is calculated into the coordinate system of the wire. Once in this frame, the magnetic field can be calculated at an arbitrary point for a finite length wire. The field in the laboratory frame can be obtained through a second rotation. The quadrupole field can be calculated by approximating the poles as infinitely long wires. The tricubic interpolator used to calculate the field gradient at an arbitrary point was also described. The algorithm generates a 64×64 matrix describing the relationship between the derivatives of the potential and the coefficients of the tricubic interpolator for each cell of the generated field. The benefit of a local interpolator, such as that described here, is that they do not require fitting to the entire data set.

The effects of the synthesised current waveform on the dynamics of the trap was also discussed. To achieve the former, the trap generated by the synthesised waveform was compared to that generated by a pure current waveform. The PWM results in the trap depth varying over time as well as a change in the velocity of the trap. The trap minima oscillates around the trajectory of the average fitted velocity with an amplitude of approximately 1 mm. The occurrence of these oscillations are consistent with the switching events that produce the synthesised current waveform. The magnitude of these oscillations is dependent on the number of switching events. The amplitude tends to be smaller for waveforms that contain more switching events. The pure waveforms considered here also show trap oscillations, however, these are on the order of μm. In each of the velocities discussed, the PWM resulted in a trap velocity lower than the target. For instance while trying to synthesise a trap moving at 300 $\mathrm{m\,s^{-1}}$ the actual trap moves at an average velocity of 297.4 ± 0.2 $\mathrm{m\,s^{-1}}$. The synthesised waveforms introduces large fluctuations in the trap depth, on the order of 10 mT in x, 80 mT in y, and 130 mT in z for both frequencies considered. The amplitude of the fluctuations for the synthesised waveform in the z direction are on the order of approximately 5 % of the average field depth.

Chapter 4 also justified the method used to emulate the variation of the trap in the simulations. The characteristic frequency of the trap does not exceed the order of a few kHz which is true for all the atoms and molecules studied in this thesis. The properties of the trap vary within a frequency range of 40 to 180 kHz depending on the number of switching events present in the current waveform. This range has been derived through consideration of the rate of switching events and analysing the periodicity of the oscillations in position and trap depths. This difference in frequencies is large enough that the particles do not respond fast enough to react to the rapidly changing field but instead feel the average potential. To create the potential, a single 3D trap is calculated for a pure current waveform. Then a correction factor is applied which lowers the field depth. The correction factor is calculated from time-dependent 1D simulations which can be calculated quickly while maintaining a high sample rate to accurately capture the changes in the field. The limitation of this method is that despite the potential along the z axis possessing many of the features of the transverse fields, the magnitudes of these features tend to differ. After scaling, the average difference is approximately 1.4 % in x, and 2.5 % in y. The oscillations of the trap around its average trajectory is added in the Monte Carlo simulations, which is approximated by modifying the trajectory of the trap with a sinusoidal oscillation in position. The magnitude is set through the 1D simulations while the frequency is set by the occurrence of the current switching events. This chapter concluded by explaining the formation of the travelling magnetic wave using two interpolated traps. This builds further time dependencies into the simulation in order to more accurately capture the fields while keeping the complexity of the simulations low.

The characterisation of the decelerator, both theoretically and experimentally, with metastable argon was the focus of chapter 5. Metastable argon is a convenient species because of its magnetic characteristics and the properties of a gas pulse after supersonic expansion. The acceptance of the decelerator, using both a pure sine wave and the synthesied current waveforms, has been analysed for the $m_J = 2$ state of metastable argon. The acceptance, while 3D guiding, is proportional to the trap velocity which is a result of the extended interaction time with the field. This trend holds for the two types of current waveforms employed and is also true for the four and nine module long decelerators considered. In this mode of operation, the synthesised waveform has little impact on the acceptance of the trap although the acceptance of the trap tends to be smaller for higher target velocities. This is probably a consequence of the lower trap depth that is produced by the synthesised current waveform. The rapid trap oscillations caused by the PWM seem to increase the transverse confinement at the longitudinal maxima of the trap. This tends to increase the acceptance of the trap compared to a trap generated by a pure current waveform. The acceptance of a nine module long decelerator in the deceleration mode has also been explored. The acceptance of the decelerator with a synthesised current waveform rapidly decreases because the velocity of the trap cannot be fine tuned and because of the lower trap depth that the synthesised current waveform produces. The acceptance of the decelerator decreases by four orders of magnitude in the range of deceleration magnitudes between 0 and 5.56×10^4 m s^{-2}. The general trend in the acceptance is very different for the 1D and 3D simulations, which means that there are additional transverse effects that limit the acceptance of the decelerator. Further study has shown that the decelerator tends to benefit from lower initial velocities. For initial velocities above 350 m s^{-1} the limiting factor is the lack of transverse confinement near the longitudinal trap maxima. This limits the maximum deceleration to approximately 5×10^4 m s^{-2} for a trap generated from 1000 A peak. Below an initial trap velocity of 350 m s^{-1}, the acceptance behaves more like the 1D case which indicates that the longitudinal and transverse motion of the particles in the trap remain uncoupled. The simulations have shown that the limiting factor for the decelerator in its current form is certainly the lack of transverse confinement particularly in the x direction. This results in the longitudinal and transverse motion of the particles experiencing some coupling. The advantage of this form of decelerator is that the transverse field can be altered separately to that generated by the decelerator coils. This allows more complex arrangements of magnetic poles to be tested. It has been shown that even a modest increase in the transverse confinement can further enhance the acceptance of the decelerator in the 3D guiding mode.

The experimental results from the four module long decelerator have been reported for the Even-Lavie valve held at 138.5 K. Due to the highly directional nature of the valve, the measured and calculated TOF profiles exhibited little increase in the integrated signal when the quadrupole field generated by 700 A was applied. A modest increase in signal could be achieved in an ideal quadrupole where the entirety of the quadrupole could be utilised and the current source could be instantaneously switched. The results of the decelerator operating in the 3D guiding mode were presented. The effects of the delay between the activation of the DBD and the decelerator coils have been examined in 1D. This was used to highlight the unique problem associated with trap loading due to the wave-like nature of the magnetic field. Due to the temperature of the gas pulse, multiple traps can be loaded which makes the choice of the delay between the DBD and the activation of the decelerator an important variable since only a few traps can traverse across the boundary between two adjacent coils. Both the experimentally and numerically produced TOF profiles for three trap velocities were presented. From the 1D field simulations the average trap velocity was actually found to be 351, 373 and 393 $\mathrm{m\,s^{-1}}$, this difference for the target trap velocities is a consequence of the PWM technique while trying to maximise the peak current to 500 A. The ability to 3D guide and decelerate were severely hampered by the failure of the contactors used to isolate the power electronic modules. Nevertheless, peaks in the velocity distribution of the simulated data showed successful 3D guiding. The deceleration results in particular are limited as the coils operating at 100 A peak as this lowers the acceptance of the decelerator. Due to the delay between the DBD and the activation of the deceleration coils, the initial velocity of these decelerated particles was lower than expected. The trap which is loaded is not the first but one of the subsequent traps after the wave begins to move. The peaks of interest for two examples of deceleration shown here actually have fitted initial and final trap velocities of 350 to 346 $\mathrm{m\,s^{-1}}$ and 342 to 304 $\mathrm{m\,s^{-1}}$. The final peaks in the velocity distribution occur at 347.3 and 310.3 $\mathrm{m\,s^{-1}}$ due to the hard switch off of the potential used in the simulations. This indicates deceleration to some extent, although not by the amount originally intended.

The differences of the arrival time of the peaks in the simulated and experimental data arise from a number of factors. These include errors associated with parameters such as the location of the first coil and where the first trap is considered to be formed. Even standard errors in position on the order of 1 mm causes the peaks to shift up to 10 µs. Subtle differences such as those between the ideal and the actual coils were also considered. The average period length of the decelerator was found to be approximately 0.4 mm longer than the ideal period which led to further deviations in the simulated data. Finally, the limitations in the current experiment were discussed. Addressing the issues with the current apparatus would allow the deceleration from 360 to 290 $\mathrm{m\,s^{-1}}$. This is an exciting prospect because starting at a lower initial velocity (i.e. slower than the peak velocity of the distribution), the final velocity of the decelerated gas packet could be taken outside of the main distribution. Additionally, the intensity of the guided or decelerated peaks can be maximised by further increasing the interaction time with the quadrupole. Optimisation software could be used to find a suitable starting set of parameters particularly for the delay between the DBD and the activation of the decelerator. The current experiment is severely limited by only being able to examine important characteristics such as the velocity of the trap *post factum*. Even 1D optimisation software would be an invaluable tool to inform the operator of the experiment on their choice of parameters.

Chapter 6 presented the short and long term goals of the decelerator project. The immediate objective is to study the decelerator while operating at its full potential with metastable argon. The goal after that would be to decelerate the methyl radical. The long term goal of the decelerator is to use the decelerator to produce large ensembles of cold molecules. In order to increase the efficiency of the deceleration process, it is advantageous to extend the decelerator to nine coil modules. Combining this longer decelerator with a buffer gas source would further minimise the magnitude of the pseudo potential experienced by the molecules during deceleration. This will allow a wide range of molecules to be decelerated to the cold (mK) regime. In order to investigate the collisions of atoms and molecules down to the ultracold regime (µK) although additional cooling would be needed. Sympathetic cooling of the cold molecular sample with an ultracold atomic species seems a promising technique. One system which already has received experimental and theoretical attention is CaH and Li. This also offers the possibility to investigate the dependence of reaction and collision cross-sections on the molecular orientation (in the presence of an external field) and the quantum state that the molecules and atoms occupy.

Additional improvements to the decelerator design have also been discussed. Using a permanent magnet quadrupole has advantages such as the lack of fringe fields and negation of the need to dissipate heat. With an N50 NdFeB magnet, the field gradient is a factor of two greater than the wire quadrupole at 700 A. The trade off, however, for a decelerator of length 1.18 m, is that the 6D acceptance decreases. It was found that the acceptance fell from 1.9 $\times 10^4$ (mm m s^{-1})^3 to 9.2 $\times 10^3$ (mm m s^{-1})^3 of CaH and from 2.1 $\times 10^6$ (mm m s^{-1})^3 to 4.5 $\times 10^5$ (mm m s^{-1})^3 for Li. The explanation of this is that the potential generated by the combination of the decelerator coils and the permanent magnet quadrupole has a turning point near the inner edge of the steel tube. This is particularly problematic in the x direction as the weaker transverse confinement couples the longitudinal and transverse motions of the particles leading to an increase in losses in the x direction. Although it is unlikely that a permanent magnet quadrupole with the same geometry as the current quadrupole will increase the acceptance of the decelerator, the clear advantages of the permanent magnet quadrupole merit further work.

The concept of a trap suitable for capturing the co-decelerated packets of Li and CaH was also described in chapter 6. The combination of the steep hexapole potential and the weaker dipole field produce a potential that should allow the formation of a 3D MOT. Moreover, the weak quadrupole field lifts the flat bottom of the potential which should keep the rate of Majorana transitions low. The MOT will allow the further cooling of the Li. Only the simplified characteristics of the MOT were explained, however, this suggests that the MOT should be able to capture the entirety of the Li loaded into the trap. It has also been possible to estimate that 63 % of the molecules will enter the MOT volume in approximately 18.2 ms, assuming that the MOT volume is a sphere with radius of 1.5 mm. The design of a set of three coils has been discussed and how they are applied in the loading sequence described. The purpose of these coils are to guide the gas packet to the edge of the trap from the decelerator coils, open the trap, and bring the molecules to near rest within the trap. The efficiency of the loading process in a 1D model is 52.2 % for CaH and 7.3 % for Li. This will require a Li source at least 130 times brighter than the CaH source to allow sympathetic cooling to occur. Estimates of the trap density of CaH was found to be 4.98×10^6 molecules cm^{-1} in the spin stretched $|N = 0, F = 1, m_{\mathrm{F}} = 1\rangle$ state. Further work must be undertaken to find the effects of the transverse field. The model presented here kept the current through the slowing coil low to minimise the defocusing nature of the transverse field. Understanding the effect this has may allow the loading of the trap to be further optimised, particularly for Li.

Appendices

Appendix A

Tensor Relations and Wigner Functions

A.1 Tensor relations

A spherical tensor can be used to represent a vector angular momentum operator, $\hat{J}$. The rank of the tensor is given by k. A tensor of rank k has $2k$+1 Cartesian components q. Where q can take the value of $-k$,$k + 1$, ..., k. For instance, a tensor of rank $k = 1$ has components of

$$\mathrm{T}^{k=1}_{q=0}\left(\hat{\mathbf{J}}\right) = \hat{J}_{\mathrm{z}} \tag{A.1}$$

$$\mathrm{T}^{k=1}_{q=1}\left(\hat{\mathbf{J}}\right) = -\frac{1}{\sqrt{2}}\left(\hat{J}_{\mathrm{x}} + i\hat{J}_{\mathrm{y}}\right) \tag{A.2}$$

$$\mathrm{T}^{k=1}_{q=-1}\left(\hat{\mathbf{J}}\right) = \frac{1}{\sqrt{2}}\left(\hat{J}_{\mathrm{x}} - i\hat{J}_{\mathrm{y}}\right) \tag{A.3}$$

The necessary tensor relationships used in this thesis are listed below. Additional relationships, proofs, and a complete description of spherical tensor operators can be found in reference [3].

The Wigner-Eckart theorem

This theorem produces the reduced matrix elements. The Wigner-Eckart theorem allows the evaluation of the dependence of the projection of j on to the molecular (equivalently z) axis m_{j}.

$$\left\langle j, m_{\mathrm{j}} \middle| \mathrm{T}^{k}_{q}\left(\hat{\mathbf{J}}\right) \middle| j', m_{\mathrm{j}}' \right\rangle = (-1)^{j-m_{\mathrm{j}}} \begin{pmatrix} j & k & j' \\ -m_{\mathrm{j}} & q & m_{\mathrm{j}}' \end{pmatrix} \left\langle j \middle\| \mathrm{T}^{k}\left(\hat{\mathbf{J}}\right) \middle\| j' \right\rangle \tag{A.4}$$

The matrix elements of a tensor product

The tensor product of two angular momentum vector operators, $\hat{\mathbf{A_1}}$ with quantum number j_1, and $\hat{\mathbf{A_2}}$, with quantum number j_2, that couple to form $\hat{\mathbf{A_3}}$, with quantum number j_{12}, can be defined by

$\mathrm{T}^{k1}\left(\hat{\mathbf{A}}_{\mathbf{1}}\right) \times \mathrm{T}^{k2}\left(\hat{\mathbf{A}}_{\mathbf{2}}\right) = \mathrm{W}^{k12}\left(k_1, k_2\right)$. The reduced matrix elements resulting for this coupling can be shown to be

$$
\begin{aligned}
&\left\langle j_1, j_2, j_{12} \middle| \mathrm{W}^{k12}\left(k_1, k_2\right) \middle| j'_1, j'_2, j'_{12} \right\rangle \\
&= \sqrt{\left(2 j_{12}+1\right)\left(2 j'_{12}+1\right)\left(2 k_{12}+1\right)} \begin{Bmatrix} j & j' & k_{12} \\ j_1 & j'_1 & k_1 \\ j_2 & j'_2 & k_2 \end{Bmatrix} \left\langle j_1 \middle\| \mathrm{T}^{k_1}\left(\hat{\mathbf{A}}_{\mathbf{1}}\right) \middle\| j'_1 \right\rangle \left\langle j_2 \middle\| \mathrm{T}^{k_2}\left(\hat{\mathbf{A}}_{\mathbf{2}}\right) \middle\| j'_2 \right\rangle .
\end{aligned}
\tag{A.5}
$$

Where the 3 × 3 matrix represents a 9j Wigner function. This treatment is fairly general and can be expanded to higher order coupling. For example, $\hat{\mathbf{C}} \times \hat{\mathbf{D}} = \hat{\mathbf{E}} = \left(\hat{\mathbf{A}} \times \hat{\mathbf{B}}\right) \times \hat{\mathbf{D}}$ where $\hat{\mathbf{D}}$ has the quantum number j_{123}.

The matrix elements of a scalar product

In this case the dependence of j_1 quantum numbers belonging to $\mathrm{T}^{k}\left(\hat{\mathbf{A}}_{\mathbf{1}}\right)$ and the j_2 quantum numbers belonging to $\mathrm{T}^{k}_{q=0}\left(\hat{\mathbf{B}}_{\mathbf{2}}\right)$ must be evaluated. Note, this is a special case of the matrix elements of a tensor product where $k_1 = k_2 = k$ and $k_{12} = 0$.

$$
\begin{aligned}
&\left\langle j_1, j_2, j_{12}, m_{\mathrm{j}} \middle| \mathrm{T}^{k}\left(\hat{\mathbf{A}}_{\mathbf{1}}\right) \cdot \mathrm{T}^{k}\left(\hat{\mathbf{B}}_{\mathbf{2}}\right) \middle| j'_1, j'_2, j'_{12}, m_{\mathrm{j}}{}' \right\rangle \\
&= (-1)^{j'_1+j_2+j_{12}}\, \delta_{j_{12} j'_{12}} \delta_{m_{\mathrm{j}} m_{\mathrm{j}}{}'} \begin{Bmatrix} j'_2 & j_1{}' & j_{12} \\ j_1 & j_2 & k \end{Bmatrix} \left\langle j_1 \middle\| \mathrm{T}^{k}\left(\hat{\mathbf{A}}_{\mathbf{1}}\right) \middle\| j'_1 \right\rangle \left\langle j_2 \middle\| \mathrm{T}^{k}\left(\hat{\mathbf{A}}_{\mathbf{2}}\right) \middle\| j'_2 \right\rangle
\end{aligned}
\tag{A.6}
$$

The matrix elements of a single operator in a coupled scheme

In this case the dependence of j_1 quantum numbers belonging to $\mathrm{T}^{k}\left(\hat{\mathbf{A}}_{\mathbf{1}}\right)$ must be evaluated. Note, this again is a special case of the matrix elements of a tensor product.

$$
\begin{aligned}
&\left\langle j_1, j_2, j_{12}, m_{\mathrm{j}} \middle| \mathrm{T}^{k_1}\left(\hat{\mathbf{A}}_{\mathbf{1}}\right) \middle| j'_1, j'_2, j'_{12}, m_{\mathrm{j}}{}' \right\rangle \\
&= (-1)^{j'_{12}+j_1+k_1+j_2}\, \delta_{j_2 j'_2} \sqrt{\left(2 j_{12}+1\right)\left(2 j'_{12}+1\right)} \begin{Bmatrix} j'_1 & j'_{12} & j_2 \\ j_{12} & j_1 & k_1 \end{Bmatrix} \left\langle j_1 \middle\| \mathrm{T}^{k_1}\left(\hat{\mathbf{A}}_{\mathbf{1}}\right) \middle\| j'_1 \right\rangle
\end{aligned}
\tag{A.7}
$$

Evaluation of the reduced matrix elements

The reduced matrix elements for a tensor of rank one are

$$
\left\langle j \middle\| \mathrm{T}^{k_1}\left(\hat{\mathbf{A}}\right) \middle\| j' \right\rangle = \delta_{j j'} \sqrt{j\,(j+1)\,(2j+1)} \tag{A.8}
$$

A.2 Useful 3j Wigner Functions

The 3j Wigner functions that were used in this thesis are shown below. The results were calculated using Mathematica version 10. A complete list of 3j Wigner functions can be found in reference [3].

$$\begin{pmatrix} J & 1 & J \\ -m_{\mathrm{J}} & 0 & m_{\mathrm{J}} \end{pmatrix} = (-1)^{J-m_{\mathrm{J}}} \frac{m_{\mathrm{J}}}{\sqrt{J\,(J+1)\,(2J+1)}} \tag{A.9}$$

$$\begin{pmatrix} J+1 & 1 & J \\ -m_{\mathrm{J}} & 0 & m_{\mathrm{J}} \end{pmatrix} = (-1)^{J-m_{\mathrm{J}}+1} \sqrt{\frac{2\,(J+m_{\mathrm{J}}+1)\,(J-m_{\mathrm{J}}+1)}{(2J+1)\,(2J+2)\,(2J+3)}} \tag{A.10}$$

A.3 Useful 6j Wigner Functions

In the following expressions, $x = a + b + c$. These are 6j Wigner function that were used in this thesis, however, a more complete list can be found in reference [3]. The results were calculated using Mathematica version 10.

$$\begin{Bmatrix} b & c & a \\ c & b & 1 \end{Bmatrix} = (-1)^{x+1} \frac{2\,[b\,(b+1)+c\,(c+1)-a\,(a+1)]}{\sqrt{2b\,(2b+1)\,(2b+2)\,(2c)\,(2c+1)\,(2c+2)}} \tag{A.11}$$

$$\begin{Bmatrix} b & c & a \\ c-1 & b & 1 \end{Bmatrix} = (-1)^{x} \sqrt{\frac{2\,(x+1)\,(x-2a)\,(x-2b)\,(x-2c+1)}{2b\,(2b+1)\,(2b+2)\,(2c-1)\,(2c)\,(2c+1)}} \tag{A.12}$$

Appendix B

Hyperfine Structure of CaH

This section will discuss how the hyperfine structure in the $N = 0$ state of the $X^2\Sigma^+$ ground state of CaH has been calculated. In order to calculate the hyperfine structure of molecules the hyperfine coupled basis must be used where $\mathbf{F} = \mathbf{J} + \mathbf{I}$. The effective Hamiltonian for the $N = 0$ state is

$$\begin{aligned} H_{\text{eff}} &= H_{\text{rot}} + H_{\text{cd}} + H_{\text{sr}} + H_{\text{Fc}} + H_{\text{dip}} + H_{\text{Z}} \\ &= \left(B_{v=0}\hat{\mathbf{N}}^2 - D_{v=0}\hat{\mathbf{N}}^4\right) + \gamma_{v=0}\mathrm{T}^1\left(\hat{\mathbf{N}}\right)\cdot\mathrm{T}^1\left(\hat{\mathbf{S}}\right) + b_{\text{F}}\mathrm{T}^1\left(\hat{\mathbf{I}}\right)\cdot\mathrm{T}^1\left(\hat{\mathbf{S}}\right) - c_{\text{F}}\mathrm{T}^1\left(\hat{\mathbf{S}},\hat{\mathbf{C}}^2\right)\cdot\mathrm{T}^1\left(\hat{\mathbf{I}}\right) \\ &- g_{\text{e}}\mu_{\text{B}}B_z\mathrm{T}^1\left(\hat{\mathbf{S}}\right) - g_{\text{R}}\mu_{\text{B}}B_z\mathrm{T}^1\left(\hat{\mathbf{N}}\right) - g_{\text{N}}\mu_{\text{B}}B_z\mathrm{T}^1\left(\hat{\mathbf{I}}\right). \end{aligned} \tag{B.1}$$

The nuclear electric quadrupole interaction is unnecessary in this instance since the total nuclear spin, I_{tot}, of CaH is 1/2. Once again, the Zeeman interactions of the rotational and the nuclear dipole moments will be ignored for the reasons explained in the main text. Most of the terms have no dependence on $\mathbf{F}$ and therefore the solution remains as presented in the main text. For completeness, the expressions for the electron spin Zeeman interaction, Fermi contact interaction and the dipolar hyperfine interaction will be calculated. Unlike the main body of text, the solution of these terms are not straight forward and will be kept in terms of the Wigner functions. Languages such as Mathematica or the sympy module for python can be used to populate the matrix form of the Hamiltonian.

B.1 The Fermi contact interaction

The Fermi contact interaction is largely diagonal, however, it introduces off-diagonal matrix elements in J. The magnitude of which become significant if the spinrotation interaction is small. The matrix representation of the Hamiltonian has elements given by

$$\frac{b_{\text{F}}}{\hbar^2}\left\langle \eta, N, S, J, I, F, m_{\text{F}} \middle| \mathrm{T}^1\left(\hat{\mathbf{I}}\right)\cdot\mathrm{T}^1\left(\hat{\mathbf{S}}\right) \middle| \eta, N', S', J', I', F', m'_{\text{F}} \right\rangle. \tag{B.2}$$

As before, the spherical tensors presented above can be used to rewrite the Hamiltonian as

$$\begin{aligned}
&\frac{b_{\mathrm{F}}}{\hbar^2}\left\langle \eta,\Lambda,N,S,J,I,F,m_{\mathrm{F}} \middle| \mathrm{T}^1\left(\hat{\mathbf{I}}\right)\cdot \mathrm{T}^1\left(\hat{\mathbf{S}}\right) \middle| \eta,\Lambda,N',S',J',I',F',m_{\mathrm{F}}' \right\rangle \\
&= \frac{b_{\mathrm{F}}}{\hbar^2}\left(-1\right)^{J+F+1}\delta_{FF'}\delta_{m_{\mathrm{F}}m_{\mathrm{F}}'}\begin{Bmatrix} I' & J' & F \\ J & I & 1 \end{Bmatrix}\left\langle N,S,J \middle\| \mathrm{T}^1\left(\hat{\mathbf{S}}\right) \middle\| N',S',J' \right\rangle \left\langle \mathrm{I} \middle\| \mathrm{T}^1\left(\hat{\mathbf{I}}\right) \middle\| \mathrm{I}' \right\rangle \\
&= b_{\mathrm{F}}\left(-1\right)^{J+F+1+J'+S+1+N}\delta_{FF'}\delta_{m_{\mathrm{F}}m_{\mathrm{F}}'}\delta_{II'}\delta_{NN'}\delta_{SS'}\begin{Bmatrix} I & J' & F \\ J & I & 1 \end{Bmatrix}\begin{Bmatrix} S & J' & N \\ J & S & 1 \end{Bmatrix} \\
&\qquad \times \sqrt{I\left(I+1\right)\left(2I+1\right)S\left(S+1\right)\left(2S+1\right)\left(2J+1\right)\left(2J'+1\right)}.
\end{aligned} \tag{B.3}$$

B.2 Dipole hyperfine interaction

For CaH, the dipolar hyperfine interaction Hamiltonian is given by

$$H_{\mathrm{dip}} = -\sqrt{10}g_{\mathrm{e}}\mu_{\mathrm{B}}g_{\mathrm{N}}\mu_{\mathrm{N}}\left(\frac{\mu_{\mathrm{o}}}{4\pi}\right)\mathrm{T}^1\left(\hat{\mathbf{I}}\right)\cdot\mathrm{T}^1\left(\hat{\mathbf{S}},\mathbf{C}^2\right). \tag{B.4}$$

The tensor, $\mathrm{T}^1\left(\hat{\mathbf{S}},\mathbf{C}^2\right)$, is used to reconstruct the interaction Hamiltonian in terms of spherical tensors rather than in Cartesian coordinates. The treatment of this component of the Hamiltonian is rather involved and is beyond the scope of this thesis. As such, only the main result will be given here, a full derivation can be found in [3]. To simplify the solution, only the vibrational ground state will considered, moreover, any contribution from excited electronic states have also been neglected. As a result the Hamiltonian has off-diagonal elements in J only.

$$\begin{aligned}
&\left\langle \eta,\Lambda,N,S,J,I,F,m_{\mathrm{F}} \middle| H_{\mathrm{dip}} \middle| \eta,\Lambda,N,S,J',I,F,m_{\mathrm{F}} \right\rangle \\
&= c_{\mathrm{dip}}\left(-1\right)^{J+F+I+N}\begin{pmatrix} N & 2 & N \\ 0 & 0 & 0 \end{pmatrix}\begin{Bmatrix} I & J' & F \\ J & I & 1 \end{Bmatrix}\begin{Bmatrix} J & J' & 1 \\ N & N & 2 \\ S & S & 1 \end{Bmatrix}\left(2N+1\right). \\
&\qquad \times \sqrt{I\left(I+1\right)\left(2I+1\right)\left(2J+1\right)\left(2J'+1\right)S\left(S+1\right)\left(2S+1\right)}
\end{aligned} \tag{B.5}$$

The constant, c_{dip}, is the dipolar hyperfine coupling strength. Unlike the previous examples, this expression includes a Wigner 9-j. As stated before terms such as this are more conveniently evaluated using Mathematica or the sympy module for python.

B.3 Hyperfine Zeeman interaction

The with simplifications described above, the Hamiltonian of the Zeeman interaction between the electron spin and an external magnetic field along the z axis is

$$\frac{g_{\mathrm{e}}\mu_{\mathrm{B}}}{\hbar}\left\langle \eta,\Lambda,N,S,J,I,F,m_{\mathrm{F}} \middle| \mathrm{T}^1\left(\mathbf{B}\right)\mathrm{T}^1\left(\hat{\mathbf{S}}\right) \middle| \eta,\Lambda,N',S',J',I',F',m_{\mathrm{F}} \right\rangle. \tag{B.6}$$

Once again, the matrix elements are largely diagonal with off diagonal elements in F. In strong fields, where the Zeeman energy becomes comparable to the hyperfine and spin coupling energies, the Zeeman interaction becomes non-linear. As a consequence, neither F or J remain good quantum numbers. The interaction Hamiltonian can be evaluated in the same fashion described in the main text,

$$\begin{aligned}
&\frac{g_{\mathrm{e}}\mu_{\mathrm{B}}B_{\mathrm{z}}}{\hbar}\left(-1\right)^{F-m_{\mathrm{F}}}\begin{pmatrix} F & 1 & F' \\ -m_{\mathrm{F}} & 0 & m_{\mathrm{F}} \end{pmatrix}\left\langle \eta, N, S, J, I, F, m_{\mathrm{F}} \middle| \mathrm{T}^{1}\left(\hat{\mathbf{S}}\right) \middle| \eta, N', S', J', I', F', m_{\mathrm{F}} \right\rangle \\
&= \frac{g_{\mathrm{e}}\mu_{\mathrm{B}}B_{\mathrm{z}}}{\hbar}\left(-1\right)^{2F-m_{\mathrm{F}}+J+1+I}\delta_{II'}\sqrt{\left(2F+1\right)\left(2F'+1\right)}\begin{pmatrix} F & 1 & F' \\ -m_{\mathrm{F}} & 0 & m_{\mathrm{F}} \end{pmatrix}\begin{Bmatrix} J' & F' & I \\ F & J & 1 \end{Bmatrix} \\
&\qquad \times \left\langle N, S, J \middle\| \mathrm{T}^{1}\left(\hat{\mathbf{S}}\right) \middle\| N', S', J' \right\rangle \\
&= g_{\mathrm{e}}\mu_{\mathrm{B}}B_{\mathrm{z}}\left(-1\right)^{2F-m_{\mathrm{F}}+J+1+I}\delta_{II'}\delta_{NN'}\delta_{SS'}\begin{pmatrix} F & 1 & F' \\ -m_{\mathrm{F}} & 0 & m_{\mathrm{F}} \end{pmatrix}\begin{Bmatrix} J' & F' & I \\ F & J & 1 \end{Bmatrix}\begin{Bmatrix} S & J' & N \\ J & S & 1 \end{Bmatrix} \\
&\qquad \times \sqrt{\left(2F+1\right)\left(2F'+1\right)\left(2J+1\right)\left(2J'+1\right)S\left(S+1\right)\left(2S+1\right)}
\end{aligned} \quad . \tag{B.7}$$

Appendix C

Coil Winder

This appendix aims to explain the fabrication of the decelerator coils. This was by no means a straight forward exercise and took time to learn and refine the necessary skills. Initially, the coils were formed on a mechanical (hand powered) winder. The coils were formed by feeding two sets of sixteen wires onto a 3 mm thick, rectangular armature. One set of the wires crosses the armatures on the top face whereas the other crosses the bottom face. The wire sets are clamped into place with a custom clamp. This is supported by a cradle mounted on a linear guide rail. Hence by simultaneously pushing the cradle along and turning the armature the coil can be wound. The main issue with this design was judging the correct linear distance to move the cradle for a certain amount of rotation. The solution was to automate the process with motors. The appropriate amount of movement and be controlled through a computer programme.

The motorised coil former has two stepper motors, one to drive the lead screw (*1067 Phidget Bipolar Stepper motor*) to achieve the linear motion, the second to perform the rotation of the armature (*3319 Phidget Nema 17 Bipolar Stepper with Planetary Gearbox*). A pair of rails and carriages are used to ensure smooth motion of the former. The torque required to turn the armature is fairly large, due to the stiffness of the wires, thus the torque from the rotation motor was maximised. Firstly, the motor is fitted with a planetary gearbox to increase the torque of the motor. Secondly, the armature is driven via a timing belt system. The teeth ratio of the drive pulley to load pulley is 1:2, this further increases the torque to around 8 N m. The stepper motors are controlled by a Labview programme via separate driver cards (*3052 SSR relay board*). The code was modified to control two motors simultaneously. Figure C.1 shows a drawing and render of the motorised coil winder and some additional parts. The important parts of the diagram have been annotated. Figure C.2 shows a photograph of a coil formed on the winder.

As mentioned previously, the armature has a 3 mm thickness, leaving an air gap in the coils. In order to get the wires in the centre of the coil to lay correctly, the coils must be pressed flat. Therefore a coil press had to be developed to flatten the coil while not displacing the wires from their original position. In order to stop this, a form of mould was designed which encloses the sides and the triangular inset of the coil. This prevents the outer most wires from being pressed out of position. As described previously, the outer coils are not pressed completely flat since this increases the inductance of the coil. By pressing the coil around 3 mm diameter rods placed in the inner curved faces of the coils, the aforementioned loop in the coil is formed. Once pressed the coils can be encapsulated in thermally conductive epoxy resin (*Stycast 2850FT with catalyst 9*). Figure C.3 shows several views of the press assembly. Panel a) shows a render of the mould and press while panels b) and c) show drawings of the mould and a cross section through the press. The drawing also shows how the outer coils (with a loop) are formed.

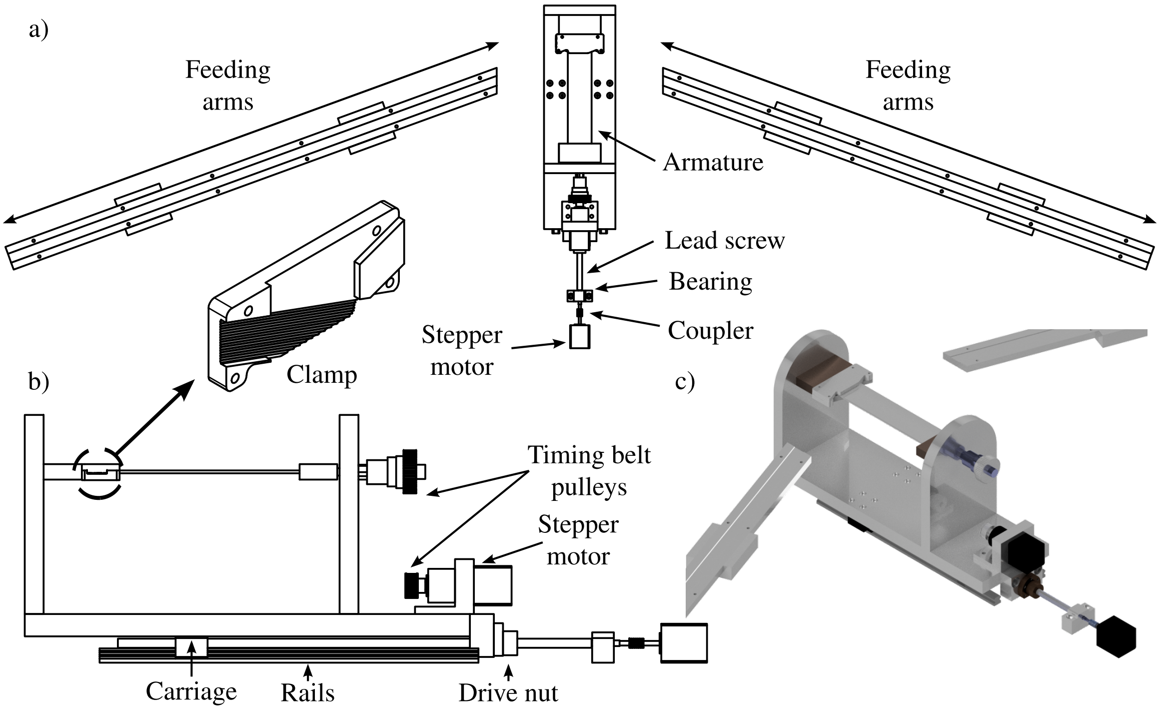

Figure C.1: Panel a) shows an over-head view of the motorised coil winder. This view includes the two feeding arms which are used to hold the two sets of 16 wires. The wires are clamped to the armature, a close-up of the clamp has been included. Panel b) shows the side view of the coil winder. The coils can be wound once the wires are clamped to the armature, one set is clamp above the armature, the other from below. The armature is bolted directly to a shaft which is driven by the larger of the two timing pulleys. This is driven by a stepper motor fitted with a gearbox. The shaft of which is fitted with another timing pulley in order to drive the one above with a timing belt. The belt has been omitted from the drawing. The former can also be translated and for smooth motion the winder is mounted on a pair of rails and carriages. A stepper motor is used to drive this motion using a combination of a lead screw and driving nut. The lead screw is supported by a bearing and is linked to the stepper motor by a coupler. A Labview programme is used to simultaneously drive the two motors to ensure that the former is translated by the appropriate amount per revolution. Panel c) shows a render of the motorised coil winder. Original drawings by Paul White.

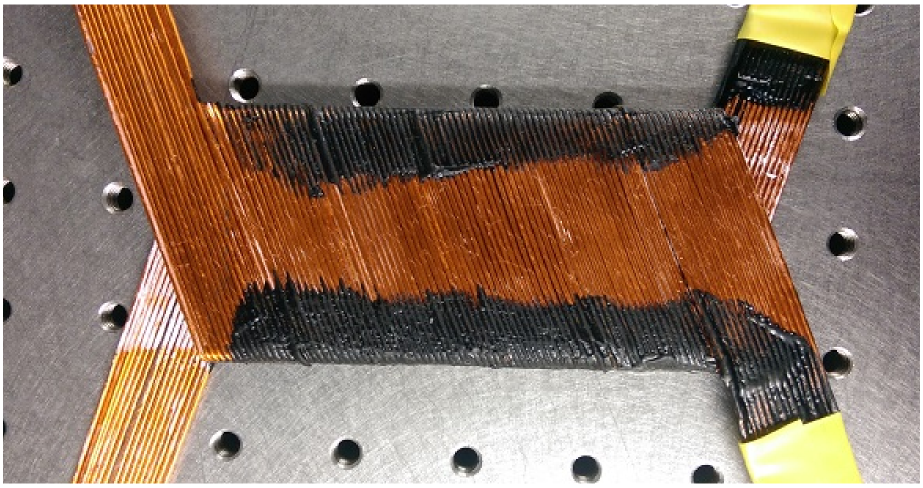

Figure C.2: A photograph of a coil formed on the motorised former. The coils are partially coated in epoxy in order to remove them from the armature.

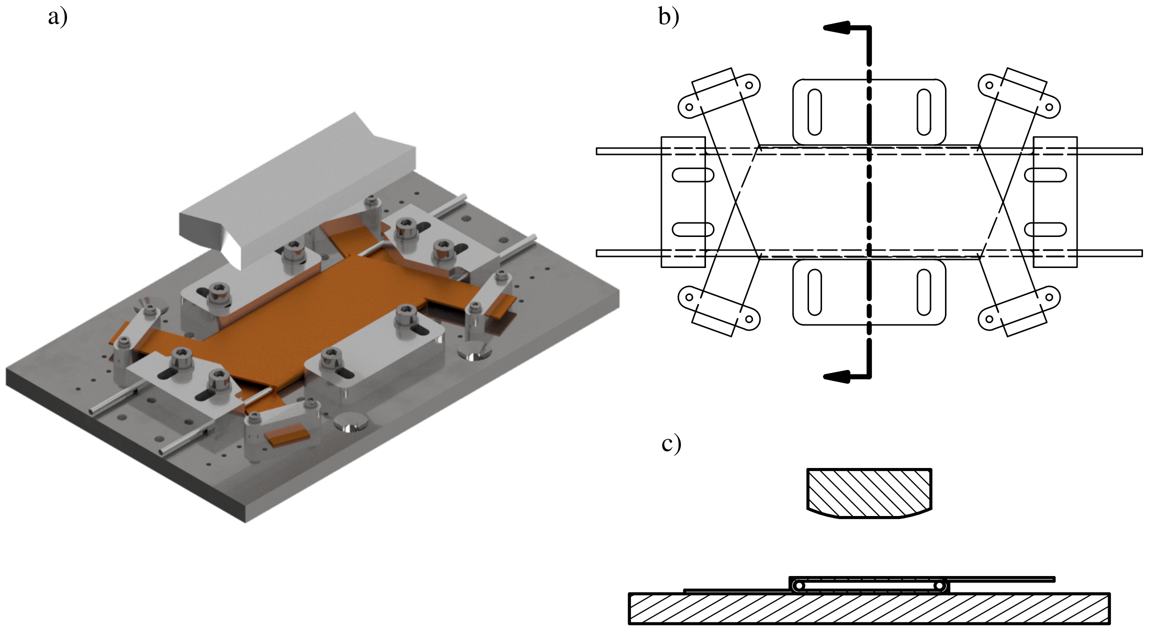

Figure C.3: The coils formed on the winder initially possess a 3 mm air gap. In order for this to be removed it is necessary to press the coils. Panel a) shows a render of the coil fixed into place by the mould. This ensures that the press does not deform the outer most wires of the coil. Panel b) shows a sketch of the coil in the mould, while panel c) shows a cross section through the dashed line in panel b). This shows the formation of the loop along the edges of the outer coils due to the size and shape of the press and the presence of the 3 mm diameter rods.

Appendix D

Discharge Circuitry

This section describes the charge and discharge circuitry used for the decelerator power electronics. Despite the relative simplicity in connecting the modules in parallel, additional circuitry is required in order for the modules to operate as intended. For instance, let's assume that all the modules are charged to a voltage of V_{o}. In this experiment only coil one is pulsed after the charging sequence is complete. As a result of coil one drawing a current from module one, the voltage across the capacitors in that module fall below V_{o}. In order to establish an equilibrium, the other electronics modules discharge to charge module one. This results in each module reaching a new equilibrium voltage, V_{e}. This is problematic if coil two were now to be pulsed as the peak current achievable through the second coil is now lower as $V_{\mathrm{e}} < V_{\mathrm{o}}$. In order to overcome this problem it is necessary to install a diode on the charging circuit to prevent the modules from establishing a new equilibrium. This, however, causes additional problems as the power electronics cannot be discharged other than with the bleed resistors. In order to meet with safety standards, an emergency stop must be fitted into the experiment which rapidly discharges the power electronics. Therefore a separate discharge circuit had to be added. This consists of five NC contactors (*TE Connectivity - Kilovac EV200BAANA*). A simplified circuit diagram of this circuit is shown in figure D.1. In normal operation, the contactors are open and isolate the power electronics. If a panel that covers the decelerator is removed or the emergency stop is pressed, the power supply is inhibited and the relays close. This shorts the power electronics to ground, discharging the capacitors through the discharge resistors, R1 and R2 (*TE Connectivity HSC100*).

Figure D.2 compares the voltage measured across the coil modules. Figure D.2a) shows the voltage across the power electronics connected in parallel while figure D.2c) shows the voltage over the modules in the configuration shown in figure D.1. These simulations were performed on LTspice which provides a toy model of the real system. The simulations assume that the modules are initially charged to 800 V and the coils sequentially discharge the power electronics in between the times of 1 and 6 ms. At 10 ms the power supply is activated allowing the power electronics to charge back to 800 V. In this simple simulation the coils are triggered with a single pulse for differing amounts of time. It should be noted, however, that in reality the PWM modulation does not discharge the capacitors to such an extent. The advantage of the parallel connection is that the charge time is fractionally shorter than that of the second configuration. The circuitry implemented in the experiment does, however, allow the same peak current to be drawn by each coil. This is shown in figures D.2b) and D.2d) which shows the current through each coil for the power electronics connected in parallel and that of the configuration implemented in the experiment respectively. During the data acquisition phase relays RY3 and RY5 failed resulting in the partial discharge of modules two and four during the operation of the decelerator. This severely limited the peak current that the decelerator coils could run at.

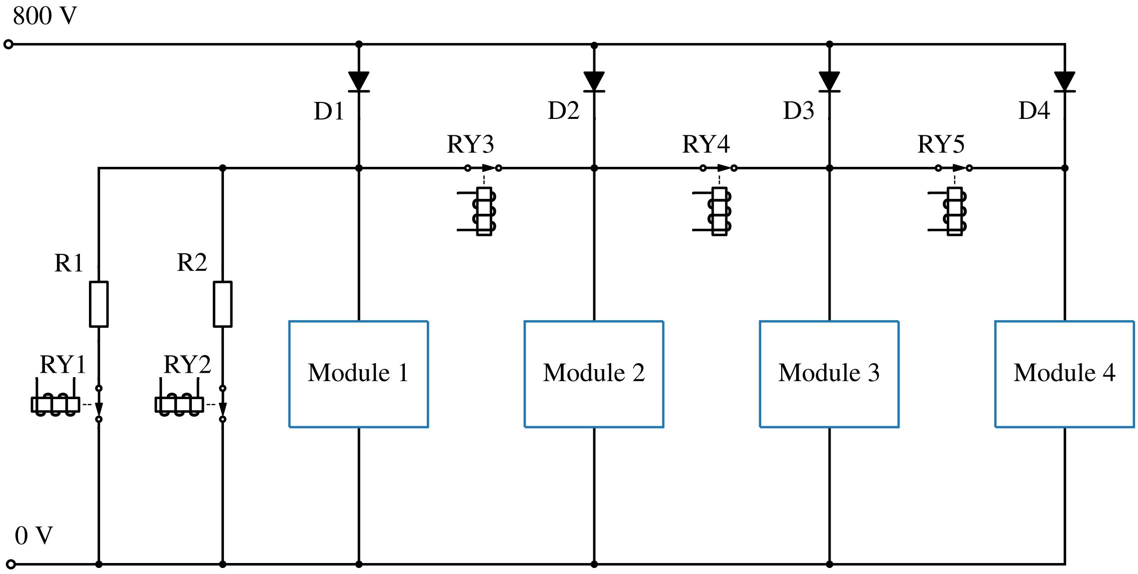

Figure D.1: Schematic of the charge and discharge circuitry of the decelerator power electronics. The power electronics are charged through diodes D1 to D4 which prevents modules from charging one another. The modules are isolated using relays RY3 to RY5. Relays RY1 and RY2 can be used to rapidly discharge the power electronics through resistors R1 and R2.

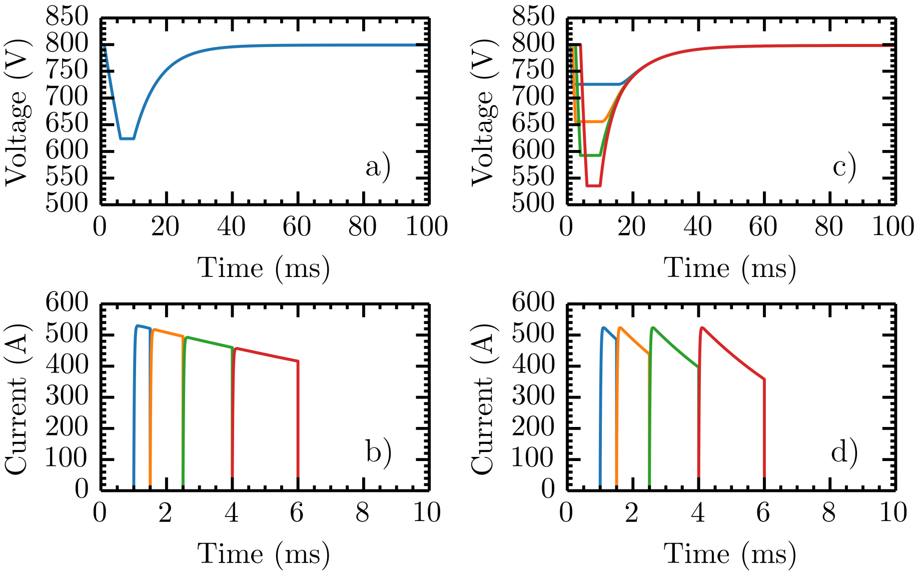

Figure D.2: Analysis of the two methods described to connect the modules to the power supply. The panels show the results of the electronics connected in parallel and while using the discharge circuitry described in the main text. The simulations assume that the modules are initially charged to 800 V and the coils sequentially discharge from 1 ms to 6 ms. At 10 ms the power supply is activated allowing the power electronics modules to charge back to 800 V. Panels a) and c) show the voltage across the power electronic modules (blue - module 1, orange - module 2, green - module 3 and , red - module 4). Panels b) and d) show the current that flows through the coils. The colour corresponds to the coil module that the current was measured through.

Appendix E

Decelerator Coils

This appendix describes the electrical connections of the decelerator coils. The wires that form a phase of the decelerator coils are connected in series. As such, electrical connections must be made between the wires within a phase. In the past, crimp connections were used, however, these were fairly bulky and made adding additional coil modules difficult. Ed Hinds and John Dyne from Imperial College designed a compact connector for the decelerator coils. Figure E.1 shows a series of drawings of the components that form the electrical connectors. The connectors are made of two elements, the larger outer connector is shown in panel a) while panel b) shows the smaller inner connector. The inner connector is mainly used for the inner two coils, while the larger connectors link the outer two coils. In both cases the wires are pushed into brass pins (shown in panels d) and e)) and fixed in place with a grub screw. The pins are held in place in PEEK blocks. The complete assembly is shown in figure E.1c). Each connector can accommodate 21 wire connections, which is more than adequate to make the 16 electrical connections required for each coil.

In order to make all the electrical connections, four of these connectors are required. Figure E.2 shows the wiring diagram for a single phase of a coil. The figure shows the location of the wires in the coil assembly and are numbered by the order in which they are connected. The location of the connectors shown as coloured links between wire layers. For instance, points 1 and 2 are the two ends of one wire (the path of this wire is shown). The larger connector then joins point 2 to point 3 thereby electrically connecting two wires of upper and lower coils. After the electrical connections between the outer coils have been made, the link between points 16 and 17 makes the first connection to the inner coils. The smaller electrical connectors that make the rest of the joints between the inner two coils. In this configuration, a wire link (32 to 33) is necessary to connect the left and right parts of the coil. After this link is made the right hand side of the coil can be wired in the same fashion.

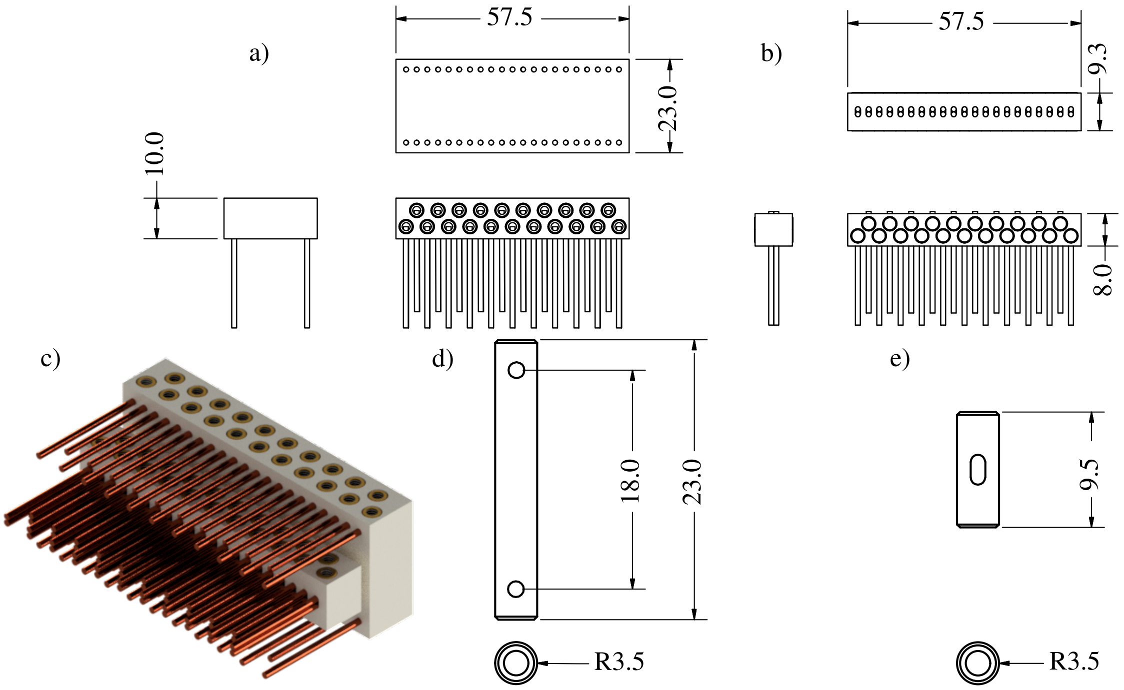

Figure E.1: Drawing of the electrical connectors used to wire the decelerator coils. View a) shows an annotated drawing of the larger connector assembly.View b) shows an annotated drawing of the smaller inner connector. In both cases the wires have been included to show how the electrical connection is made. Both parts of the connector are constructed from 21 brass pins which sit in a PEEK block. The wires are then pushed to the brass pins and held in place with grub screws. A drawing of the complete connector assembly in shown in panel c). The drawings shown in d) and e) show the annotated brass pins for the larger and smaller connectors respectively. Original drawings by John Dyne.

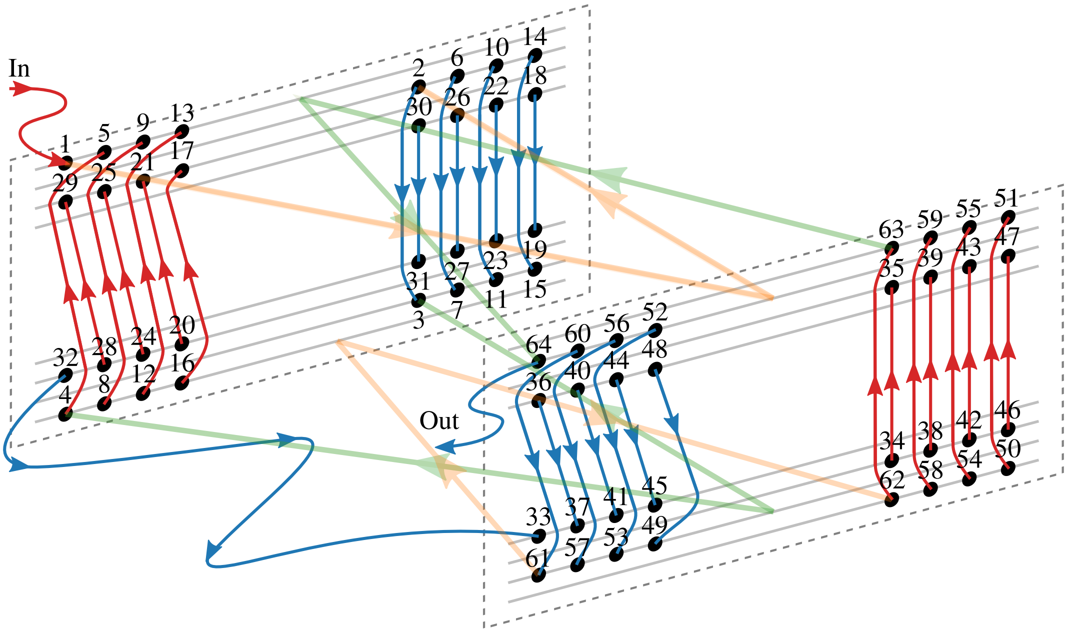

Figure E.2: The wiring diagram for a single phase of the decelerator coils. The diagram shows how the connectors described in the main text are used to make the electrical connections necessary to connect the wires in series. The ends of the wires are labelled to show the order in which the connections are made. Examples of the paths of the wires in the coil have been shown (orange and green). The current flow through the electrical connectors have been shown and are coloured to further highlight this (red and blue). In this configuration, a wire link (32 to 33) is necessary to connect the left and right parts of the coil. After this link is made the right hand side of the coil can be wired in the same fashion.

Appendix F

Proposed Apparatus

This appendix describes the additional pieces of equipment required to allow the decelerator project to achieve its long term goals. The decelerator coils are located outside of vacuum, therefore, one engineering challenge is to place the coils near to the trap. Placing the coils directly into vacuum is not an option. The electrical connections alone would be difficult to make in an enclosed space, moreover, the coil and the electrical connections may introduce volumes that are difficult to evacuate effectively. A flange must be designed to accommodate the coil and the electrical connections outside of vacuum while allowing the end of the coil to sit 25 mm away from the trap. The flange should also accommodate the water cooling and mechanical mounts required for the coil while not diminishing the optical access to the trap. The chamber will need to be large enough to house the trap and decelerator coils. A spherical octagon similar to that used for the source chamber in the current experiment would be ideal. The decelerator coils could then sit in a custom CF100 flange providing adequate space for the electrical connections. The flange would be shaped to fit in the recess of the coils and makes allowance for the bulky nature of the electrical connections. Like in the current experiment, the stainless steel tube, and permanent magnet quadrupole can be fed through the flange. An airtight seal can then be formed using torseal. Although not shown in the diagram, a series of mounts attached to groove grabbers in the chamber will mount the trap.

In addition to this flange, it would be prudent to fit the chamber with a cold head. This provision must be made for polar molecules and the effect black body radiation has on them. The lifetime of a polar molecule in traps is typically limited by background gas collisions and optical pumping by black body radiation. Although the black body spectrum at room temperature cannot drive electronic transitions from the ground state to an excited state, rovibrational transitions are possible. This potentially can limit the trap lifetime of the molecule [219]. In order to increase the lifetime of the trap it is necessary to both shield the chamber and cool the local trap environment. As a result it will be necessary to fit a cold head to the trap which is cooled by liquid nitrogen. This can also be used to cool the coils within the chamber to ensure that the coupling to the environment is kept to a minimum. In the case of CaH the trap lifetime is likely to be limited by background gas collisions as the blackbody pumping rate at 300 K is low (0.048 s^{-1}) [52].

In order to control the inelastic collisions and reaction pathways between the CaH and Li it will be necessary to optically pump the Li into the spin stretched $|F = 2, m_{\mathrm{F}} = 2\rangle$ state [207]. This may be particularly important if the electron-spin-stretched state is not sufficient enough to suppress inelastic and reactive collisions. In order to optically pump the hyperfine structure of Li, it is necessary to apply a slight, near-uniform magnetic field to lift the degeneracy of the hyperfine levels. The field must be small so that a single frequency laser can be used to drive the transitions. This means that the Zeeman shift must be less than the natural linewidth of the Li which sets the magnetic field strength to be 4 G [220]. Such a field can be generated in the region of the centre of the trap by the slowing coil operating at 0.5 A. The interaction volume can be further increased using a combination of the cancellation coil and the slowing coil.

Finally, in terms of detection it would be beneficial to make absolute density measurements of the atoms and molecules in the trap. Such measurements, for instance, would allow the feasibility of sympathetic cooling or even evaporative cooling to be determined. One technique for trapped atoms and molecules is Laser-Induced Fluorescence (LIF). The drawback to this method is that careful calibration of the experimental parameters must be made in order to find the density of the sample [136]. This issue can be overcome with Cavity-Enhanced Laser-Induced Fluorescence (CELIF) [221]. This method employs a cross-correlated combination of cavity ring-down (CRD) spectroscopy and LIF detection. This technique is capable of overcoming the difficulties with absolute density measurements of LIF. CELIF measurements can be performed on the 634 nm $X^2\Sigma^+(v = 0) \rightarrow B^2\Sigma^+(v = 0)$ transition in CaH and the D1 transition at 671 nm in Li. Figure F.1 shows the drawing of the proposed vacuum flange and chamber in which the trap will be mounted. The drawing is annotated to include the suggested direction that the vacuum pumps, cold head and optical access for the MOT and CELIF beams are also annotated.

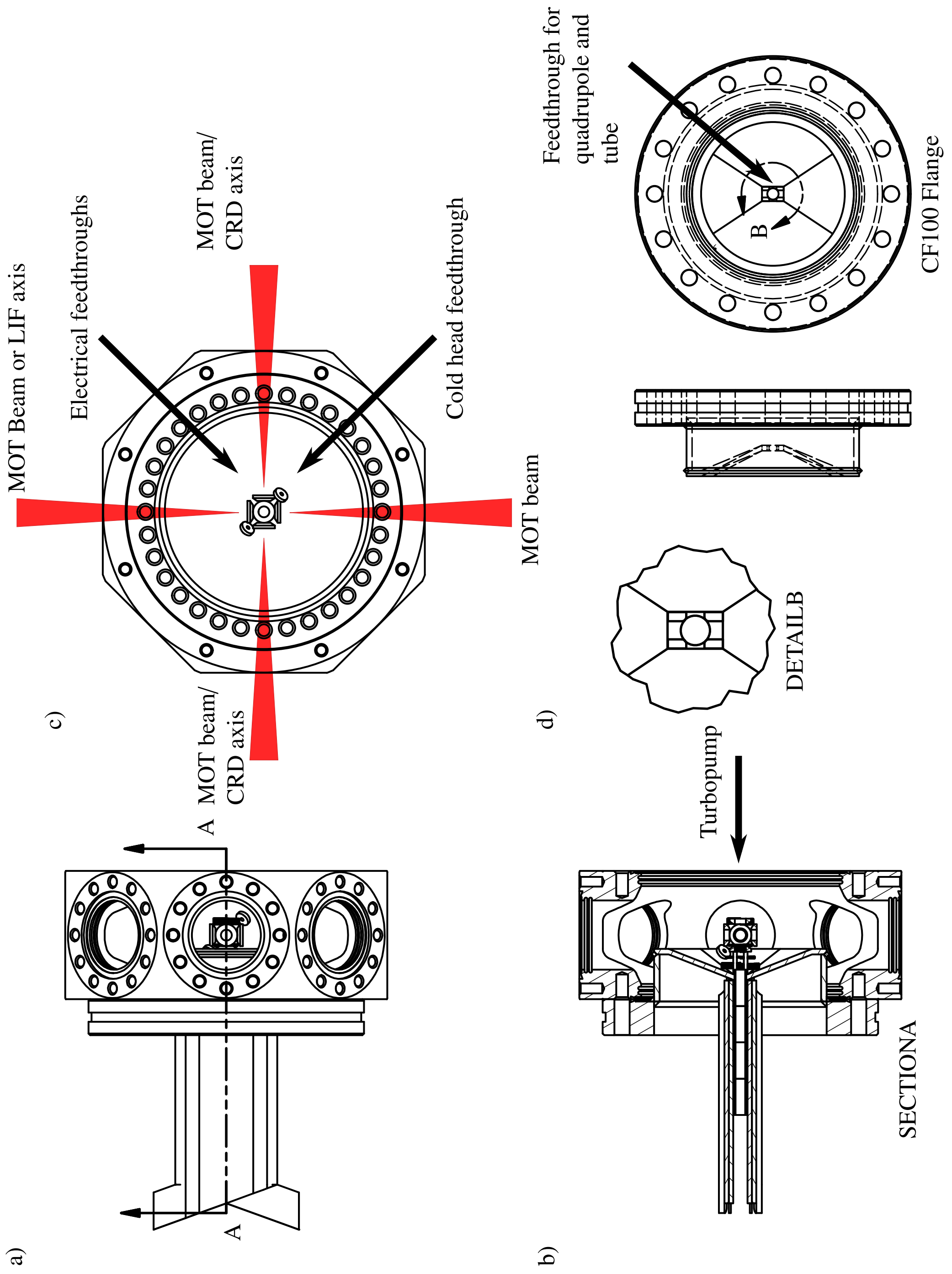

Figure F.1: An annotated drawing of the proposed vacuum system, labelled with the required pieces of equipment. Panel a) shows the xz view of the proposed change and custom flange to place the decelerator coils near to the trap. This view shows that the flange does not interfere with the optical axis into the trap. The cross-section of this is shown in panel b). This view demonstrates how the flange sits in the recess of the helical coils. The diagram labelled with the direction that the turbo-pump will be mounted. View c) shows the xy view of the chamber with the trap in the centre. The MOT axes, the LIF axis, and the CRD axes have been labelled. A possible feedthrough for the cold head and electrical connections have also been labelled. Panel d) shows the views of the flange. The large interior of the flange allows the electrical connection for the helical coils to be made and provides room for the mechanical mounts of the coil. The feedthrough of the permanent magnet quadrupole and stainless steel tube is also shown. These components can be sealed to the flange with torseal.

Bibliography

[1] A. W. Wiederkehr, S. D. Hogan, and F. Merkt, *Phase stability in a multistage Zeeman decelerator*, Physical Review A **82**, 1 (2010).

[2] M.-O. Mewes, G. Ferrari, F. Schreck, A. Sinatra, and C. Salomon, *Simultaneous magneto-optical trapping of two lithium isotopes*, Physical Review A **61** (1999).

[3] J. M. Brown and A. Carrington, *Rotational spectroscopy of diatomic molecules.* (Cambridge University Press, 2003).

[4] L.-E. Berg and L. Klynning, *Rotational Analysis of the A-X and B-X Band Systems of CaH*, Physica Scripta **10** (1974).

[5] O. Dulieu and C. Gabbanini, *The formation and interactions of cold and ultracold molecules: new challenges for interdisciplinary physics*, Reports on Progress in Physics **72** (2009).

[6] D. J. Wineland, R. E. Drullinger, and F. L. Walls, *Radiation-pressure cooling of bound resonant absorbers*, Physical Review Letters **40** (1978).

[7] E. A. Leanhardt, T. A. Pasquini, M. Saba, A. Schirotzek, Y. Shin, D. Kielpinski, D. E. Pritchard, and W. Ketterle, *Cooling Bose-Einstein Condensates Below 500 Picokelvin*, Science **301**, 1513 (2003).

[8] W. Demtröder, *Atoms, Molecules and Photons: An Introduction to Atomic, Molecular and Quantum physics* (Springer, 2006).

[9] M. T. Bell and T. P. Softley, *Ultracold molecules and ultracold chemistry*, Molecular Physics **107**, 99 (2009).

[10] L. D. Carr, D. DeMille, R. V. Krems, and J. Ye, *Cold and ultracold molecules: science, technology and applications*, New Journal of Physics **11**, 055049 (2009).

[11] M. Lemeshko, R. V. Krems, J. M. Doyle, and S. Kais, *Manipulation of molecules with electromagnetic fields*, Molecular Physics **111**, 1648 (2013).

[12] T. E. Wall, *Preparation of cold molecules for high-precision measurements*, Journal of Physics B **49** (2016).

[13] M. D. Rosa, *Laser-cooling molecules*, The European Physical Journal D **31**, 395 (2004).

[14] B. K. Stuhl, B. C. Sawyer, D. Wang, and J. Ye, *Magneto-optical Trap for Polar Molecules*, Physical Review Letters **101**, 243002 (2008).

[15] E. S. Shuman, J. F. Barry, and D. Demille, *Laser cooling of a diatomic molecule.*, Nature **467**, 820 (2010).

[16] V. Zhelyazkova, A. Cournol, T. E. Wall, A. Matsushima, J. J. Hudson, E. A. Hinds, M. R. Tarbutt, and B. E. Sauer, *Laser cooling and slowing of CaF molecules*, Physical Review A **89**, 1 (2014).

[17] B. Hemmerling, E. Chae, A. Ravi, L. Anderegg, G. K. Drayna, N. R. Hutzler, A. L. Collopy, J. Ye, W. Ketterle, and J. M. Doyle, *Laser slowing of CaF molecules to near the capture velocity of a molecular MOT*, Pre-Print **49**, 1 (2016).

[18] M. T. Hummon, M. Yeo, B. K. Stuhl, A. L. Collopy, Y. Xia, and J. Ye, *2D magneto-optical trapping of diatomic molecules*, Physical Review Letters **110** (2013).

[19] M. A. Chieda and E. E. Eyler, *Prospects for rapid deceleration of small molecules by optical bichromatic forces*, Physical Review A **84**, 1 (2011).

[20] K. M. Jones, E. Tiesinga, P. D. Lett, and P. S. Julienne, *Ultracold photoassociation spectroscopy: Long-range molecules and atomic scattering*, Reviews of Modern Physics **78**, 483 (2006).

[21] B. K. Stuhl, M. T. Hummon, M. Yeo, G. Quéméner, J. L. Bohn, and J. Ye, *Evaporative cooling of the dipolar hydroxyl radical*, Nature **492**, 396 (2012).

[22] S. Truppe, H. J. Williams, M. Hambach, L. Caldwell, N. J. Fitch, E. A. Hinds, B. E. Sauer, and M. R. Tarbutt, *Molecules cooled below the Doppler limit*, arXiv preprint arXiv:1703.00580 (2017).

[23] M. Strebel, F. Stienkemeier, and M. Mudrich, *Improved setup for producing slow beams of cold molecules using a rotating nozzle*, Physical Review A **81**, 1 (2010).

[24] R. Fulton, A. Bishop, M. Shneider, and P. Barker, *Controlling the motion of cold molecules with deep periodic optical potentials*, Nature Physics **2**, 465 (2006).

[25] P. D. Gregory, J. Aldegunde, J. M. Hutson, and S. L. Cornish, *Controlling the rotational and hyperfine state of ultracold Rb 87 Cs 133 molecules*, Physical Review A **94**, 3 (2016).

[26] K. Ni, S. Ospelkaus, M. H. G. D. Miranda, A. Pe, B. Neyenhuis, J. J. Zirbel, S. Kotochigova, P. S. Julienne, D. S. Jin, and J. Ye, *A High Phase-Space-Density Gas of Polar Molecules*, Science **322**, 231 (2008).

[27] S. D. Hogan, *Rydberg-Stark deceleration of atoms and molecules*, EPJ Techniques and Instrumentation **3**, 2 (2016).

[28] A. Trottier, D. Carty, and E. Wrede, *Photostop: Production of zero-velocity molecules by photodissociation in a molecular beam*, Molecular Physics **109**, 6 (2010).

[29] K. E. Strecker and D. W. Chandler, *Kinematic production of isolated millikelvin molecules*, Physical Review A **78**, 3 (2008).

[30] V. Singh, K. S. Hardman, N. Tariq, M.-J. Lu, A. Ellis, M. J. Morrison, and J. D. Weinstein, *Chemical Reactions of Atomic Lithium and Molecular Calcium Monohydride at 1 K*, Physical Review Letters **108**, 203201 (2012).

[31] C. Meng, A. P. P. Van Der Poel, C. Cheng, and H. L. Bethlem, *Femtosecond laser detection of Stark-decelerated and trapped methylfluoride molecules*, Physical Review A **92**, 90 (2015).

[32] N. Akerman, M. Karpov, Y. Segev, N. Bibelnik, J. Narevicius, and E. Narevicius, *Trapping of molecular Oxygen together with Lithium atoms*, Physical Review Letters **119**, 073204 (2016).

[33] Y. Liu, M. Vashishta, P. Djuricanin, S. Zhou, W. Zhong, T. Mittertreiner, D. Carty, and T. Momose, *Magnetic Trapping of Cold Methyl Radicals*, p. 1 (2016).

[34] E. R. I. Abraham, W. I. McAlexander, J. M. Gerton, R. G. Hulet, R. Côté, and A. Dalgarno, *Triplet s-wave resonance in* ^{6}*Li collisions and scattering lengths of* ^{6}*Li and* ^{7}*Li*, Physical Review A **55**, R3299 (1997).

[35] C. C. Tsai, R. S. Freeland, J. M. Vogels, H. M. J. M. Boesten, B. J. Verhaar, and D. J. Heinzen, *Two-Color Photoassociation Spectroscopy of Ground State* Rb_2, Physical Review Letters **79**, 1245 (1997).

[36] F. A. van Abeelen and B. J. Verhaar, *Determination of collisional properties of cold Na atoms from analysis of bound-state photoassociation and Feshbach resonance field data*, Physical Review A **59**, 578 (1999).

[37] H. Wang, A. N. Nikolov, J. R. Ensher, P. L. Gould, E. E. Eyler, W. C. Stwalley, J. P. Burke, J. L. Bohn, C. H. Greene, E. Tiesinga, C. J. Williams, and P. S. Julienne, *Ground-state scattering lengths for potassium isotopes determined by double-resonance photoassociative spectroscopy of ultracold 39K*, Physical Review A **62**, 052704 (2000).

[38] E. Pachomow, V. P. Dahlke, E. Tiemann, F. Riehle, and U. Sterr, *Ground-state properties of* Ca_2 *from narrow line two-color photoassociation*, p. 1 (2017).

[39] M. S. Heo, T. T. Wang, C. A. Christensen, T. M. Rvachov, D. A. Cotta, J. H. Choi, Y. R. Lee, and W. Ketterle, *Formation of ultracold fermionic NaLi Feshbach molecules*, Physical Review A **86**, 3 (2012).

[40] T. Takekoshi, L. Reichsöllner, A. Schindewolf, J. M. Hutson, C. R. Le Sueur, O. Dulieu, F. Ferlaino, R. Grimm, and H. C. Nägerl, *Ultracold dense samples of dipolar RbCs molecules in the rovibrational and hyperfine ground state*, Physical Review Letters **113**, 1 (2014).

[41] J. W. Park, S. A. Will, and M. W. Zwierlein, *Ultracold Dipolar Gas of Fermionic Na23K40 Molecules in Their Absolute Ground State*, Physical Review Letters **114**, 1 (2015).

[42] F. Wang, X. He, X. Li, B. Zhu, J. Chen, and D. Wang, *Formation of ultracold NaRb Feshbach molecules*, New Journal of Physics **17** (2015).

[43] M. Guo, B. Zhu, B. Lu, X. Ye, F. Wang, R. Vexiau, N. Bouloufa-Maafa, G. Quéméner, O. Dulieu, and D. Wang, *Creation of an Ultracold Gas of Ground-State Dipolar* $^{23}Na^{87}Rb$ *Molecules*, Physical Review Letters **116**, 1 (2016).

[44] M. W. Zwierlein, C. A. Stan, C. H. Schunck, S. M. F. Raupach, S. Gupta, Z. Hadzibabic, and W. Ketterle, *Observation of Bose-Einstein condensation of molecules*, Physical Review Letters **91**, 250401 (2003).

[45] S. Jochim, M. Bartenstein, A. Altmeyer, G. Hendl, S. Riedl, C. Chin, J. Hecker Denschlag, and R. Grimm, *Bose-Einstein Condensation of Molecules*, Science **302**, 2101 (2003).

[46] M. Greiner, C. a. Regal, and D. S. Jin, *Emergence of a molecular BoseEinstein condensate from a Fermi gas*, Nature **426**, 537 (2003).

[47] P. K. Molony, A. Kumar, P. D. Gregory, R. Kliese, T. Puppe, C. R. Le Sueur, J. Aldegunde, J. M. Hutson, and S. L. Cornish, *Measurement of the binding energy of ultracold* $^{87}Rb^{133}Cs$ *molecules using an offset-free optical frequency comb*, Physical Review A **94**, 022507 (2016).

[48] H. Bethlem, G. Berden, and G. Meijer, *Decelerating Neutral Dipolar Molecules*, Physical Review Letters **83**, 1558 (1999).

[49] H. L. Bethlem, G. Berden, F. M. H. Crompvoets, R. T. Jongma, A. J. A. van Roij, and G. Meijer, *Electrostatic trapping of ammonia molecules*, Nature **406**, 491 (2000).

[50] H. Bethlem, F. Crompvoets, R. Jongma, S. van de Meerakker, and G. Meijer, *Deceleration and trapping of ammonia using time-varying electric fields*, Physical Review A **65**, 1 (2002).

[51] J. R. Bochinski, E. R. Hudson, H. J. Lewandowski, J. Ye, and G. Meijer, *Phase space manipulation of cold free radical OH molecules*, Physical Review Letters **91**, 5 (2003).

[52] S. Hoekstra, J. J. Gilijamse, B. Sartakov, N. Vanhaecke, L. Scharfenberg, S. Y. T. Van De Meerakker, and G. Meijer, *Optical pumping of trapped neutral molecules by blackbody radiation*, Physical Review Letters **98**, 1 (2007).

[53] S. Hoekstra, M. Metsälä, P. C. Zieger, L. Scharfenberg, J. J. Gilijamse, G. Meijer, and S. Y. T. Van De Meerakker, *Electrostatic trapping of metastable NH molecules*, Physical Review A **76** (2007).

[54] E. R. Hudson, C. Ticknor, B. C. Sawyer, C. A. Taatjes, H. J. Lewandowski, J. R. Bochinski, J. L. Bohn, and J. Ye, *Production of cold formaldehyde molecules for study and control of chemical reaction dynamics with hydroxyl radicals*, Physical Review A **73**, 6 (2006).

[55] S. Jung, E. Tiemann, and C. Lisdat, *Cold atoms and molecules from fragmentation of decelerated* SO_2, Physical Review A **74**, 1 (2006).

[56] X. Wang, M. Kirste, G. Meijer, and S. Y. T. van de Meerakker, *Stark Deceleration of NO Radicals*, Molecular Physics **111**, 1648 (2013).

[57] O. Nourbakhsh, J. M. Michan, T. Mittertreiner, D. Carty, E. Wrede, P. Djuricanin, and T. Momose, *State purified deceleration of SD radicals by a Stark decelerator*, Molecular Physics **113**, 4007 (2015).

[58] A. Osterwalder, S. A. Meek, G. Hammer, H. Haak, and G. Meijer, *Deceleration of neutral molecules in macroscopic traveling traps*, Physical Review A **81**, 1 (2010).

[59] S. K. Tokunaga, J. M. Dyne, E. a. Hinds, and M. R. Tarbutt, *Stark deceleration of lithium hydride molecules*, New Journal of Physics **11**, 055038 (2009).

[60] T. E. Wall, S. K. Tokunaga, E. a. Hinds, and M. R. Tarbutt, *Nonadiabatic transitions in a stark decelerator*, Physical Review A **81**, 1 (2010).

[61] N. E. Bulleid, R. J. Hendricks, E. a. Hinds, S. a. Meek, G. Meijer, A. Osterwalder, and M. R. Tarbutt, *Traveling-wave deceleration of heavy polar molecules in low-field-seeking states*, Physical Review A **86**, 2 (2012).

[62] S. C. Mathavan, A. Zapara, Q. Esajas, and S. Hoekstra, *Deceleration of a Supersonic Beam of SrF Molecules to 120 m* s^{-1}, ChemPhysChem **17**, 3709 (2016).

[63] Y. Yamakita, S. R. Procter, A. L. Goodgame, T. P. Softley, and F. Merkt, *Deflection and deceleration of hydrogen Rydberg molecules in inhomogeneous electric fields*, Journal of Chemical Physics **121**, 1419 (2004).

[64] S. A. Meek, H. L. Bethlem, H. Conrad, and G. Meijer, *Trapping molecules on a chip in traveling potential wells*, Physical Review Letters **100**, 18 (2008).

[65] S. A. Meek, G. Santambrogio, B. G. Sartakov, H. Conrad, and G. Meijer, *Suppression of nonadiabatic losses of molecules from chip-based microtraps*, Physical Review A **83**, 1 (2011).

[66] C. Seiler, S. D. Hogan, and F. Merkt, *Trapping cold molecular hydrogen*, Physical Chemistry Chemical Physics **13**, 19000 (2011).

[67] H. L. Bethlem, A. J. A. van Roij, R. T. Jongma, and G. Meijer, *Alternate Gradient Focusing and Deceleration of a Molecular Beam*, Physical Review Letters **88**, 133003 (2002).

[68] H. L. Bethlem, M. R. Tarbutt, J. Küpper, D. Carty, K. Wohlfart, E. A. Hinds, and G. Meijer, *Alternating Gradient Focusing and Deceleration of Polar Molecules*, Journal of Physics B **39**, R263 (2006).

[69] M. R. Tarbutt, H. L. Bethlem, J. J. Hudson, V. L. Ryabov, V. A. Ryzhov, B. E. Sauer, G. Meijer, and E. A. Hinds, *Slowing heavy, ground-state molecules using an alternating gradient decelerator*, Physical Review Letters **92**, 173002 (2004).

[70] K. Wohlfart, F. Grätz, F. Filsinger, H. Haak, G. Meijer, and J. Küpper, *Alternating-gradient focusing and deceleration of large molecules*, Physical Review A **77**, 1 (2008).

[71] T. E. Wall, J. F. Kanem, J. M. Dyne, J. J. Hudson, B. E. Sauer, E. a. Hinds, and M. R. Tarbutt, *Stark deceleration of CaF molecules in strong- and weak-field seeking states.*, Physical chemistry chemical physics **13**, 18991 (2011).

[72] N. Vanhaecke, U. Meier, M. Andrist, B. H. Meier, and F. Merkt, *Multistage Zeeman deceleration of hydrogen atoms*, Physical Review A **75**, 1 (2007).

[73] E. Narevicius, C. G. Parthey, A. Libson, J. Narevicius, I. Chavez, U. Even, and M. G. Raizen, *An atomic coilgun: Using pulsed magnetic fields to slow a supersonic beam*, New Journal of Physics **9**, 358 (2007).

[74] E. Lavert-Ofir, L. David, A. B. Henson, S. Gersten, J. Narevicius, and E. Narevicius, *Stopping paramagnetic supersonic beams: the advantage of a co-moving magnetic trap decelerator*, Physical Chemistry Chemical Physics **13**, 18948 (2011).

[75] A. Trimeche, M. N. Bera, J. P. Cromières, J. Robert, and N. Vanhaecke, *Trapping of a supersonic beam in a traveling magnetic wave*, European Physical Journal D **65**, 263 (2011).

[76] S. A. Rangwala, T. Junglen, T. Rieger, P. W. H. Pinkse, and G. Rempe, *Continuous source of translationally cold dipolar molecules*, Physical Review A **67**, 043406 (2003).

[77] M. Motsch, L. D. Van Buuren, C. Sommer, M. Zeppenfeld, G. Rempe, and P. W. H. Pinkse, *Cold guided beams of water isotopologs*, Physical Review A **79**, 1 (2009).

[78] H. Tsuji, T. Sekiguchi, T. Mori, T. Momose, and H. Kanamori, *Stark velocity filter for nonlinear polar molecules*, Journal of Physics B **43**, 95202 (2010).

[79] D. Patterson and J. M. Doyle, *Bright, guided molecular beam with hydrodynamic enhancement*, Journal of Chemical Physics **126**, 154307 (2007).

[80] R. Fulton, A. I. Bishop, and P. F. Barker, *Optical stark decelerator for molecules*, Physical Review Letters **93**, 10 (2004).

[81] J. Ramirez-Serrano, K. E. Strecker, and D. W. Chandler, *Modification of the velocity distribution of H_2 molecules in a supersonic beam by intense pulsed optical gradients*, Physical chemistry chemical physics **8**, 2985 (2006).

[82] S. Merz, N. Vanhaecke, W. Jäger, M. Schnell, and G. Meijer, *Decelerating molecules with microwave fields*, Physical Review A **85**, 6 (2012).

[83] N. J. Fitch and M. R. Tarbutt, *Principles and Design of a Zeeman-Sisyphus Decelerator for Molecular Beams*, ChemPhysChem **17**, 3609 (2016).

[84] M. Zeppenfeld, B. G. U. Englert, R. Glöckner, A. Prehn, M. Mielenz, C. Sommer, L. D. van Buuren, M. Motsch, and G. Rempe, *Sisyphus cooling of electrically trapped polyatomic molecules*, Nature **491**, 570 (2012).

[85] A. Prehn, M. Ibrügger, R. Glöckner, G. Rempe, and M. Zeppenfeld, *Optoelectrical Cooling of Polar Molecules to Submillikelvin Temperatures*, Physical Review Letters **116**, 1 (2016).

[86] M. Gupta and D. Herschbach, *A Mechanical Means to Produce Intense Beams of Slow Molecules*, The Journal of Physical Chemistry A **103**, 10670 (1999).

[87] M. Gupta and D. Herschbach, *Slowing and Speeding Molecular Beams by Means of a Rapidly Rotating Source* , The Journal of Physical Chemistry A **105**, 1626 (2001).

[88] E. Narevicius, A. Libson, M. F. Riedel, C. G. Parthey, I. Chavez, U. Even, and M. G. Raizen, *Coherent slowing of a supersonic beam with an atomic paddle*, Physical Review Letters **98**, 1 (2007).

[89] S. Chervenkov, X. Wu, J. Bayerl, A. Rohlfes, T. Gantner, M. Zeppenfeld, and G. Rempe, *Continuous centrifuge decelerator for polar molecules*, Physical Review Letters **112**, 1 (2014).

[90] J. K. Messer and F. C. De Lucia, *Measurement of pressure-broadening parameters for the CO-He system at 4 K*, Physical Review Letters **53**, 2555 (1984).

[91] J. M. Doyle, B. Friedrich, J. Kim, and D. Patterson, *Buffer-gas loading of atoms and molecules into a magnetic trap*, Physical Review A **52**, R2515 (1995).

[92] N. R. Hutzler, H. I. Lu, and J. M. Doyle, *The buffer gas beam: An intense, cold, and slow source for atoms and molecules*, Chemical Reviews **112**, 4803 (2012).

[93] D. Patterson, J. Rasmussen, and J. M. Doyle, *Intense atomic and molecular beams via neon buffer-gas cooling*, New Journal of Physics **11**, 1 (2009).

[94] S. E. Maxwell, N. Brahms, R. Decarvalho, D. R. Glenn, J. S. Helton, S. V. Nguyen, D. Patterson, J. Petricka, D. Demille, and J. M. Doyle, *High-flux beam source for cold, slow atoms or molecules*, Physical Review Letters **95**, 1 (2005).

[95] S. M. Skoff, R. J. Hendricks, C. D. J. Sinclair, M. R. Tarbutt, J. J. Hudson, D. M. Segal, B. E. Sauer, and E. A. Hinds, *Doppler-free laser spectroscopy of buffer-gas-cooled molecular radicals*, New Journal of Physics **11** (2009).

[96] D. Patterson, E. Tsikata, and J. M. Doyle, *Cooling and collisions of large gas phase molecules*, Physical Chemistry Chemical Physics **12**, 9736 (2010).

[97] D. Patterson and J. M. Doyle, *A slow, continuous beam of cold benzonitrile*, Physical chemistry chemical physics **17**, 5372 (2015).

[98] N. N. Liu and H. Loesch, *Kinematic slowing of molecules formed by reactive collisions*, Physical Review Letters **98**, 1 (2007).

[99] J. S. Eardley, N. Warner, L. Deng, D. Carty, and E. Wrede, *Magnetic Trapping of SH Radicals*, Physical chemistry chemical physics **19**, 8423 (2017).

[100] W. G. Doherty, M. T. Bell, T. P. Softley, A. Rowland, E. Wrede, and D. Carty, *Production of cold bromine atoms at zero mean velocity by photodissociation.*, Physical chemistry chemical physics **13**, 8441 (2011).

[101] E. B. Norrgard, D. J. McCarron, M. H. Steinecker, M. R. Tarbutt, and D. DeMille, *Submillikelvin Dipolar Molecules in a Radio-Frequency Magneto-Optical Trap*, Physical Review Letters **116**, 1 (2016).

[102] G. Quéméner and P. S. Julienne, *Ultracold molecules under control!*, Chemical Reviews **112**, 4949 (2012).

[103] B. K. Stuhl, M. T. Hummon, and J. Ye, *Cold State-Selected Molecular Collisions and Reactions*, Annual review of physical chemistry **65**, 501 (2014).

[104] J. Veldhoven, J. Küpper, H. L. Bethlem, B. Sartakov, A. J. A. Roij, and G. Meijer, *Decelerated molecular beams for high-resolution spectroscopy*, The European Physical Journal D **31**, 337 (2004).

[105] M. R. Tarbutt, B. E. Sauer, J. J. Hudson, and E. A. Hinds, *Design for a fountain of YbF molecules to measure the electron's electric dipole moment*, New Journal of Physics **15**, 053034 (2013).

[106] D. Kawall, F. Bay, S. Bickman, Y. Jiang, and D. DeMille, *Precision Zeeman-Stark spectroscopy of the metastable a(1)[$^3\Sigma^+$] state of PbO*, Physical Review Letters **92**, 133007 (2004).

[107] J. J. Hudson, D. M. Kara, I. J. Smallman, B. E. Sauer, M. R. Tarbutt, and E. a. Hinds, *Improved measurement of the shape of the electron*, Nature **473**, 493 (2011).

[108] J. Baron, W. C. Campbell, D. DeMille, J. M. Doyle, G. Gabrielse, Y. V. Gurevich, P. W. Hess, N. R. Hutzler, E. Kirilov, I. Kozyryev, B. R. O'Leary, C. D. Panda, M. F. Parsons, E. S. Petrik, B. Spaun, A. C. Vutha, and A. D. West, *Order of magnitude smaller limit on the electric dipole moment of the electron*, Science **343**, 269 (2014).

[109] D. Demille, S. Sainis, J. Sage, T. Bergeman, S. Kotochigova, and E. Tiesinga, *Enhanced sensitivity to variation of m_e/m_p in molecular spectra*, Physical Review Letters **100**, 1 (2008).

[110] R. P. Feynman, *Simulating physics with computers*, International Journal of Theoretical Physics **21**, 467 (1982).

[111] S. Lloyd, *A Potentially Relizable Quantum Computer*, Science **261**, 1569 (1993).

[112] S. Lloyd, *Universal Quantum Simulators*, Science **273**, 1073 (1996).

[113] E. Manousakis, *A quantum-dot array as model for copper-oxide superconductors: A dedicated quantum simulator for the many-fermion problem*, Journal of Low Temperature Physics **126**, 1501 (2002).

[114] G.-B. Jo, Y.-R. Lee, J.-H. Choi, C. A. Christensen, T. H. Kim, J. H. Thywissen, D. E. Pritchard, and W. Ketterle, *Itinerant Ferromagnetism in a Fermi Gas of Ultracold Atoms*, Science **325**, 1521 (2009).

[115] A. V. Gorshkov, S. R. Manmana, G. Chen, J. Ye, E. Demler, M. D. Lukin, and A. M. Rey, *Tunable superfluidity and quantum magnetism with ultracold polar molecules*, Physical Review Letters **107**, 1 (2011).

[116] S. Giovanazzi, *Hawking radiation in sonic black holes*, Physical Review Letters **94**, 1 (2005).

[117] I. M. Georgescu, S. Ashhab, and F. Nori, *Quantum simulation*, Reviews of Modern Physics **86**, 153 (2014).

[118] G. K. Brennen, A. Micheli, and P. Zoller, *Designing spin-1 lattice models using polar molecules*, New Journal of Physics **9**, 138 (2007).

[119] G. Pupillo, A. Micheli, H. P. Büchler, and P. Zoller, *Condensed Matter Physics with Cold Polar Molecules* (Cold Molecules: Creation and Applications ed R V Krems et al London: Taylor and Francis, 2008).

[120] I. Buluta and F. Nori, *Quantum Simulators*, Science **326** (2009).

[121] I. Bloch, *Ultracold quantum gases in optical lattices*, Nature Physics **1**, 23 (2005).

[122] B. Friedrich and D. Herschbach, *Alignment and Trapping of Molecules in Intense Laser Fields*, Physical Review Letters **74**, 4623 (1995).

[123] A. Micheli, G. Pupillo, H. P. Büchler, and P. Zoller, *Cold polar molecules in two-dimensional traps: Tailoring interactions with external fields for novel quantum phases*, Physical Review A **76**, 1 (2007).

[124] R. Barnett, D. Petrov, M. Lukin, and E. Demler, *Quantum magnetism with multicomponent dipolar molecules in an optical lattice*, Physical Review Letters **96**, 3 (2006).

[125] M. L. Wall, K. Maeda, and L. D. Carr, *Simulating quantum magnets with symmetric top molecules*, Annalen der Physik **525**, 845 (2013).

[126] L. Pollet, J. D. Picon, H. P. Büchler, and M. Troyer, *Supersolid phase with cold polar molecules on a triangular lattice*, Physical Review Letters **104**, 1 (2010).

[127] B. Capogrosso-Sansone, C. Trefzger, M. Lewenstein, P. Zoller, and G. Pupillo, *Quantum phases of cold polar molecules in 2D optical lattices*, Physical Review Letters **104**, 1 (2010).

[128] H. P. Büchler, E. Demler, M. Lukin, A. Micheli, N. Prokof'ev, G. Pupillo, and P. Zoller, *Strongly correlated 2D quantum phases with cold polar molecules: Controlling the shape of the interaction potential*, Physical Review Letters **98**, 1 (2007).

[129] A. Micheli, G. K. Brennen, and P. Zoller, *A toolbox for lattice-spin models with polar molecules*, Nature Physics **2**, 341 (2006).

[130] S. Chefdeville, T. Stoecklin, A. Bergeat, K. M. Hickson, C. Naulin, and M. Costes, *Appearance of Low Energy Resonances in CO-Para-H_2 Inelastic Collisions*, Physical Review Letters **109**, 1 (2012).

[131] A. B. Henson, S. Gersten, Y. Shagam, J. Narevicius, and E. Narevicius, *Observation of Resonances in Penning Ionization Reactions at Sub-Kelvin Temperaures in Merged Beams*, Science **338**, 234 (2010).

[132] J. J. Gilijamse, S. Hoekstra, S. Y. T. van de Meerakker, G. C. Groenenboom, and G. Meijer, *Near-Threshold Inelastic Collisions Using Molecular Beams with a Tunable Velocity*, Science **313**, 1617 (2006).

[133] M. Kirste, L. Scharfenberg, J. Kłos, F. Lique, M. H. Alexander, G. Meijer, and S. Y. T. Van De Meerakker, *Low-energy inelastic collisions of OH radicals with He atoms and D_2 molecules*, Physical Review A **82**, 1 (2010).

[134] L. Scharfenberg, J. Kłos, P. J. Dagdigian, M. H. Alexander, G. Meijer, and S. Y. T. van de Meerakker, *State-to-state inelastic scattering of Stark-decelerated OH radicals with Ar atoms*, Physical chemistry chemical physics **12**, 10660 (2010).

[135] L. Scharfenberg, K. B. Gubbels, M. Kirste, G. C. Groenenboom, A. Van Der Avoird, G. Meijer, and S. Y. T. Van De Meerakker, *Scattering of Stark-decelerated OH radicals with rare-gas atoms*, European Physical Journal D **65**, 189 (2011).

[136] M. Kirste, X. Wang, H. C. Schewe, G. Meijer, K. Liu, A. V. D. Avoird, L. M. C. Janssen, K. B. Gubbels, G. C. Groenenboom, and S. Y. T. V. D. Meerakker, *Quantum-State Resolved Bimolecular Collisions of Velocity-Controlled OH with NO Radicals*, Science **338**, 1060 (2012).

[137] J. Onvlee, S. N. Vogels, A. V. Zastrow, D. H. Parker, and S. Y. T. van de Meerakker, *Molecular collisions coming into focus.*, Physical chemistry chemical physics **17**, 12365 (2014).

[138] A. von Zastrow, J. Onvlee, S. N. Vogels, G. C. Groenenboom, A. van der Avoird, and S. Y. T. van de Meerakker, *State-resolved diffraction oscillations imaged for inelastic collisions of NO radicals with He, Ne and Ar*, Nature Chemistry **6**, 216 (2014).

[139] A. T. J. B. Eppink and D. H. Parker, *Velocity map imaging of ions and electrons using electrostatic lenses: Application in photoelectron and photofragment ion imaging of molecular oxygen*, Review of Scientific Instruments **68**, 3477 (1997).

[140] J. Onvlee, S. D. S. Gordon, S. N. Vogels, T. Auth, T. Karman, B. Nichols, A. van der Avoird, G. C. Groenenboom, M. Brouard, and S. Y. T. van de Meerakker, *Imaging quantum stereody-*

namics through Fraunhofer scattering of NO radicals with rare-gas atoms, Nature Chemistry **9**, 226 (2016).

[141] M. Lemeshko, P. G. Jambrina, M. P. de Miranda, and B. Friedrich, *Communications: when diffraction rules the stereodynamics of rotationally inelastic collisions*, Journal of Chemical Physics **132** (2010).

[142] M. Lemeshko and B. Friedrich, *An analytic model of the stereodynamics of rotationally inelastic molecular collisions*, Physical Chemistry Chemical Physics **12**, 1038 (2010).

[143] B. C. Sawyer, B. K. Stuhl, D. Wang, M. Yeo, and J. Ye, *Molecular beam collisions with a magnetically trapped target*, Physical Review Letters **101**, 1 (2008).

[144] D. Carty, V. Le Page, I. R. Sims, and I. W. M. Smith, *Low temperature rate coefficients for the reactions of CN and C_2H radicals with allene (CH_2=C=CH_2) and methyl acetylene ($CH_3C{\equiv}CH$)*, Chemical Physics Letters **344**, 310 (2001).

[145] P. Zeeman, *The effect of magnetisation on the nature of light emitted by a substance*, Nature **55**, 347 (1897).

[146] O. Stern and W. Gerlach, *Der experimentelle Nachweis der Richtungsquantelung im Magnetfeld*, Zeitschrift für Physik **9**, 349 (1922).

[147] A. H. Futch and F. A. Grant, *Mean Life of the $^3P_2$ Metastable Argon Level*, Physal Review **102**, 356 (1956).

[148] S. Y. van de Meerakker, H. L. Bethlem, N. Vanhaecke, and G. Meijer, *Manipulation and control of molecular beams*, Chemical Reviews **112**, 4828 (2012).

[149] E. Arimondo, M. Inguscio, and P. Violino, *Experimental determinations of the hyperfine structure in the alkali atoms*, Reviews of Modern Physics **49**, 31 (1977).

[150] I. C. Bowater, J. M. Brown, and A. Carrington, *Microwave spectroscopy of nonlinear free radicals*, Proceedings A **333** (1973).

[151] C. I. Frum, J. J. Oh, E. A. Cohen, and H. M. Pickett, *Rotational spectra of the $X\ ^2\Sigma^{(+)}$ states of CaH and CaD*, The Astrophysical Journal Letters **408**, L61 (1993).

[152] K. Dulitz, M. Motsch, N. Vanhaecke, and T. P. Softley, *Getting a grip on the transverse motion in a Zeeman decelerator*, Journal of Chemical Physics **140**, 1 (2014).

[153] T. Cremers, S. Chefdeville, N. Janssen, E. Sweers, S. Koot, P. Claus, and S. Y. T. Van De Meerakker, *A new concept multi-stage Zeeman decelerator: experimental implementation*, arXiv preprint arXiv:1702.05477 (2017).

[154] E. Lavert-Ofir, S. Gersten, A. B. Henson, I. Shani, L. David, J. Narevicius, and E. Narevicius, *A moving magnetic trap decelerator: A new source of cold atoms and molecules*, New Journal of Physics **13** (2011).

[155] S. D. Hogan, D. Sprecher, M. Andrist, N. Vanhaecke, and F. Merkt, *Zeeman deceleration of H and D*, Physical Review A **76**, 1 (2007).

[156] S. D. Hogan, A. W. Wiederkehr, M. Andrist, H. Schmutz, and F. Merkt, *Slow beams of atomic hydrogen by multistage Zeeman deceleration*, Journal of Physics B: Atomic, Molecular and Optical Physics **41**, 081005 (2008).

[157] S. D. Hogan, A. W. Wiederkehr, H. Schmutz, and F. Merkt, *Magnetic trapping of hydrogen after multistage zeeman deceleration*, Physical Review Letters **101**, 1 (2008).

[158] A. W. Wiederkehr, S. D. Hogan, B. Lambillotte, M. Andrist, H. Schmutz, J. Agner, Y. Salathé, and F. Merkt, *Trapping deuterium atoms*, Physical Review A **81**, 1 (2010).

[159] A. W. Wiederkehr, M. Motsch, S. D. Hogan, M. Andrist, H. Schmutz, B. Lambillotte, J. a. Agner, and F. Merkt, *Multistage Zeeman deceleration of metastable neon*, Journal of Chemical Physics **135** (2011).

[160] A. W. Wiederkehr, H. Schmutz, M. Motsch, and F. Merkt, *Velocity-tunable slow beams of cold O_2 in a single spin-rovibronic state with full angular-momentum orientation by multistage Zeeman deceleration*, Molecular Physics **110**, 1807 (2012).

[161] M. Motsch, P. Jansen, J. A. Agner, H. Schmutz, and F. Merkt, *Slow and velocity-tunable beams of metastable He_2 by multistage Zeeman deceleration*, Physical Review A **89**, 1 (2014).

[162] E. Narevicius, A. Libson, C. G. Parthey, I. Chavez, J. Narevicius, U. Even, and M. G. Raizen, *Stopping supersonic beams with a series of pulsed electromagnetic coils: An atomic coilgun*, Physical Review Letters **100**, 18 (2008).

[163] E. Narevicius, A. Libson, C. G. Parthey, I. Chavez, J. Narevicius, U. Even, and M. G. Raizen, *Stopping supersonic oxygen with a series of pulsed electromagnetic coils: A molecular coilgun*, Physical Review A **77**, 1 (2008).

[164] T. Momose, Y. Liu, S. Zhou, P. Djuricanin, and D. Carty, *Manipulation of translational motion of methyl radicals by pulsed magnetic fields*, Physical chemistry chemical physics **15**, 1772 (2013).

[165] Y. Liu, S. Zhou, W. Zhong, P. Djuricanin, and T. Momose, *One-dimensional confinement of magnetically decelerated supersonic beams of O_2 molecules*, Physical Review A **91**, 4 (2015).

[166] K. Dulitz, N. Vanhaecke, and T. P. Softley, *Model for the overall phase-space acceptance in a Zeeman decelerator*, Physical Review A **91**, 1 (2015).

[167] K. Dulitz, J. Toscano, A. Tauschinsky, and T. P. Softley, *Zeeman deceleration of metastable nitrogen atoms*, Journal of Physics B: Atomic, Molecular and Optical Physics **49**, 075203 (2016).

[168] N. Akerman, M. Karpov, L. David, E. Lavert-Ofir, J. Narevicius, and E. Narevicius, *Simultaneous deceleration of atoms and molecules in a supersonic beam*, New Journal of Physics **17** (2015).

[169] M. N. Bera, *Zeeman Deceleration of Supersonic Beam: Trapping of Paramagnetic Atoms in a Traveling Magnetic Wave*, PhD thesis, Université Paris sud Orsay, 2011.

[170] L. P. Parazzoli, N. J. Fitch, P. S. Zuchowski, J. M. Hutson, and H. J. Lewandowski, *Large effects of electric fields on atom-molecule collisions at millikelvin temperatures*, Physical Review Letters **106**, 1 (2011).

[171] G. Quéméner and J. L. Bohn, *Ultracold molecular collisions in combined electric and magnetic fields*, Physical Review A **88**, 1 (2013).

[172] A. Mizouri, *A Moving-Trap Zeeman Decelerator*, PhD thesis, Durham University, 2016.

[173] G. B. Kistiakowsky and W. P. Slichter, *A high intensity source for the molecular beam. Part II. Experimental*, Review of Scientific Instruments **22**, 333 (1951).

[174] B. Bertsche, J. Jankunas, and A. Osterwalder, *Low-temperature Collisions between Neutral Molecules in Merged Molecular Beams*, Chimia **68**, 256 (2014).

[175] M. D. Morse, *Supersonic beam sources*, Experimental methods in the physical sciences **29**, 21 (1996).

[176] J. B. Anderson and J. B. Fenn, *Velocity Distributions in Molecular Beams from Nozzle Sources*, Physics of Fluids **8**, 780 (1965).

[177] H. Haberland, U. Buck, and M. Tolle, *Velocity distribution of supersonic nozzle beams*, Review of Scientific Instruments **56**, 1712 (1985).

[178] J. Li and S. K. Dhali, *Simulation of microdischarges in a dielectric-barrier discharge*, Journal of Applied Physics **82**, 4205 (1997).

[179] K. Luria, N. Lavie, and U. Even, *Dielectric barrier discharge source for supersonic beams*, The Review of scientific instruments **80**, 104102 (2009).

[180] U. Even, *Pulsed Supersonic Beams from High Pressure Source: Simulation Results and Experimental Measurements*, Advances in Chemistry **2014**, 1 (2014).

[181] J. Jankunas, K. S. Reisyan, A. Osterwalder, J. Jankunas, K. S. Reisyan, and A. Osterwalder, *Preparation of state purified beams of He, Ne, C, N, and O atoms*, The Journal of Chemical Physics **142**, 104311 (2015).

[182] W. Ketterle and D. E. Pritchard, *Atom cooling by time-dependent potentials*, Physical Review A **46**, 4051 (1992).

[183] M. Greiner, I. Bloch, T. W. Hänsch, and T. Esslinger, *Magnetic transport of trapped cold atoms over a large distance*, Physical Review A **63**, 1 (2001).

[184] J. H. Moore, C. C. Davis, and M. A. Coplan, *Building Scientific Apparatus*, Fourth ed. (Cambridge University Press, 2009).

[185] H. W. Ott, *Noise reduction techniques in electronic systems* (John Wiley and Sons, 1976).

[186] M. Mardiguian, *How to Control Electrical Noise* (Interference Control Technologies, 1983).

[187] D. R. J. White and M. Mardiguian, *EMI Control Methodology and Procedures*, Fourth ed. (Interference Control Technologies, 1985).

[188] A. V. Mezhiba and E. G. Friedman, *Inductive properties of high-performance power distribution grids*, IEEE Transactions on Very Large Scale Integration (VLSI) Systems **10**, 762 (2002).

[189] J. M. Guichon, J. Aimé, J. L. Schanen, C. Martin, J. Roudet, E. Clavel, M. Arpillière, R. Pasterczyk, and Y. Le Floch, *Busbar design: How to spare nanohenries?*, Conference Record - IAS Annual Meeting (IEEE Industry Applications Society) **4**, 1865 (2006).

[190] F. W. Grover, *Inductance Calculations: Working Formulas and Tables* (Courier Corporation, 2002).

[191] A. E. Ruehli, *Inductance Calculations in a Complex Integrated Circuit Environment*, IBM Journal of Research and Development **16**, 470 (1972).

[192] N. Mohan, T. M. Undeland, and W. P. Robbins, *Power Electronics: Converters, Applications, and Design*, 3rd ed. (John Wiley and Sons, 2002).

[193] F. Blaabjerg, *Snubbers in PWM-VSI-inverter*, PESC '91 Record 22nd Annual IEEE Power Electronics Specialists Conference , 104 (1991).

[194] L. Sandrolini, U. Reggiani, and G. Puccetti, *Analytical calculation of the inductance of planar zig-zag spiral inductors*, Progress In Electromagnetics Research **142**, 207 (2013).

[195] F. Lekien and J. Marsden, *Tricubic interpolation in three dimensions*, International Journal for Numerical Methods in Engineering **63**, 455 (2005).

[196] L. Landau and E. M. Lifshitz, *Mechanics (Volume 1 of A Course of Theoretical Physics)* (Pergamon Press, 1969).

[197] M. R. Tarbutt, J. J. Hudson, B. E. Sauer, and E. A. Hinds, *Preparation and manipulation of molecules for fundamental physics tests*, in *Cold molecules: Theory, Experiment, Applications*, chap. Chapter 15, CRC Press, 2009.

[198] A. O. G. Wallis, E. J. J. Longdon, P. S. Żuchowski, and J. M. Hutson, *The prospects of sympathetic cooling of NH molecules with Li atoms*, The European Physical Journal D **65**, 151 (2011).

[199] N. E. Bulleid, S. M. Skoff, R. J. Hendricks, B. E. Sauer, E. A. Hinds, and M. R. Tarbutt, *Characterization of a cryogenic beam source for atoms and molecules*, Physical chemistry chemical physics **15**, 12299 (2013).

[200] N. E. Bulleid, *Slow, cold beams of polar molecules for precision measurements*, PhD thesis, Imperial College London, 2013.

[201] M. Lara, J. L. Bohn, D. E. Potter, P. Soldán, and J. M. Hutson, *Cold collisions between OH and Rb: The field-free case*, Physical Review A **75**, 1 (2007).

[202] A. O. G. Wallis and J. M. Hutson, *Production of Ultracold NH Molecules by Sympathetic Cooling with Mg*, Physical Review Letters **103**, 183201 (2009).

[203] M. L. González-Martínez and J. M. Hutson, *Ultracold hydrogen atoms: A versatile coolant to produce ultracold molecules*, Physical Review Letters **111**, 1 (2013).

[204] P. Soldan, P. S. Zuchowski, and J. M. Hutson, *Prospects for sympathetic cooling of polar molecules: NH with alkali-metal and alkaline-earth atoms - a new hope*, Faraday Discuss. **142**, 191 (2009).

[205] W. C. Campbell, *Magnetic trapping of imidogen molecules*, PhD thesis, Harvard University, 2008.

[206] J. Lim, M. D. Frye, J. M. Hutson, and M. R. Tarbutt, *Modeling sympathetic cooling of molecules by ultracold atoms*, p. 1 (2015).

[207] T. V. Tscherbul, J. Kłos, and A. A. Buchachenko, *Ultracold spin-polarized mixtures of $^2\Sigma$ molecules with S-state atoms: Collisional stability and implications for sympathetic*, Physical Review A **84**, 040701 (2011).

[208] M. Warehime and J. Kłos, *Nonadiabatic collisions of CaH with Li: Importance of spin-orbit-induced spin relaxation in spin-polarized sympathetic cooling of CaH*, Physical Review A **92**, 032703 (2015).

[209] M. D. Frye, M. Morita, C. L. Vaillant, D. G. Green, and J. M. Hutson, *The approach to chaos in ultracold atomic and molecular physics: statistics of near-threshold bound states for Li+CaH and Li+CaF*, Physical Review A **93**, 052713 (2015).

[210] M. D. M. Nohlmans, *A permanent magnetic trap for buffer gas cooled atoms*, PhD thesis, Imperial College London, 2015.

[211] T. G. Tiecke, S. D. Gensemer, and A. Ludewig, *A high-flux 2D MOT source for cold lithium atoms*, Physical Review A **80**, 013409 (2009).

[212] Z. Lin, K. Shimizu, M. Zhan, F. Shimizu, and H. Takuma, *Laser cooling and trapping of Li*, Japanese Journal of Applied Physics **30**, 1324 (1991).

[213] C. C. Bradley, C. A. Sackett, J. J. Tollett, and R. G. Hulet, *Evidence of Bose-Einstein condensation in an atomic gas with attractive interactions*, Physical Review Letters **75**, 1687 (1995).

[214] H. J. Metcalf and P. van der Straten, *Laser cooling and trapping of atoms*, Journal of Optical Society of America **20**, 887 (2003).

[215] J. E. Sansonetti and W. C. Martin, *Handbook of basic atomic spectroscopic data*, Journal of Physical and Chemical Reference Data **34**, 1559 (2005).

[216] P. Hamilton, G. Kim, T. Joshi, B. Mukherjee, D. Tiarks, and H. Müller, *Sisyphus cooling of lithium*, Physical Review A **89**, 1 (2014).

[217] A. T. Grier, I. Ferrier-Barbut, B. S. Rem, M. Delehaye, L. Khaykovich, F. Chevy, and C. Salomon, *Λ-enhanced sub-Doppler cooling of lithium atoms in D1 gray molasses*, Physical Review A **87**, 1 (2013).

[218] U. Schünemann, H. Engler, M. Zielonkowski, M. Weidemüller, and R. Grimm, *Magneto-optic trapping of lithium using semiconductor lasers*, Optics Communications **158**, 263 (1998).

[219] N. Vanhaecke and O. Dulieu, *Precision measurements with polar molecules: the role of the black body radiation*, Molecular Physics **105**, 1723 (2007).

[220] J. Gillot, A. Gauguet, M. Büchner, and J. Vigué, *Optical pumping of a lithium atomic beam for atom interferometry*, European Physical Journal D **67**, 1 (2013).

[221] A. Mizouri, L. Z. Deng, J. S. Eardley, N. H. Nahler, E. Wrede, and D. Carty, *Absolute density measurement of SD radicals in a supersonic jet at the quantum-noise-limit*, Physical chemistry chemical physics **15**, 19575 (2013).